Thermo-Optical System Design of the Delft Deployable Space Telescope Baffle

MSc. Thesis
Yi-Qiang Fabbio Hu

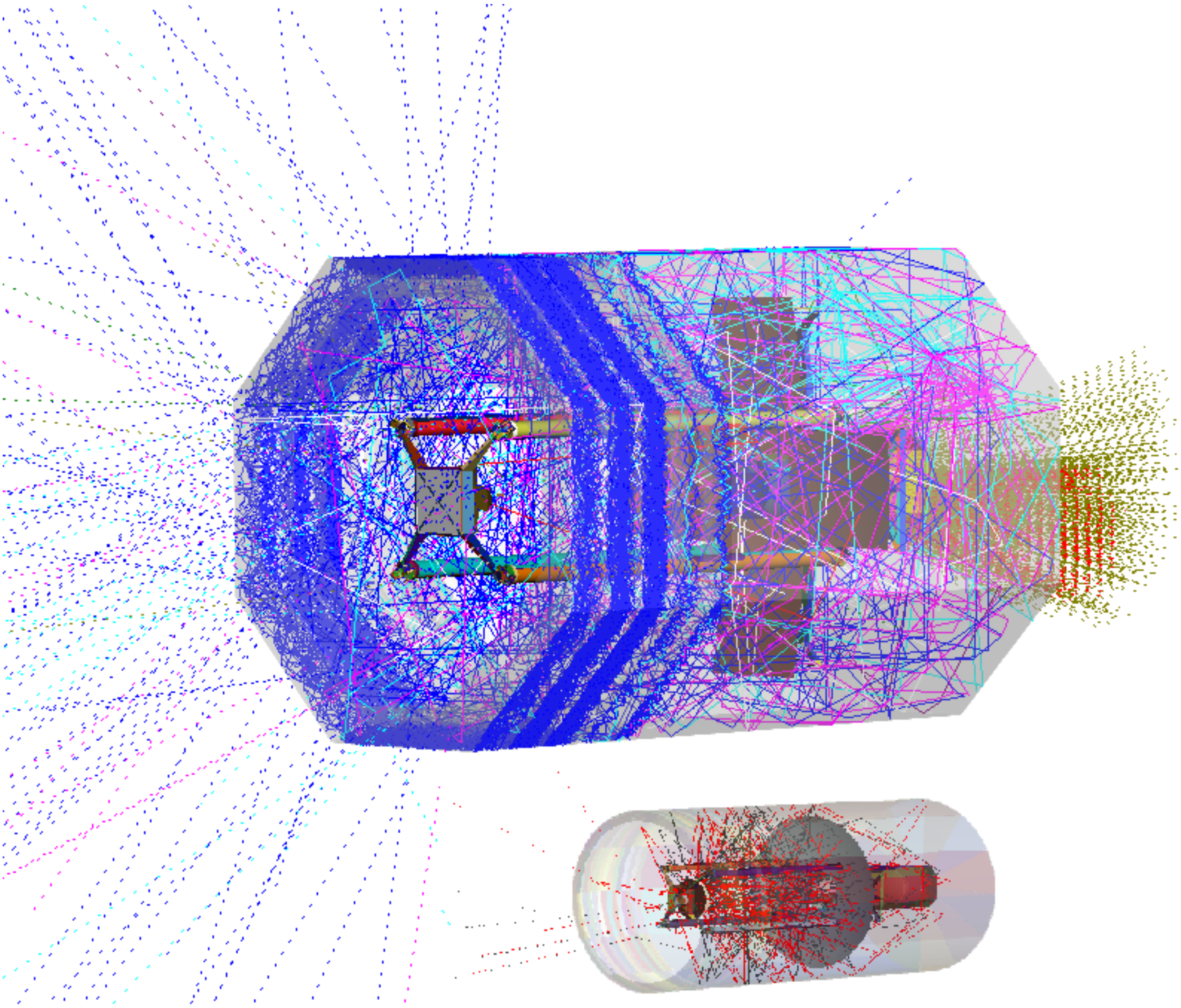

Thermo-Optical System Design of the Delft Deployable Space Telescope Baffle

MSc. Thesis

by

Y.F. Hu

Student number	4163095	
Thesis committee:	Dr. ir. J M. Kuiper	TU Delft, daily supervisor
	Dr. J. Guo	TU Delft, committee chair
	Dr. R.M. Groves	TU Delft

TU Delft

Summary

This thesis reports the further improvements to the baffle for the DST (Deployable Space Telescope). The baffle is a work-in-progress and a key element for enabling the DST by providing a stable thermal environment. This thesis is about the fundamentals of stray light design features and benefits to the baffle for both the visible light (VIS-DST) and thermal infrared (TIR DST) design.

Stray light is unwanted light reaching the detector as noise. Stray light can be categorised as either external i.e. from a light source or internal stray light to the system. External sources can provide an off-axis direct illumination if the detector is not well shielded. Internal stray light is scattered reflection from the surfaces of the instrument itself. Surfaces which can be seen by the detector are critical surfaces. Illuminated surfaces are those that receive light from a source. Scatter from surfaces which end up on the detector have to be both critical and illuminated. By obstructing the view from the detector to critical surfaces, the stray light can be reduced to zero. Internal stray light is furthermore a concern for thermally sensitive TIR DST as thermal self-emission (TSE). Multiple reflections on the internal baffle wall can lead to unwanted build-up or entrapment of heat. This can lead to a rise in temperature of the component, leading to a rise in thermal noise as TSE. Therefore, understanding the behaviour of internal stray light is fundamental in accelerating the feasibility of both DST versions. The method for controlling stray light can be summarised by either moving, blocking, painting, coating and cleaning surfaces.

The starting point of this thesis was the octagonal baffle design of Arink. The design process started with generating stray light adapted baffles. These changes are based upon geometric changes, following the moving or blocking process to prevent an object from being critical or illuminated. Several baffle concepts and design parameters were identified. Baffle concepts can be identified as either a regular (black) absorbing baffle or a reflective baffle design. The reflective baffle design is often characterised with precise vane geometry and location, highly sensitive to a deviation in shape and location. Due to the deployability of the baffle, reflective baffles were deemed to be unfeasible with current deployment technology. Other design parameters included the length, width and shape of the baffle. In addition, vanes could differ in angle, size and amount. These baffles were then analysed through a stray light analysis and thermal analysis. The stray light performance was performed with FRED, a ray tracing programme from Photon Engineering. The thermal performance of the baffles were analysed in ESATAN. The findings of both analyses were then compared to form the basis of the optimised baffle geometry for both the VIS-DST version and TIR-DST version.

The improvements to the VIS-DST baffle improved the compliance to the in-orbit drift requirement from 12% to 40%. Although not fully compliant, it is a step in making the VIS-DST more feasible. The proposed design rotates the original baffle by 22.5° about the optical axis. This change allows for a larger vane depth, increasing the blockage area induced by the vane with 39%. Furthermore, the amount of vanes is increased from 1 to 4 vanes, such that the scatter towards the secondary mirror is minimised. The second proposed implementation is to lengthen the booms by the average decrease in length due to thermal expansion. The deployment of the baffle can make use of the pantographic deployment system of Nagy which allows for attachment of multiple vanes.

The switch from the VIS domain to TIR domain, results in an in-orbit drift budget relaxation of about 10 times. Because TSE is in the same wavelength as the observing wavelength, the detector can sense TSE. The designed TIR baffles are all compliant to the in-orbit drift. The best performing baffle for the TIR-DST is the 60 cm cylindrical baffle with one vane at the entrance of the baffle. This baffle allows for deploying the baffle into multiple sections, as was requested during the top-level systems engineering meeting of the DST team. The single vane proved to be enough and also decrease the temperature range of the components by 2 K. The total TSE analysis provided insight on the main contributor to TSE which was the spider at 70%.

The thesis goal was reached by providing a geometrical design for the deployable baffle for the VIS and TIR DST which improves the stability of the temperature and reduce stray light. The stray light from TSE of the TIR DST baffle only contributes to 1% of the total TSE entering the system. The improvements made with the baffle contribute to better observational data by minimising noise.

Preface

At last. After many years of combining student life, work, sports, association and voluntary work, I am delighted to finish my thesis. Ever since I saw Star Wars as a young kid, I have been grasped by flying objects. This sparked a younger self to search through the library for knowledge on airplanes and space shuttles. From that moment, I have always been in pursuit of an Aerospace degree. It was a tough road to get there, but the turbulence was not enough to bring me down. I would like to thank my family and friends for the tremendous support and believe!

Special thanks go out to Hans Kuiper for allowing me to work on this special project and allowing me to digress slightly, which ultimately led to taking a bit more time to complete the thesis. Dennis Dolkens for the amazing help and insight on all things related to optics and optical system. Furthermore the DST team, that I spoke to multiple times throughout the week even through COVID-19! Last but not least, Photon Engineering has been a major supporter for allowing me to use FRED license to finish my thesis!

Y.F. Hu
Delft, July 2022

Contents

List of acronyms

AO	Atomix Oxygen
ATC	Active Thermal Control
CEC	Compound Elliptical Concentrator
CORE	COmpliant Rolling-contact Element
CPC	Compound Parabolic Concentrator
CTE	Coefficient of Thermal Expansion
FORTA	Fast Optical RayTrace Application
GCF	Geometrical Configuration Factor
GUI	Graphical User Interface
HEXOBA	High EXpansion Optical Barrel Assembly
JWST	James Webb Space Telescope
LEOP	Launch and Early Operations
M1	Primary Mirror
M2	Secondary Mirror
M3	Tertiary Mirror
PM	Primary Mirror
PMAO	Primary Mirror Active Optics
PMSS	Primary Mirror Support Structure
PSF	Point Spread Function
PST	Point Source Transmittance
SEDOBA	Strain Energy Deployable Optical Barrel Assembly
SM	Secondary Mirror
SMSS	Secondary Mirror Support Structure
SST	Solar Space Telescope
TIR DST	thermal infrared version of the Deployable Space Telescope
TMA	three-mirror anastigmatic
TRL	Technnology Readiness Level
TSE	Thermal Self-Emission
VIS DST	visible light version of the Deployable Space Telescope

List of Figures

List of Tables

1

Introduction

Earth observation satellites have existed for a few decades. These satellite aid humans in obtaining a large view of Earth, to provide insight on for example seasonal changes or predict the weather. WorldView is currently the highest resolution commercial satellite in the visible spectrum with a ground resolution of 31 cm [15]. These satellites are bounded by the volume and mass constraint of the launch vehicle. Delft University of Technology developed the visible light version of the Deployable Space Telescope (VIS DST) to liberate from the constraints of the launch vehicle without a decrease in optical performance. An overview of the progress made on the Deployable Space Telescope is given in Chapter 2. One of these challenges is to design a baffle which shields the optical system from the harsh space conditions. The DST experiences continuous exposure to Earth albedo and infrared, whilst receiving roughly $1400W/m^2$ of sun in the sunlit part of the orbit. When the telescope goes into eclipse, the heat flux from the sun is temporarily stopped. This causes a large thermal disturbance, resulting in defocus caused by thermal expansion. The function of the deployable baffle is to combat the defocus by lowering the thermal gradients. The first iteration of the baffle was developed by Korhonen [16]. The design of Korhonen was further improved by Arink [3], however the deployment mechanism was questionable and the thermal performance could be improved on. Arink made the recommendation of using stray light methods to improve the thermal performance of the baffle, sparking the beginning of this thesis. The goal and research questions of this thesis are provided in Chapter 3.

Chapter 4 provides theory on the causes of stray light and how to quantify the stray light performance. Existing stray light adapted baffles are given, which can be split up into a reflective and a specular baffle. This information provides the backbone for generating stray-light adapted baffle concepts. Only the geometry of the baffles are changed. This allows for quantifying the stray light and thermal performance of the baffles due to only a geometric change of the baffles. These VIS DST baffles are then used to analyse the stray light and thermal performance in the subsequent chapters. Chapter 5 documents the stray light analysis performed in FRED, a ray tracing programme[17]. The optical model of the VIS system have already been modelled in FORTA and ZEMAX, but not in FRED. Therefore this chapter first starts off with validating the optical model in FRED, followed by validation of the integration of the mechanical model with the optical model. Afterwards, the stray light performance of the baffles can then be quantified using a script ran in FRED. Chapter 6 documents the thermal analysis of the VIS DST baffle performed in ESATAN. The temperature of key components related to the in-orbit drift are given for each baffle concept. This allows for analysing the thermal performance of the baffles. The baffles are compared to eachother and two systems engineering tools for comparing the baffles are given in Section 6.4. The final baffle design for the VIS DST and the trade-off considerations are given in Chapter 7. This chapter furthermore summarizes the key take-aways from the preceding chapters on the visible light baffle.

There was also interest in a DST that was capable of taking observations in the thermal infrared domain with the thermal infrared version of the Deployable Space Telescope (TIR DST) [18]. The longer wavelength observations used for the TIR DST does not require as tight of a mechanical and optical tolerance as the VIS version[11]. Background information is given on the switch from the VIS-baffle to a TIR-baffle is given in Chapter 8. As the observed wavelength of the system is changed, the budgets for in-orbit drift is changed. Several optical systems which emerged from top-level design are given and scaled towards 30 cm. The generated baffle concepts for the TIR DST are given in Section 8.5. The thermal performance of the TIR baffles is given in Chapter 9. The stray light analysis of the TIR baffle is given in Chapter 10. Due to the observed wavelength of the TIR DST, the detector is able to sense Thermal Self-Emission (TSE) from itself. The influence of TSE is investigated in Chapter 11 which provide the 2D image due to TSE, the major contributors to the TSE signal and potential ways to reduce the influence of TSE. From these two analyses, the trade-off can be made to select the baffle for the TIR. The conclusion on the selected DST TIR baffle is given in Chapter 12.

Finally, the conclusion and recommendation are given in Chapter 13. The answer to the main research question and smaller research questions are given. Recommendation on further improvements and design ideas are given which can be worked out by future students working on the DST project.

2

Overview of the Deployable Space Telescope

The goal of this chapter is to introduce the VIS DST project and the current status on the VIS DST. The DST will operate in the Earth Observation market given in Section 2.1, from which several requirements are derived for the DST. The optical design of the VIS DST is given by Section 2.2. The working principle and performance of several subsystems of the DST are given in Section 2.3. Mainly the performance of the secondary mirror is given, as it is crucial for the baffle to obtain desirable thermal gradients in the Secondary Mirror Support Structure (SMSS). The previous iteration of the deployable baffle are given in Section 2.4.

2.1. Earth Observation Market

The DST is an optical telescope which observes the Earth in the VIS domain (λ between 390 to 750 nm). Earth Observation (EO) satellites, which the DST classifies to, are used in a variety of domains for local and global mapping but also to monitor environmental changes. Furthermore, observing the Earth from a large distance allows for monitoring of large areas which are difficult to reach or hazardous to observe such as tropical cyclones or areas destroyed by wildfire.

The market for satellite-based EO industry is expected to have a total value of $3.5 billion in 2026, with an annual growth of 8% [19]. The report expects that from 2014 to 2024, more than 400 civil and commercial EO satellites with a total mass of 50 kg or higher will launch. These satellites will boast a continuous development towards smaller ground sampling distance (GSD) [20]. In order to observe and detect small objects and changes, a high spatial resolution is needed. The current highest spatial resolution available is obtained with the WorldView-3 and WorldView-4 satellite from the company called DigitalGlobe, which have a panchromatic spatial resolution of 31 cm [15]. These two satellites from DigitalGlobe are rather large, with the WorldView-4 weighing 2600 kg and being 5.40 m high. The development cost for the WorldView-4 satellite was estimated to be roughly $835 million [21]. Furthermore, the large outer dimension and weight of the WorldView-4 resulted in the satellite being launched by an expensive launcher such as the Atlas V.

The Deployable Space Telescope wants to develop a small, lightweight optical telescope which can compete against the WorldView-class satellites, whilst keeping the development cost low. The Deployable Space Telescope is an initiative and developed by TU Delft.

2.2. Design of the Optical System

The spatial resolution which can be achieved by an optical instrument is based on the diffraction limit. Light from a point-source going through a single-slit gives an Airy pattern, a central spot surrounded by several diffraction rings around it. By measuring the angle from the center at which the first minimum occurs is known as the diffraction limit, see Equation 2.1[22].

$$\sin\theta_r = 1.220\frac{\lambda}{D} \tag{2.1}$$

In this equation, θ_r is the angular resolution given by the Rayleigh diffraction limit in radians, λ is the frequency of the light being measured in Hertz and D is the aperture diameter in meter. For a satellite at orbital altitude h, the GSD at nadir is the distance between pixel centers and is given by Equation 2.2.

$$GSD = 2.44\frac{h\lambda}{D} \tag{2.2}$$

$$x = 2.44\frac{f\lambda}{D} \tag{2.3}$$

Equation 2.2 can be rewritten to 2.3 to introduce the f-number, which describes the light collection efficiency of an instrument [22]. The f-number is defined as the ratio of the focal length f to the aperture diameter D.
The f-number can be increased by decreasing the focal length or increasing the aperture diameter. In order to obtain a more accurate observation, the GSD should decrease which can be done by two ways:

1. Increase the aperture diameter
2. Increase the focal length

However, traditional space telescope systems consist of fixed non-moving mirrors. Traditional space telescopes cannot change the aperture diameter nor focal length of the system. These two parameters are limited to the size of maximum diameter which can be fitted inside a selected launch vehicle, therefore putting a restraint on the maximum obtainable aperture diameter. Thus, in order to obtain a more accurate observation, the spatial resolution should increase. This increases the size of the satellite which carries the optical imaging system as well as the development cost. Furthermore, a larger satellite requires the use of a large, more expensive launch vehicle.

The Deployable Space Telescope aims to provide the same or better spatial resolution as traditional telescopes such as those from WorldView at a lower price. This will be done by lowering the mass and volume of the telescope by utilising a deployable optics system. This allows for a larger aperture diameter by using multiple deployable mirrors which form one Primary Mirror (M1). In addition, the focal length of the system is increased by using a deployable system to increase the distance between the primary and Secondary Mirror (M2).

The deployable optics system carries several thermal-mechanical challenges. The mirror system has to deploy accurately and align itself in space. Once deployed, deformations in the optical system due to thermo-elastic influences have to be maintained within the spatial deformation budget. The spatial deformation budget has been put in place to ensure the alignment of the mirrors. One way to stay within the spatial deformation budget is to employ a baffle system which acts as a thermal barrier. The main functions of the baffle are enumerated below from Arink [3]:

1. Create a stable thermal environment by decreasing temperature fluctuations and thermal gradients
2. To attenuate and reject stray-light
3. To mitigate micrometeoroid- and debris impacts that would otherwise impact with the optical system

2.3. Working Principle of the Deployable Space Telescope Design

The first design of the DST shown in Figure 2.1 was made by Dolkens in 2015 [1]. The initial optical design by Dolkens is based on a full-field Korsch three mirror anastigmat. The first design comprised of three rectangular Primary Mirror (PM) segments which were folded along the main housing of the instrument in stowed configuration. The Secondary Mirror (SM) would deploy post launch phase using an articulated boom system.

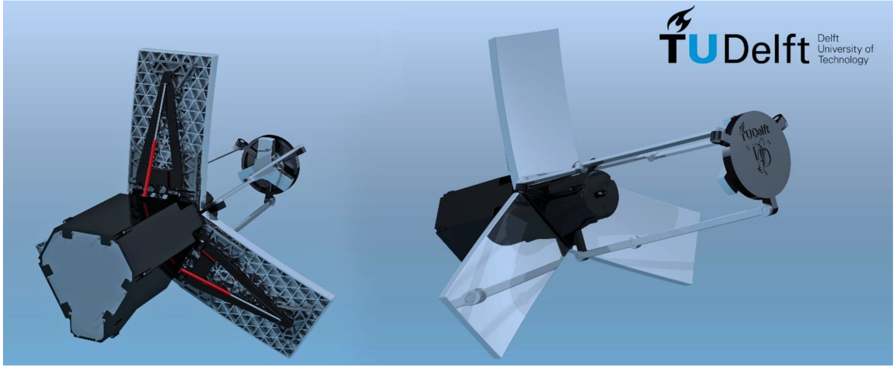

Figure 2.1: The first version of the DST by Dolkens in 2015 [1]

There are two different phases in the working principle of the DST. During the Launch and Early Operations (LEOP), several different segments of the DST are in stowed configuration. During the Operation Phase, all segments have been deployed and the DST is actively measuring scientific data.

- LEOP. During LEOP, the primary mirror, secondary mirror and baffle are in stowed position. The deployment sequence of the PM, SM and baffle starts after the DST is released from the launch vehicle and inserted into the right orbital configuration.
- Operational Phase. The PM, SM and baffle are deployed and the DST is obtaining scientific data.

Over the years, one of the main design changes to the DST is to use four instead of three primary mirror segments. In addition, the optical design changed to a Korsch annular-field three mirror anastigmat configuration. This configuration has several advantages [2]: no introduction of chromatic aberrations to the image, a highly accessible focal plane and a large proportion of usable field. Furthermore the configuration has an innate correction of spherical aberration, astigmatism, field curvature and coma. The DST consists of two deployable mirrors (the PM and SM) and one stationary mirror (the tertiary mirror) located within the spacecraft bus. An overview of the components, their function and the optical path are given in Figure 2.2. The functional flow block diagram for the DST alongside the deployment sequence of the optical system of the DST are given in Figure 2.3. The SM will deploy first, followed by the PM. After all the mirrors are in their final configuration, the baffle deploys.

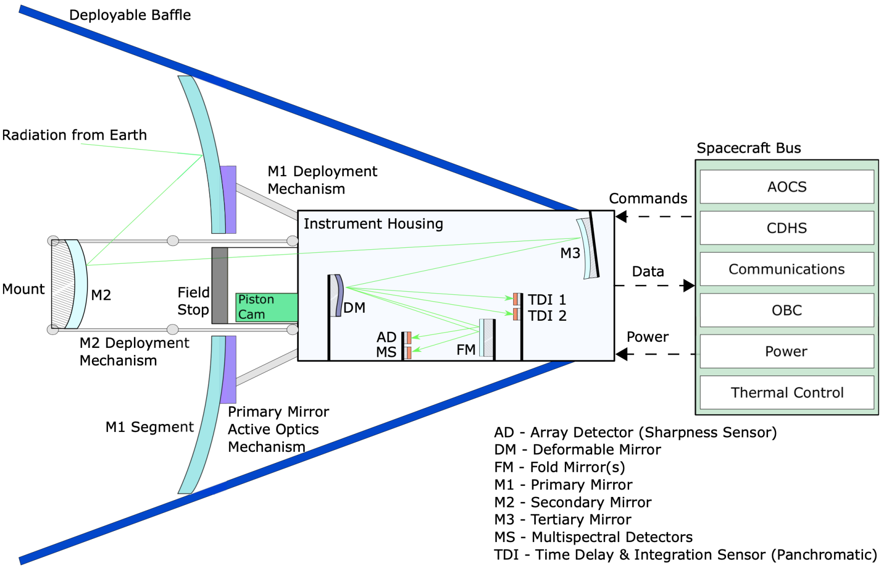

Figure 2.2: Schematic of the optical system of the DST and the optical paths, from Pepper [2]

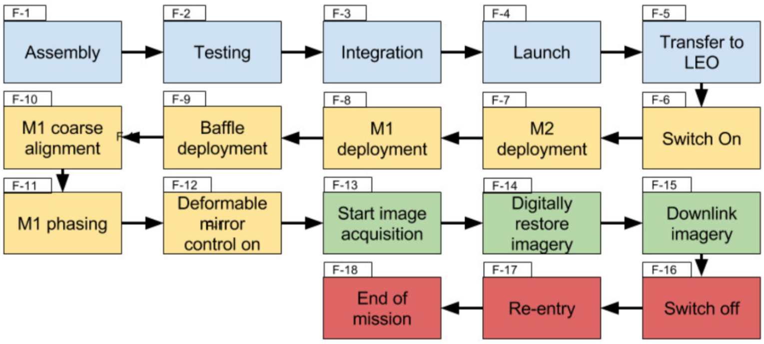

Figure 2.3: Functional flow block diagram for the Deployable Space Telescope from Pepper [2]

An overview of the primary mirror support system, the secondary mirror support system, instrument housing and baffle are summarised below and will be explained in further detail.

1. The **Primary Mirror Support Structure (PMSS)** supports the PM, unfolds from a stowed position towards the final operational position. The PMSS is calibrated using a Primary Mirror Active Optics (PMAO) system to remove deformations caused by external influences such as mechanical stress or temperature differences.
2. The **SMSS** supports the SM. It deploys using deployable booms to extend the focal length whilst complying with structural requirements.
3. The **baffle** creates a stable thermal environment such that thermo-elastic deformations are kept within the mechanical budget. In addition, the baffle creates a barrier to attenuate or reject stray-light from entering. Furthermore, the baffle aims to protect the optical system from debris and micrometeorite impact.
4. The **instrument housing** houses the tertiary mirror (Tertiary Mirror (M3)), the Deformable Mirror (DM), the Fold Mirror (FM), multiple optical detectors and sensors (AD, MS and TDI). The PMSS, SMSS and baffle are attached to the instrument housing. Misalignment of the PM is measured by a piston cam which is contained in the instrument housing.

5. The **spacecraft bus** contains all the other necessary satellite components which are not part of the optic system: attitude and orbit control system, command and date handling system, communications, on board computer, power and thermal control system. The spacecraft bus will be designed by Airbus Space and Defence Leiden.

2.3.1. Primary Mirror Support Structure

The PMSS was initially designed by van Putten [23] in 2017, but was updated by Corvers [24] in 2018 see Figure 2.4. An overview of the parts of the PMSS and its function are given. Secondly, the performance of the PMSS is reviewed with careful attention to the thermal performance.

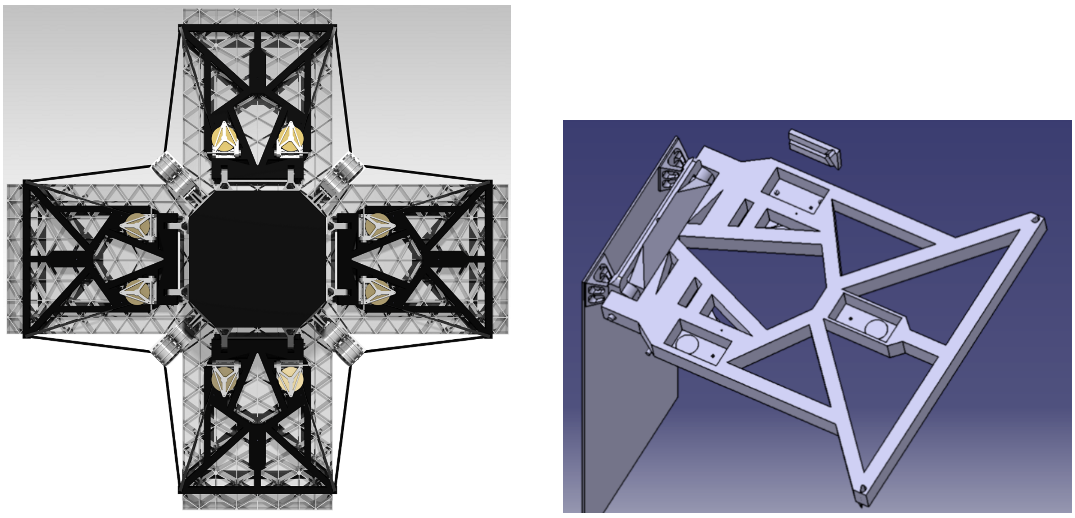

(a) The primary mirror support system deployed as seen from the spacecraft bus from Corvers [24]

(b) The support frame of the primary mirror support system from Corvers [24]

Figure 2.4: The primary support system of the DST

Design of the Primary Mirror Support Structure

- The **support frame** provides support to all the PMAO actuated flexures, whiffle plates, whiffle flexures in order to hold the PM segment in the desired orientation.
- The **whiffle plates** forms the interface between the whiffle flexures and actuated flexures.
- The **whiffle flexures** support the PM segments and provide a kinematic constraint to the PM.
- The **primary mirror actuated flexures** form the basis of the PMAO actuation system, these make it possible to adjust the PM in three degrees of freedom.

The support frame holds the primary mirror actuated flexures. The whiffle flexures consist of three flexures placed in the support frame to hold the PM, which are sufficient enough to remove discontinuous wavefront errors [1]. The flexures need to exhibit minimal local yielding in order to survive the launch loads. Furthermore, there has to be minimal shape change due to the exposure to rapidly changing thermal loads. The titanium alloy Ti-6Al-4V was chosen for the whiffle flexures, whiffle plates and actuated flexures after a design trade-off was made between different materials [2]. Beryllium I-70 and Al-7075 came in as secondary options if a light-weight structure or better transient thermal performance was needed.

Performance of the Primary Mirror Support Structure

The performance of the PMSS is based on Corvers design [24] and of Pepper [2]. The mass requirement of 16 kg for the PMSS was not met, the current design has a mass estimate of 25kg. Corvers found the in-orbit drift budget to be the most stringent to comply to. The in-orbit drift budget was defined by Pepper to be the maximum allowable spatial deviation between completion of an optical surface that can occur between completion of the last active calibration procedure and the end of the next image acquisition.

Pepper made a first in-orbit drift budget for the PMAO. It was found that in order to limit thermal expansion, an aluminium spacer with high Coefficient of Thermal Expansion (CTE) had to used with a low CTE Ti-6Al-4V piston. This was based on the principle of passively compensated athermalization by using a secondary material which either expands or contracts in the opposite direction of net growth of the assembly when exposed to a change in temperature [25]. The operational temperature for the PMAO system is 298 K with a temperature margin of ± 1 K. In order to account for uncertainties in the preliminary design, a margin of ± 15 K was established. The operational temperature including margin is 298 K ± 16 K. The resulting Δz drift of 12.8 nm happens with the aforementioned aluminium spacer and titanium piston for the ± 16 K case.

2.3.2. Secondary Mirror Support Structure

The SMSS holds the SM. The SMSS will deploy first from the spacecraft during LEOP. The most recent version of the SMSS is from the works of Krikken [26] in 2018. An overview of the parts of the SMSS and its function are given in Section 2.3.2. Secondly, the performance of the SMSS is reviewed with careful attention to the thermal performance in Section 2.3.2.

Design of the Secondary Mirror Support Structure

The required distance the SMSS has to protract the SM from the PM was established by Voorn [27] to be 1.6 m. This was chosen after a trade-off was made between increasing the focal length and optical stability of the SM. The design of Krikken of the SMSS consists of four deployable booms with tape-spring hinges, a spider structure, four top aluminium COmpliant Rolling-contact Element (CORE) hinges, four bottom aluminium CORE hinge and eight Kevlar ribbons. The SM is mounted to a hexapod structure. This hexapod is mounted to the spider.

The four deployable booms can protract a length of 1765.7 mm away from the PM. Each boom has a tape-spring hinge at 658 mm, measured from the bottom. During launch, the tape-spring hinges are folded up to stow the SMSS. The booms are made out of CFRP. The CTE was set to $\alpha = 0.8$ µm/m/K, deemed to be achievable in order to make the SMSS athermal.

The SM is held in place by a hexapod structure. The spider holds the hexapod structure and is 15 mm in width. The hexapod has six rods and these hold the mirror in place. The hexapod allows for thermal expansion of the spider and mirror, while keeping the mirror kinematically constrained. The material selected for the rods is Aluminium 7075-T6 to ensure athermalisation with a CTE of 0.8 µm/m/K. The spider is made of CFRP and connects the booms to the SM. The spider has the shape of a cross with a circular structure in the middle. To ensure stiffness of the spider, four crossbeams are added and are placed at the edge of the primary mirror segments to not obscure light. In order to minimise the gravitational effect, the hexapod is 2/3 the diameter of the SM [28] [29]. The part of the spider connecting to the top of the SMSS with CORE hinges is flanged to save mass as it is not a critical load-bearing component. This is a result of the CORE hinges not being able to transfer moment-forces, resulting in no internal moments at the tip.

The folding mechanism to deploy the SM consists of the CORE hinges to ensure accurate deployment and tape-spring mid hinges. The tape-spring hinge gives a low hysteresis and friction behaviour, without the need of lubrication. This was shown by Voorn [27] and Krikken [26].

Kevlar ribbons are added for stiffness to the spider structure and run from the PMSS to the top CORE hinges. It was mentioned by Krikken that during LEOP, the SMSS was exposed to the most extreme thermal environment due to the baffle still being stowed.

Performance of the Secondary Mirror Support Structure

In this subsection, the performance of the SMSS is reviewed with careful attention to the thermal performance. The total mass of the SMSS after updates by Voorn is 7.28 kg including a preliminary design safety margin of 20% [27]. The volume, AIT and deployment geometries are met based on verification of analysis. The SMSS was made athermal by using materials with different CTE in order to reduce deflections caused by thermal influences. The CFRP booms were set to a CTE of $\alpha = 0.8$ µm/m/K, deemed to be achievable in order to guarantee a constant offset between the PM and SM of 1600 mm by means of the SMSS being athermalised.

The deployment budgets have not been confirmed yet, as it follows from a thorough deployment analysis, out of the scope of Krikken [26]. However, it was mentioned that the deployment budgets are likely to be met due to having low hysteresis, namely the tape-spring hinge depends on elastic deformation and the CORE hinge depend on pure rolling contact.

The three main accuracy budgets: deployment accuracy, in-orbit drift and stability are met through modal- and random vibration analysis by Krikken [26]. The dampening effect the CFRP booms and Kevlar ribbons resulted in a maximum amplitude of 0.337 µm, within the stability budget.

The thermal aspects of the design of of the SMSS were not covered in detail by Krikken. The author did recommend some possible thermal improvements to the SMSS. Even though the system is made athermal in design, temperature gradients can still occur due to incoming heat fluxes. The author recommends the possibility of using sleeves as a protective thermal shield around the booms. The sleeves could absorb most of the heat flux in order to reduce translation of the booms due to thermally induced forces. In this approach, the sleeves should be thermally insulated from the booms and should not come into contact with the root and top hinges.

Furthermore, the spider is subjected to incoming heat fluxes. Lowering the thermal fluctuations of the spider whilst not blocking light for the primary mirror segments will decrease the thermal drifts of the whole system and is thus recommended as well.

2.4. Deployable Baffle

The need for a baffle for the DST emerged from van Putten his preliminary thermal analysis on the PMSS and SMSS [23]. A more thorough thermal analysis of the entire DST was done by van Wees with a focus on the baffle [30]. Simultaneously, the mechanical deployment system as well as the constituents of the thermal layers of the baffle were designed by Korhonen [16]. The thermal-mechanical design of the baffle was further optimised by Arink [3]. The importance of the baffle is to create a stable thermal environment for all the sub-systems and to attenuate and reject external and internal stray-light. The baffle has to adhere to a maximum stowed volume requirement of 1.5 m^3 and maximum mass requirement of 15 kg. The goal for the baffle is to have a stowed volume of 0.75 m^3.

The mechanical top-down budgets, found in Figure 2.5 were established by Pepper and determine the thermal requirements of the system [2]. The most stringent budgets arise from the in-orbit drift budget for M2. The reason for this is that M2 does not have Active Optics to correct the position of M2. The change of position is caused by thermal expansion in the booms and rods of the SMSS which hold M2. The most stringent translational requirement is 2 μm. The most stringent rotational requirement is 6 μrad. An explanation of the budgets is needed to further understand the budgets given by Pepper [2]. An overview of the requirements were implemented in the Systems Engineering tool of de Vries [31].

1. **Deployment Budget.** The maximum allowable deviation of the position of the optical surface from the desired datum after deployment and prior to coarse (or fine) calibration. This only applies to the the deployable elements: M1 and M2.
2. **Coarse Alignment Budget.** The maximum allowable deviation of the position of the optical surface from the desired datum after coarse alignment. This only applies to the active optics elements: M1 and M3. The coarse alignment budget holds for the eclipse time Δt_{coarse}.
3. **In-Orbit Drift Budget.** The maximum allowable spatial deviation of an optical surface that can occur between completion of the last active calibration procedure and the end of the next image acquisition, provided that the deviation can be considered (pseudo-)static over the period of image acquisition. The image acquisition period is Δt_{drift}.
4. **Stability Budget.** The maximum allowable spatial deviation of an optical surface during image acquisition

Note that though the numbers for the stability budget are lower than the in-orbit drift budget, the in-orbit drift budget is more stringent. This is because the stability budget is only taken over the course of time of an image acquisition period, which is in the order of microseconds to a second. The duration of time of the in-orbit drift budget which was named t_{drift} by Arink [32], was determined to be equal to the entire time the DST is able to acquire images. Which is equal to the total orbit time minus the time in eclipse. The coarse alignment budget is of importance during the eclipse time, in which there are no images being taken [32]. The coarse alignment budget is the maximum deviation allowed to align the mirrors during eclipse.

		Position			**Orientation**		**Radius**	**Shape Error**
Element	**X** [μm]	**Y** [μm]	**Z** [μm]	**X** [μrad]	**Y** [μrad]	**Z** [μrad]	[%]	[nm]
				Deployment/ Coarse Alignment Budget				
M1	2	2	2	2	4	50	1×10^{-3}	50
M2	15	15	10	100	100	100	1×10^{-2}	25
M3	4	4	4	10	10	50	1×10^{-3}	10
				In-Orbit Drift Budget				
M1	2×10^{-2}	2×10^{-2}	2×10^{-2}	1×10^{-2}	2×10^{-2}	5	1×10^{-4}	5
M2	4	4	2	6	6	12	1×10^{-4}	5
M3	1×10^{-1}	1×10^{-1}	1×10^{-1}	1	1	5	1×10^{-4}	5
				Stability Budget				
M1	5×10^{-3}	5×10^{-3}	5×10^{-3}	2.5×10^{-3}	1×10^{-2}	5×10^{-1}	n/a	n/a
M2	1	1	5×10^{-1}	1.5	1.5	3	n/a	n/a
M3	2.5×10^{-2}	2.5×10^{-2}	2.5×10^{-2}	2.5×10^{-1}	2.5×10^{-1}	1.25	n/a	n/a

Figure 2.5: Mechanical top-down budgets, from Pepper [2]

The baseline baffle from Korhonen and van Wees resulted in a baffle which weighed 23.6 kg and had a stowed volume of 1.8 m^3. The thermo-elastic deformations (translation and rotation) of M2 were 3.2 μm and 9.1 μrad, not conforming to the mechanical top-down budget of Pepper. This lead to the further optimisation of the thermal mechanical baffle done by Arink. The improvements resulted in a mass of 12.18 kg, stowed volume of 1.44 m^3 and thermo-elastic deformation of 2.7 μm and 2.6 μrad of M2 with passive thermal control. In order to meet the most stringent mechanical top-down budget, Active Thermal Control (ATC) had to be added. The addition of ATC to the baffle, lead to a maximum translation and rotation of 0.9 μm and 2.4 μrad in worst case condition. An overview of the thermal shielding performance of the different baffle designs are given in Table 2.1.

The ATC of Arink his baffle consists of eight individual 287 W Polymide Thermofoil heater [3]. The heaters are activated when the inner baffle temperature goes below +15 ^{o}C and switched off when the inner baffle temperature goes above +22 ^{o}C. When all the heaters are switched on, the ATC uses 2.3 kW of energy.

Though the baffle of Arink meet the requirements set for his thesis work, it is hypothesised that the baffle can be further optimised. Arink recommends optimisation of the baffle through stray-light control. Ultimately, the goal is valorisation of a passive thermal baffle which can be used for a multitude of scientific spacecraft instruments such as EO instruments and infrared cameras. The deployed baffle as designed by Arink can be seen in Figure 2.6 from [3]. A render of the stowed configuration was not made and hence is not available.

Table 2.1: Baseline thermo-elastic performances of Baffle. Most stringent thermo-elastic deformations which occur in the booms and rods of the Secondary Mirror Support Structure which hold the Secondary Mirror M2 are given, from [3]

	Maximum In-Orbit Drift	**Thermo-Elastic Deformation Booms**	**Thermo-Elastic Deformation Rods**	**|Athermalized M2|**
Baseline 1, without baffle				
Translation [μm]	2	32.4	42.1	9.7
Rotation [μrad]	6	8.3	928.3	920.1
Baseline 2, Korhonen design				
Translation [μm]	2	5.4	2.2	3.2
Rotation [μrad]	6	35.9	44.9	9.1
Baseline 3, Arink baffle without ATC *(Nominal Case)*				
Translation [μm]	2	3.2	0.6	2.7
Rotation [μrad]	6	1.5	4.1	2.6
Baseline 4, Arink baffle with ATC *(Worst Case)*				
Translation [μm]	2	1.3	0.4	0.9
Rotation [μrad]	6	2.7	5.1	2.4

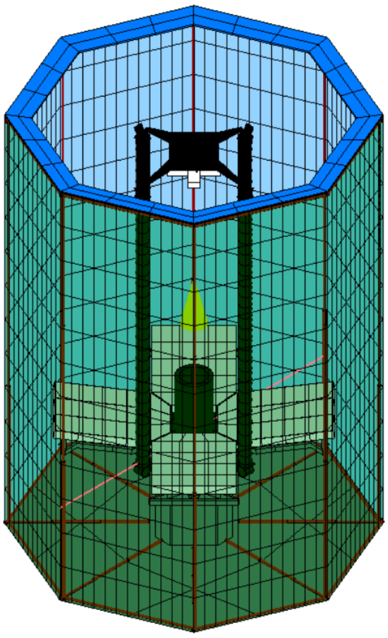

Figure 2.6: Final design of Arink his baffle in deployed configuration. The baffle sides are made transparent. In red, the support frame of the deployable baffle can be seen. From Arink [3]

2.4.1. Thermal-Mechanical Overview of the Deployable Baffle of Arink

Several design changes were made by Arink on the original deployable baffle design of Korhonen. In this section, the changes are each highlighted and the rationale of Arink is explained[3].

Shape of Baffle: Octagonal Cylindrical Shape

The shape of the baffle was analysed again by Arink in order to combine the findings of van Wees whom analysed the thermal performance and of Korhonen whom analysed the mechanical performance. The baseline trade-off was performed on the cylindrical- and cubical baffle shape, as Korhonen concluded that these two shapes performed the best. The thermal performance trade-off was done with three different coatings. The cylindrical shaped baffle lead to superior thermal gradients in the booms and rods for all coatings. The mechanical performance was also found to be better for the cylindrical shape. The cylindrical shape is more efficient in terms of the area to be covered by thermal shielding. Naturally, less thermal shielding material is needed to cover a cylindrical area in comparison to a cubical area. The lower mass of the cylindrical shape leads to a higher eigenfrequency as can be seen from Equation 2.4. In addition, ANSYS analysis of both shapes showed that the cylindrical shape (triangulated to an octagonal shape) showed a higher eigenfrequency than the cubical concept (1.53 Hz compared to 1.27 Hz) [16].

$$\omega_n = \sqrt{\frac{k}{m}} \tag{2.4}$$

Height of Baffle: 2.65 m

The height of the baffle design was revisited by Arink. The importance of selecting the height of the baffle is caused by the quadratic relationship to the view-factors which influence the Gebhart factor between multi surfaces. The selected range of heights to be assessed was between 2.5 m and 2.9 m.

- The **minimum height of 2.5 m** was set as a minimum to cover the SMSS spider.
- The **maximum height of 2.9 m** was set as the maximum because at that height, the temperature of the M2 is 50.3 ^{o}C. Higher heights exceed requirement BAF-T-01-03 which imposes that all sub-systems shall stay within -20 to +50 ^{o}C.

The thermal analysis by Arink showed that two heights showed promising thermal results: 2.65 m and 2.725 m. It is not clear, how these two data points emerged from the analysis and whether smaller increments in the range between 2.65 and 2.725 m were present which might show a better thermal performance. Ultimately Arink chose the 2.65 m baffle height over the 2.725 m height due to the following reasons [3]:

1. The 2.65 m baffle has lower thermo-elastic athermalized rotation: 69.5 μrad compared to 125.8 μrad
2. The 2.725 m baffle has lower athermalized translation: 18.5 μrad compared to 19.8 μrad
3. The 2.65 m baffle yields a lower mass and volume when the same materials are used.
4. The 2.65 m high baffle yields better structural integrity
5. The 2.65 m high baffle needs less deployment force to deploy the booms.

Radius of the Baffle: 1000 mm

The radius of the baffle had to be minimised in order to minimise heat entering the interior of the baffle. The constraint to the minimum radius of the baffle, is the requirement BAF-MEC-04-04-02-01 which states that the minimum clearance between M1 and any point of the baffle in deployed configuration is 200 mm. The arc length of M1 was 750 mm. The selected radius by Arink including safety margin was 1000 mm.

MLI Lay-Up: five layers

The MLI is modelled as a surface with two layers (the inside and outside) with an effective emissivity and conductivity. The effective emissivity takes into account various factors which were demonstrated through real-life performance data and accounts for the performance degradation experienced by MLI in the space environment. This method is called the Doenecke method [33] which has a strong heritage in literature [34]. The MLI for the DST consisted of alumimized Kapton as shield material and Dacron as the spacer layer. Arink chose five layers of MLI for the DST due to the following reasons:

1. The foldability of MLI was analysed by using the Euler-Bernoulli beam theory [35]. An analytical expression was obtained in which the minimum radius of curvature and thickness of the layers are related to the Yield point of MLI. Based on the maximum stowed threshold volume requirement of 1.5 m^3, a maximum of five layers of MLI could be used. This resulted in a stowed volume of 1.44 m^3 for five layers of MLI. Six layers of MLI violated the volume threshold at 1.96 m^3.
2. Five layers of sunshield has been selected by other space missions such as the James Webb Space Telescope (JWST) [36].
3. The mass budget allocated for MLI was 4.668 kg. Ten layers of MLI would fill up the mass budget for MLI. Five layers of MLI weigh 2.431 kg.
4. The stowed structural eigenfrequency requirement of ≥100 Hz is met by a maximum of seven layers of MLI. In other words, a maximum weight of 3.271 kg for the MLI. Thus five layers fit well within the budget.

To obtain an athermal system, 24 layers of MLI are needed. This was however not possible for the DST due to the established structural, mass and packing requirements. Furthermore, more layers of MLI could have potentially act as a shield against debris and micro-asteroid impact. But the marginal thickness of five layers of MLI is not enough to act as something as a whipple shield.

Outer Coating: SiOx/VDA/Kapton

The outer coating for the baffle was chosen by Arink to be a coating consisting of SiOx/VDA/0.5mil Kapton with $\frac{\alpha}{\epsilon} = \frac{0.19}{0.14} = 1.36$ [37]. The outer coating influences the temperature within the baffle, which have to be between -20 to +50 ^{o}C from requirement BAF-T-01-03. The optimal ratio for the outer coating being $\frac{\alpha}{\epsilon} \approx 2$ to account for sensitivity and uncertainty within the system. The SiOx/VDA/0.5mil Kapton was chosen due to its resistance against Atomix Oxygen (AO), prevention of outgassing and flight heritage.

Inner Coating: Magic Black

The inner coating was unchanged from Korhonen her decision of using Magic Black from Acktar with $\frac{\alpha}{\epsilon} = \frac{0.93}{0.84} = 1.11$ [16]. The inner coating should absorb as much heat flux as possible into the baffle in order to keep the heat inside of the baffle rather than emitting it back into the system.

Truncated Cone

The truncated cone was added by Arink to Korhonen her design. The four main requirements which Arink established for the truncated cone were:

1. Aspect angle $\leq$ 35 degrees
2. Emissivity ≤ 0.02 and absorptivity ≤ 0.07
3. Total mass of baffle including truncated cone shall not exceed the 15 kg requirement
4. Truncated cone shall be deployable

The truncated cone was added to the baffle for three reasons:

1. The truncated cone was a first approach to implement stray-light mitigation [38]
2. Decrease the thermal gradients in the SMSS athermalized system
3. Decrease temperature levels of the baffle telescopic boom structures

Arink performed a thermal analyses to determine the optimal aspect angle for the truncated cone. The athermal translational ratio saw the highest decrease for an aspect angle of 10 degrees with SiOx/VDA/Kapton coating. The author recommends further investigation on the coating and truncated cone in a proper stray-light analysis. The chosen material for the truncated cone was M55J, the same material which is used for the baffle. The truncated cone acts as a reflector and does not need to absorb the heat flux. Therefore, a thickness of 1 mm was chosen by Arink for a low mass of the truncated cone. Though a smaller ply thickness of 0.0061 mm is possible for M55J tape [39].

Active Thermal Control

ATC consisting of eight flexible Polymide Thermofoil heaters embedded in the MLI layers were added. These heaters turn on when the temperature is below +15^{o} C and switched off when the temperature is above +22^{o} C. Each heater uses 287 W, resulting in a total of Power of 2.3 kW when all the heaters are switched on.

Selection of the Telescopic Boom Structure

The first design of Korhonen consisted of eight inflatable booms which deploy from an origami-like stowed position. In the trade-off performed by Korhonen, the inflatable boom system performed the best with the telescopic boom system coming in second. This trade-off by Korhonen used the following trade-off variables: mass, stowed volume, deployment complexity, deployed stiffness and heritage. This was due to the assessed high mass, low storage efficiency and low heritage of the telescopic boom system [16]. However, Arink repeated the trade-off between the inflatable and telescopic boom systems because the design of Korhonen did not meet the stowed volume requirement BAF-SYS-11 of 1.5 m^3, was too complex and lacked structural integrity in stowed configuration. Three trade-off variables were added by Arink [3]: stowed stiffness, deployment control and flexibility.

1. **Stowed stiffness** comes from the functional requirement of the natural frequency of the stowed baffle to be in excess of 100 Hz in order to survive LEOP. This requirement came from discussion with ADS and the project team, to account for worst-case loading and has additional safety factors included.
2. **Deployment control** results in a more accurate deployed configuration of the intended design to enable the operational benefits of the baffle.
3. **Flexibility** of design is to allow for modifications such as attachment points or stray-light attenuation surfaces

3

Project Overview

In this Chapter, the main thesis need and goals are given in Section 3.1. Furthermore, the main research question is given in Section 3.2. In order to answer the research question, it is split up into smaller questions. The format in how these research questions should be answered are the thesis deliverables, which can be found in Section 3.3. Finally, the thesis methodology and set-up is given in Section 3.4.

3.1. Thesis Need and Goal

There is a need for understanding the influence of the baffle shape on the thermal environment inside of the baffle in order to progress the feasibility of the Deployable Space Telescope for the VIS and TIR DST.

The thesis goal is to reduce the stray light and stabilise the temperature of the DST components by using stray light methodology to design a baffle for both the VIS and TIR version.

3.2. Research Question

The main research question is formed through the prior work of previous students working on the DST project, and from dr. ir. J.M. Kuiper idea to improve the baffle:

"Can the drift between the primary and secondary mirror be reduced by applying stray light design methodology?"

The main research question can be divided into smaller research questions to guide the process of answering the main research question.

1. Which factors influence the drift between the primary and secondary mirror?
2. Which changes to the baffle can be made by applying stray light methodology?
3. How do these changes influence the thermal stability within the baffle?
4. How do these changes influence the stray light performance of the system?

3.3. Thesis Deliverables

The thesis deliverables are listed below.

1. Stray light adapted baffles for the VIS design which will be given in Section 7
2. Stray light adapted baffles for the TIR design which will be given in Section 12
3. Provide insight on the influence of design parameters of the baffle on the stray light performance in Section 13
4. Provide insight on the influence of design parameters of the baffle on the thermal budget in Section 13

3.4. Thesis Methodology and Set-Up

Thesis set-up follows roughly the stray light engineering process flowchart provided by Fest [4] found in Figure 3.1 with slight adaptations. The methodology and set-up will follow the foundation laid out from the research questions to form the desired output. The desired output being the baffles for the VIS and TIR version.

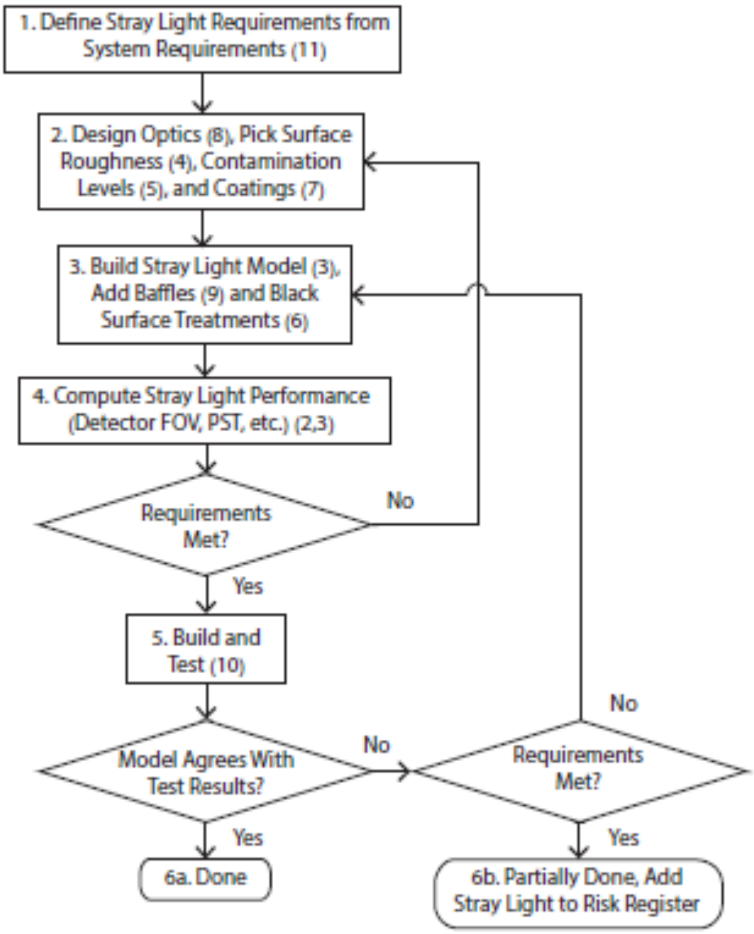

Figure 3.1: General stray light engineering process flowchart. Numbers refer to chapters from the Stray Light Analysis and Control book [4]

The breadboard model cannot be build and tested due to a constraint in time and cost, therefore the steps related to that are omitted. Following the process outlined by Fest, the thesis work is split up into two parts. This is needed because of the difference between the baffle concepts for the VIS DST and TIR DST. Both parts will therefore output a baffle specifically for the VIS version and TIR version.

In order to reach towards the output, the design parameters for the baffle first need to be established. These design parameters stem from literature study, looking at state-of-art baffles and legacy baffles. But other design parameters are of course size limitations set-up by requirements. From these design parameters, baffle designs can be formed for respectively the VIS and TIR version. These baffles are then assessed in terms of their stray light performance. Individually, the thermal performance of the baffle can be assessed. From both analyses, conclusions can be made and the best performing baffle can be selected. The influence of the TIR baffle on the TSE noise is added to strengthen the validity of the TIR concept. The information of the TSE is used to further develop key aspects such as the detector cooling for the thesis of L. Boer [40].

4

Stray Light

The causes for stray light is given in Section 4.1. Quantification of the stray light performance is often given in terms of the point source transmittance, described in Section 4.2. Calculation is performed to form an initial stray light requirement in Section 4.3. The baffle vane design parameters are given in Section 4.4. Baffles can be subdivided into two categories: specular baffles and reflective baffles, which provides some guidelines into their capability and feasibility for a deployable baffle design in Section 4.5. Finally, the generated preliminary baffle concepts are given in Section 4.6

4.1. Stray Light Causes

Stray light can be defined as unwanted light reaching the focal plane of an optical system [4]. The primary source of stray light for the DST is the sun. Sunlight could for example scatter on the internal wall of the baffle or on the SMSS. This scatter could reach the focal plane through multiple scattering paths. The scattering of light is generally called flare or veiling glare. Another type of stray light is ghost reflection. Ghost reflections occur when a light source within the image field undergoes multiple unwanted reflections to form a secondary image.

4.2. Point Source Transmittance

Description of the stray light performance is often described as a Point Source Transmittance (PST) metric given in Equation 4.1 [4]. The PST is equal to the amount of stray light on the focal plane E_{SL} due to stray light divided by E_{inc}. Where E_{inc} is the total irradiance received at the entrance aperture from a point source at infinity incident on the plane normal to the incident beam. The PST can be calculated by summing up the contribution of stray light sources or integrating the PST over the projected solid angle.

$$PST = \frac{E_{det}}{E_{src}} \tag{4.1}$$

In which E_{det} represents the irradiance at the detector, which can be calculated using Equation:

$$E_{det} = \frac{\Phi cos(\theta)}{A_{det}} \tag{4.2}$$

At the source, irradiance at normal incidence E_0 through:

$$E_0 = \frac{\Phi_{src}}{A_{src}} \tag{4.3}$$

In the PST calculation, the irradiance of the source E_{src} is taken normal to the plane wave direction. Thus source irradiance for a given incident angle is:

$$E_{src} = \frac{E_0}{cos(\theta)} \tag{4.4}$$

The PST is then finally calculated as:

$$PST = \frac{E_{det}}{E_{src}} \tag{4.5}$$

4.3. Stray Light Requirements

The maximum allowed image plane irradiance E_{SL} equal to minimum detectable irradiance, which is dependent on detector performance [4]. Accompanied by an exclusion angle requirement, which defines the minimum angle of stray light source at which the maximum allowed image plane irradiance is met. This requirement can be set to be equivalent to a single grayscale bit [4]:

$$E_{SL} = \frac{E_{scene}}{2^b} \tag{4.6}$$

Assuming an 8-bit grayscale bits, this equation expands to:

$$E_{SL} = \frac{L_{sun}\Omega_{sun-Earth}(\alpha/\pi)\Omega_{f/\#}}{2^8} \tag{4.7}$$

However, since the detector is not finalised yet. It was suggested by Dolkens to keep the detector out of the stray light analysis and instead compare the intensity of the stray light to the intensity of light originating from Earth [11]. The intensity of light originating from Earth consists of largely two components: Φ_{earth} and $\Phi_{Earth,sun}$. Where Φ_{earth} is the Earth component and $\Phi_{Earth,sun}$ is the reflection of the Sun from Earth onto the DST.

The radiant flux from the Earth can be simplified to Equation 4.8 [4]. In which L is the spectral radiance, A_s the surface of the source, A_c the surface of the collector surface and d the distance between the surfaces. In the case of the DST, the surface of the source is equal to the observable area of the DST. The FOV of the DST is 0.6° in the cross track direction and 0.25° in the along track direction. The surface of the collector is equal to the surface area of the primary mirror M1, which is $A_{M1} = 1.08\ m^2$. The distance d between the two surfaces is the orbital height H of the DST.

$$\Phi = \frac{L \cdot A_s \cdot A_c}{d^2} \tag{4.8}$$

The swath width in the cross track direction $S_{w,cross-track}$:

$$S_{w,cross-track} = H \cdot tan(0.6) \approx 5236m \tag{4.9}$$

The swath width in the along track direction $S_{w,along-track}$:

$$S_{w,along-track} = H \cdot tan(0.25) \approx 2182m \tag{4.10}$$

The area of the source A_s, or observable area, is then:

$$A_s = S_{w,cross-track} \cdot S_{w,along-track} \approx 11.4 \cdot 10^3 m^2 \tag{4.11}$$

The spectral radiance L can be expressed per unit wavelength using Equation 4.12 [22], where h is Planck's constant in $J \cdot s$, c the speed of light in m/s, k the Boltzmann constant in J/deg, λ the wavelength in m and T the temperature in K. For the red wavelength at $\lambda = 7 \cdot 10^{-7} m$, this leads to a spectral radiance of $L \approx 7 \cdot 10^{-21} W/m^3$.

$$L_\lambda = \frac{2hc^2}{\lambda^5} \frac{1}{e^{hc/\lambda kT} - 1} \approx 7 \cdot 10^{-21} W/m^3 \tag{4.12}$$

The total radiance L in the waveband can be calculated by integrating Equation 4.12 over the waveband of VIS [4]:

$$L = \int_{\lambda_1}^{\lambda_2} L_\lambda d\lambda \tag{4.13}$$

The visible light spectrum has a waveband of 300 nm. This results in a total power on the detector from the Earth Φ_{earth} in the VIS spectrum to be $1 \cdot 10^{-31} W$.

The radiant flux power of the Sun Φ_{sun} using Stephan-Boltzmann law, where A_{sun} is the area of the sun in m^2, σ the Stephan-boltzmann constant in J/k and T_{sun} the temperature of the sun in k, can be calculated as followed:

$$\Phi_{sun} = A_{sun}\sigma T_{sun}^4 = 3.826 \cdot 10^{26} W/m^2 \tag{4.14}$$

Where A_{sun} is calculated as:

$$A_{sun} = 4\pi R_{sun}^4 = 6.09 \cdot 10^{18} m^2 \tag{4.15}$$

The irradiance of Earth in Earth orbit $E_{earth,sun}$ is then, where AU is the astronomical unit in m:

$$E_{earth,sun} = \frac{\Phi_{sun}}{4\pi AU^2} = 1360 W/m^2 \tag{4.16}$$

The radiance from Earth due to the reflection of the sun is then, where ρ_{albedo} is the albedo reflection of Earth at 0.367, is calculated as followed:

$$L_{earth,sun} = \frac{\rho_{albedo} E_{earth,sun}}{\pi} = 158.9\ W/m^2 \cdot sr \tag{4.17}$$

It is assumed that the power on the detector $\Phi_{earth,sun}$ is equal to the absorbed power on the primary mirror that is received within the FOV. Therefore, the power on the detector from the sun reflected off of the surface of the Earth is calculated as:

$$\Phi_{earth,sun} = L_{earth,sun}\Omega_{dst}A_{M1} \tag{4.18}$$

The solid angle from the FOV in sr can be calculated as:

$$\Omega_{dst} = FOV_x \cdot FOV_y \cdot (\frac{\pi}{180})^2 = 0.6 \cdot 0.25 \cdot (\frac{\pi}{180})^2 \approx 4.6 \cdot 10^{-5} sr \tag{4.19}$$

This leads to $\Phi_{earth,sun}$ to be 0.0078 W. The total power on the detector is therefore $\Phi_{earth,sun} + \Phi_{earth} \approx 0.00784W$. The irradiance on the detector E_{det}:

$$E_{det} = L_{earth,sun}\Omega_{dst} = 7.3 \cdot 10^{-3}\ W/m^2 \tag{4.20}$$

If only 1% of the total power that is received on the detector, can be a consequence of stray light, then the stray light requirement can be calculated:

$$PST = E_{det} \cdot 1\% = 7 \cdot 10^{-5} \tag{4.21}$$

Therefore, the PST requirement can be formulated as:
T0.2-BAF-SHR-002: The Point Source Transmittance of the the VIS DST shall not be higher than $7 \cdot 10^{-5}$ [−]

4.4. Vane Design Parameters

Mitigation of stray light can be summarised through "move it, block it, paint it or clean it" [4]. The mitigation strategies applied, will be mainly based upon the two terms "move it, block it" which are the design parameters described in Section 4.4.1. The method for determining the location and size of these components is given in Section 4.4.2.

4.4.1. Baffle and Vane Design Parameters

The methods used to control stray light can be rewritten as design parameters for a stray light adapted baffle. In general, stray light methodology can be summarised as "move it, block it, paint/coat it or clean it" [4]. By moving a surface, the surface can be made not critical or illuminated. When a surface is no longer illuminated, it cannot cause scatter towards the focal plane. Blocking is usually referred to placing a surface in between the source and illuminated surface, such that the illuminated surface no longer receives incident light. "Paint/coat it" refers to altering the scatter properties of a surface through applying a paint or coating. Coatings can also alter the scatter properties by increasing the surface smoothness. Whereas "clean it" refers to reducing the contamination levels of particulates on the surface to reduce the scatter properties. These stray light optimisation strategies can be rewritten to form the design parameters of the baffle. These design parameters are summarised below:

- Baffle shape (specular, reflective baffle and sugar scoop)
- Vanes
- Coating for optical elements and paint for other items
- Cleanliness

The preliminary baffle concepts will only focuses on geometrical features. The preliminary baffle concept will utilise the same coating and materials chosen by previous designs from Arink and Akkerhuis [12, 32]. These choices allow for examining purely the effect of changing the geometry onto the stray light and thermal performance of the baffle. The detailed design will feature an analysis on the effects of choosing different coatings and cleanliness. The design parameters for vanes are given in Table 4.1 and illustrated in Figure 4.1.

Table 4.1: Design parameters for baffle vanes [4]

Vane Parameter	Definition
Angle	Angle relative to main baffle
Aperture	Diameter of the hole inbetween two opposing vanes
Bevel angle	Angle of bevel relative to vane surface
Coating	Type of paint or treatment
Depth	Distance from the tip of the vane to the baffle wall (length perpendicular to baffle wall)
Edge radius	Radius of curvature of edge of vane aperture
Spacing	Distance between adjacent vanes

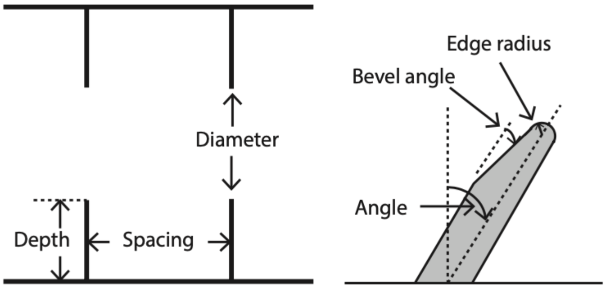

Figure 4.1: Baffle vane parameters [4]

4.4.2. Determination of vane location and size

The goal of the vane is to block first-order stray light paths without vignetting the FOV of the optical collector [4]. The vane radius $l_{v,depth}$ given by Equation 4.22 can be geometrically determined using Figure 4.2 where the vane radius is half of the vane diameter. Where L represents the length from the collector to the entrance aperture taken about the optical axis and θ_{min} the largest acceptance angle. The design of the DST requires a 0.347° off-axis angle of the incoming beam applied about the X-axis [11]. This general offset angle is needed to pass the light through the field stop which is placed off-axis. Furthermore, the maximum off-axis light which should pass through the field stop is light from a 0.25 degree along track direction (applied about the X-axis). For the DST, the angle $\theta_m in$ is equal to 0.347+0.25 = 0.597° with a length L of 1970 mm. The minimum vane radius $l_{v,r}$ equates to 20.6 mm, which is the minimal distance needed between M1 and the vane.

Since the final deployment mechanism has not been designed yet, it is chosen to take a margin into account. Arink reports an uncertainty margin of 1% for the deployment, which amounted to almost ±10 mm for the baffle width[3]. Taking into account an uncertainty margin of 1% would have a very small impact on the vane radius, therefore it is chosen to take into account the ± 10 mm margin. This results in a rounded value of 30 mm for $l_{v,r}$ for the distance between the top marginal ray and the tip of the vane. This should ensure that no vignetting occurs due to the placement of the vanes.

$$l_{v,depth} = L \cdot tan(\theta_{min}) \tag{4.22}$$

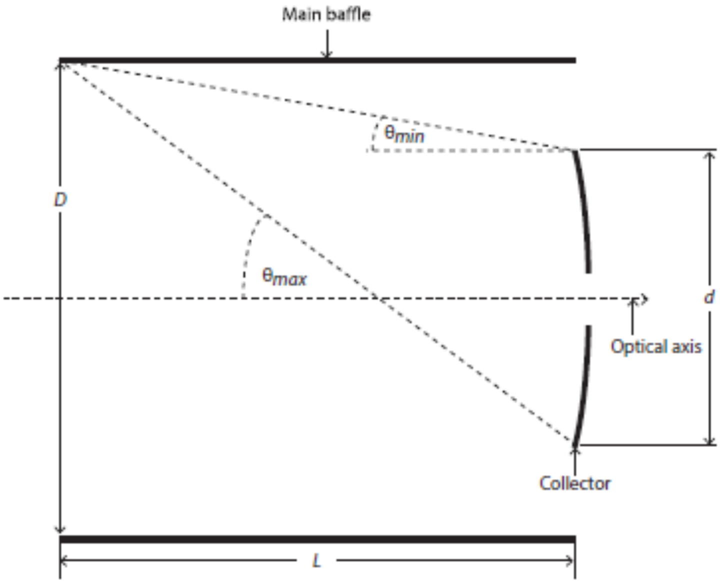

Figure 4.2: Vane diameter determination, D equals baffle diameter, L length of the baffle, $\theta_{min,max}$ minimum and maximum off-axis source and d the diameter of the collector [4]

The procedure for finding the vane location is given below [4]:

1. Draw a ray between the +y edge of the entrance aperture and the +y edge of the collector. This ray defines the "keep-out" zone that prevents the FOV of collector from being vignetted
2. Draw a ray from the -y edge of the critical portion of the collector to the +y corner of the main baffle
3. Place a baffle at the intersection between the horizontal ray from step 1 and the diagonal ray from line 2
4. Draw a ray from the -y edge of the entrance aperture to the +y edge of the second baffle vane from step 3
5. Draw a ray from the intersection point between the ray from step 4 and the main baffle to the -y edge of the critical portion of the collector
6. Place a baffle at the intersection point between the ray from step 1 and the ray from step 5

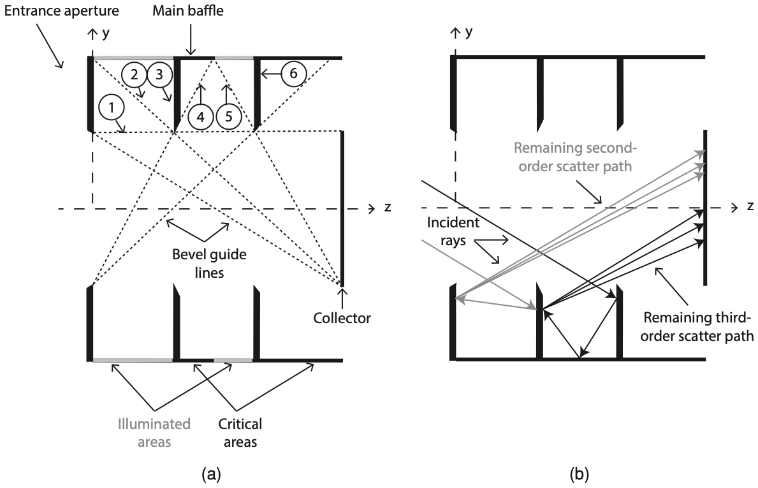

Figure 4.3: (a) Steps in a diffuse baffle vane design for a cold shield , and (b) examples of the remaining (higher-order) paths to the collector [4]

This method can be determined graphically by using the parametric design capability in CATIA. This is illustrated in Figure 4.4. By changing the lengths that are defined in green, the lengths of the other features change.

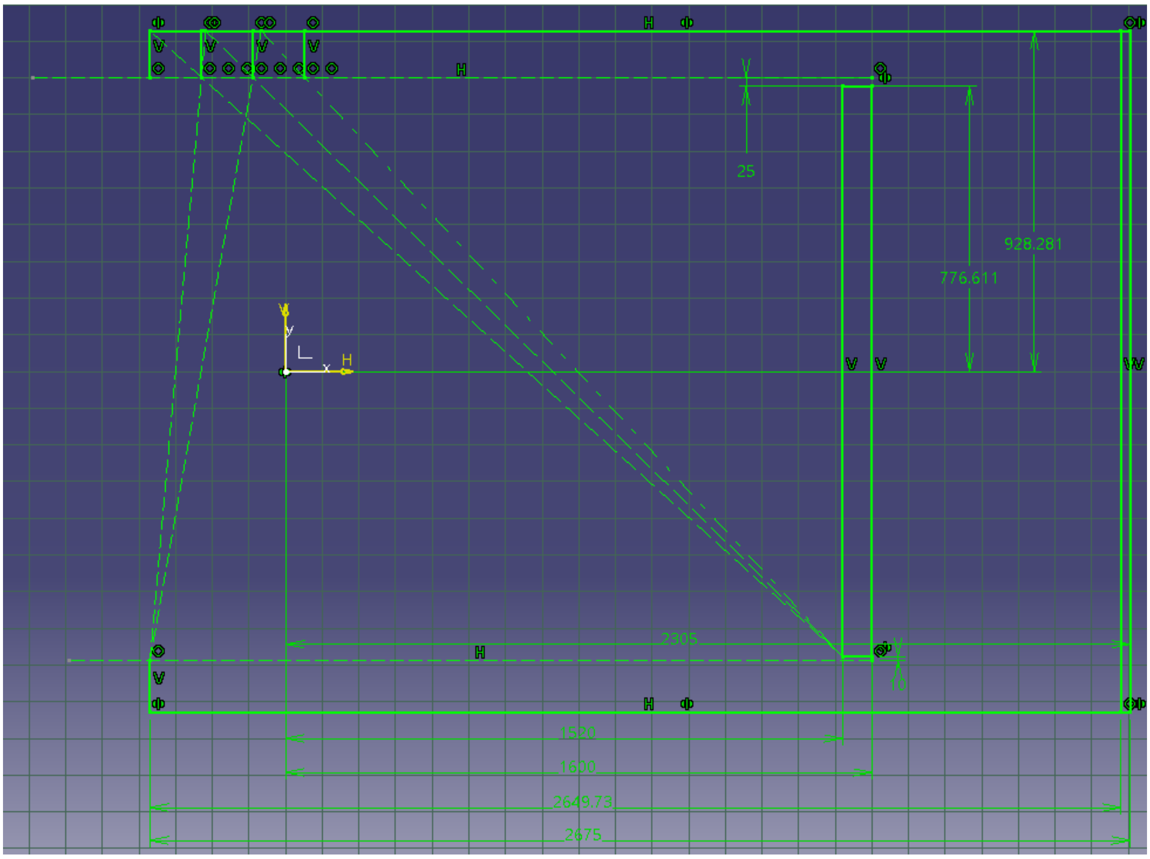

Figure 4.4: Determining vane location using parametric design in CATIA []

4.5. Existing Baffle Designs

In this section, existing baffle design are given. The baffles can be categorised into a (black) absorbing baffle design in Section 4.5.1 or reflective baffles in Section 4.5.2. The current state of art for these various baffles are given in Section 4.5.3.

4.5.1. Black Absorbing Baffles

The traditional approach to stray light reduction is with a black diffuse baffle. The black coating used is then low in reflectance and high in absorptance in order to attenuate single-scatter paths. However, the diffuse (high-emissivity) black baffle can absorb heat and become a source of increased background radiation at infrared wavelengths [5, 6].

4.5.2. Reflective Baffles

Reflective baffles utilise the method of having two extreme focal points, where incident light is reflected back out of the entrance aperture of the system inbetween the two extreme focal points [4, 6]. Types of reflective baffles are: elliptical, bielliptical, Linlor, Lockheed-Stavroudis, Compound Elliptical Concentrator (CEC) and Compound Parabolic Concentrator (CPC). Reflective baffle make use of specular, high reflective surface on the inside of the baffle facing the front aperture to increase the reflection out of the entrance aperture, reducing the power absorbed. For example, a copper layer coated with gold was deposited on the BELA instrument to enhance the specularity [41]. The surface near the optics should be diffuse, highly absorbing and low in emissivity to further reduce radiation towards the interior.

The amount of reflections outward determine the effectiveness of reducing the thermal load of the reflective baffle. Each reflecting vector going outward, is a source of second or higher order scatter. A small amount of the second degree or higher reflections go back towards the radiator at near-grazing angles. Due to the reflective surface of the baffle, far less energy is absorbed by the baffle before reaching the radiator [42].

Reflective Baffle: Elliptical Baffle

The simplest of reflective vanes is the elliptical vane design found in Figure 4.5 with the two extreme focal points indicated as focus point F1 and F2 [4]. The vanes must be positioned such that the incident rays cannot fall onto the baffle wall. When a secondary mirror is present within the baffle, the elliptical vanes should be limited to the entrance baffle portion. This to prevents undesirable scattering [5]. The initial reduction in aperture heat load in comparison to a diffuse black baffle design is 85%. Further optimisation of the elliptical baffle can be accomplished through the following points which are illustrated in Figure (4.6 left):

- Radially shift the focus points inwards to make it easier for skew rays to go past the vane in front
- Include a short forward extension, which prevents that meridional rays pass between the most front vane which would scatter to the entrance aperture as can be seen in Figure (4.6 left)
- Lower the BRDF of the back entrance aperture by applying a low-scatter specular black coating to contain unrejected rays between the entrance aperture and the first vane, which prevents specular paths to the primary optics as can be seen in Figure (4.6 right)

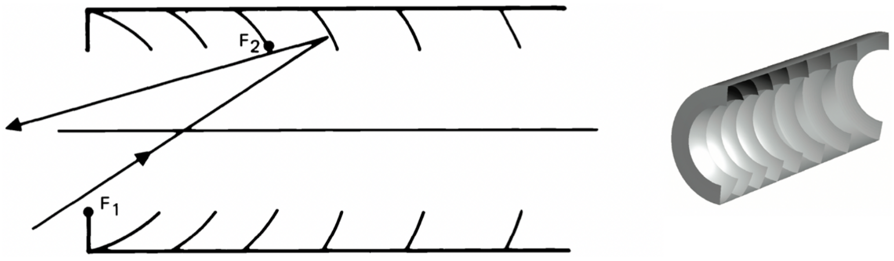

Figure 4.5: (left) Incident rays are rejected by the elliptical vane, which has one focus at the edge of the entrance aperture point F1 and another focus at the edge of the vane in front of it (point F2), (right) oblique view of the elliptical baffle [4, 5]

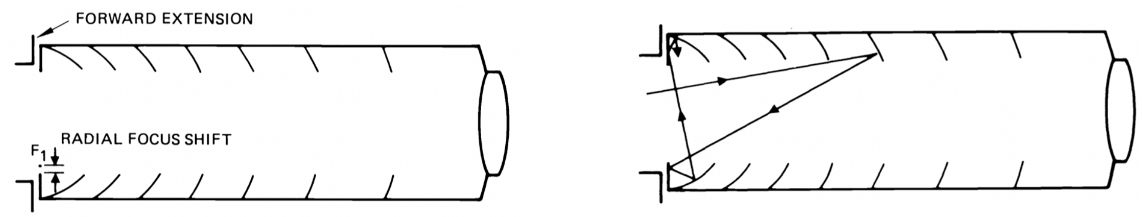

Figure 4.6: (left) Optimisation of the elliptical baffle through radial shift of the focus and addition of the forward extension. (right) entrapment of unrejected rays between the entrance aperture and the first vane [5]

Reflective Baffle: Linlor

The reflective Linlor design is shown in Figure 4.7. Each sharp vane edge has its unique curvature, which makes it more difficult to fabricate than the elliptical baffle due to the tight tolerances needed. The incoming light is seen to be reflected a couple of times between the vanes before exiting through almost the exact same incidence angle [6].

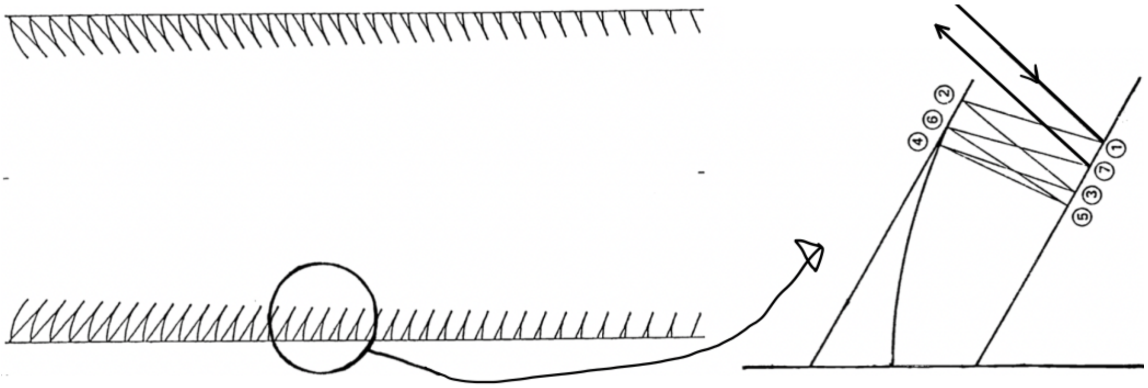

Figure 4.7: The reflective Linlor baffle. The magnified area shows how incident light is reflected back after multiple reflections [6]

Reflective Baffle: Bielliptical

The bielliptical baffle of Alan Greynolds consist of elliptical vanes which face forward and backward as shown in Figure 4.8. It needs fewer vanes than the Linlor baffle. Some skew incident rays reflect backwards.

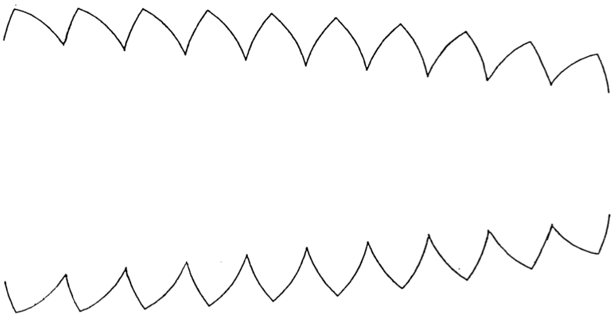

Figure 4.8: The bielliptical baffle, the vanes is made of ellipses facing forward and backward [6]

Reflective Baffle: Lockheed-Stavroudis

The patented Lockheed-Stavroudis design is shown in Figure 4.9 which vanes consists of alternating ellipses and hyperbolas [6]. The focus points of the different vanes causes that all incident rays reflect through the entrance aperture. The ellipses and hyperbolas intersect at right angles, which lead to robust vanes. The fabrication tolerance is looser than most typical tolerances [6]. At the rear of the baffle, multiple first-order scatter rays reflect back towards the optics which causes entrapment.

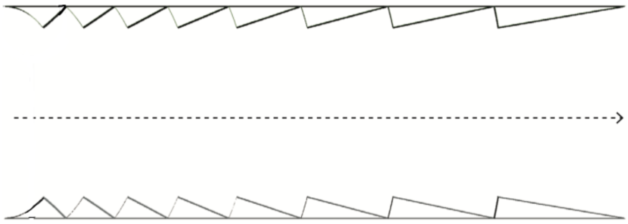

Figure 4.9: The patented Lockheed-Stavroudis baffle, which consists of a sequence of alternating ellipses and hyperbolas [6]

Reflective Baffle: CPC/CEC

CPC/CEC design becomes a solar concentrator and planetary thermal power if they are within the acceptance angle. Furthermore, large entry aperture.

$$L_{cpc} = \frac{D_{entrance} + D_{exit}}{2tan(\theta)} \tag{4.23}$$

$$D_{entrance} = \frac{D_{exit}}{sin(\theta)} \tag{4.24}$$

The minimum length of the baffle is 1.6 m, to barely cover M2. The diameter of the entrance aperture is 1.85m. With an acceptance angle of 0.597° , this leads to an unfeasible entrance diameter of 163.7 m for a CPC design. This length is unfeasible to be implemented.

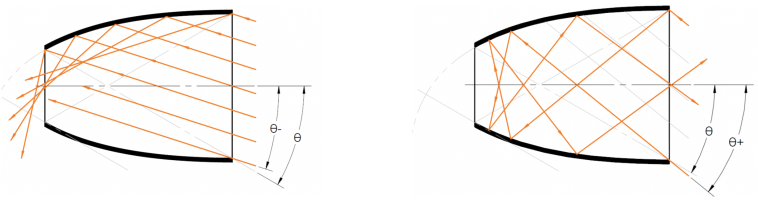

Figure 4.10: The Compound Parabolic Concentrator. (left) Accepts rays which enter at an angle below the acceptance angle. (right) Rejects incident rays which enter at an angle greater than the acceptance angle [7]

Other Design Considerations of Reflective Baffles

It is key to obtain an accurate mechanical representation of the intended reflective baffle design. The sensitivity of the misalignment due to fabrication and deployment accuracy should be carefully monitored. If the tolerances are too tight, it prevents the baffle from achieving the intended performance. Breault noted the following misalignment effect on aperture heat load [5]:

- From analysis, axial displacement or decenter of 0.3% of the baffle diameter causes a 10% increase in aperture heat load. From experience, a tolerance of 0.2% generally increases the aperture heat load by less than 10%
- A tilt or surface distortion that causes a 0.3% sag causes a 6% increase in aperture heat load

Approximation of the exact shape may have the same influence as misalignment. Smits analysed the effect of building the CEC shape of SEVIRI in conical segments on the stray light performance of the detector[43]. The amount of radiation on the cold radiator could be approximated correctly with at least 1000 segments. When the CEC-shape was approximated by 100 segments, an accuracy of 1%, the percentage of radiation on the radiator increased fivefold (from roughly 0.0012% to 0.005%). The amount of stray radiation and scattered light after multiple reflections within the CEC reflector seemed to be unaffected by the approximation into segments. An approximation of the shape into 1000 segments (i.e. 0.1% allowable misalignment) provides an accurate enough performance as to that of the original reflector [43].

The mass of specular baffles will usually be higher than diffuse baffles, which is related to the tight fabrication tolerance of the shape [5]. The baffle and support structure need to be stiff enough to maintain the shape. In addition, the baffle must be stiff enough to maintain the correct alignment between each vane. Misalignment between the vanes can lead to unwanted edge scatter, which would have been blocked by a correctly positioned vane. The ability of a reflective baffle to reflect incident flux depend on the surface smoothness. A rough surface will act as an entrapment of light and causes the light to scatter in unpredictable (unwanted) directions. Verification of the correctness of the focal points of the ellipses is costly, increasing the development cost of reflective baffles.

4.5.3. Current State-of-Art Baffles

In this section, some notable current state-of-art and experimental baffles are highlighted. There were two deployable baffles found in literature, the SEDOBA/HEXOBA in Section 4.5.3 and the 'novel deployable baffle' in Section 4.5.3. The treatment of the design process of the reflective baffle for the BepiColombo Laser Altimeter is shortly given in Section 4.5.3. Furthermore, the design of the Solar Space Telescope 4.5.3 provides insight in the design of a forward extension.

Deployable Baffle: SEDOBA and HEXOBA

Warren et al [8] noted that conventional optical systems are limited by the size of the optical barrel assembly due to the size restriction imposed by the spacecraft bus. They present two optical barrel assembly which are deployable and allow for larger optical baffle systems: High EXpansion Optical Barrel Assembly (HEXOBA) and Strain Energy Deployable Optical Barrel Assembly (SEDOBA) [8]. Both systems use flexible composite hinge technology, which enabled their truss structure to be folded in many places and without introducing unwanted nonlinear dynamics. Furthermore, the flexible hinges are used to maintain the deployed shape of the assembly. Unfortunately, no performance data on the thermal shielding and stray light attenuation could be found.

Table 4.2: Performance of the SEDOBA and HEXOBA [8]

	HEXOBA	**SEDOBA (as built 15% scale)**
Focal length to diameter ratio	1.0	1.0
Deployed height (m)	3.96	3.9
Deployed diameter (m)	2.1	1.88
Primary mirror diameter (m)	1.5	1.8
Stowed height (m)	0.77	188
Stowed diameter	2.1	0.91
Sugar scoop angle	45	45
Total mass	-	30.6 kg + 4.2 kg of MLI

The HEXOBA shown in Figure 4.11 is a deployable barrel and secondary mirror support structure, which deploys straight upward along the optical axis. The deployable barrel features a sugar-scoop design and simultaneously deploys the secondary mirror support structure.

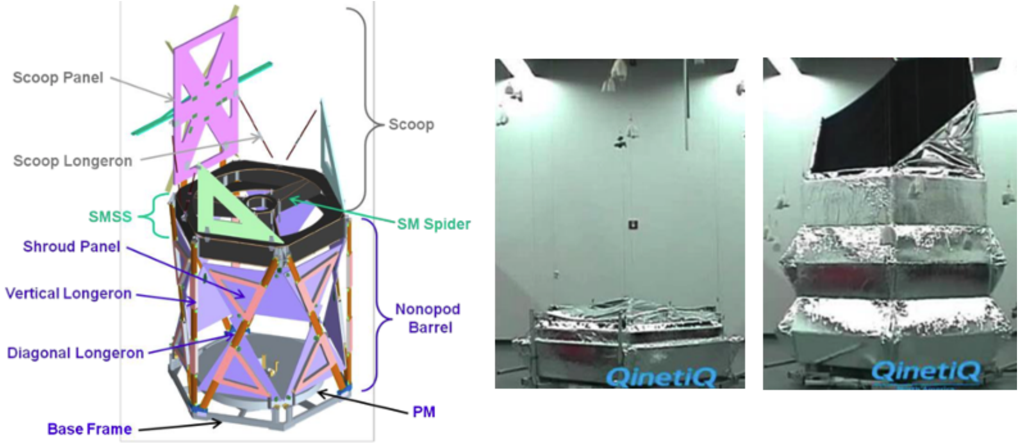

Figure 4.11: HEXOBA which extends a deployable baffle along the optical axis. (left) design, (middle) start of deployment sequence, (right) end of deployment sequence [8]

The SEDOBA is a more complex concept which deploys a shield from behind the telescope. The shield contains deployment mechanisms to increase both the diameter and length of the baffle. The two-stage deployment first deploys a base around the telescope (steps 3 to 5), from which vertical risers extend along the optical axis (step 6) towards the final stage (step 7) as can be seen in Figure (4.12 left).

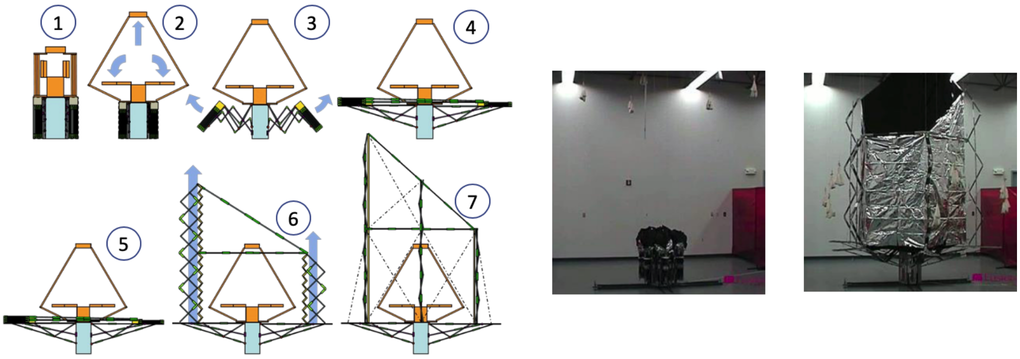

Figure 4.12: SEDOBA which extends a deployable baffle along the radial and optical axis. (left) deployment sequence, (middle) start of deployment sequence, (right) end of deployment sequence [8]

Deployable Baffle: Novel Self-Deployable Baffle

The novel self-deployable baffle consists of three cylindrical sleeves of equal length which extend in the optical direction. The baffle extends from a stowed length of 0.26 m to extended length of 0.6 m, using a spring assemble and flexible folding beams. The original design did not feature vanes and had a PST of close to zero at 30° [44]. The improved design incorporates up to 15 vanes at different length with an interval of roughly 1.2 mm, a PST of almost zero was reached at 24°.

Reflective Baffle: BepiColombo Laser Altimeter

As was already described in Section 4.5.2, the BELA instrument operates in a hot environment near Mercury and needed a baffle system with excellent thermal performance. A conventional black absorbing baffle was not an option due to the thermal loads, therefore it was chosen to select a reflective baffle design [45]. Trade-off between an elliptical, Linlor, Lockheed-Stavroudis, CPC and CEC designs were made. Ultimately, the Lockheed-Stavroudis design was chosen which consists of 11 segments (6 elliptical and 5 hyperbolic). The Lockheed-Stavroudis design was chosen for the low number of reflections to reduce thermal load and robustness of the design. The CPC lost due to the large field of view of BELA which resulted in a too large entrance aperture diameter. The authors note that this disadvantage would not have occured for payload with a FOV of 10^o or smaller. Another disadvantage of the CPC was the concentration of Planetary thermal power of flux falling within the acceptance angle [46]. The vanes of the BELA are visible in Figure 4.13 along with the manufactured baffle. The 300 mm length reflective baffle is made of diamond turned aluminium to obtain the required shape tolerance of 50 μm[9]. In order to obtain the needed thermal performance, a coating of deposited silver, Al_2O_3 and SiO_2 was used.

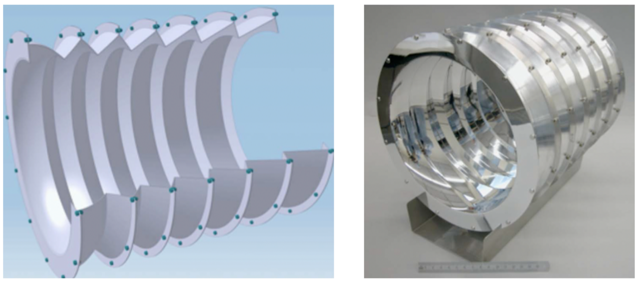

Figure 4.13: (left)3D segmented view of the Lockheed-Stavroudis reflective baffle for the BepiColombo Laser Altimeter (right) the manufactured reflective baffle, from [9]

Sugar scoop: Solar Space Telescope

The Solar Space Telescope (SST) has a primary mirror of 1 m in diameter [47]. The stray-light and thermal performance of the SST were analysed through varying the baffle length of 4100 mm to 4900 mm in increments of 100 mm. The highest temperature was found at the edge of the PMSS, at the base of the baffle. The lowest temperature was found at the inner baffle-wall at the entrance aperture. The thermal analysis showed that with increasing baffle length, the maximum temperature increased due to the larger heat receiving area. In addition, the radiative surface area increased which resulted in a lower minimum temperature. This lead to the selection of the shortest length possible of 4100 mm. Reduction of the thermal influence was done through a forward extension, similar to the baffle in Figure (4.6 left). Thermal analysis showed that the forward extension with the smallest allowable inner diameter (i.e. largest thermal mass and capacity) decreased the maximum temperature and increased the minimum temperature experienced within the baffle. The same temperature distribution of the SST could be found on the Exo-C Exoplanet

Program of NASA. EXO-C is a community mission study for a space telescope. The temperature map of Exo-C can be seen in Figure 4.14

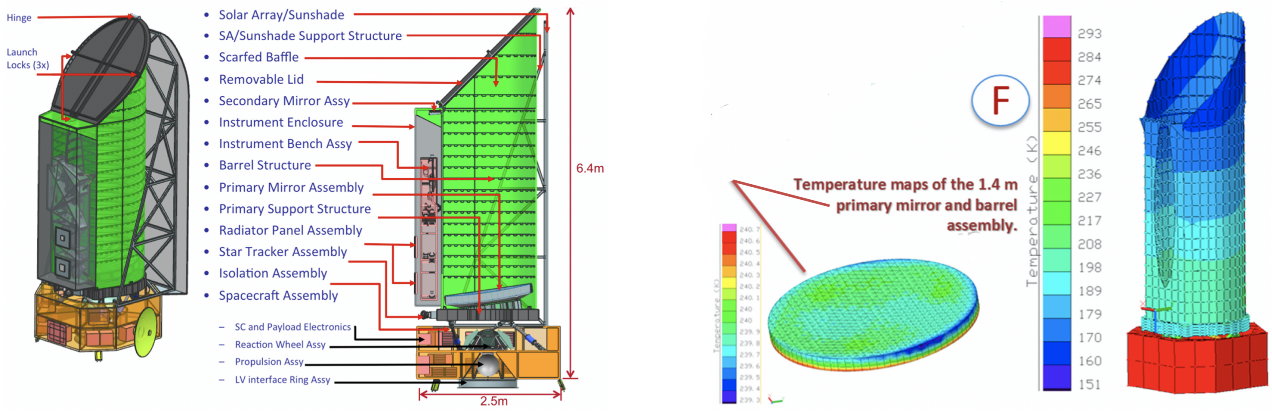

Figure 4.14: (left) Isometric and sectioned view of the Exo-C ,(right) Temperature map of the primary mirror and baffle, from [10]

4.6. Baffle Concept Generation

Due to complexity of deployment system for such a large deployable baffle, it is assumed that deployability plays a large limiting factor on feasibility. In addition, complex deployment systems carry an unavoidable weight-penalty. Currently, no large deployable baffle system with a Technnology Readiness Level (TRL) level of 6 or higher exists. Thus, complex baffle shapes and arrangement of vanes are deemed to be out of reach with the current knowledge and technology.

Therefore, chosen to only generate baffle concepts which have a constant cross-sectional area. This choice limits the design parameters, completely eliminating the class of reflective baffle designs. Reflective baffles require more complex geometry with a large variation in cross-sectional area and complex vane orientation. These vanes have to be accurately positioned and oriented relative to each vane in order to be effective. The focal point of each vane is focused at a specified location such that the system of vanes work in harmony with the accompanied baffle shape. An incorrectly orientated or positioned reflective baffle vane can lead to multiple scatters towards the detector [4, 46]

Black diffuse baffles are more tolerant to deviations in location and orientation. The lower sensitivity to changes in geometry, makes them more suitable to be pared with a complex deployment system. The baffle concepts generated in this section are therefore, more of the nature of using the black diffusive principles. One concept utilises the method of reflecting the incoming rays at off-axis angles by angling the vane geometry [5].

4.6.1. Baseline Baffle

The baseline baffle used for the generation of baffle concepts, is the octagonal baffle shape from Arink [3] which can be found in Figure 2.6. The key parameters of the baseline baffle can be found in Table 4.3. The truncated cone design implemented by Arink has a vane angle of 35 .

Table 4.3: Baseline baffle design key parameters

Design	Baseline baffle
Type	Specular black baffle with one angled vane
Baffle Length (m)	2.65
Total amount of straight vanes	0
Total amount of angled vanes	1
Vane angle (degrees)	35

4.6.2. Design 2.1

The baseline design is slightly altered by increasing the vane depth of the truncated cone. The design of the truncated cone of Arink was erroneously designed for the requirement of having to provide an aspect angle of less than 35 . This requirement belonged to the specific to the used optical instrument on the BepiColombo mission [9]. The truncated cone from the baseline design is straightened out, such that the vane angle is 0 degree (vanes are perpendicular to the baffle wall). Design 2.1 changes the vane depth such that there is a 30 mm distance between the optical path and the vanes. Furthermore, three additional vanes are placed. The furthest inward vane being slightly behind the M2 mirror in order to reduce the chance of scatter towards M2. Baffle design 2.1 can be seen in Figure 4.15 along with a render of the M1 mirror placed at the front of the baffle to provide a visual reference of the orientation of the baffle around the DST.

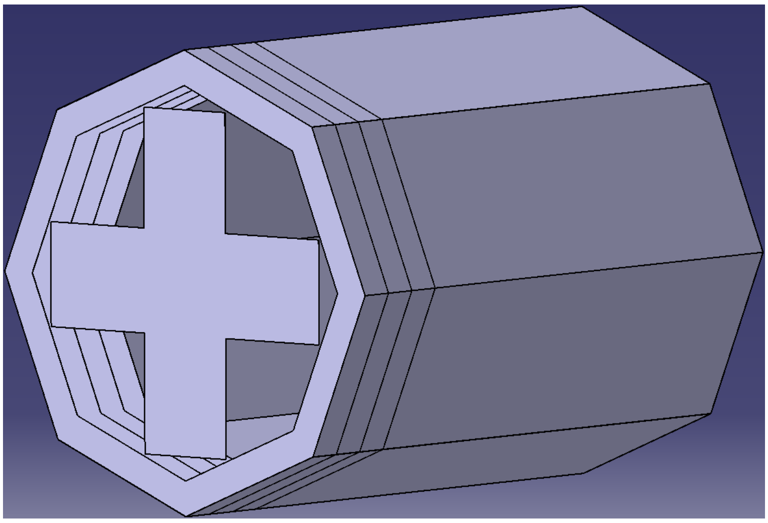

Figure 4.15: Baffle design 2.1 with the primary mirror rendered at the entrance aperture

In design 2.1, the sides of the truncated cone do not run parallel to the four edges of the M1 closest to the baffle. The points of M1 closest to the truncated cone are therefore the corners of the M1 mirror. The length of each M1 segment has a length of 620 mm and width of 450 mm. The distance between the center and corner of M1 is 776 mm. This increases the collector length to be used and decreases the allowable vane depth. The vane depth is 122 mm, whilst still having a vane radius of 30 mm. The key parameters of design 2.1 can be found in Table 4.4.

Table 4.4: Design 2.1 key parameters

Design	2.1
Type	Specular black baffle with four straight vanes
Baffle length (m)	2.65
Total amount of straight vanes	4
Total amount of angled vanes	0
Vane angle (degrees)	0

4.6.3. Design 3.1

Design 3.1 differs from 2.1 in that the baffle is rotated 22.5 ° about the Z-axis. The rotation angle is chosen such that the sides truncated cone and vanes run parallel to the sides of M1. This allows for a larger vane depth of 150.8 mm. Design 3.1 can be seen in Figure 4.16. The key parameters of design 3.1 can be found in Table 4.5.

Table 4.5: Design 3.1 key parameters

Design	3.1
Type	Specular black baffle rotated 22.5 ° along Z-axis with four straight vanes
Baffle length (m)	2.65
Total amount of straight vanes	4
Total amount of angled vanes	0
Vane angle (degrees)	0

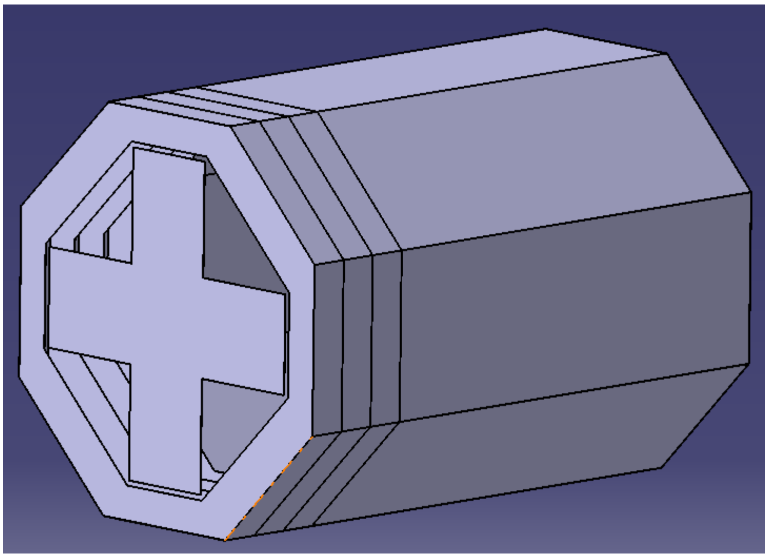

Figure 4.16: Baffle design 3.1 with the primary mirror rendered at the entrance aperture

4.6.4. Design 4.1

Analysis of the heat flux received by the DST in orbit, shows that the spacecraft receives the largest amount of heat flux at the instance before entering and after exciting eclipse. This phenomena causes a large solar heat flux decrease when entering eclipse, and solar heat flux increase when exciting eclipse. The sudden change in heat flux leads to a large change in the thermal gradient.

At the true anomaly θ of 88 ° in Figure 4.17, the solar heat flux impinges on the inside of the baffle. The incident solar heat flux increases prior to entering eclipse, up to $\theta = 110$ ° in Figure 4.18. At $\theta = 111$ ° the spacecraft is in the eclipse phase of the orbit up to $\theta = 243$ ° . The solar heat flux impinges the interior baffle wall upon exciting eclipse at θ 244 = ° until 266 ° . The incident solar heat flux rapidly increases upon exiting eclipse at $\theta = 244$ ° which can be seen in Figure 4.19. The impingement of solar heat on the interior baffle stops after the orbital angle of 266 ° , which can be seen in Figure 4.20.

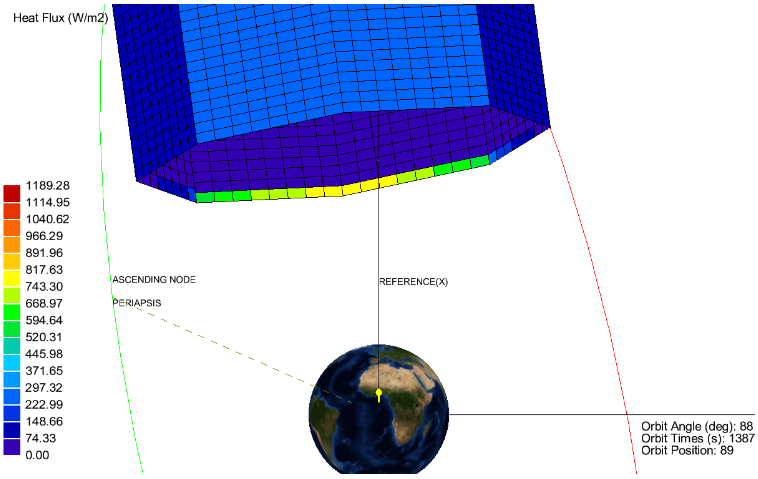

Figure 4.17: Heat flux from the sun impinging on the baffle interior at $\theta = 88°$

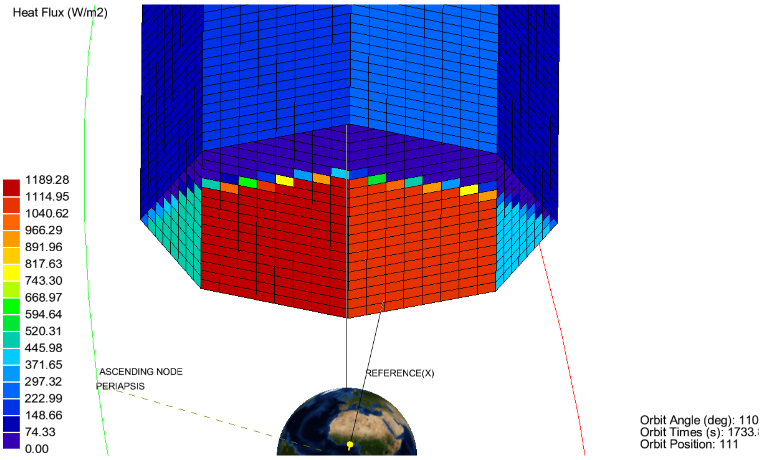

Figure 4.18: Heat flux from the sun on the baffle prior to entering eclipse at θ = 110°

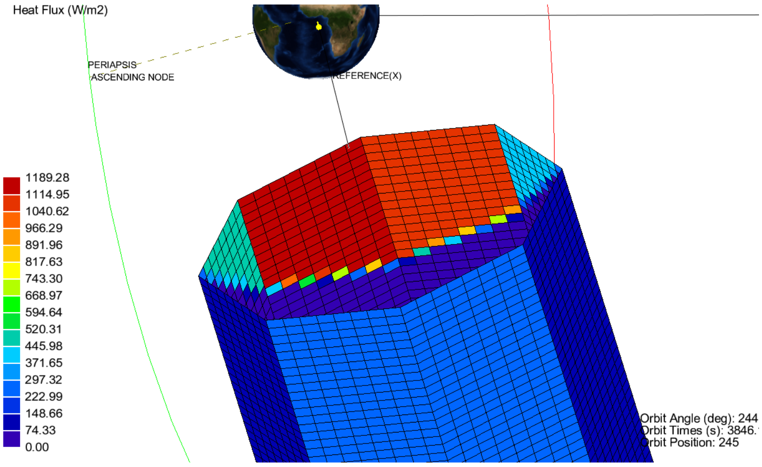

Figure 4.19: Heat flux from the sun on the baffle prior to exiting eclipse at θ = 244°

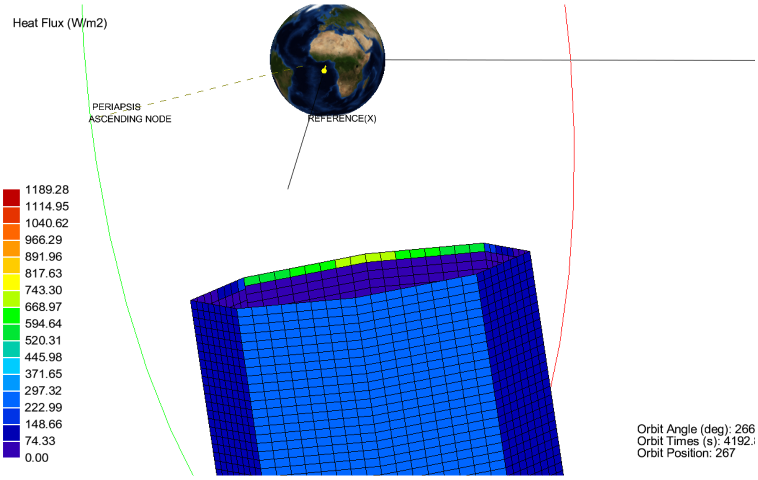

Figure 4.20: Heat flux from the sun impinging on the baffle interior at θ = 266°

From Figure 4.17, it can be concluded that the solar heat radiates the interior baffle wall at θ = 87°. From the analysis of the incident solar angle, it can be concluded that the maximum solar heat flux occurs at θ = 110 and θ = 244°. Ideally, this solar heat is rejected out of the entrance aperture by using angled baffle vanes which reflects the incoming heat flux [5]. The largest angle at which the solar heat flux radiates the baffle is at 244°. By placing an angled vane at the same angle as the incoming solar heat, the solar heat can be rejected out of the baffle. Some safety margin should be included in the vane angle of the angled vane to account for variations in beta-angle and deployment accuracy. It is therefore chosen to place the angled vanes at a 30° angle, with 4° as a safety margin included. The rationale for adding interim baffle vanes, instead of angling the straight vane is to prevent the interior of the baffle to be seen by the M1 mirror. Because the straight vanes (with a vane angle of 90°) prevents the angled vane from being a critical surface for the M1 mirror. The straight vane will act as a barrier and absorbs scatter from the angled vane which could otherwise propagate towards M1 through multiple scatter events [5, 48]. From trigonometrical analysis for design 4.1, similar to the analysis from Figure 4.4 the internal baffle will receive solar heat up to the point Z = 1142 mm. The amount of vanes and angled vanes for design 4.1 should thus provide enough coverage to prevent scatter from the internal baffle wall to the detector. Baffle design 4.1 can be seen in Figure 4.21 along with the key parameters in Table 4.6.

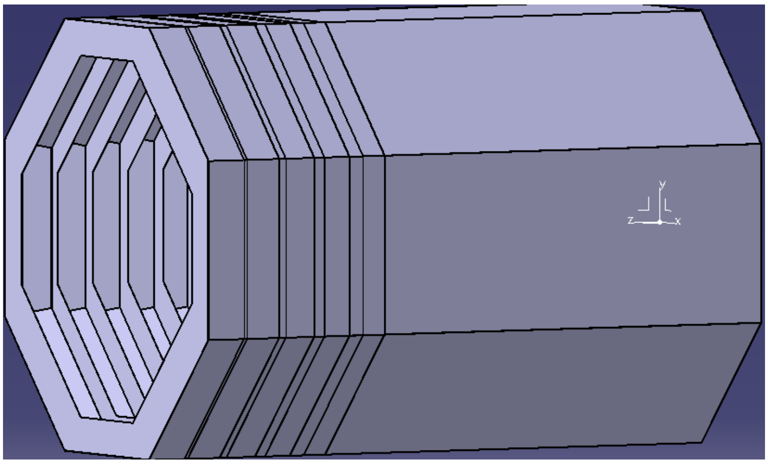

Figure 4.21: Design 4.1 with 6 straight vanes and 5 angled vanes

Table 4.6: Design 4.1 key parameters

Design	4.1
Type	Specular black baffle rotated 22.5^{o} about Z-axis with 6 straight vanes and 5 angled vanes
Baffle length (m)	2.65
Total amount of straight vanes	6
Total amount of angled vanes	5
Vane angle (degrees)	0
Angled vanes angle (degrees)	30

4.6.5. Design 5.1

Design 5.1 incorporates a sugar-scoop baffle. One of the reasons for utilising a sugar-scoop baffle, is for weight saving purposes [4]. When the baffle geometry is not illuminated due to their shape or due to a controlled orientated of the baffle, the excess baffle surface can be removed as it serves no purpose. Another reason to use a sugar scoop baffle is to avoid incident solar flux into the baffle. By removing the internal surface, the incident solar flux cannot reflect back into the baffle as the rays will shoot past the baffle into space [49].

In order to incorporate a sugar-scoop design, the orientation of the baffle has to be actively controlled. The rotation about the Z-axis has to orient the spacecraft such that the sugar-scoop is placed at the correct orientation. The VIS DST uses a push-broom scanning method. As such, rotating the full spacecraft in order to position the long side of the baffle is not feasible since it will produce unusable imaging data. However, it might be possible to only rotate the baffle using existing technology such as a solar array drive and array drive electronics (SAD / ADE). These components are capable of rotating the solar panels with respect to the body of the spacecraft. Typical stepping motors provide a stepping rate of 1.8 °/step at 8 Hz in the slewing mode [50].

From Figures 4.18 and 4.19 the surfaces which would have received incident solar heat flux are different for the case before and after eclipse. The sugar-scoop adapted baffle design 5.1 is shown in Figure 4.22, in which the sugar-scoop is composed of cutting away the baffle from a 30 degree plane about the X-axis. The choice for the 30 angle is of course based solely on one solar beta angle. For a detailed design, one has to keep in mind that the solar beta angle β changes over the year [51].

When a sugar-scoop with at a 30 degree angle is applied to the original baffle length, the SMSS and M2 become unprotected. This is an undesired consequence of the sugar-scoop, because it will cause large fluctuations in the temperature of temperature-sensitive components. In order to fairly compare the thermal performance of a sugar-scoop, the baffle has to be lengthened by 0.5 m such that the SMSS and M2 are not directly exposed to solar heat.

Table 4.7: Baffle design 5.1 key parameters

Design	Baseline baffle
Type	Specular black baffle with vanes, angled vanes and sugar-scoop
Sugar scoop angle (degrees)	30
Baffle length (m)	3.15
Total amount of straight vanes	6
Total amount of angled vanes	5
Vane angle (degrees)	0
Angled vane angle (degrees)	30

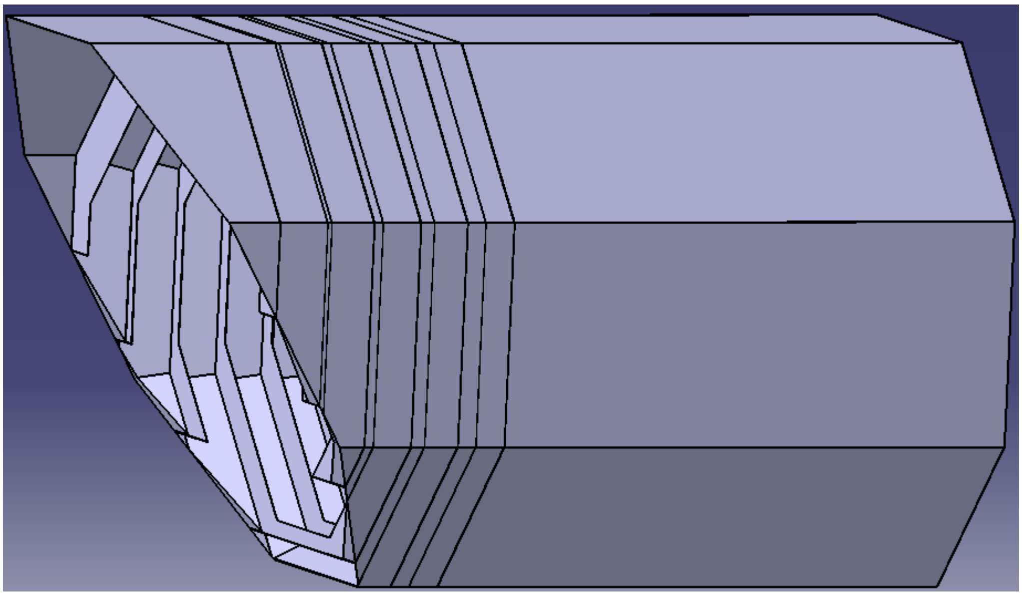

Figure 4.22: Design 5.1 which incorporates the sugar-scoop with a total baffle length of 3.15 m

5

Stray Light Model

Analytical evaluation of stray light performance are prone to error. As even simple models often require the use of a plethora of complicated equations with many different parameters to describe the simple model [4]. The development of ray tracing analysis software greatly aid in performing stray light analysis by automatically computing view-factors. The programme chosen for this thesis work is FRED by Photon Engineering [17] as explained in Section 5.1. The ray tracing model of the baseline system is validated and given in Section 5.2. The various baffles are then imported into FRED and prepared for analysis in Section 5.3. Finally, the stray light analysis of the various baffles is given in Section 5.4

5.1. Ray Tracing Programme Selection

The original optical model was created by Dolkens in Zemax [11]. The Zemax file can then be used in an optical ray trace program such as FRED, ASAP [52], or TracePro[53]. From these software, FRED was chosen as it provides a free license for graduate students working on their thesis.

5.2. Baseline Model Creation

This section is about validation of the baseline DST model. The creation of an optical systems generally occurs in two steps: definition of the geometry of both the optical and mechanical part, and then defining the optical properties of the optical surfaces and structural surfaces [4]. The optical model is first imported into FRED and validated in Subsection 5.2.1. The validation of the mechanical model is given in Section 5.2.2 Then, the optical and mechanical models are merged together and validated again in Section 5.2.3.

5.2.1. Optical Model Validation

The optical model used was created by ir. Dolkens in the optical design software of Zemax, which accurately describes the geometrical properties of the mirror and lenses[11]. The positional values and geometrical properties of the optical elements are generated with a Matlab based raytracing programme by Dolkens called Fast Optical RayTrace Application (FORTA)[54]. The output generated by FORTA on the DST is shown in Figure 5.1.

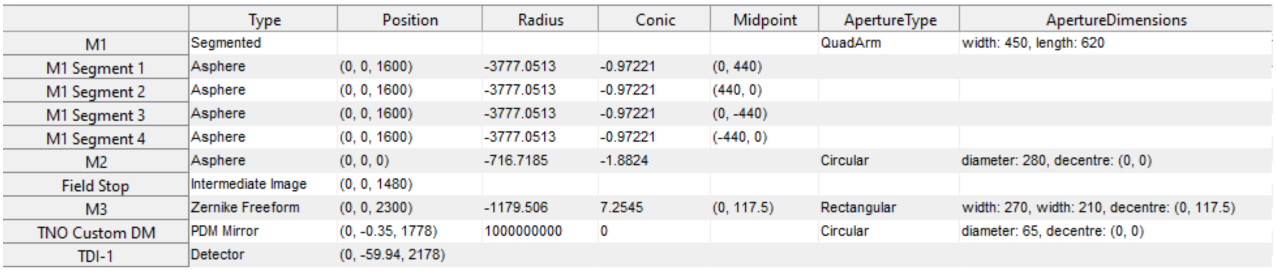

	Type	Position	Radius	Conic	Midpoint	ApertureType	ApertureDimensions
M1	Segmented					QuadArm	width: 450, length: 620
M1 Segment 1	Asphere	(0, 0, 1600)	-3777.0513	-0.97221	(0, 440)		
M1 Segment 2	Asphere	(0, 0, 1600)	-3777.0513	-0.97221	(440, 0)		
M1 Segment 3	Asphere	(0, 0, 1600)	-3777.0513	-0.97221	(0, -440)		
M1 Segment 4	Asphere	(0, 0, 1600)	-3777.0513	-0.97221	(-440, 0)		
M2	Asphere	(0, 0, 0)	-716.7185	-1.8824		Circular	diameter: 280, decentre: (0, 0)
Field Stop	Intermediate Image	(0, 0, 1480)					
M3	Zernike Freeform	(0, 0, 2300)	-1179.506	7.2545	(0, 117.5)	Rectangular	width: 270, width: 210, decentre: (0, 117.5)
TNO Custom DM	PDM Mirror	(0, -0.35, 1778)	1000000000	0		Circular	diameter: 65, decentre: (0, 0)
TDI-1	Detector	(0, -59.94, 2178)					

Figure 5.1: Position information and geometric properties of the DST generated by FORTA

The optical model does not contain any baffle or structural elements, as they serve no purpose for analysing the image quality of the optical model. The optical model does contain the detector surface of multiple detectors, to analyse different wavelengths. In addition, the optical model contains surfaces and coordinate breaks to aid in modelling the optics. However, some of these surfaces of the imported optical file were omitted as they do not aid in the stray light analysis. The optical surfaces which are used for the stray light analysis are: M1, M2, M3, TNO Custom DM and TDI-1. An overview of the bare optical model and coordinate axis used can be found in Figure 5.2.

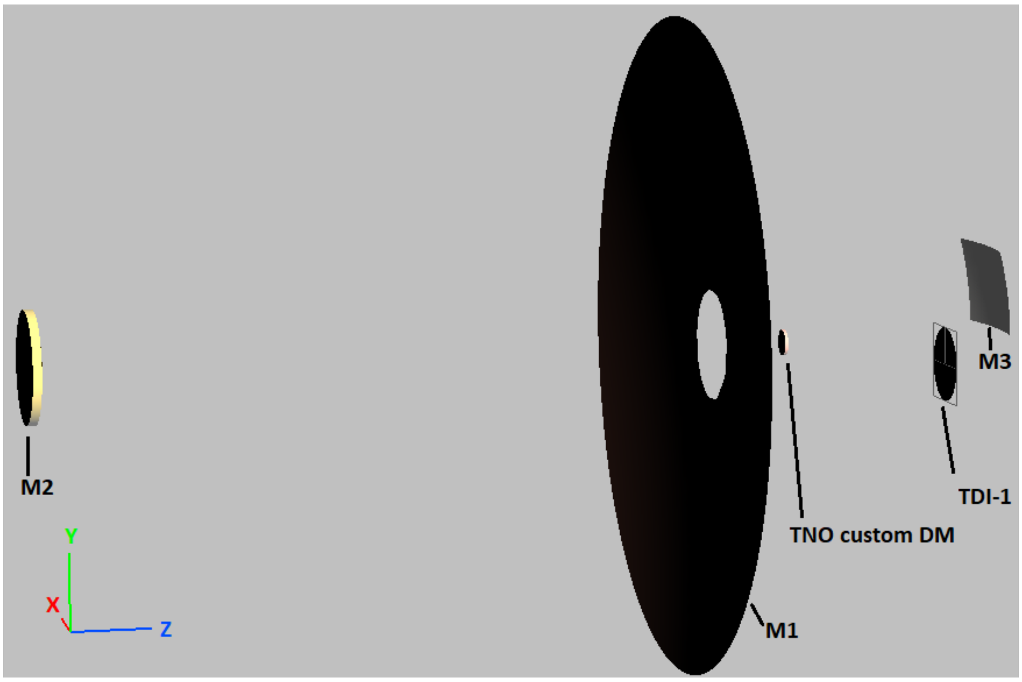

Figure 5.2: Imported optical model from Zemax in FRED along with the positive direction of the X, Y, Z-axis

The optical model does not represent the quad-aperture shape of M1 and shape of the M2 mirror. The reason is not known, but it could be due to an incompatibility issue between Zemax and FRED for complicated surfaces such as a quad-aperture [11]. The remodelling of M1 and M2 will be later-on performed in FRED in Subsection 5.2.3.

Closer inspection of the model shows that each optical element is rotated about the X-axis equal to 0.3478673762854°. The optical sources are not rotated. The optical instrument has this rotation to ensure that images taken from near the edges of the swath are still sharp. However, this X-axis rotation on each optical element causes a slight off-set in the Y and Z-location of each optical element compared to the FORTA positions generated from Figure 5.1. To ease up the stray light modelling, the X-axis rotation can be removed from the optical elements and added onto the optical source. Therefore, each optical source has a base X-axis rotation of -0.3478673762854°. , even the optical source which is considered to have no offset in the cross and along track direction. Removal of the X-axis rotation in each optical element needs to be accompanied by correcting the positions according to the generated output of FORTA from Figure 5.1.

The ZEMAX file does not take into account scatter. In order to model the scatter, a K-correlation with sigma 0.002 (RMS surface roughness) was adviced to be applied to the optical surfaces in FRED [11]. The K-correlation models the surface roughness which can be expected from manufacturing the optical elements. Furthermore, the Zernike coefficients of M3 were imported wrongly from Zemax into FRED. The corrected Zernike coefficients can be found in Table 5.1.

Table 5.1: Corrected Zernike values for M3 mirror in FRED

Zernike Coefficient	Corrected Value	Description
Zern 3	-0.04892965955427	$R^2 cos(2A)$
Zern 4	-3.193144585	$2R^2 - 1$
Zern 10	-0.011593616608	$R^4 cos(4A)$
Zern 12	0.408960032285	$6R^4 - 6R^2 + 1$
Zern 21	0.007708286456	$R^6 cos(6A)$
Zern 24	0.015552694855	$20R^6 - 30R^4 + 12R^2 - 1$
Zern 36	-0.001850932277	$R^8 cos(8A)$
Zern 40	-0.001100328171	$70R^8 - 140R^6 + 90R^4 - 20R^2 + 1$

Ray tracing programme use different algorithm to compute the ray-trace, which could lead to a difference in comparing for example the Point Spread Function (PSF). The PSF of two equal systems analysed by two different programmes can differ due to difference between defining diffraction and scaling of wavelengths. In addition, stray light analyses do not use coherent light sources which further strengthens the argument of not comparing the similarity of the PSF. The validation strategy used is comparison of the geometric spot size between the optical file and the

FRED file [4]. The geometric spot size should create the same output for all ray tracing programmes. This method is also supported by ir. Dolkens [11]. The geometric spot diagram generated in FORTA can be seen in Figure 5.3 (left) from Dolkens [11]. The coordinates of the geometric spot size generated by FRED was exported and visualised in Figure 5.3 (right).

The geometric spot diagram generated by FRED is also given in Figure 5.4. There are minor differences noticeable between the FRED and FORTA model, which can be attributed to rounding errors in the Zernike coefficient and interference with the geometrical model. However, these minor differences are negligible. After the above mentioned changes to the optical file in FRED, the optical file is verified and deemed to be correct [11].

Note that the introduced K-scatter in the optical model does result in a different geometric spot diagram compared to a model without K-scatter. The geometric spot has a diameter of 80 mm with the K-scatter applied. Since the K-scatter model was the only variable changed, it is safe to say that the spot diagram was caused by the K-scatter model. When zooming into the same region,

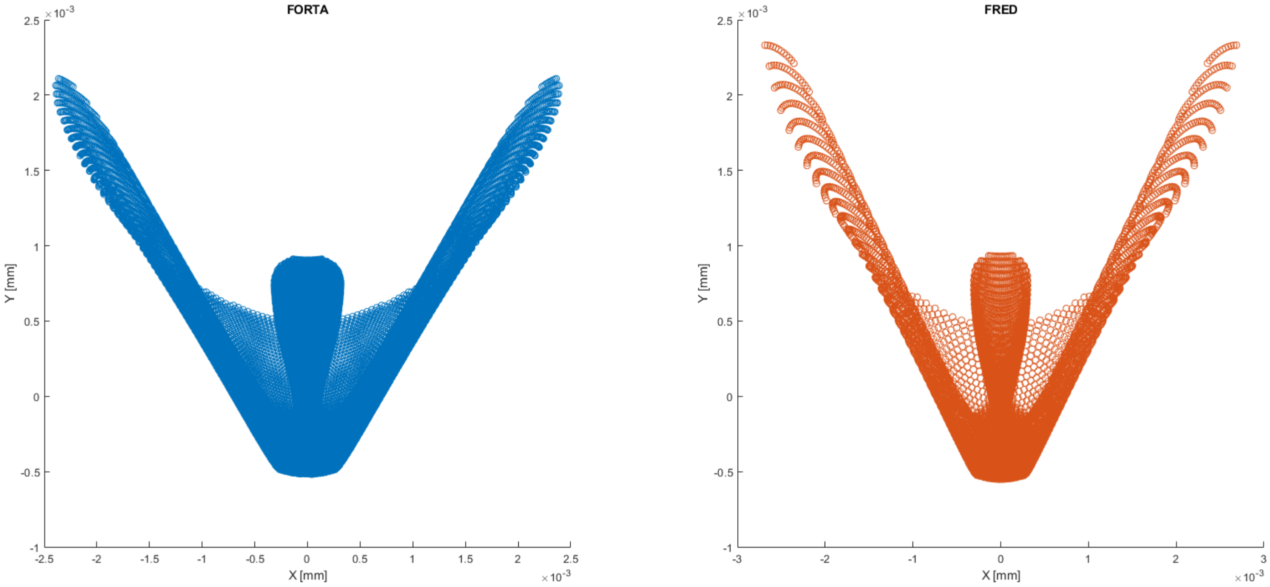

Figure 5.3: Geometric spot size comparison between FORTA and FRED from ir. Dolkens [11]

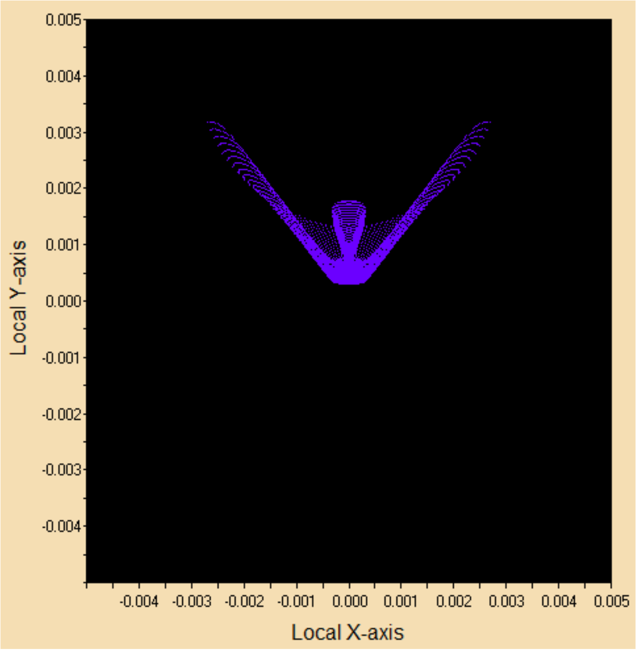

Figure 5.4: Geometric spot diagram of the optical model generated with FRED

5.2.2. Mechanical Model Validation

The mechanical system (e.g. optical lens housing, struts and baffles) can be obtained by importing a CAD file into FRED. The CAD file taken for this thesis is based upon the work of previous master thesis students. The latest, updated CAD from Akkerhuis taken as a starting point for the mechanical system of the DST. The imported CAD file into FRED can be seen in Figure 5.5 in which the model is rotated about the Y-axis with 180 °. This is done such that the Z-axis in blue represents the distance between the origin (i.e. Z = 0 mm at M2) and other optics (e.g. Z = 1600 mm for M1), the X-axis in red represents the cross track direction and the Y-axis in green represents the along track direction. It is opted to randomly assign colours to the surfaces of the mechanical model, to be able to distinguish between the parts more easily.

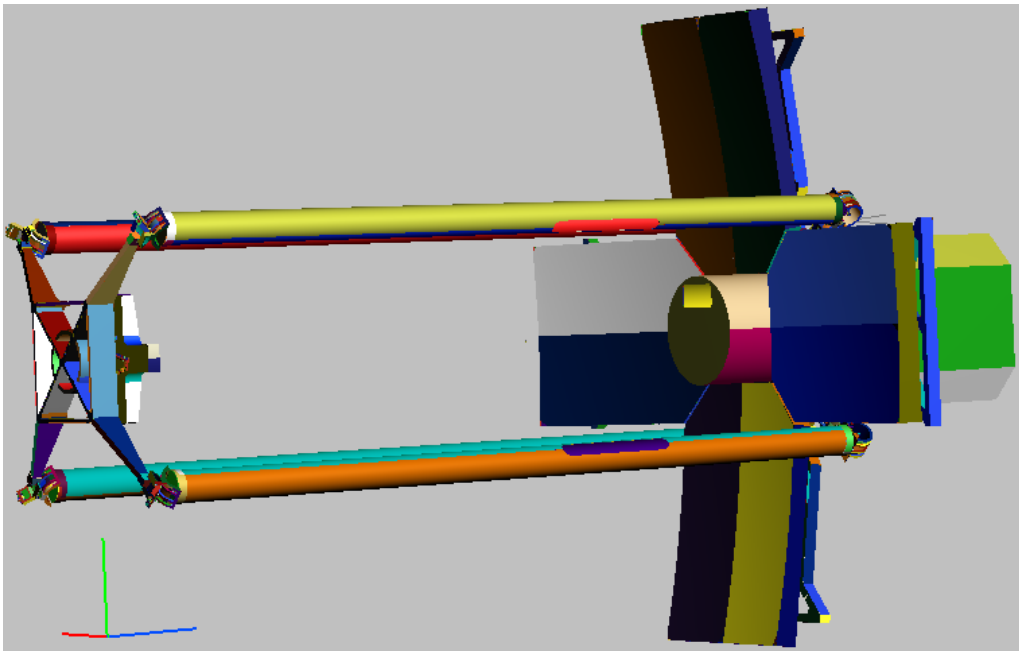

Figure 5.5: Unaltered DST mechanical file imported into FRED along with the reference frame used (Z-axis is blue,

This model obviously shows the quad-aperture shape of M1 and the shape of M2. However, these shapes do not accurately represent the optical properties of the DST and will therefore not ray trace properly [4]. The surfaces in the mechanical model, representing the optical elements have to be replaced by the optical elements from the optical model.

5.2.3. FRED Baseline Model

The baseline model is created by merging together the mechanical and optical file. After merging both files together, the surfaces from the mechanical model which represent the optical system are put as ’untraceable’ such that it does not interfere with ray tracing mechanics. Furthermore, the optical elements such as M1 and M2 are still represented by a circular geometry. This intermittent model can be seen in Figure 5.6.

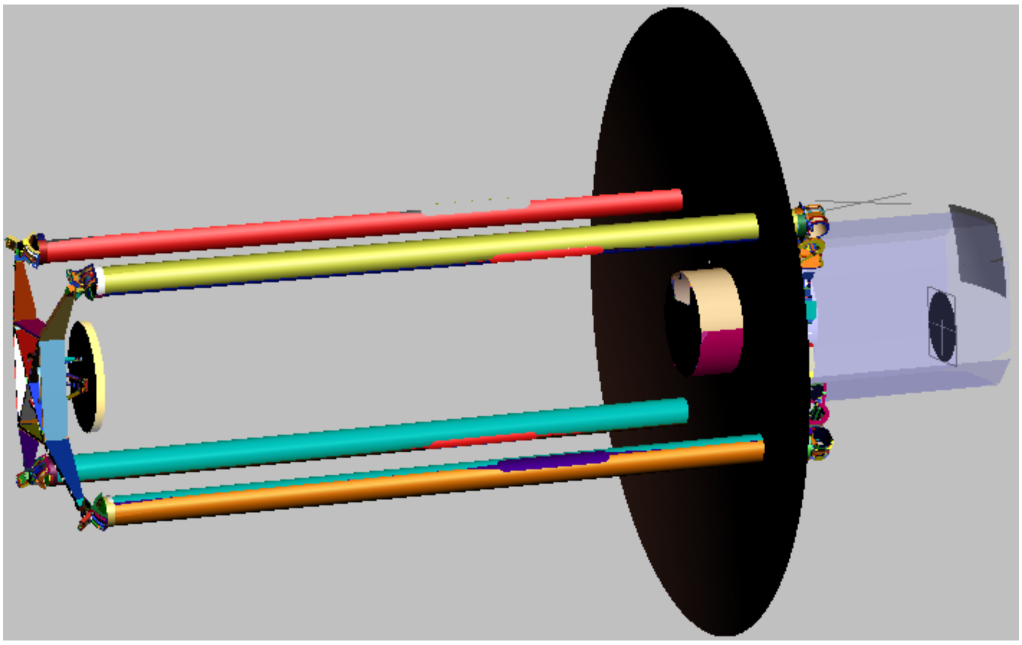

Figure 5.6: Mechanical and optical files merged together, intermittent result with circular optics in FRED

The position of the optical elements are then checked with respect to the mechanical model. The positional and directional check is performed using a script from FRED [17]. The position of the backside of the M2 mirror is checked against the position of the spider rods. In addition, the pointing direction of the M2 mirror is checked whether it points towards the Z-axis. The same is done to assess the position and direction of M1. In order to check the model, a new geometric spot diagram is made to compare the result with the optical model. The geometric spot diagram of the mechanical model with circular optical model can be found in Figure 5.7. It can be seen that a small inner part of the left and right-extremity are missing, which can be attributed to the booms partially blocking the incoming light. The shape of the geometric spot diagram does not differ much, therefore being verified.

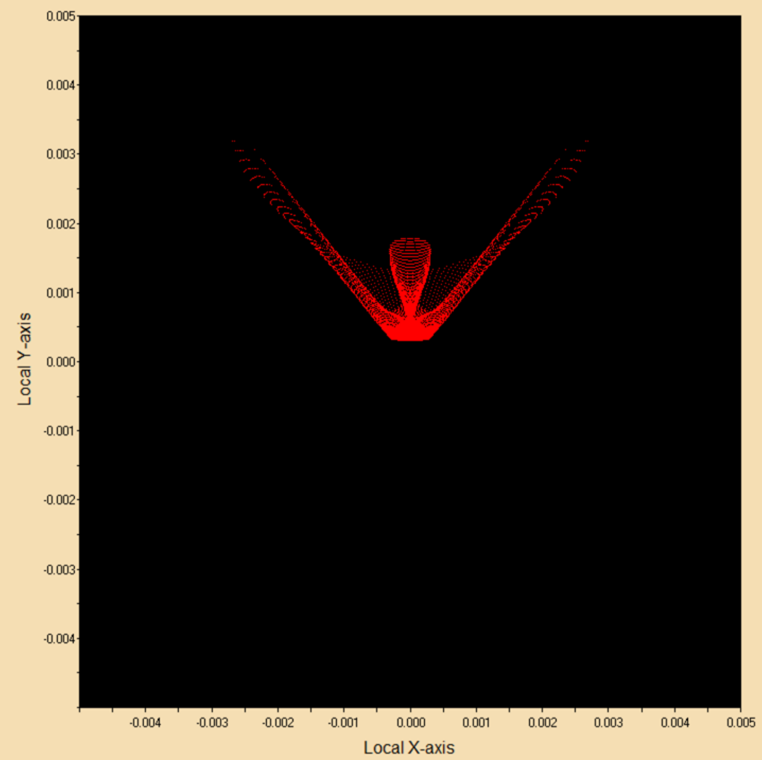

Figure 5.7: Geometric spot diagram of the DST mechanical model with the optical model (circular optics) generated with FRED

The optical elements can now be formed. First the primary mirror M1 is formed. The mechanical file of the primary mirror M1 contains the correct dimensions of the primary mirror [11]. From these coordinates, extrusions of the quad aperture are made. These cut-outs are then combined to form the quad aperture of the M1 mirror, using the original circular aperture. The intermittent model can be seen in Figure 5.8. A new geometric spot diagram is generated and can be seen in Figure 5.9. It can be seen that the left-and right extremity became shorter due to the quad-aperture shape of M1. Though different, it was verified to be correct with the ZEMAX model [11].

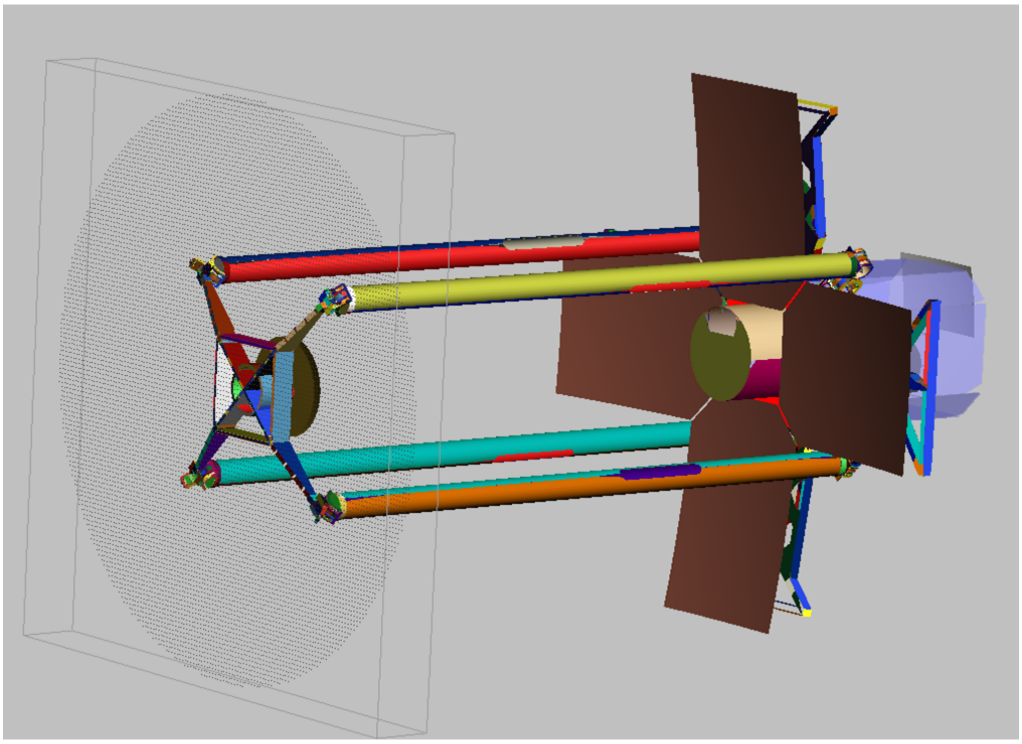

Figure 5.8: Intermittent baseline model: quad-aperture M1 with circular M2 mirror

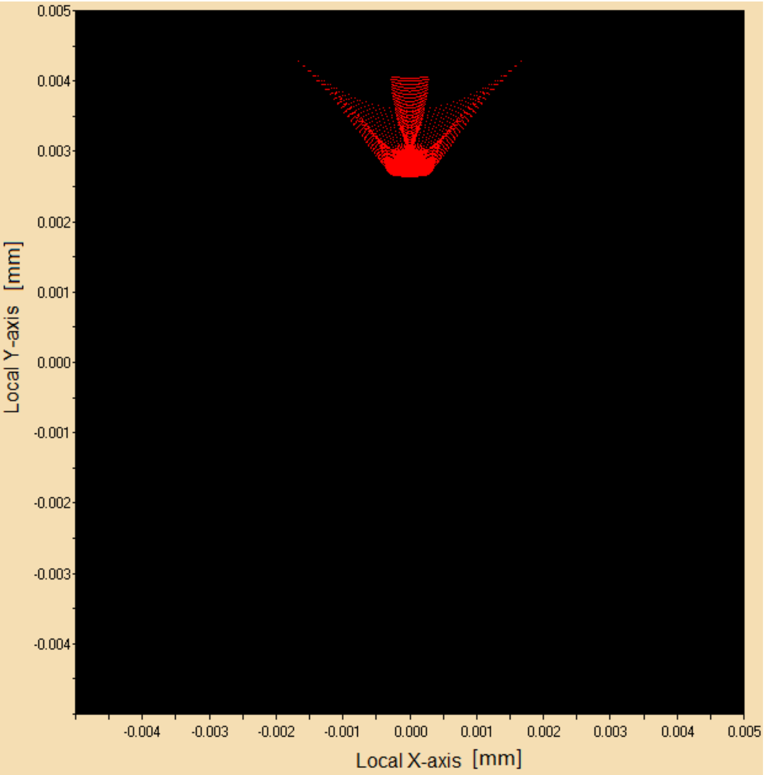

Figure 5.9: Geometric spot diagram of the DST mechanical model with the quad-aperture M1 and circular M2 generated with FRED

The formation of the cross-shaped M2 was originally formed using the mechanical representation of M2. However, the CAD-file did not accurately represent the shape of the M2 [11]. In order to obtain the correct model, ray traces had to be performed to obtain the shape of M2. Unscattered rays with an offset of ±0.3 ° in the cross-track direction and 0 to 0.25° in the along track shall pass through the system without vignetting. Thus, in order to obtain the shape of M2, rays were traced with the above criteria. This was accomplished by creating multiple source which each has a different off-axis and represent the boundary condition:

- Source with no-offset
- Source with -0.3° offset in the cross-track direction
- Source with +0.3° offset in the cross-track direction
- Source with 0.25° offset in the along-track direction
- Source with -0.3° offset in the cross-track direction and 0.25° offset in the along-track direction
- Source with +0.3° offset in the cross-track direction and 0.25° offset in the along-track direction

These boundary conditions form a requirement for the development of the geometry of M2:
REQ.ID: Unscattered light from ±0.3 cross-track and 0 to 0.25° along-track reflecting off of M1, shall pass through the optical system without vignetting

Rays from the above sources reflect off of M1 and are focused towards the location of M2. Under the ideal circumstances (no scattering), all of the rays that reflect off of M1 should intersect with the surface of M2. An analysis surface is placed at the location of the M2 mirror. The analysis surface is then used to perform an irradiance spread function, which provides information on the irradiance received from the quad-aperture M1 and can be seen in Figure 5.10. The information includes the intensity and location of where the rays intersect the analysis surface. The intersection points provides the outer-bound of the shape of M2. The result of the baseline model can be found in Figure 5.11. For this model, a new geometric spot diagram was made (Figure 5.12. There seem to be no difference between the geometric spot diagram with the circular M2 and cross-shaped M2, which verifies that the cross-shaped M2 provides the same optical performance as the circular M2. Thus verifying that the baseline model is correctly modelled to enable further optical analysis.

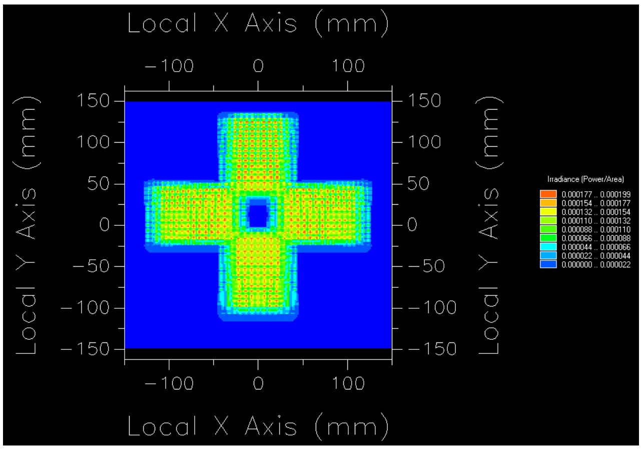

Figure 5.10: Irradiance spread function on the analysis surface at the location of M2 with FRED

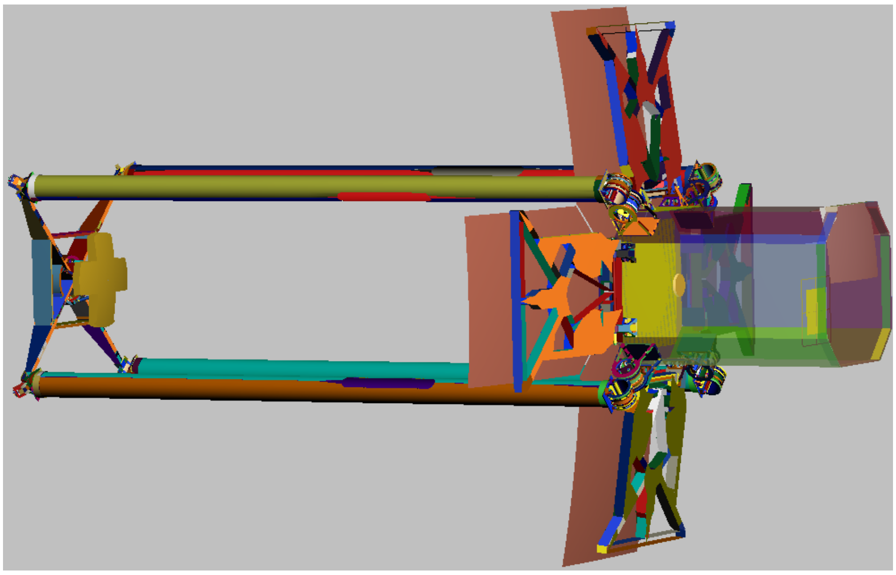

Figure 5.11: Baseline model with the quad-aperture M1 and cross-shaped M2 mirror in FRED

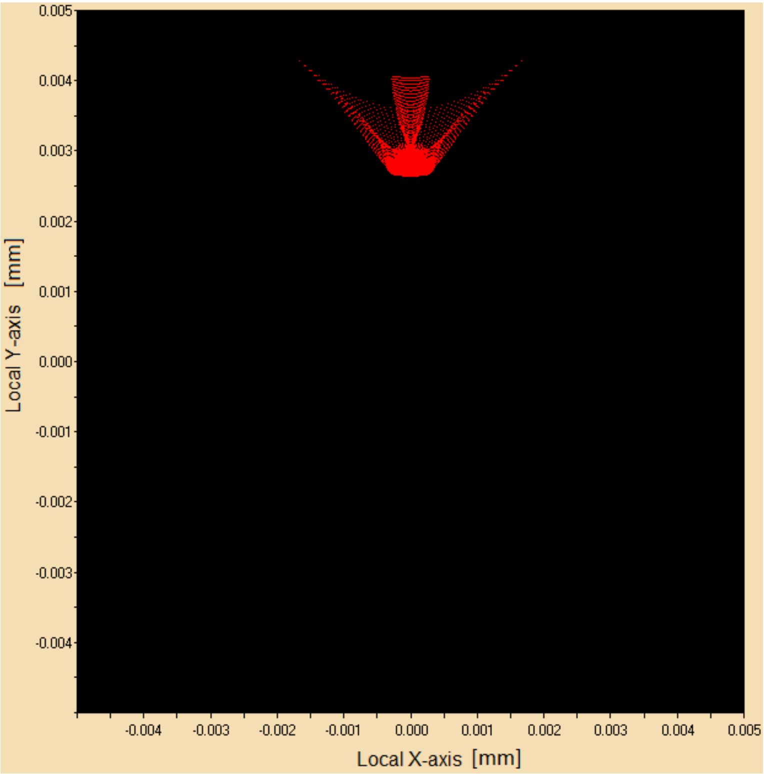

Figure 5.12: Geometric spot diagram of the DST mechanical model with the quad-aperture M1 and cross-shaped M2 mirror generated with FRED

5.3. Stray Light Model Generation

The ray-trace model used for the stray light analysis consists of the baseline model found in Figure 5.11 from Section 5.2.3. The mechanical CATIA file from the various baffle models from Section 4.6 were imported into the baseline model. The baffles are then positioned towards the correct position and orientation. For example, design 5.1 implemented in FRED can be seen in Figure 5.13.

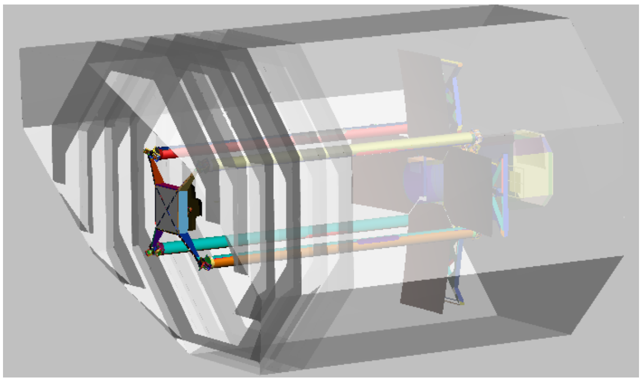

Figure 5.13: Baffle design 5.1 in FRED, note that the opacity of the baffle is set to 50% to showcase the DST

In FRED, different 'Coating' options can be set to the (optical) material. Note that the 'Coating' option in general applies to optical elements. The baffles (in-)ability to reflect light sources from on-and off-axis sources is the primary reason for analysing the stray light performance of the baffles. Therefore, the hypothetical worst case scenario is analysed: a fully reflective coating. The 100% reflective coating increases the chance of rays reflecting to unwanted areas, whilst maintaining as much radiant exitance as possible (due to no absorption in the hypothetical case of 100% reflection). Furthermore, raytrace control is possible with FRED with the default set to 'Allow All'. The default setting is set for the stray light analysis. The standard coatings and ray-trace control settings in FRED can be found in Figure 5.14

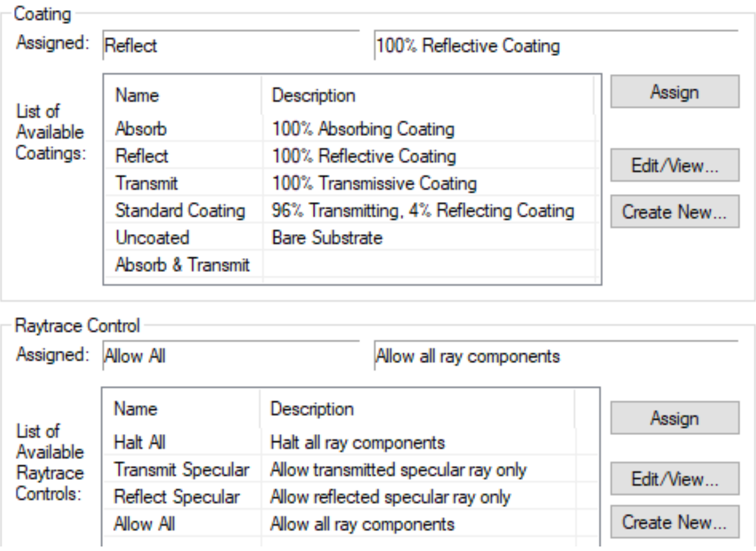

Coating

Assigned: Reflect | 100% Reflective Coating

List of Available Coatings:

Name	Description
Absorb	100% Absorbing Coating
Reflect	100% Reflective Coating
Transmit	100% Transmissive Coating
Standard Coating	96% Transmitting, 4% Reflecting Coating
Uncoated	Bare Substrate
Absorb & Transmit	

Raytrace Control

Assigned: Allow All | Allow all ray components

List of Available Raytrace Controls:

Name	Description
Halt All	Halt all ray components
Transmit Specular	Allow transmitted specular ray only
Reflect Specular	Allow reflected specular ray only
Allow All	Allow all ray components

Figure 5.14: Standard available coatings and raytrace control settings in FRED

The material property is reserved for optical (glass) elements, such as refractive index. The material property do not have to be assigned to the material property for the mechanical parts. Rather a scatter property should be set for mechanical parts. FRED has some scatterers available, such as Black Lambertian or flat black paint. Coatings from Acktar are also present in the FRED database (Acktar Ultra Black 10.6 μm, Acktar Vacuum Black 3.39 μm, Acktar Metal Velvet μm and Acktar Fractal Black μm). The applied coating for all stray light models was chosen to be Acktar Vacuum Black 3.39 μm due to its stray light suppression capability [55]. The intent of the preliminary stray light analysis is to identify the effect of the baffle geometry on the stray light performance. Therefore, only the baffle geometry is changed to obtain the effect of changing geometry.

5.4. Stray Light Conclusion

The stray light performance of the system is analysed to assess the effectiveness of the baffles. The stray light analysis performed is the PST from Section 4.2, using a FRED script from FRED itself [17]. The script analyses the PST for a source power defined for a unit incident radiation. This script was slightly altered such that it would be able to calculate the PST for any source power. From preliminary thermal analysis, the maximum angle at which solar heat can impinge the interior baffle is at 26°. It is therefore chosen to perform the PST analysis from 0 to 45° to take into account inaccuracy in pointing the spacecraft perfectly nadir.

The calculation of the PST in general considers the amount of energy on the detector to the energy incident in the system. In the case for the DST, the detector is reached through multiple reflections (from M1 to M2 to M3 to TNO Custom DM to the detector). On-axis rays (within ± 0.3° cross-track and 0 to 0.25° along track) which are reflected off of M1 towards M2, are focused towards the field stop. Off-axis rays fall onto the cylindrical housing and are thus prevented from progressing towards the remaining optical elements. Thus preventing off-axis rays from propagating towards the detector plane. The cylindrical housing and field stop can be seen in Figure 5.15.

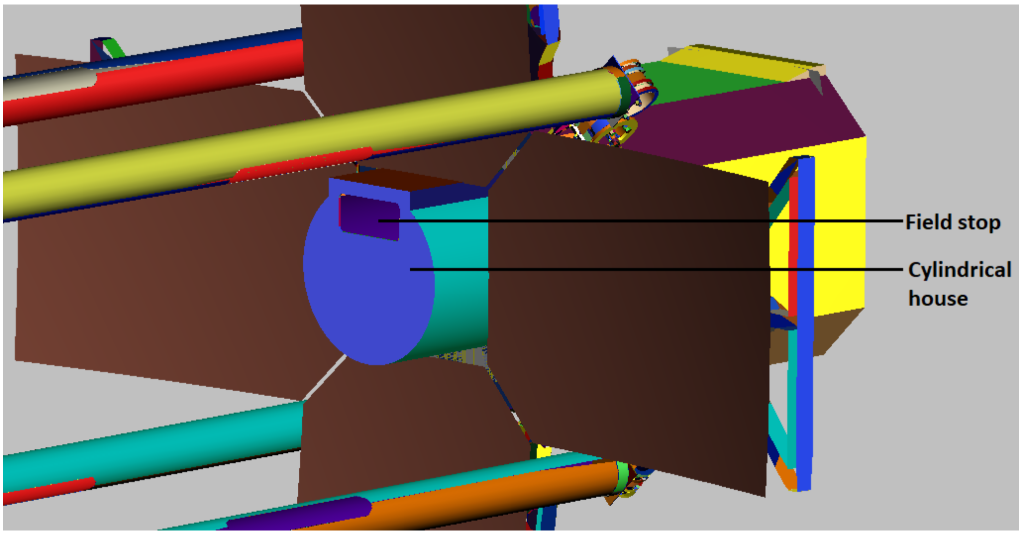

Figure 5.15: The cylindrical housing and field stop of the DST modelled in FRED

These elements together provide a good barrier for blocking off-axis (stray) light to propagate within the system. Off-axis rays do not reach the detector (for a source of approximately $1x10^5$ rays). This gives the system a hypothetical PST of 0 for every off-axis angle. Since analyses of one angle takes approximately 8 hours, it is decided to select a different analysis surface for the PST calculation. The surface selected is the M2 mirror, due to the mirror being the last optical element before the field stop. The rays on the optical axis that fall onto M2 are focused through the field stop, but rays that fall outside of the on-axis budget do not pass through the field stop. The off-axis rays that reflect off of M2 are rather focused on the exterior of the spacecraft bus in between the M1 mirror.

The result of the PST analyses of all the baffles can be found in Figure 5.17. It can be seen that the baffles (logically) introduce some stray light paths and unwanted bounces off of the baffle wall. As a result, more energy is absorbed by the analysis surface. In the absence of a baffle i.e. no baffle case, this energy would have propagated past the system into deep space and would have not been absorbed by a component of the DST. There are off-axis angles which could reach the detector but only with a baffleless DST. Protection against rays from these very off-axis angles is done through placing a surface e.g. baffle wall. Simulation of a hemisphere radiating towards the detector would take too much computing time. Therefore these extreme cases are not taken into account because they would have been blocked anyhow by a baffle. This skews the result of the PST analysis with no baffle. In reality, a baffleless system would be far worse due to all the off-axis rays hitting the detector as can be seen in Figure 5.16.

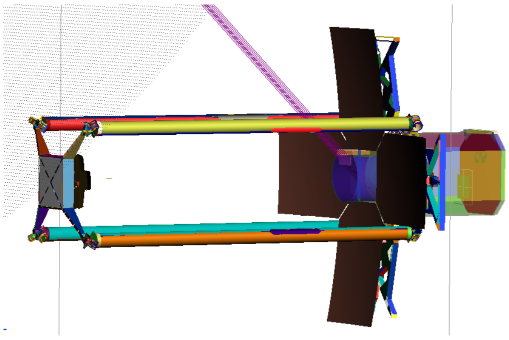

Figure 5.16: Off-axis ray propagating through the internal optical house. This ray would have been stopped by a baffle

From 0 to 6°, the PST values are the same for all variations (including the case for an absent baffle). Remarkably, the PST values of all the baffles do not exceed the PST value for the on-axis case (of 0 degree). This can be attributed to the field stop which limits the direction from which light can propagate through the spacecraft bus. The baseline baffle and design 2.1 track eachother relatively close, which is logical due to their equal vane area. There is some minor difference between the baseline and 2.1, but this can be attributed to 2.1 having more vanes which reduces the amount of energy reaching the analysis surface due to multiple reflections. Both baseline and 2.1 perform the worst due to their smaller vane area. Design 3.1 is seen to perform the best due to the larger vane area. Whilst design 4.1, which has angled vanes that introduces some more scatter and reflections inside of the baffle. The sugar-scoop of design 5.1 shows that a peak is present at 27°, which can be due to the vanes being designed to minimise stray light towards M1 instead of towards M2. From the PST comparison between the baseline and designs 3.1, 4.1 and 5.1, it can be concluded that a larger vane area increases the PST performance. The sugar-scoop does not inherently bring worse PST performance, but there is a peak which shows some worsening stray light behaviour at 25°.

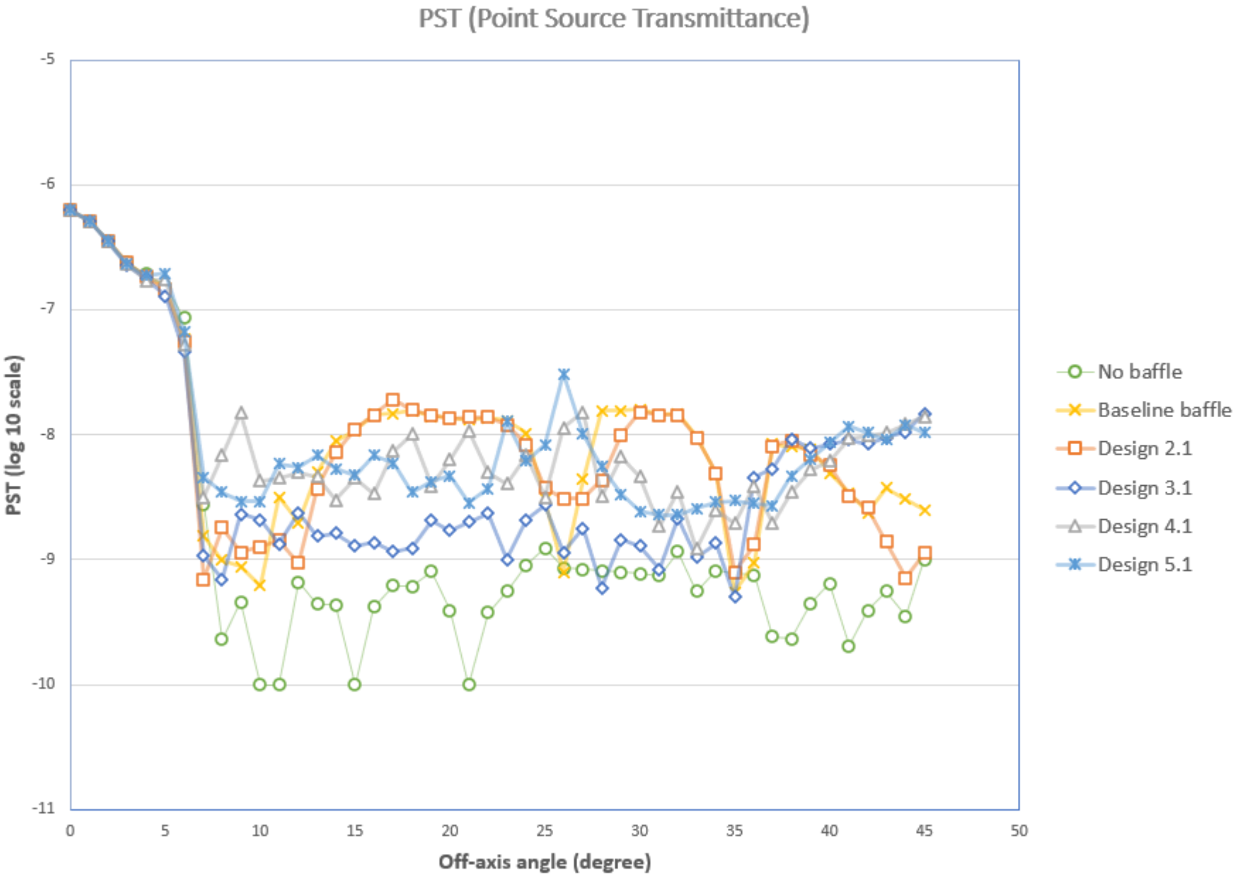

Figure 5.17: PST of all the preliminary design baffles which are plotted in Excel. PST is written in log10 scale

The stray light requirement was defined in Section 4.3 to be PST = $7 \cdot 10^{-5}$, which corresponds to a PST of -5 in the log scale. Because all of the designs are below PST = -6 on the log scale, all of the baffles comply to the stray light requirement.

6

Thermal Model

In this chapter, the thermal analysis of the VIS-baffles is given. First the development of the in-orbit drift and related components is given in Section 6.1. ESATAN is used to analyse the thermal performance of the baffle. In order to set-up the thermal analysis, the baffles have to first be modelled in ESATAN which is described in Section 6.2. The thermal analysis of the various VIS baffles is given in Section 6.3. From the result of the analysis, some conclusions can be developed alongside with systems engineering tools to compare the baffles in Section 6.4. From the analysis, a proposal to the improvement for the thermal design is given in Section 6.5. Finally, a discussion on the thermal results is given in Section 6.6.

6.1. In-orbit drift: Thermal Budget

Pepper determined the budgets for the maximum longitudinal elongation and maximum rotation for the SMSS for the VIS DST [2], to be $2\mu m$ for the longitodunal elongation and $6\mu rad$ for the maximum rotation. The components which contribute to the position of the SMSS are the booms, CORE hinges, rods, SM and spider. This thermal budget is expanded into two different formats a temperature based budget for the components by Arink and an individual components expansion equation by Akkerhuis [12]. The method of Arink looks at the thermal range experienced by the component throughout the orbit. Whereas the method set-up by Akkerhuis emphasises the instantaneous temperature of each component at a certain time in the orbit. The length of a component affected by a change in temperature (thermoelastic expansion) can be described by Equation 6.1. Where the thermal length expansion ΔL is due to a change in temperature ΔL applied to the original length L with a coefficient of thermal expansion (CTE) α.

$$\Delta L = \alpha \Delta T L \tag{6.1}$$

The equation established by Akkerhuis to calculate the thermal expansion can be found in Equation 6.2. This equation highlights the effect of each component which contributes to the position of M2, by looking at each individual material composition and length. Akkerhuis notes that the effect of the thermal expansion of the spider itself has negligible effect and is therefore left out (a 10 K change results a length change in the order of picometers). The relative lengths can be seen in Figure 6.1. The longitudinal in-orbit drift budget established by Akkerhuis provides a method to calculate the change in distance Δz at an instantaneous time. As was highlighted by Akkerhuis, the different temperature of each component at each position in the orbit will determine the longitudinal translation of the SMSS. This allows for analysing when the in-orbit drift budget is met, and at how many instances throughout the orbit.

$$\begin{aligned}\Delta z &= \Delta L_B + \Delta L_{HT} + \Delta L_{HR} - \Delta L_{SMSS_Z}\\ \Delta z &= \alpha_B L_B \Delta T_B + \alpha_H \left(L_{HT}\Delta T_{HT} + L_{HR}\Delta T_{HR}\right) - \alpha_R L_R \Delta T_R \leq 2\mu m\end{aligned} \tag{6.2}$$

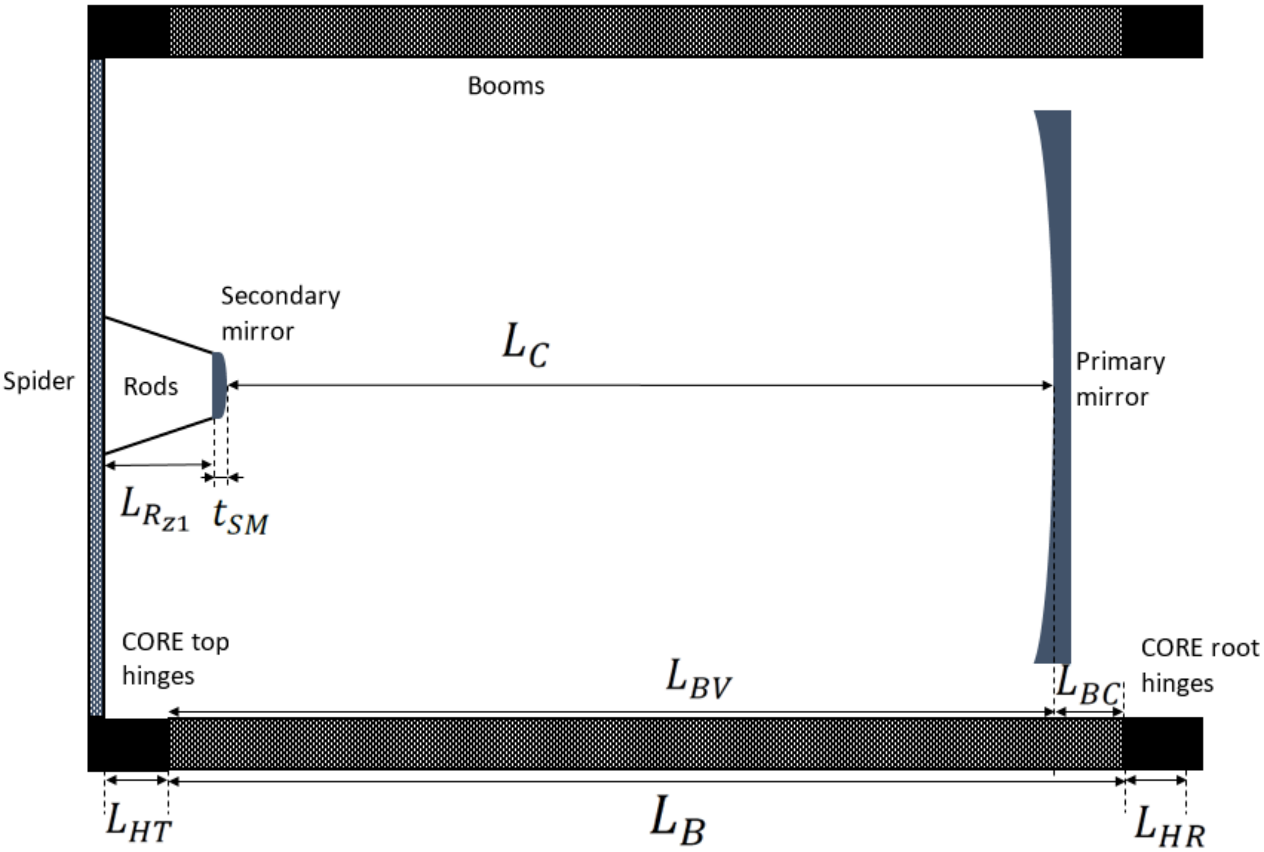

Figure 6.1: Schematic overview of the relevant lengths for the thermal expansion budgets from Akkerhuis [12]

The rotational budget around the X- and Y-axes was also established by Pepper [2]. The rotation of the SM can be due to a different expansion between different opposing components. For example, the sun can partially heat up one side of the booms whilst the opposite boom remains in the shadow, which causes a different thermal expansion between the opposite booms. The angle of rotation (γ) is also caused by thermal expansion of the booms, CORE hinges and rods and was defined by Akkerhuis in Equation 6.3. Akkerhuis noted that the maximum rotation around the X- or Y-axis was calculated to be 2.8 μrad for the baseline design, complying with the maximum rotational budget of 6 μrad [12].

$$\Delta\gamma = tan^{-1}\left(\frac{\Delta L_{B_P} + \Delta L_{HT_P} + \Delta L_{HR_P} - \Delta L_{B_N} - \Delta L_{HT_N} - \Delta L_{HR_N}}{w_{sp}}\right) - tan^{-1}\left(\frac{\Delta L_{R_P} - \Delta L_{R_N}}{w_{M2,a}}\right) \leq 6\mu rad \tag{6.3}$$

6.2. Baffle Modelling in ESATAN

In this section, the baseline thermal model is shown and checked. The starting point for the thermal model, is the thermal model of Akkerhuis seen in Figure 6.2. The thermal model of Akkerhuis is an improved model of the thermal model of Arink [12]. However, it was unclear which thermal model was the final thermal model used by Akkerhuis due to an unsolvable software issue prohibiting the opening of the most logical recent thermal model. As a consequence, the thermal model starting point used in this thesis is a thermal model used by Akkerhuis, but it is unknown what the differences are with the final thermal model of Akkerhuis. Therefore, the temperatures of the components given in Figure 6.4 are compared to the baseline values of the components in the thesis of Akkerhuis. The baseline values can be found in Figure 6.3 which are taken from Akkerhuis [12].

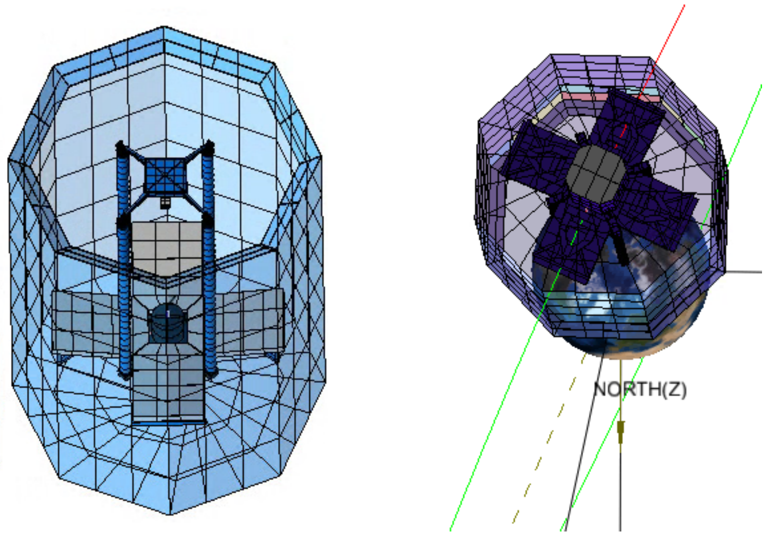

Figure 6.2: Baseline thermal model rendered in ESATAN, the baffle is made transparent for visualisation purposes only

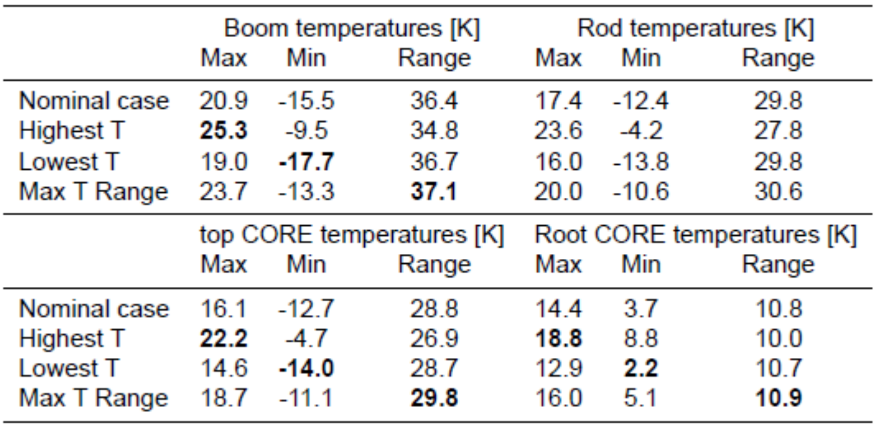

	Boom temperatures [K]			Rod temperatures [K]		
	Max	Min	Range	Max	Min	Range
Nominal case	20.9	-15.5	36.4	17.4	-12.4	29.8
Highest T	**25.3**	-9.5	34.8	23.6	-4.2	27.8
Lowest T	19.0	**-17.7**	36.7	16.0	-13.8	29.8
Max T Range	23.7	-13.3	**37.1**	20.0	-10.6	30.6
	top CORE temperatures [K]			Root CORE temperatures [K]		
	Max	Min	Range	Max	Min	Range
Nominal case	16.1	-12.7	28.8	14.4	3.7	10.8
Highest T	**22.2**	-4.7	26.9	**18.8**	8.8	10.0
Lowest T	14.6	**-14.0**	28.7	12.9	**2.2**	10.7
Max T Range	18.7	-11.1	**29.8**	16.0	5.1	**10.9**

Figure 6.3: Temperatures of the booms, rods and CORE hinges of the baseline model from Akkerhuis [12]

Table 6.1: Maximum and minimum temperatures of the baffle interior, booms, rods and CORE hinges obtained with the baseline thermal model using Akkerhuis radiative input and solution control

	Baffle interior	Booms	Rods	Top CORE	Root CORE Hinges
Max T [°C]	23.52	20.99	23.89	17.73	14.81
Min T [°C]	-16.42	-13.15	-5.51	-9.36	4.96
T Range [°C]	39.94	34.14	29.40	27.09	9.85

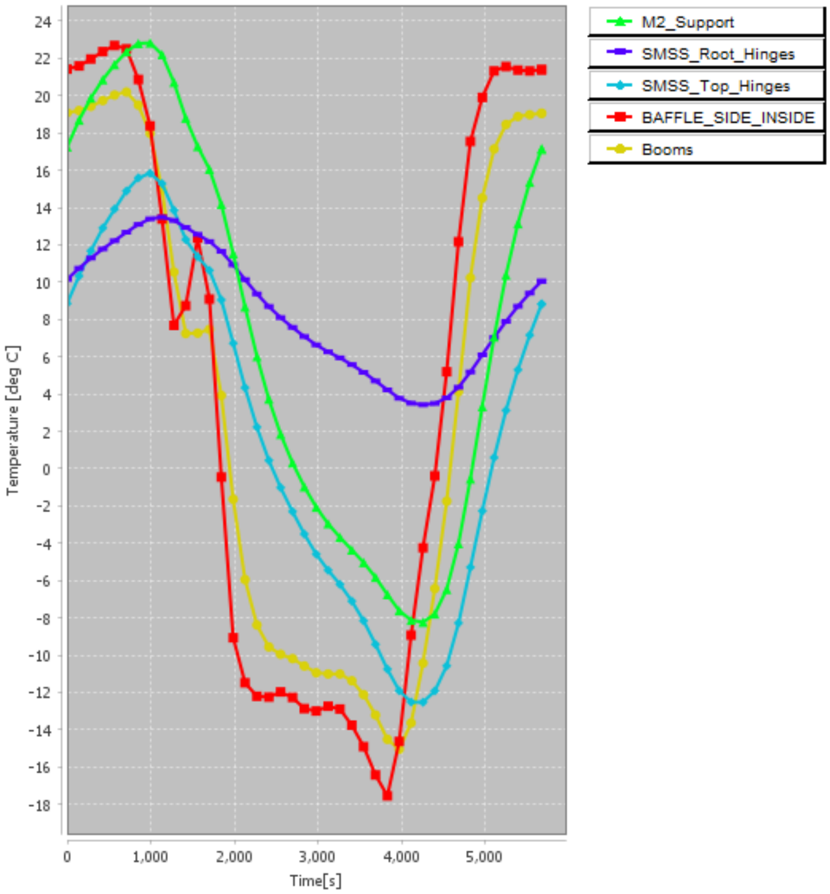

Figure 6.4: Average temperatures of the booms, rods (denoted as M2_Support), CORE hinges (SMSS_Root_hinges and SMSS_top_hinges) and interior baffle wall of the baseline model over one orbit

Because of the iterative nature of thermal modelling, it can be assumed that some properties of the thermal model have been changed with respect to the baseline thermal model. These changes might incorporate some of the work of Akkerhuis in order to progress to the thesis deliverable of Akkerhuis. Comparing the temperatures between the baseline thermal model from Figure 6.4 and reported thermal values of Akkerhuis of Figure 6.3, it can be seen that the temperatures of the booms, top CORE hinges and root CORE hinges fall within 1°C of the reported nominal values of Akkerhuis. The temperature of the rods (denoted by M2_Support in Figure 6.4) differ from the reported nominal case. However, the reported nominal values of Akkerhuis seem to differ from the temperatures obtained by Akkerhuis in graphical format. Akkerhuis investigated the influence of changing the conductance of various parts and their influence on the rods, which resulted in a confidence boundary in which the temperature of the rods should fall within. The influence of the change of conductance can be seen in in Figure 6.5. The temperature of the rods in the graphical nominal case do resemble the temperatures closely found in the baseline model. This gives confidence to proceed using the baseline model as the basis of forming the established thermal models from Section 4.6

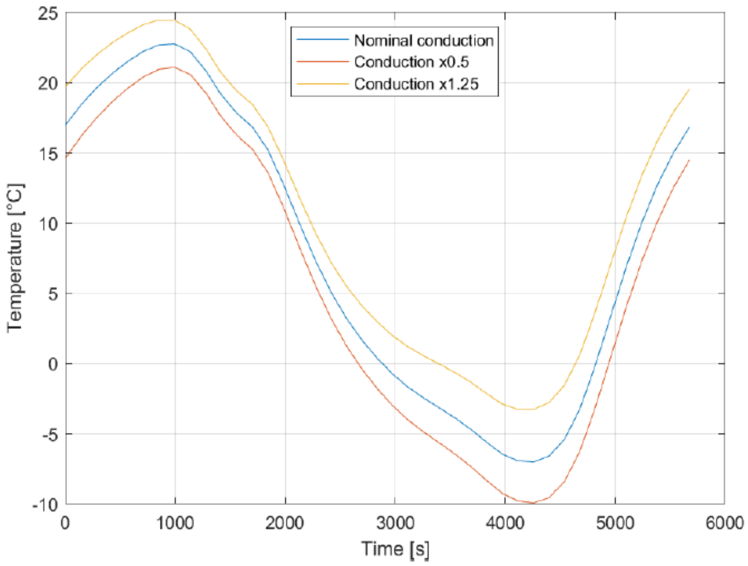

Figure 6.5: Temperature range of the rods through different conductance of the M2 mirror from Akkerhuis [12]

There are some improvements to the thermal analysis of the baseline model which can be made. In order to execute an analysis case, ESATAN first needs to execute a radiative case. The original radiative case uses a large angle gap of 20°between each orbital position, which results in a time gap of 315 s. In addition, the solution control set by Akkerhuis imposes a *OUTINT* value of 141.9 s such that the temperature charts display the temperature on a 141.9 s interval. Furthermore, the solution control time step between calculations *DTIMEI* is set to 100 s, thus generating a result for the temperature every 100 s. Changing the solution control, such that both OUTINT and DTIMEI are set to 50 s leads to a more accurate result displayed in Figure 6.6. The updated solution control script can be found in Appendix A.1.

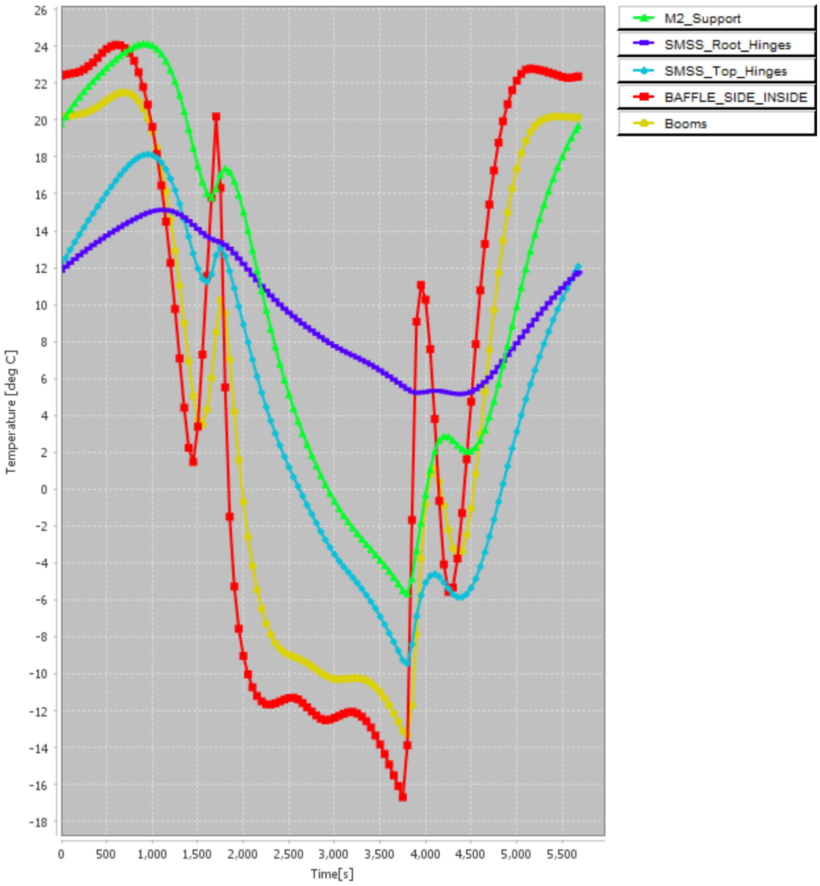

Figure 6.6: Average temperatures of the booms, rods (denoted as M2_Support), CORE hinges (SMSS_Root_hinges and SMSS_top_hinges) and interior baffle wall of the baseline model over one orbit with increased output frequency

The change in output frequency magnifies the change in temperature of the different components between roughly 1450 to 1750 s and 3750 to 4500 s, which would otherwise not be visible when looking at the temperature graph. The larger output frequency will make changes to the thermal model more clear. The sharp temperature increases found in the ranges 1450 to 1750 is due to the sun being able to directly heat up the interior of the baffle wall to approximately 20 °C. Furthermore, the SMSS and top CORE hinges are exposed to direct solar heat as can be seen in Figure 6.7. The average temperature of the booms rises due to radiative coupling with the interior baffle wall and conductive coupling to the top CORE hinges.

Table 6.2: Maximum and minimum temperatures of the baffle interior, booms, rods and CORE hinges obtained with the baseline thermal model

	Baffle interior	Booms	Rods	Top CORE	Root CORE Hinges
Max T [°C]	24.08	21.50	24.15	18.149	15.14
Min T [°C]	-16.69	-13.29	-5.64	-9.45	5.16
T Range [°C]	40.7	34.8	29.8	27.6	9.98

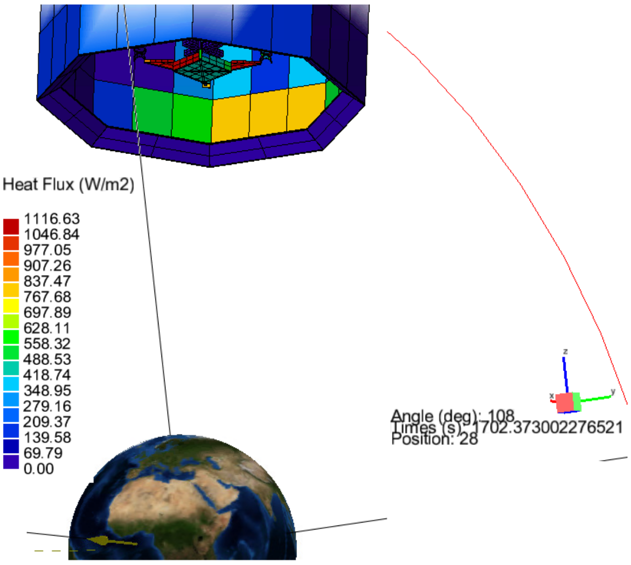

Figure 6.7: Solar heat flux on the DST, prior to entering eclipse

6.3. Thermal Analysis

In this section, the thermal analysis of the baffle concepts are given. The aim of the thermal analysis is to quantify the ability of the baffle geometry to provide a more stable thermal environment. Therefore, influencing factors to thermal performance such as coating, material or material thickness are unchanged from the baseline model. The thermal response to the different baffle concepts are thus solely due to a geometrical change.

6.3.1. Thermal Analysis of Design 2.1

The thermal model of Design 2.1 can be seen in Figure 6.8. The basis for thermal model of design 2.1, is the baseline thermal model. The geometry of the truncated cone is changed to a straight cone. The additional vanes are then copies of the first vane, translated in the Z-axis.

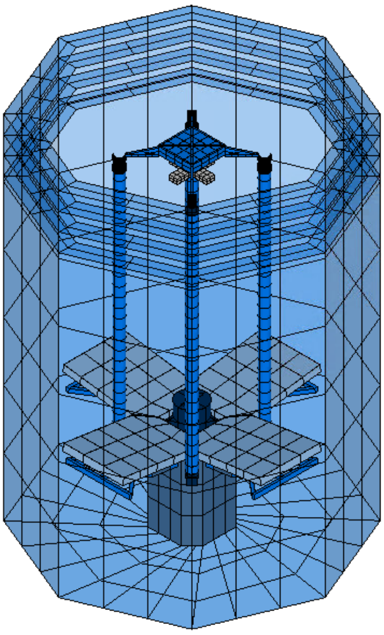

Figure 6.8: Thermal model V2_1 rendered in ESATAN, the baffle is made transparent for visualisation purposes only

The average temperature of the interior baffle wall, booms and rods of Design 2.1 with one and four vanes are given in Figure 6.9. Though the temperature range of the components reduces minimally when going from one to four vanes, the temperature gradients around the orbital time of 1700 and 4000 s is reduced.

Table 6.3: Maximum and minimum temperatures of the baffle interior, booms, rods and CORE hinges obtained with thermal model 2.1

	Baffle interior	Booms	Rods	Top CORE	Root CORE Hinges
Max T [°C]	21.26	19.37	23.14	16.39	13.07
Min T [°C]	-17.74	-13.81	-6.10	-10.16	3.35
T Range [°C]	39.00	33.18	29.24	26.54	9.72

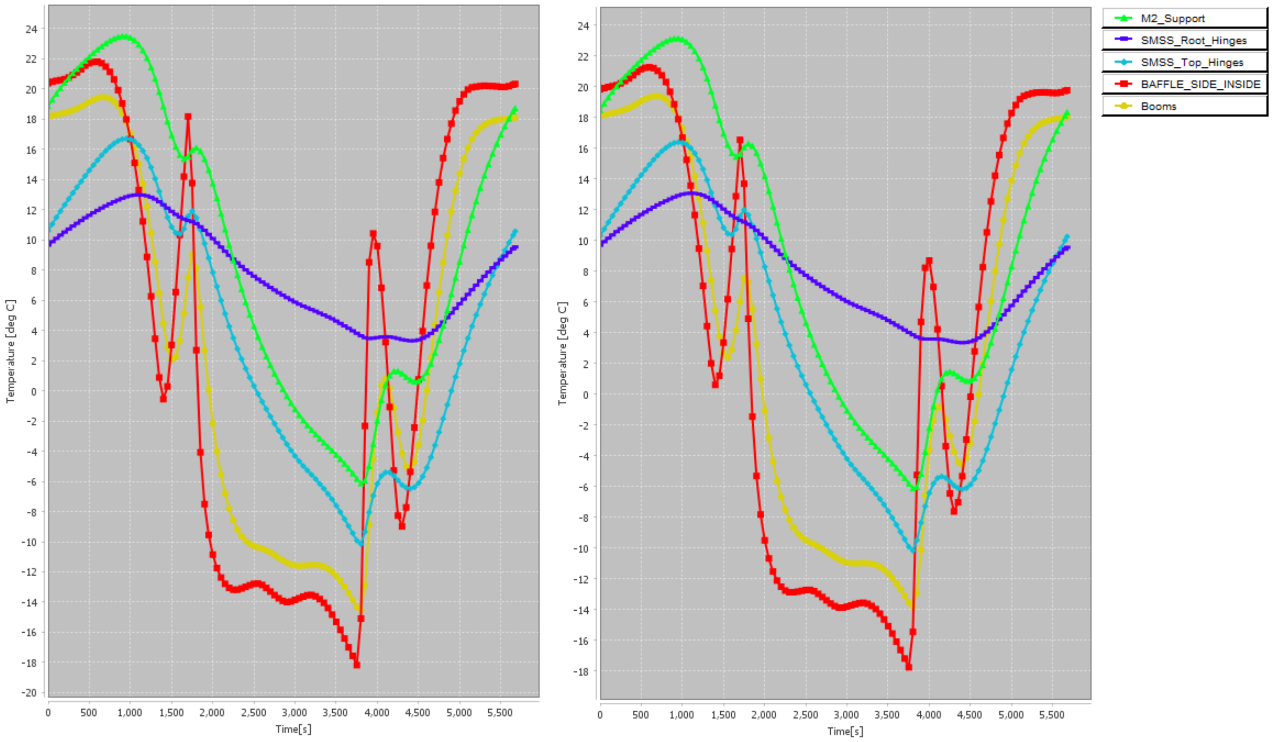

Figure 6.9: Design 2.1: Average temperatures of the booms, rods (denoted as M2_Support), CORE hinges (SMSS_Root_hinges and SMSS_top_hinges) and interior baffle wall with one vane (left) and four vanes (right)

6.3.2. Thermal Analysis of Design 3.1

The thermal model of Design 3.1 can be seen in Figure. The baffle of the baseline model is rotated 22.5°about the Z-axis, such that the horizontal line of the baffle runs parallel to the baffle outer wall. Due to this baffle rotation, the baffle is orientated slightly different than the baseline model with respect to the sun. In order to compare the effect of the baffle only, the whole DST is orientated -22.5°about the Z-axis such that the baffle of design 3.1 has the same orientation as the baseline design. As a consequence however, the optical system and instrument housing is differently orientated than the baseline design. The thermal model in ESATAN can be seen in Figure 6.10. As was discussed in Section 4.6.3, the vanes of design 3.1 can be made larger than design 2.1 whilst still complying with the set requirements.

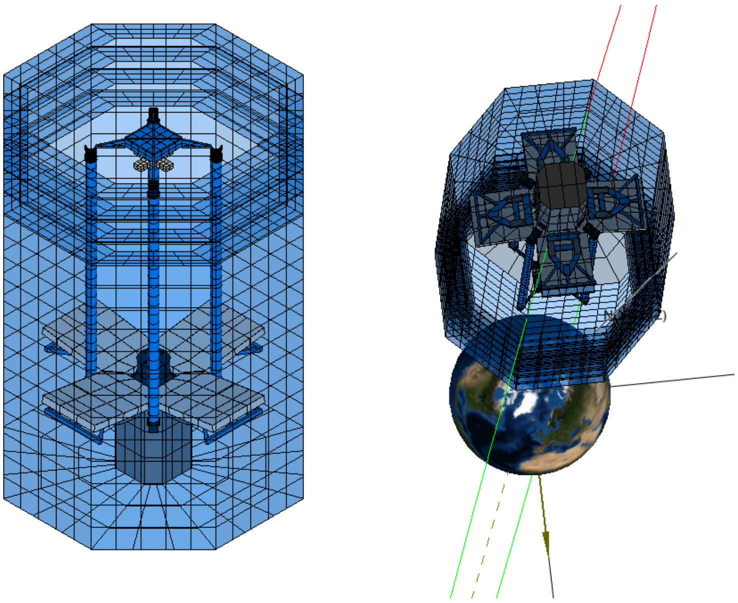

Figure 6.10: Thermal model V3_1 rendered in ESATAN, the baffle is made transparent for visualisation purposes only

As was discussed in Section 4.6.3, the vanes of design 3.1 can be made larger than design 2.1 whilst still complying with the set requirements. The average temperature of the interior baffle wall, booms and rods of Design 3.1 with one and four vanes are given in Figure 6.11.

Table 6.4: Maximum and minimum temperatures of the baffle interior, booms, rods and CORE hinges obtained with thermal model 3.1

	Baffle interior	Booms	Rods	Top CORE	Root CORE Hinges
Max T [°C]	22.64	20.71	24.51	17.66	15.55
Min T [°C]	-14.96	-11.03	-4.72	-8.59	6.04
T Range [°C]	37.60	31.74	29.23	26.24	9.51

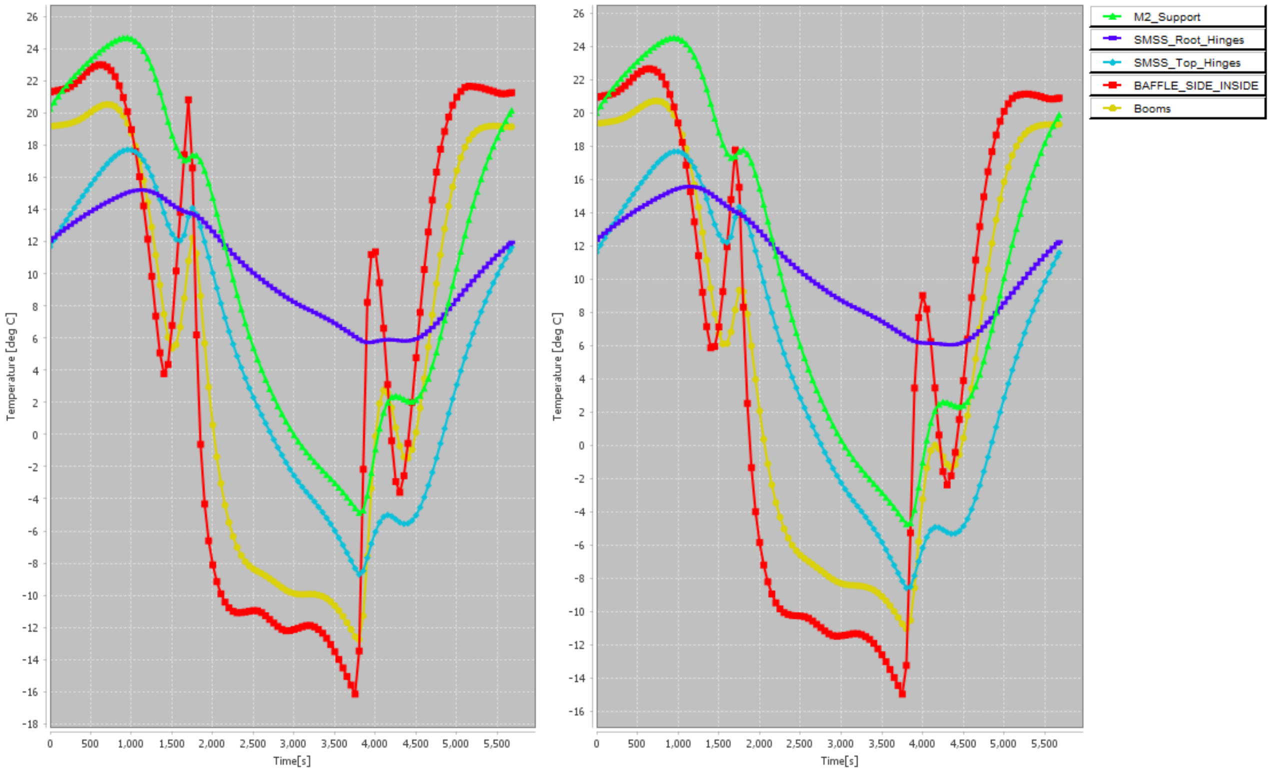

Figure 6.11: Design 3.1: Average temperatures of the booms, rods (denoted as M2_Support), CORE hinges (SMSS_Root_hinges and SMSS_top_hinges) and interior baffle wall with one vane (left) and four vanes (right)

6.3.3. Thermal Analysis of Design 4.1

Design 4.1 adds angled vanes in between the straight vanes of design 3.1. In addition, the angled vanes and straight vanes run deeper in the baffle to reflect incoming solar heat from off-axis angles. The purpose of the angled vanes is to reflect solar heat back into space, as was explained in Section 4.6.4. Design 4.1 can be seen in Figure 6.12.

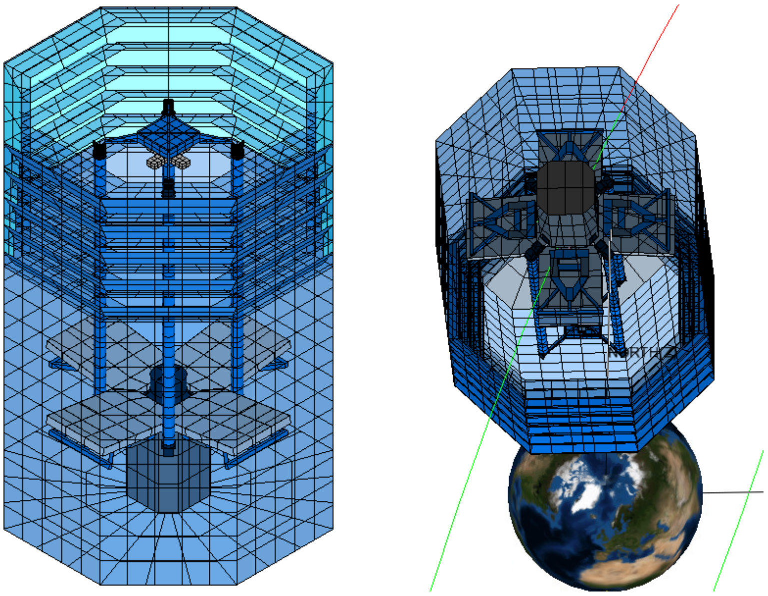

Figure 6.12: Thermal model V4_1 rendered in ESATAN, the baffle is made transparent for visualisation purposes only

The effect of adding angled vanes reduces the temperature rise experienced by the interior baffle wall before entering eclipse and after exiting eclipse. Before entering eclipse, the temperature rise of the interior baffle wall at t_{orbit} = 1500 s goes from 8.7°C to 14°C. The temperature of the booms are minimally reduced and the rods stay relatively the same. The average temperature of the interior baffle wall, booms and rods of Design 4.1 with 6 straight vanes and 5 additional angled vanes are given in Figure 6.13 (left). By comparison, design 4.1 with only 6 straight vanes is given in Figure 6.13 (right) to highlight the temperature reducing effect on the interior baffle wall of the angled vanes.

Table 6.5: Maximum and minimum temperatures of the baffle interior, booms, rods and CORE hinges obtained with thermal model 4.1

	Baffle interior	Booms	Rods	Top CORE	Root CORE Hinges
Max T [°C]	23.25	20.70	24.98	17.90	16.01
Min T [°C]	-13.24	-9.90	-4.02	-8.07	6.63
T Range [°C]	36.50	30.60	29.00	25.97	9.38

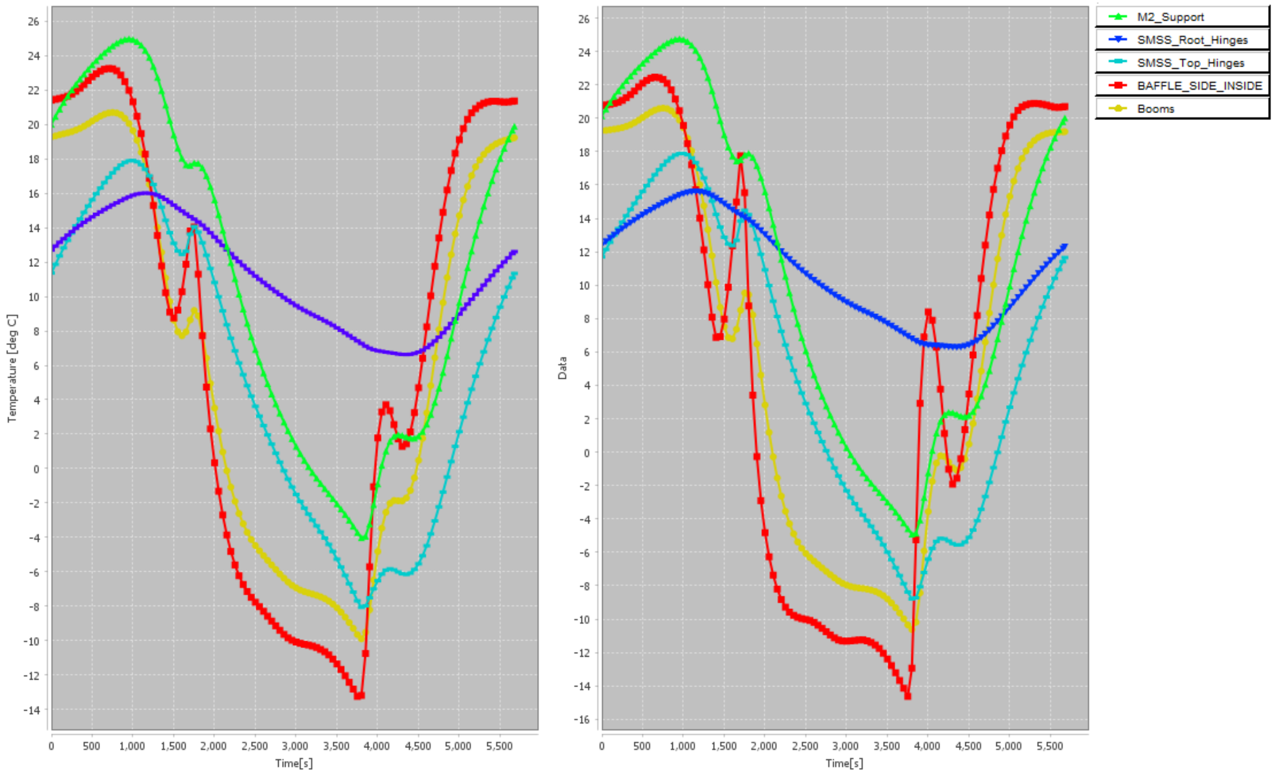

Figure 6.13: Design 4.1: Average temperatures of the booms, rods (denoted as M2_Support), CORE hinges (SMSS_Root_hinges and SMSS_top_hinges) and interior baffle wall with 6 vanes and 5 angled vanes (left) and only 6 vanes (right)

6.3.4. Thermal Analysis of Design 5.1

Design 5.1 implements a sugar-scoop, which eliminates a reflecting surface for the solar heat to reflect back into the baffle. Baffle design 5.1 can be seen in Figure 6.14, note that the baffle height is increased by 50 cm to a total height of 3.15 m to cover the SMSS. An adaptations in the radiative case had to be made in ESATAN to make the sugar-scoop effective. The sugar-scoop has to be correctly pointed towards the sun, through-out the whole orbit. Thus, the AOCS has to orient the long-face of the baffle (in the positive X-axis direction) to the sun throughout the orbit. In ESATAN, the performance of the AOCS can be applied to design 5.1 by having a primary pointing direction nadir in the Z-axis. The secondary pointing vector is chosen to be the positive direction of the X-axis (long-face of the baffle), with a pointing direction towards the centre of the sun. The effect of these changes is visualised in Figure 6.15 (left) which shows that the long-face of the baffle remains pointed towards the Sun (positioned at left-hand of the paper).

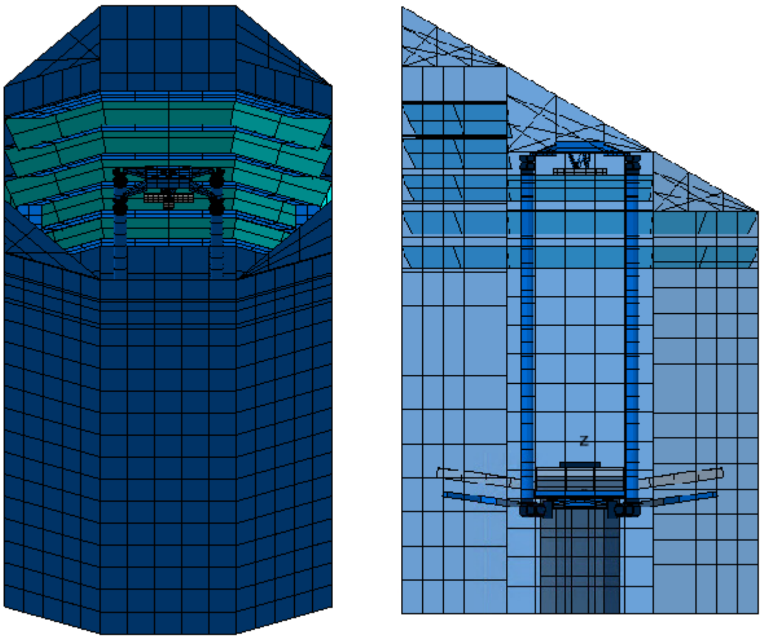

Figure 6.14: Thermal model V5 rendered in ESATAN, the baffle is made transparent for visualisation purposes only

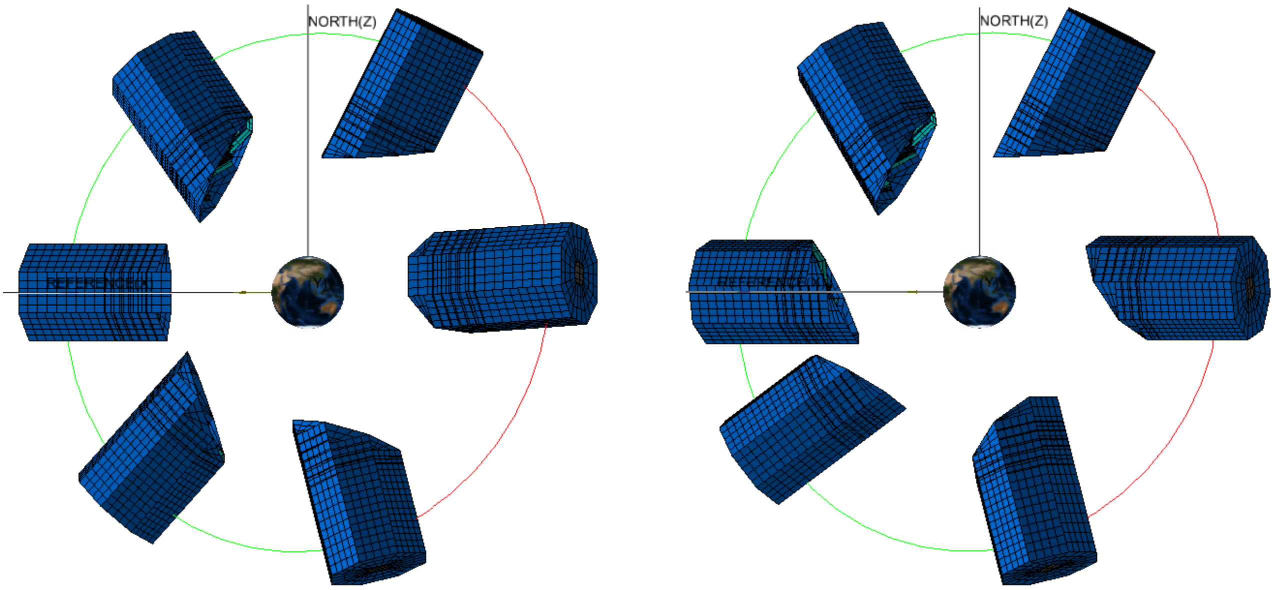

Figure 6.15: Model 5.1 with pointing on (left) and off (right), the Sun radiates from the left towards the right

The maximum and minimum temperatures of the baffle interior, booms, rods and CORE hinges can be found in Table 4.7 along with the temperature of these components in the orbit in Figure 6.16. Because of the longer baffle wall and the pointing function, the interior components inside of the baffle remain protected against the solar heat. As a result of no direct solar heat on those components, the maximum and minimum temperatures of these components are decreased. Furthermore, this results in a slightly larger temperature range for the components with the exception of the root CORE hinges.

Table 6.6: Maximum and minimum temperatures of the baffle interior, booms, rods and CORE hinges obtained with thermal model 5.1

	Baffle interior	Booms	Rods	Top CORE	Root CORE Hinges
Max T [°C]	16.40	13.18	10.87	0.61	8.40
Min T [°C]	-22.89	-22.38	-21.17	-27.91	-1.54
T Range [°C]	39.29	35.56	32.04	28.53	9.94

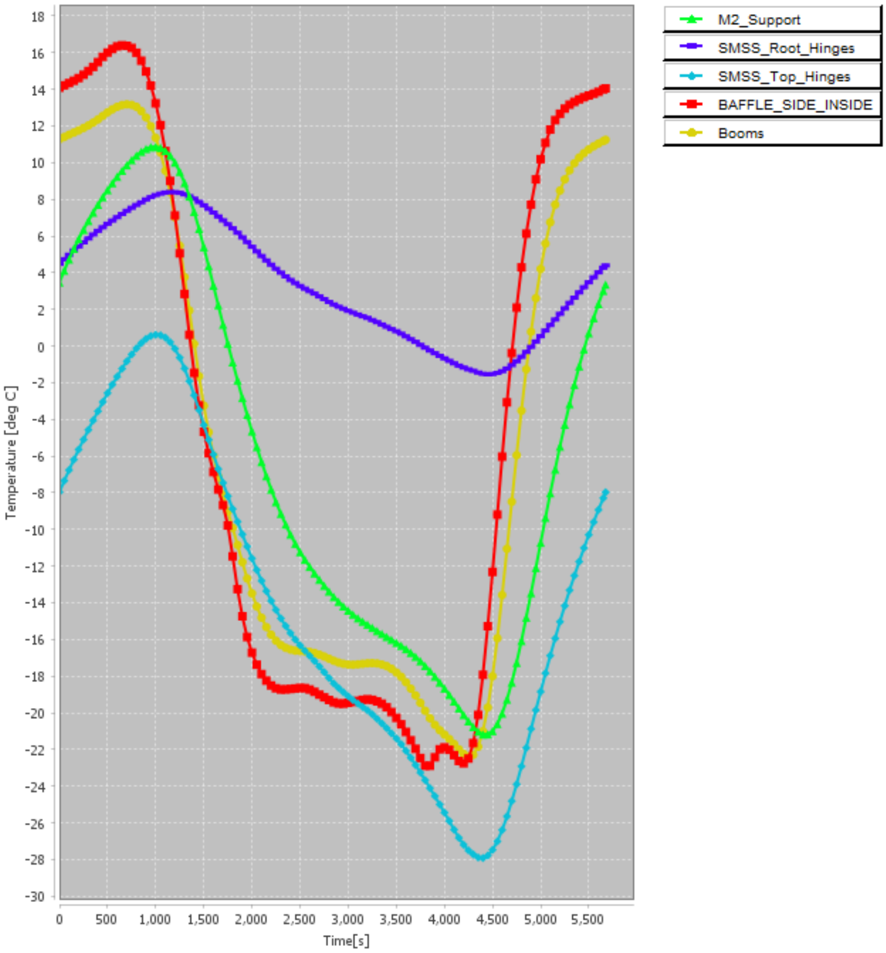

Figure 6.16: Design 5.1: Average temperatures of the booms, rods (denoted as M2_Support), CORE hinges (SMSS_Root_hinges and SMSS_top_hinges) and interior baffle wall with 6 vanes and 5 angled vanes

6.4. Thermal Analysis Overview

In this section, an overview is given of the thermal analysis from the various models. The maximum and minimum temperatures are summarised into Table 6.7. It can be seen that the temperature ranges are gradually reduced through the application of vanes and applying angled vanes, though the reduction in temperature range is minimal.

The largest change in temperature, which is not apparent from Table 6.7, is the temperature change of the interior baffle wall and booms prior to entering (around 1500 s) and exiting eclipse (around 3750 s). This change can be seen when comparing for example the baseline model to model V4.1 as can be seen in Figure 6.17. The difference between the models is the increase in vanes and larger vane depth. The temperature rise experienced by the interior baffle at 1500 s initially increases with 19 K, but with the addition of straight and angled vanes this temperature increase is reduced to 5 K. The intermediate effect of adding angled vanes in-between the straight vanes, can be seen in Figure 6.13, the angled vanes reduces the temperature increase experienced around 1500 s from 11 K to 5 K.

The application of a sugar-scoop with design 5.1 lowers the maximum and minimum temperature of the components. This is caused by the lengthened baffle wall, which shields the components inside of the baffle from direct solar heat exposure. As a result, all maximum and minimum temperatures of the components are lower. The temperature increase experienced by the other baffles, prior to entering and exiting eclipse is not experienced by the sugar-scoop. The minimum average temperature nears -30 ^{o}C, which urges some attention to the minimum allowed temperature of the components.

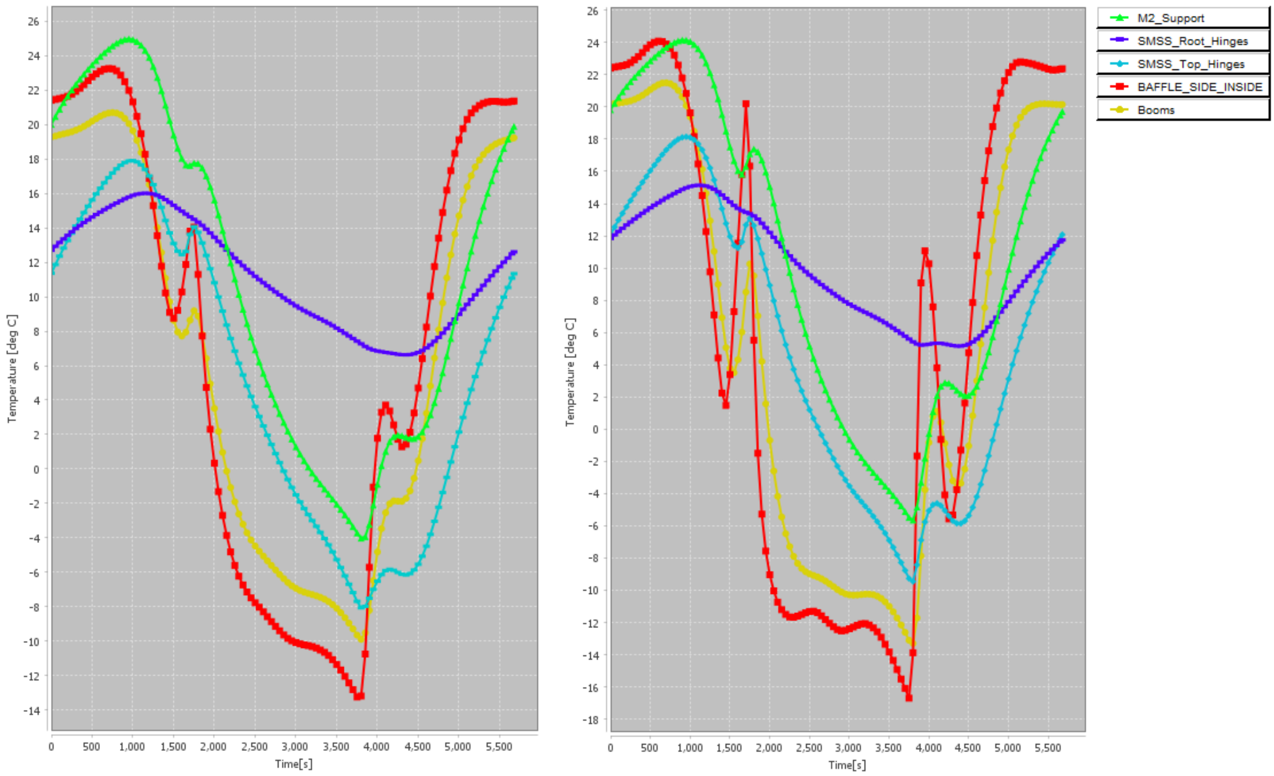

Figure 6.17: Temperature response of critical components of model 4.1 (left) and baseline model (right)

Table 6.7: Maximum and minimum temperatures of the baffle interior, booms, rods and CORE hinges obtained with the thermal models

	Baseline Thermal Model				
	Baffle interior	Booms	Rods	Top CORE	Root CORE Hinges
Max T [°C]	24.08	21.50	24.15	18.149	15.14
Min T [°C]	-16.69	-13.29	-5.64	-9.45	5.16
T Range [°C]	40.7	34.8	29.8	27.6	9.98

	Thermal model V2.1				
	Baffle interior	Booms	Rods	Top CORE	Root CORE Hinges
Max T [°C]	21.26	19.37	23.14	16.39	13.07
Min T [°C]	-17.74	-13.81	-6.10	-10.16	3.35
T Range [°C]	39.00	33.18	29.24	26.54	9.72

	Thermal model V3.1				
	Baffle interior	Booms	Rods	Top CORE	Root CORE Hinges
Max T [°C]	22.64	20.71	24.51	17.66	15.55
Min T [°C]	-14.96	-11.03	-4.72	-8.59	6.04
T Range [°C]	37.60	31.74	29.23	26.24	9.51

	Thermal model V4.1				
	Baffle interior	Booms	Rods	Top CORE	Root CORE Hinges
Max T [°C]	23.25	20.70	24.98	17.90	16.01
Min T [°C]	-13.24	-9.90	-4.02	-8.07	6.63
T Range [°C]	36.50	30.60	29.00	25.97	9.38

	Thermal model V5.1				
	Baffle interior	Booms	Rods	Top CORE	Root CORE Hinges
Max T [°C]	16.40	13.18	10.87	0.61	8.40
Min T [°C]	-22.89	-22.38	-21.17	-27.91	-1.54
T Range [°C]	39.29	35.56	32.04	28.53	9.94

As was highlighted in Section 6.1, the position of M2 due to thermal expansion should be calculated for each instance in the orbit. Therefore, less emphasis should be put on the maximum and minimum temperature of the components. Applying the thermal elongation Equation 6.2, allows for comparing the thermal performance at every orbital position in terms of meeting the translation in-orbit drift budget. The in-orbit drift for the various models for the whole orbit is given in Table 6.8. The in-orbit drift for the various model for the actual period in which the in-orbit drift budget applies to is the sunlit period t_{drift}. For this correct duration, the results can be found in Table 6.9.

The absolute sum of the in-orbit drift $|\Sigma\Delta z|$ due to thermal expansion compares the ability of the baffle to keep the in-orbit drift to a minimum. From this metric, design V5.1 performs the best as it has the lowest total in-orbit drift. Which is also highlighted by the fact that it is able to keep the in-orbit drift below $2\mu m$ in 37% of the whole orbit. In terms of this metric, V2.1 performs worse followed by the baseline and V3.1. The added vanes of 2.1 (total of four vanes) compared to the baseline model (one vane), explains that more vanes are able to trap the temperature better than one vane. This results in a higher sum in-orbit drift $|\Sigma\Delta z|$ for design 2.1 compared to the baseline model. Comparison between design V3.1 to V2.1 shows the effect of increasing the vane surface area (which was enabled by rotating the baffle 22.5 about the Z-axis). The effect of adding more vanes and angled vanes (in design V4.1) does seem to positively influence the absolute sum of the in-orbit drift. However, this result does not show up in the effectiveness of staying below a set in-orbit drift requirement. This could be because the effect of the vanes is minimal, which results in a low difference between the absolute of the in-orbit drift.

Comparison of design 4.1 with 11 vanes to design 4.1 with 7 vanes, concludes that fewer vanes perform better than the design with more vanes. This is due to the angled vanes reflecting more solar heat away into space when exciting eclipse. As a result, the components inside of the baffle warm up less fast.

The elongated baffle with the sugar-scoop completely prevents the illumination of the internal components (rods, SMSS, top CORE hinges and partial top part of the booms). This causes the temperature increase and decrease of the components to follow eachother more closely. As a result, the components thermally expand and contract more synchronously. Thus the sugar-scoop applied with design 5.1 gives the best result (least amount of in-orbit drift) when a small in-orbit drift is required.

The effect of relaxing the in-orbit drift budget to for example 10 μm shows that the sugar-scoop of design 5.1 actually does not perform as well anymore. Rather the other baffles perform better, boasting a larger percentage of the orbit fulfilling the imposed $\Delta z \leq 10\mu\ m$ requirement. The modulus of the in-orbit drifts (absolute values are plotted in Figure 6.18 against time-step (one time-step is 50 s) for the various baffles. This figure shows that the in-orbit drift after eclipse increases for design 5.1 to well beyond $\Delta z \geq 10\mu\ m$ for a large portion of the time (from time step 75 to 115), whereas the others stay below $\Delta z \leq 10\mu\ m$. The in-orbit drift plotted in Figure 6.18 also shows more clearly the benefit of adding more vanes to the design to reduce Δz. The upper-bound in which the Δz should fall in is established by the coarse alignment budget. In case of the VIS design: $\Delta z \leq 10\mu m$.

Table 6.8: In-orbit drift for the various models: total drift, number of times the drift budget is met and the percentage of times being met through entire orbit (total of 115 time steps in one orbit)

Model	$\|\Sigma\Delta z\|$ [μm]	# $\Delta z \leq 2\mu m$	% $\Delta z \leq 2\mu m$	# $\Delta z \leq 4\mu m$	% $\Delta z \leq 4\mu m$	# $\Delta z \leq 10\mu m$	% $\Delta z \leq 10\mu m$
Baseline	1038	10	9%	21	18.2%	80	70%
V2.1 (4 vanes)	1143	8	7%	20	17.4%	71	62%
V3.1 (4 vanes)	927	9	8%	23	20 %	80	70%
V4.1 (7 vanes)	876	8	7%	25	22 %	82	71%
V4.1 (11 vanes)	877	8	7%	21	18 %	82	71%
V5.1 (11 vanes)	758	42	37%	55	48%	81	70%

Table 6.9: In-orbit drift for the various models: total drift, number of times the drift budget is met and the percentage of times being met through the sunlit period t_{drift} (total of 76 time steps in the sunlit period)

Model	$\|\Sigma\Delta z\|$ [μm]	# $\Delta z \leq 2\mu m$	% $\Delta z \leq 2\mu m$	# $\Delta z \leq 4\mu m$	% $\Delta z \leq 4\mu m$	# $\Delta z \leq 10\mu m$	% $\Delta z \leq 10\mu m$
Baseline	507	10	13%	21	28%	65	86%
V2.1 (4 vanes)	572.7	8	11%	20	26%	59	78%
V3.1 (4 vanes)	489.2	9	12%	23	30%	62	82%
V4.1 (7 vanes)	477.0	8	11%	25	33%	62	82%
V4.1 (11 vanes)	481.3	8	11%	21	28%	62	82%
V5.1 (11 vanes)	597	22	29%	31	41%	48	63%

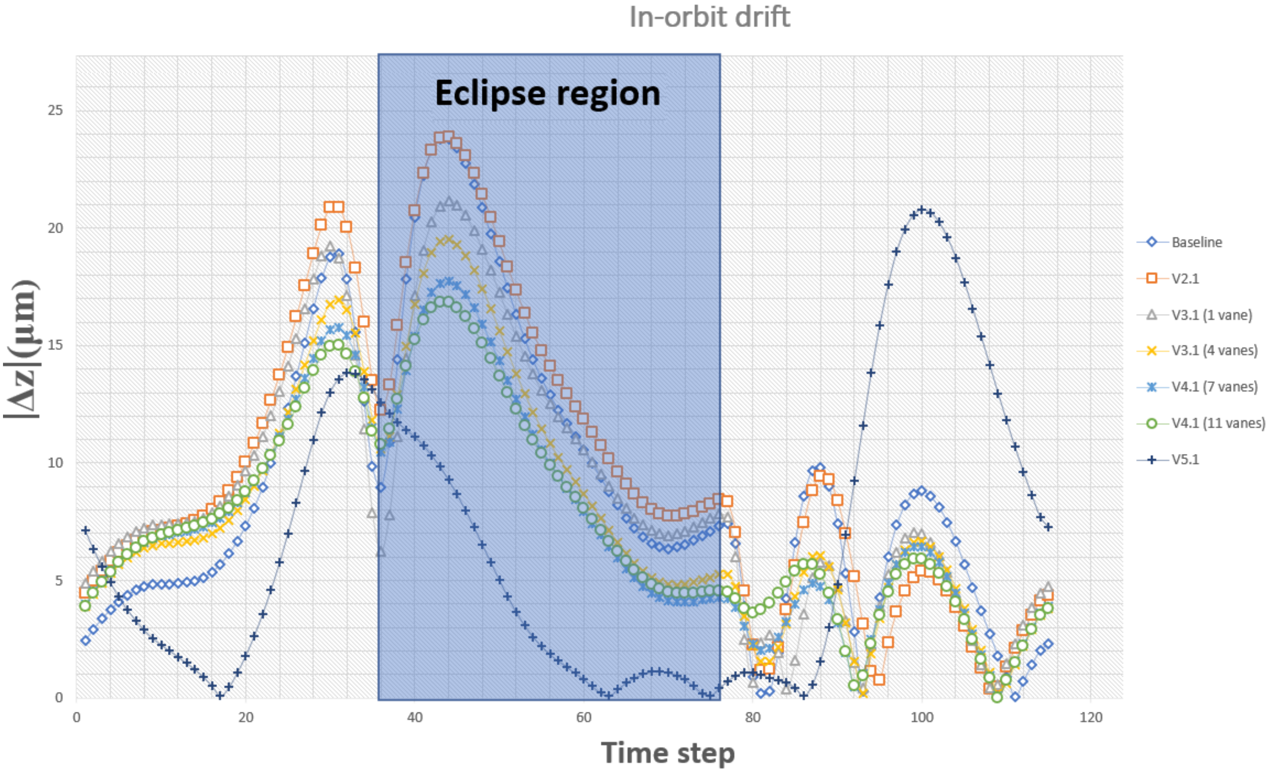

Figure 6.18: In-orbit drift $|\Delta z|$ plotted against the time-step for the various baffle designs. The eclipse region of the orbit is highlighted by the blue area. Note that the duration of one time step is 50 seconds

6.5. Proposed Improvement to Thermal Expansion

Due to the change in temperature, the total distance between the M1 and M2 changes due to thermal expansion. The proposed improvement is to calculate the average of the thermal expansion and subtract that distance from the length of the boom. The positive direction of thermal expansion is depicted in Figure 6.1. The average Δz throughout the observational period can be calculated through the thermal data. In all cases, the average Δz is negative i.e. on average the distance between M1 and M2 decreases below the required 1600 mm. The proposed improvement is to increase the length of the boom by the average linear thermal compression throughout the orbit. The only exception is the sugar-scoop, design V5. The sugar scoop has a positive linear thermal expansion, which means that on average the distance between M1 and M2 is increased beyond 1600 mm. Therefore the proposed improvement for the sugar scoop would be to decrease the length of the boom by the average increase throughout the observational period. The improvement results in a notable improvement in the compliance to the in-orbit drift requirement. The improvements are given for the observable period i.e. sunlit period in Table 6.10. Which shows that design V3.1 with 4 vanes performs the best when the proposed improvement is implemented and the de-focus $\Delta z \leq 2\mu m$

Table 6.10: In-orbit drift for the various models: average drift during the observational period $\Delta\bar{z}$ and the $\%\Delta z - \Delta\bar{z} \leq 2\mu m$ percentage of times the in-drift orbit budget is met through the observational period

Model	$\Delta\bar{z}$ [μm]	% $\Delta z - \Delta\bar{z} \leq 2\mu m$	% $\Delta z - \Delta\bar{z} \leq 4\mu m$	% $\Delta z - \Delta\bar{z} \leq 10\mu m$
Baseline	-7.4	29%	47%	78%
V2.1 (4 vanes)	-6.5	33%	50%	80%
V3.1 (4 vanes)	-5.1	40%	55%	83%
V4.1 (7 vanes)	-4.9	34%	54%	90%
V4.1 (11 vanes)	-4.7	34%	54%	95%
V5.1 (11 vanes)	1.0	27%	43%	63%

Comparison between the in-orbit drift without and with improvements are tabulated in Table 6.11. The comparison is only made for the in-orbit drift requirement of $\Delta z \leq 2\mu m$.

Table 6.11: In-orbit drift for the various models: average drift during the observational period $\Delta\overline{z}$ and the $\%\Delta z - \Delta\overline{z} \leq 2\mu m$ percentage of times the in-drift orbit budget is met through the observational period

Model	$\% \Delta z \leq 2\mu m$	$\% \Delta z - \Delta\overline{z} \leq 2\mu m$	Percentage difference
Baseline	13%	29%	16%
V2.1 (4 vanes)	11%	33%	22%
V3.1 (4 vanes)	12%	40%	28%
V4.1 (7 vanes)	11%	34%	23%
V4.1 (11 vanes)	11%	34%	23%
V5.1 (11 vanes)	29%	27%	-2%

6.6. Thermal Analysis Discussion

Without the proposed solution of Section 6.5, baffle design 5.1 performed better than the other baffles for $\Delta z \leq 2\mu m$. However, one of the main differences between design 5.1 and the others is the baffle length. Due to the unconventional shape of the sugar-scoop baffle, the thermal analysis of the sugar scoop is discussed.

In order to make sure that the performance of design 5.1 can be attributed to the sugar-scoop, the baffle length variable is isolated. Design 5.1 has an increased baffle length of 3.15 m, where a sugar-scoop was applied on. The increased baffle length could also lead to the better thermal performance, due to the longer baffle preventing solar heat from directly illuminating the interior components. In order to effectively gauge the effectiveness of the sugar-scoop, a new baffle concept was generated. Design 6.1 has the same baffle length as design 5.1, but with no sugar-scoop. This allows for direct comparison between a baffle with (design 5.1) and without a sugar-scoop (design 6.1) whilst the other parameters are more or less equal. This design can be found in Figure 6.19. Design 6.1 has an absolute sum of in-orbit drift $|\Sigma\Delta z|$ of 915 μm and compliance to in-orbit drift below 2 μm in 13.9% of the orbit and $\Delta z \leq 4\mu m$. Since design 5.1 has a compliance to in-orbit drift ≤ 2 μm in 37%, it is quite obvious that the sugar scoop is quite effective at reducing the in-orbit drift budget when a low Δz is needed.

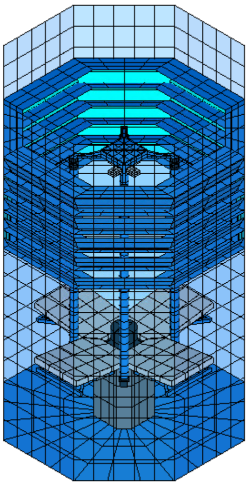

Figure 6.19: Design 6.1: which has the same baffle length as design 5.1 of 3.15 m, but no sugar-scoop

The sugar-scoop adds complexity to the system, which raises questions about the feasibility of applying the sugar-scoop to a deployable baffle concept. As was discussed in Section 4.6.5 the baffle has to be correctly orientated towards the Sun throughout the observational period. This would require the baffle to rotate throughout the orbit. However, rotating the entire spacecraft is not an option as it would interfere with the push-broom scanning method of the DST. It might however be an option to rotate only the baffle around the Z-axis. The currently designed sugar-scoop applied to the octagonal shaped baffle, has one side which has the longest face. As a consequence, the entire spacecraft has to rotate 180°about the Z-axis. This rotation could be performed during the eclipse part of the orbit, when no observations are being taken by the instrument. Another option is to rotate the spacecraft when the bottom of the baffle is closest towards the sun. Note that the eclipse duration is about 35 minutes, which could be used to desaturate the reaction wheels.

Reduction of this rotation could be possible through for example increasing the amount of long faces of the octagonal baffle. Design 5.3, a version of 5.1 with in total three long faces of equal lengths can be seen in Figure 6.20. The three long faces together lowers the precision needed for the rotating mechanism, due to a larger shielding area. In turn, the rotation about Z-axis needed can also be reduced through having more long faces. The thermal performance of design 5.3 is slightly worse than 5.1, though the difference is very small (the percentages found for design 5.1 in Tables 6.8 and 6.9 are reduced by roughly 2% for design 5.3)

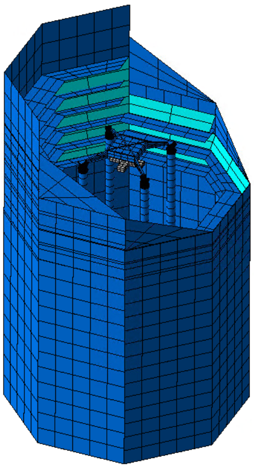

Figure 6.20: Design 5.3: three long faces of equal length of 3.15 m

The in-orbit drift for the sugar-scoop baffle increases more rapidly after exiting eclipse. At t = 5000s, the in-orbit drift for the sugar-scoop (design 5.1) is at its maximum and higher than the in-orbit drift for the octagonal baffles. In order to understand the cause of this large deviation due to the sugar-scoop, the contribution of the individual components should be investigated. The individual contribution of the components to the total in-orbit drift budget are plotted for both the sugar-scoop in Figure 6.22 and design 4.1 in Figure 6.21. The largest difference can be seen in the contribution of the M2 support (rods), which has a much larger thermal shrinkage to a peak minimum value at t = 4500s with the sugar-scoop design. Furthermore, the contribution of the booms with the sugar-scoop design goes to a more negative Δz value. The longer baffle wall permanently shades the M2 support rods from the sun and does not allow for sunlight to impinge on the interior baffle wall. This reduction in thermal input for the M2 support and interior baffle wall leads to a colder temperature of the interior components. As a result, the M2 support rods, booms and top CORE hinges are at a lower temperature than the conventional octagonal baffles. In addition, the lower baffle sidewall (opposite to the longer side of the wall) leads to a larger radiative coupling of the internal components with space as there is less thermal insulation. The shorter baffle wall thus leads to less heat being trapped inside of the baffle, leading to colder components. These phenomena cause the M2 support rods to be colder and warm-up at a slower rate than the booms. The thermal expansion of the M2 support lag behind the thermal expansion of the other components. The thermal offset caused by the booms and CORE hinges are not matched by the thermal expansion of the rods. This leads to a substantially larger in-drift Δz at 4500 s. This lag is also responsible for the adverse affect of the proposed improvement in Section 6.5. Due to the lag, a large difference in expansion of the booms and M2 rods results in an adverse affect to the proposed improvement.

One element which could increase the effective use-case of the sugar-scoop baffle, is the change of orbit. The dawn-dusk orbit had been coined before by Arink [3] as a possible improvement to increase the temperature stability within the baffle. The dawn-dusk orbit would more ideally fit the usage of the sugar-scoop, as the spacecraft would move along the dawn-dusk line. With the dawn-dusk orbit, the the sun always comes from one direction. Meaning that a rotation of the baffle or system is not necessarily required in contrast to the need for rotation with a normal sun-synchronous orbit. Furthermore, the DST would not enter or exit the eclipse with a dawn-dusk orbit. This further improves the baffle performance, not only for the sugar-scoop but also for the other baffles.

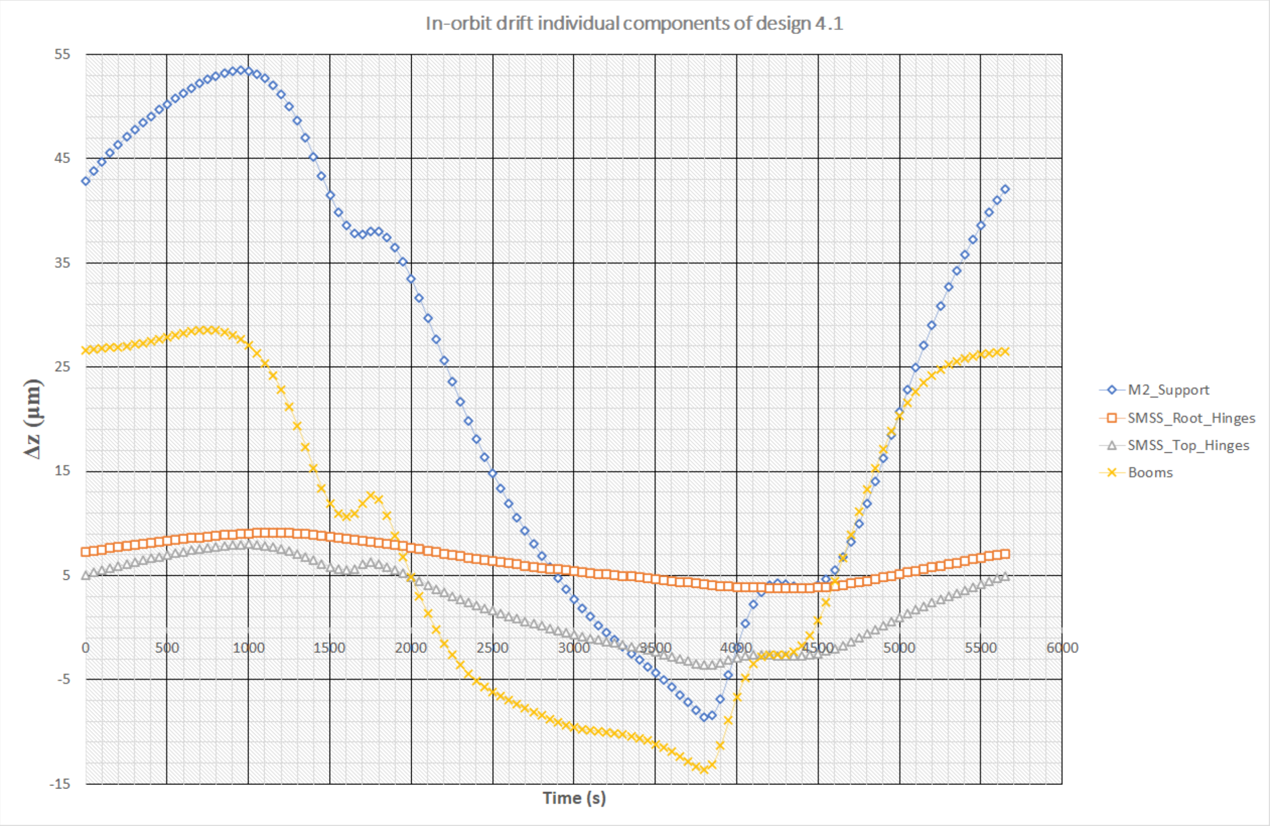

Figure 6.21: In-orbit drift contribution of the individual components of design 4.1

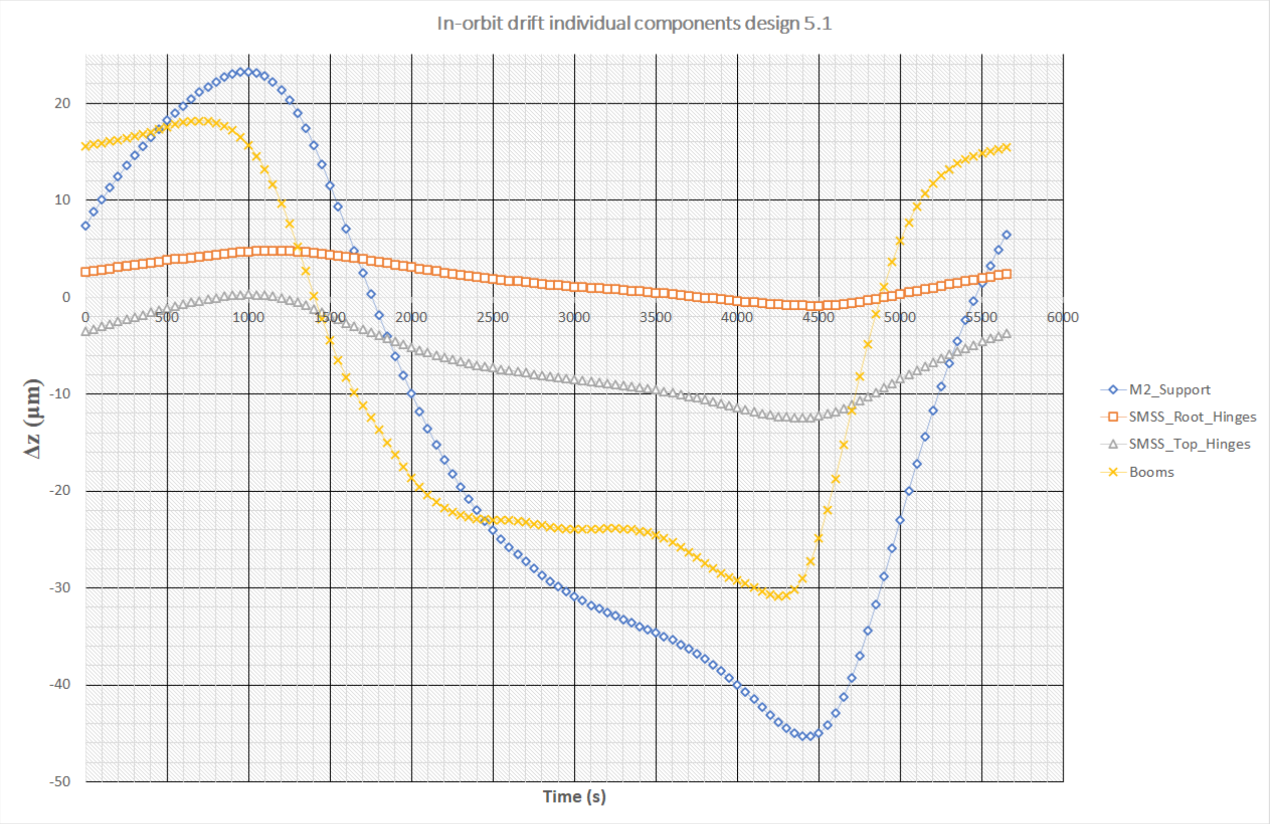

Figure 6.22: In-orbit drift contribution of the individual components of design 5.1

7

Trade-off and Baffle Selection: VIS DST

In this chapter, the final baffle design for the VIS DST version is given. The selection of the baffle is done after performing a graphical trade-off, using the results of the previous chapters to formulate the scores of the various baffle concepts. The criteria used for the graphical trade-off are the stray light performance, thermal performance and deployment complexity. Since the main objective of the baffle is to reduce the in-orbit drift, the thermal performance is of high importance. Furthermore, the deployment of the baffle is one of the key considerations of making the stray light adapted baffle work. Therefore the deployment has the same weight as the thermal performance. Due to the inherently good stray light protection of the optical system, the influence of the baffles designed did not have a large influence on the stray light performance of the VIS concept as was concluded in Section 5.4. The difference in stray light performance between the various baffles did not vary much, due to the optical system shielding off a lot of off-axis sources. Which does not allow for many off-axis rays to enter the optical house. Therefore, the stray light score for the baffles is deemed to be nominal.

From the application of stray light features such as vanes, it was apparent that the in-orbit drift budget can be reduced. This also leads to a more stable thermal environment for the components inside of the baffle. Five different stray-light adapted baffles were analysed for the VIS-based DST. The baffles were different in geometry: different number of vanes, arrangement vanes, angle of vanes or an implementation of a sugar-scoop.

Application of stray light features such as vanes can reduce the in-orbit drift budget and lead to a more stable thermal environment for the components inside of the baffle. At a first glance in Section 6.4, the most effective baffle for lowering the in-drift budget to $\Delta z \leq 2\mu m$ was the sugar scoop baffle i.e. design V5.1. The sugar scoop baffle with a total length of 3.15 m, has 5 angled vanes and 6 straight vanes with a sugar scoop angle of 30 degrees. The design made sure that the in 29% of the observable period, the requirements were met. In comparison, the second best performing baffle was at 13% compliance throughout the observable period. However, the sugar-scoop design needs either the whole spacecraft to rotate or have the baffle rotate along the Z-axis. Rotation of the spacecraft is near impossible due to a conflict in the push-broom scanning method. The second option would be to rotate the baffle. This would require two additional systems: a rotating mechanisms to rotate the baffle and an AOCS to stabilise the spacecraft. Partial rotation of the baffle through applying more long-faces on the baffle will allow for less stringent requirement on the rotation mechanism. Desaturation of the reaction wheels could occur during the non-observational period which is during eclipse. If the sugar-scoop is selected, additional work is needed to investigate the feasibility of the rotational-mechanism for baffle orientation and AOCS of the spacecraft.

Another method proposed to decrease the de-focus Δz was given in Section 6.5. The method is to decrease the length of for example the booms by the average thermal expansion experienced. The average thermal expansion is negative for all baffles. The only exception is the sugar scoop, which has a positive average thermal expansion. Therefore, the proposed method would be to increase the length of the booms by the average thermal compression. This leads to an average improvement of about 20% per baffle. The largest increase was seen for baffle design V3.1 with 4 vanes. Due to the proposed improvement, the compliance to the requirement increased for design V3.1 with 4 vanes from 12% to 40% for $\Delta z \leq 2\mu m$. Therefore, scoring the best among the other baffles.

If the in-orbit drift budget can be more relaxed to for example $\Delta z \leq 10\mu m$, the baffle with straight and angled vanes performed better. The performance of design V4.1 with the proposed improvement has a compliance to the $\Delta z \leq 4\mu m$ at 54% and 90% for $\Delta z \leq 10\mu m$. Since the compliance to the in-orbit drift budget is not fully at 100%, more work is needed to either reduce the in-orbit drift or allow the in-orbit drift budget to be higher.

The deployment complexity of the various concept is also scored highly. Successful deployment is needed, with the vanes needing to be at the correct position and orientation. Due to the size of the baffle, the most logical deployment concept to be used is the pantographic baffle system of Nagy[18]. The pantographic system allows for attachment of vanes. However, Nagy noted that the deployment of angular vanes is more difficult due to the shape. Therefore the baffles with the angular vanes score less well. Furthermore, baffle design V5.1 needs to rotate in order to work. This is not deemed to be entirely unfeasible, but it is however significantly more difficult to achieve. Since the rotation of the baffle can only occur along the Z-axis, without translating in the other direction.

To conclude, all the baffles aid in improving stray light performance of the optical system. Therefore, the baffle selection is dependent on the ability of the baffle to reduce and comply to the in-orbit drift budget. Baffle design V3.1 with 4 vanes has the best thermal performance. In terms of baffle complexity, baffle V3.1 only differs in a slight orientation of the original baffle. The graphical trade-off with the scores is given in Table 7.1

Table 7.1: Graphical trade-off for the VIS baffle selection

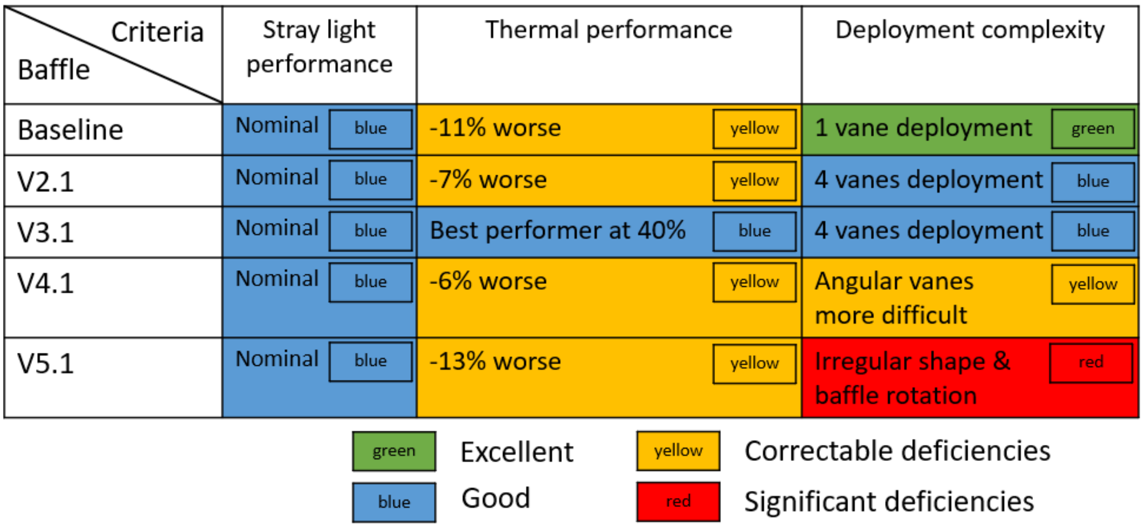

Criteria Baffle	Stray light performance	Thermal performance	Deployment complexity
Baseline	Nominal blue	-11% worse yellow	1 vane deployment green
V2.1	Nominal blue	-7% worse yellow	4 vanes deployment blue
V3.1	Nominal blue	Best performer at 40% blue	4 vanes deployment blue
V4.1	Nominal blue	-6% worse yellow	Angular vanes more difficult yellow
V5.1	Nominal blue	-13% worse yellow	Irregular shape & baffle rotation red

green Excellent
blue Good
yellow Correctable deficiencies
red Significant deficiencies

8

Baffle for the Thermal Infrared DST Concept

Though the design of the VIS concept started earlier, the TIR design will be of focus for the Deployable Space Telescope group. An introduction to the top-level design considerations for the TIR design is given in Section 8.1. From these top-level optical designs, one is chosen to continue development with. Due to various stakeholder needs, it was furthermore determined to scale the initial version down. Two scaled down versions are presented from a top-level design decision. Both of these scaled down versions are used throughout the various analysis. These two versions are given in Section 8.2. Even though the design is scaled down, some subsystems need to be redesigned. This also leads to a different in-orbit drift requirement for the TIR version which is given in Section 8.3. In order to design the baffles, the various deployment systems are revisited in Section 8.4. Finally, the various of baffle concepts for the TIR version are presented in Section 8.5

8.1. TIR design selection

The VIS concept is a design which might see fruition in 5 to 10 years. The TIR concept is based upon the VIS concept, using the same legacy to accelerate the design of the TIR. The longer imaging wavelength of the TIR design allows for relaxation of the engineering budgets and requirements. This makes the TIR design more suitable for a rapid development programme. Furthermore, the development is accelerated by using a scaled TIR design with a 30 cm aperture as a breadboard for the 1.5 m TIR design.

Two different optical models with a 40 cm primary mirror were designed by Dolkens suited for observations of 8 to 12 μm [11]. The optical design of the off-axis three-mirror anastigmatic (TMA) of the 40 cm TIR design can be found in Figure 8.1. The optical design of the Cassegrain version of the 40 cm TIR design can be found in Figure 8.2. In a trade-off study performed by Dolkens, the Cassegrain design was chosen due to its small stowed volume and ability to scale well[11]. The preliminary deployment sequence of the M2 mirror away from the primary M1 mirror can be seen in Figure 8.3. The small scale TIR design gives a reduction in size of the satellite and reduces the overall cost of the project. This makes it attractive to find academic and industry funding.

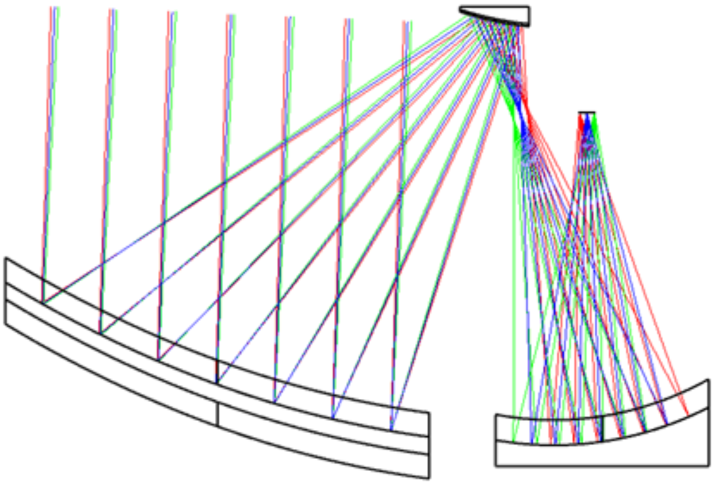

Figure 8.1: The optical lay-out of the 40 cm off-axis three-mirror anastigmatic [11]

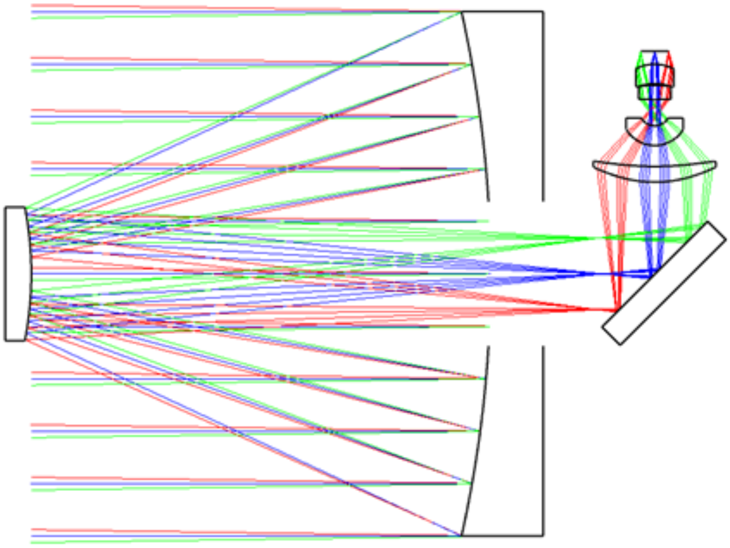

Figure 8.2: The optical lay-out of the 40 cm Cassegrain design [11]

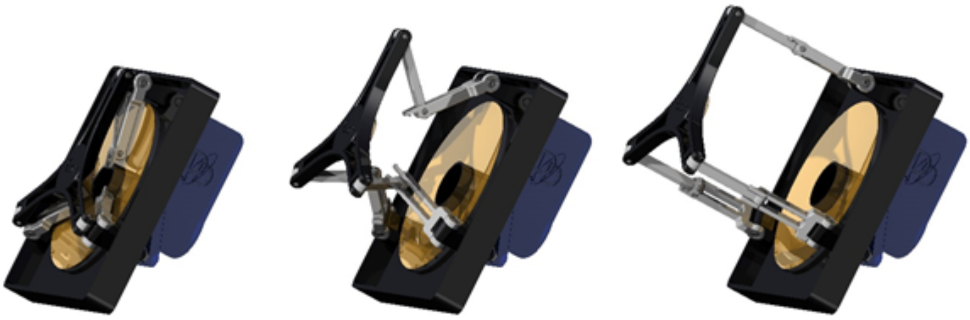

Figure 8.3: The preliminary deployment sequence of the 40 cm Cassegrain design [11]

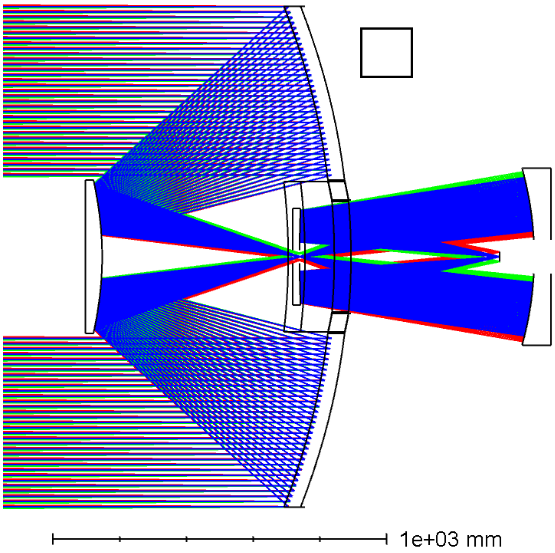

Figure 8.4: The optical lay-out of the 1.5 m aperture TIR design [11]

The Cassegrain concept utilises a fold mirror to redirect the beams upwards, as can be seen in Figure 8.5. Part of the reason of utilising a fold mirror is such that the detector is not in line with the primary and secondary mirror. This allows for the placement of the detector in an off-axis position. Which in turn, allows for a more convenient placement of a radiator surface. The internal cooling mechanism in combination with the cooling of the detector is the thesis subject of L. Boer[40]. The DST team decided that the Cassegrain system was best suited to continue development with.

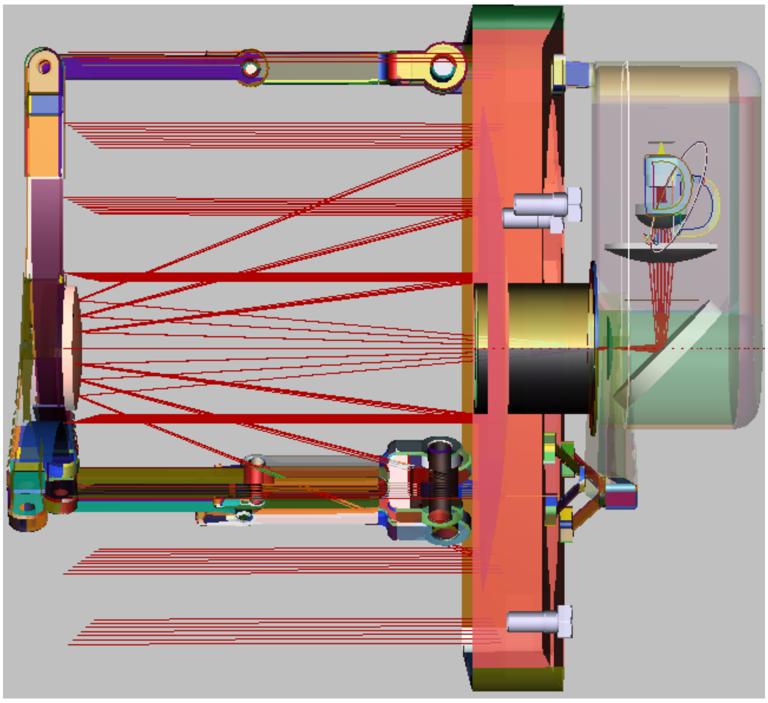

Figure 8.5: Concept for a Cassegrain 40 cm M1 TIR design which observes in the wavelength range of 8 to 12 mum, the spacecraft is made see-through to allow for viewing the optical ray path [11]

8.2. Cassegrain 30 cm TIR versions

As of June 2021, the decision was made by the internal DST team to put focus on a 30 cm aperture TIR design. The main reason for the 30 cm aperture TIR design are the cost savings associated with a smaller system. The smaller design is less costly due to e.g. smaller instruments and less stringent requirements on a launcher. Furthermore, the 40 cm TIR would require a 12U launcher platform which is difficult to come by. Therefore pivoting towards the 30 cm TIR improves the feasibility of launching a demonstrator mission. Smaller concept have been thought of, such as a 8U CubeSat. But an 8U envelope is deemed to be too limited for a demonstrator mission. In order to provide a cutting edge platform, the 30 cm TIR design should have a ground resolution of at least 30 m. The instrument will observe for a wavelength between 8 μm to 12 μm at an orbital altitude of 300 km. The requirements are bundled in the Systems Engineering tool of de Vries [31].

A second variation of the Cassegrain system was developed which does not utilise a fold mirror. This results in a straight optical path similar to the optical path of the 1.5 m TIR design found in Figure 8.4. The lessons learned from using a Cassegrain straight version for the demonstrator mission can more easily be applied to the large scale TIR design. Thus both the Cassegrain designs are used throughout the trade-off to provide information on the trade-off between using a fold mirror or straight design. The Cassegrain 30 cm Fold Mirror can be found in Subsection 8.2.1. The Cassegrain 30 cm straight design can be found in Subsection 8.2.2.

8.2.1. Cassegrain 30 cm Fold Mirror

The 30 cm Cassegrain fold mirror is obtained by scaling down the mechanical parts and optical parts by 25%. Distances between the parts are scaled down according to the same scaling number. The size of the source should also be scaled down to represent the same ray trace conditions. Optical model verification is done through comparison of the geometric spot diagram between the 40 cm and 30 cm. The geometric spot diagram of both models can be seen in Figure 8.6. The geometric spot diagram does not show any difference in the geometric spot diagram pattern. Which is logical because the source and optical elements are all scaled down with the same scaling factor. The only difference between the 40 cm and 30 cm fold mirror spot diagram is the detector size, which is reduced for the 30 cm model. However, the detector of the 30 cm could actually be the same size as the detector used in the 40 cm. Because the detector component is already small and some parts are transferable such as the detector.

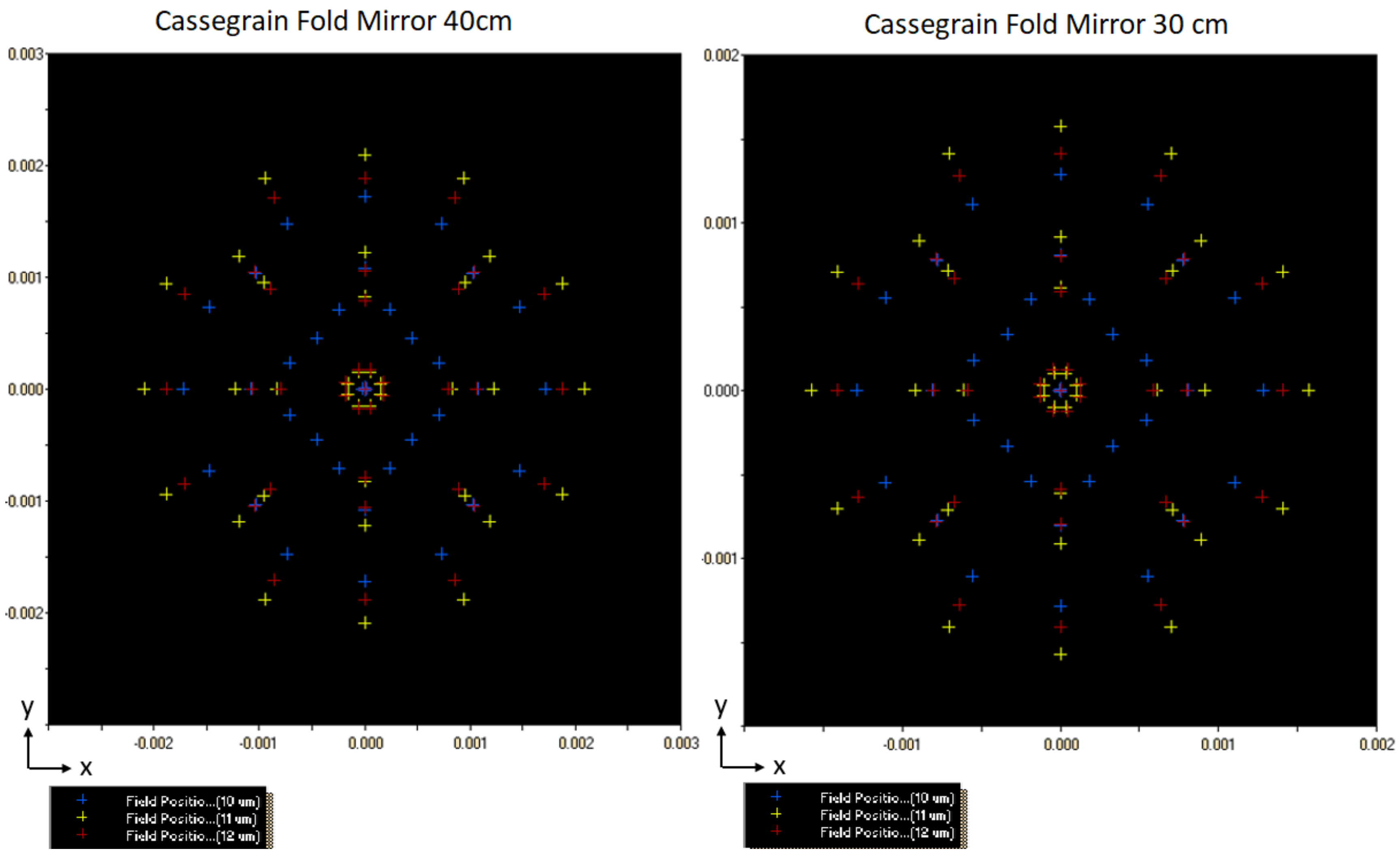

[H]

Figure 8.6: Geometric spot diagram comparison between the 40 cm and 30 cm Cassegrain Fold Mirrors

Scaling issues might be present when scaling the Cassegrain Fold Mirror design to a 1.5 m Cassegrain Fold Mirror TIR design. The fold mirror has to scale up with the size of the optical system. This can lead to a far larger spacecraft bus design needed to house the fold mirror [11]. For a large 1.5 m TIR design, a straight Cassegrain design will most likely have a smaller stowed volume than a Cassegrain fold mirror design. Furthermore, a folding M1 mirror would interfere with the fold mirror design. Because the fold mirror prevents the M1 mirror from being able to fold downwards in the stowed configuration.

8.2.2. Cassegrain 30 cm Straight

Removal of the fold mirror leads to an increase in the length (Z-direction) of the spacecraft due to the optics being placed in one straight optical path. The Cassegrain straight version provides information on the baffle length in case the fold mirror design were not to be used. The straight Cassegrain design will more likely be used for a large scale TIR design due to the scaling issues with the fold mirror design [11]. The Cassegrain 30 cm straight design could be of greater value due to a larger similarity to a large scale TIR design. The straight Cassegrain design with the optical ray path can be seen in Figure 8.7

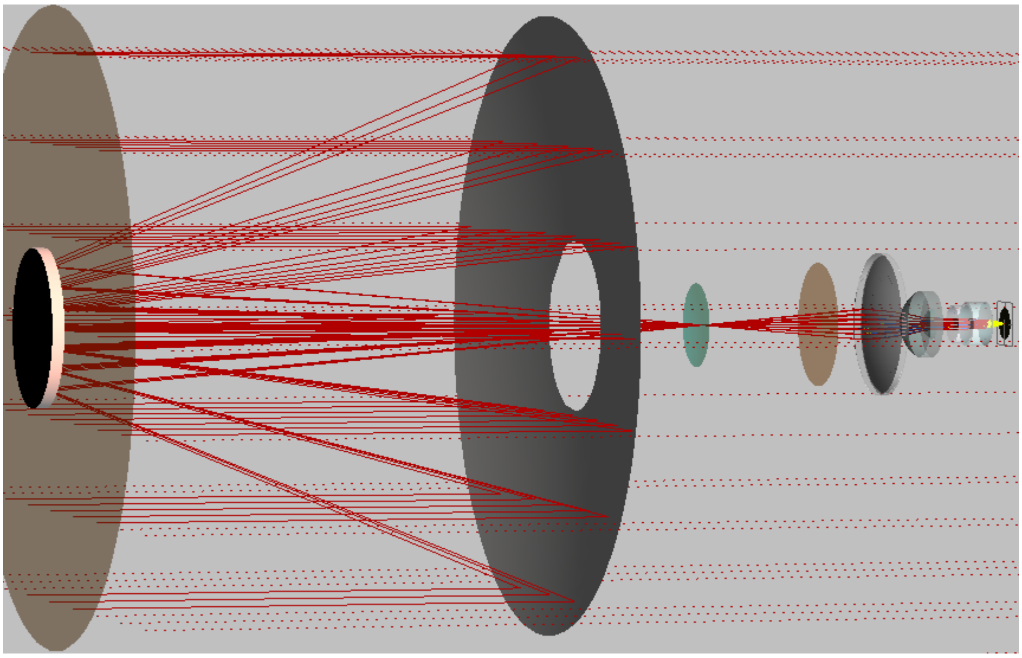

Figure 8.7: Cassegrain straight design with rays traced towards the detector []

The Cassegrain 30 cm straight design represents the worst case for TSE. As the detector has a self-view of the primary and secondary mirror. In comparison, the detector of the fold mirror design is not in line with the primary and secondary mirror which limits the TSE contribution [11]. Analysis of the TSE using the Cassegrain straight version therefore represents the worst-case scenario. Furthermore, the Cassegrain straight version is chosen to perform the analysis of the TSE due to limited resources. As the Cassegrain straight version was used to model the temperature response to the baffle design in ESATAN. The TSE analysis is still applicable to the fold mirror design because the same baffle is used [11]. In order to perform the TSE analysis, some basic adjustments are made to the optical model. These adjustment serve as a preliminary design, as the design becomes more detailed at the hand of L. Boer his thesis subject [40]. The following adjustments to the optical design are made whilst keeping an f/1.4 for the system:

- Addition of a field stop
- Addition of a cold stop
- Addition of an internal optical house around the internal optics

The field stop and cold stop elements are added to prevent off-axis rays from passing through the optical system. The cold stop is added to reduce thermal noise and is usually cooled. The internal optical house further limits the scattering and unwanted propagation of rays through the system. The addition of the field stop, cold stop and internal optical house can be seen in Figure 8.8.

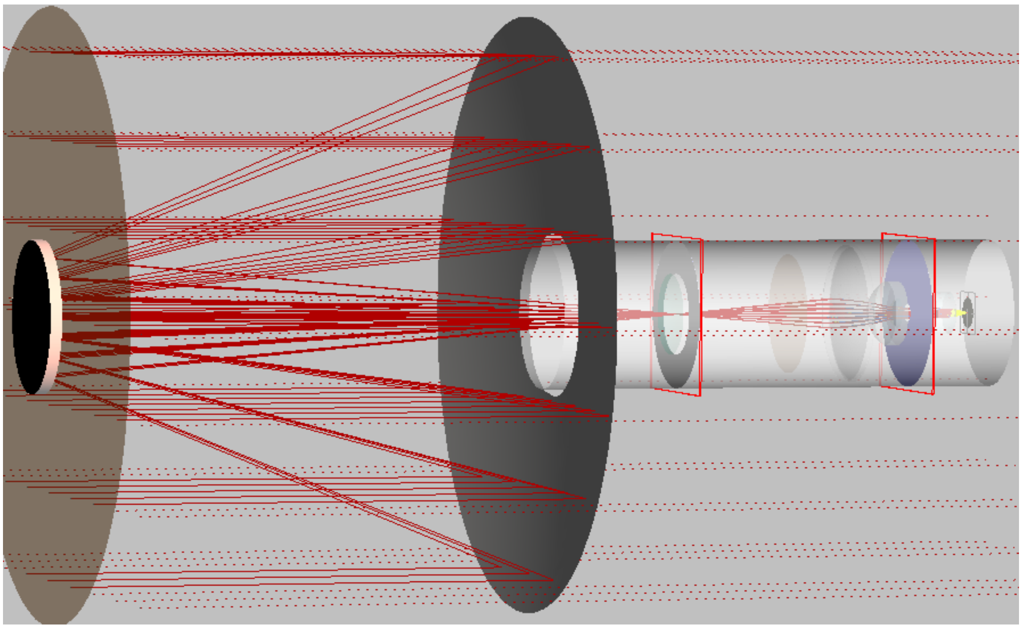

Figure 8.8: Cassegrain straight design with the addition of a field stop, cold stop and the internal optical house with rays traced towards the detector. Both stops are highlighted in red

The geometric spot diagram of the 40 cm and 30 cm Cassegrain straight model can be seen in Figure 8.9. Comparison between the geometric spot diagram of the fold mirror in Figure 8.6 and the straight version in Figure 8.9 show no difference. This concludes that the removal of the fold mirror and re-positioning of the optical elements did not significantly alter the optical performance. The addition of the stops and internal house should be added without introducing vignetting through the system. The geometric spot diagram with addition of the field stop, cold stop and internal optical house is equal to the system without these elements. Therefore the geometric spot diagram with the TSE adjustments is equal to that of Figure 8.9, which concludes that the adjustments do not interfere with the optical performance.

The material properties of the internal optical house around the internal optics is a trade-off that a student should make. The cooling of the detector is the thesis subject of L. Boer [40]. The trade-off should be made between a high absorptivity and high emissivity or low absorptivity and low emissivity optical house. When a high absorptivity coating is selected, many of the undesired incoming rays are absorbed. In general, a high absorptivity coating is a rough coating. The roughness of the coating can be undesirable due to the random scatter direction. This makes it unpredictable in which direction the rays scatter. The low absorptivity coating is a smooth coating, which absorbs less. The smoother coating also has a more predictable scatter direction. This makes it easier to smooth out noise signals [11]. Most thermal shields use a clean and well-polished i.e. low emissivity smooth metallic surface [56]. This is because reducing the emissivity of the thermal shield and the dewar component results in a reduction in radiation heat loads. The expected operating temperature for the surfaces near the detector is estimated to be 200 K [40]. The aluminium film 400A on Mylar for the dewar can be selected, which has an emissivity of 0.009 at 80 K [56]. Since the temperature of the dewar might be higher, an emissivity of 0.01 is selected.

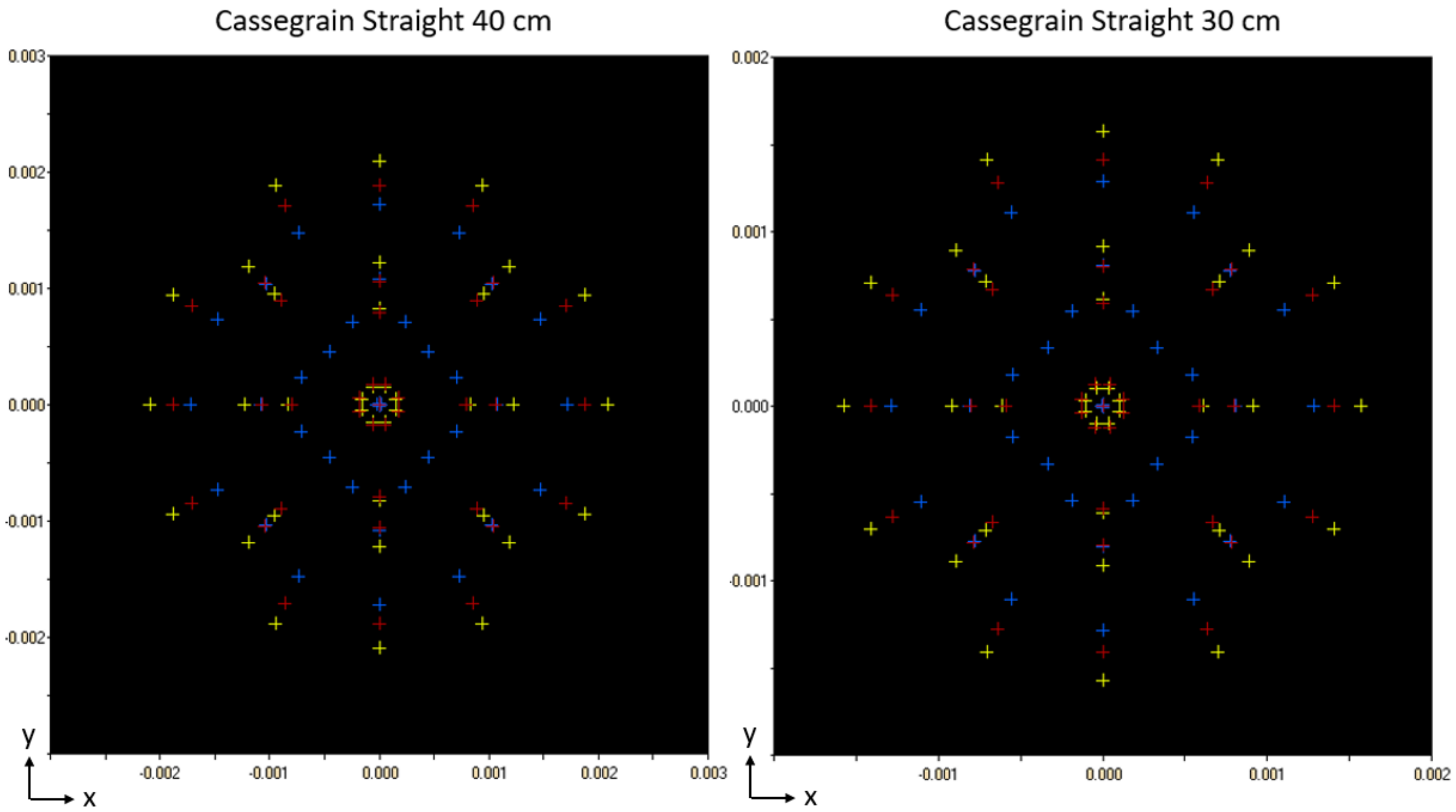

Figure 8.9: Geometric spot diagram comparison between the 40 cm and 30 cm Cassegrain straight

8.3. In-orbit Drift Requirement for TIR

The ability of the baffle to keep the position of M2 within the budget, is one of the metrics to which the baffles are compared to relative to eachother. The position of M2 is dependent on the top-down systems engineering budget. The most stringent requirement being the in-orbit drift budget due to the long time period. The top-down systems budget for the TIR design is not known yet. The in-orbit drift budget for the VIS design was determined by previous work to be the most stringent requirement [2, 12, 32]. The in-orbit drift budget quantifies the maximum deviation in the position of the optics that can occur between active calibration procedures [2]. The time period in which the in-orbit drift budget applies, is the whole orbital period in which observations can be made (i.e. taking pictures). The TIR design is not limited to daylight, thus the in-orbit drift budget could be considered for the whole orbit. This raises the question of when the coarse alignment would occur for the TIR. The coarse alignment was scheduled for the VIS version to be performed in the non-observing time period of the orbit i.e. during eclipse. One of the design solutions for correcting the alignment is the usage of actuators in the booms to correct deviations in the position of M2 [57]. At a rate of roughly 100 observations per orbit, there will be plenty of time for the actuation system to correct deviations up to 100 μm [11]

Since the top-down systems budget is not known yet for the TIR, an approximation can be made to form the top-down systems budget for the TIR version. The TIR design will operate at a longer wavelength than the VIS design. Currently the wavelength of VIS to TIR scales about tenfold, from 0.7 micron to 8 micron. The effect of scaling down the instrument might result in the in-orbit drift being less than an order of magnitude. Personal communication with Dolkens estimated that the in-drift orbit budgets for the TIR can be scaled up by 10 to 20 times of the VIS budget[11]. This results in a preliminary in-orbit drift budget of ΔZ of 20 to 40 μm. De-focus of ΔZ of 20 μm corresponds to a Strehl ratio of 84%, which is within target for the TIR satellite. The maximum allowed deviation in the Z-direction is set at a preliminary 30 μm according to requirement T0.2-OPT-SMI-013 [1, 31].

For the VIS-system, the components which contribute to the in-orbit drift budget for M2 are the booms, top and CORE hinges and rods [12]. These subsystems for the TIR design are not known or not fully developed yet. Furthermore, the location of the booms is not yet fully determined. The SMSS subsystem is the thesis subject of C. Hobijn which is currently still in-progress [57]. Therefore an approximation or dummy subsystem for these components is used in ESATAN to continue the trade-off. Dolkens provided a concept of folding arms for the Cassegrain fold-mirror version. However the folding arms are not optimised and serve mostly to strengthen the overall concept idea.

8.4. Deployment Systems for small scale Baffles

Surrey Satellite Technologies Limited (SSTL)[13] has built a breadboard model of their telescopic optical barrel shown in Figure 8.10. The SSTL telescopic optical barrel consists of three segments that are each operable by using a leadscrew into a wave spring assembly. Though no mass numbers are given for the SSTL telescopic barrel, the SSTL is thought of to be quite heavy and without the utilisation of stray light and temperature attenuation [58]. Tsinghua University developed a telescopic segmented barrel for a 1U CubeSat that utilises springs to deploy the various segments [14]. The cross-section of the telescopic segmented barrel in the stowed and deployed state of the Tsinghua University can be seen in Figure 8.11.

Figure 8.10: Surrey Satellite Technologies Limited their telescopic optical barrel in deployed and stowed configuration in Solidworks (left) and breadboard model (right) [13]

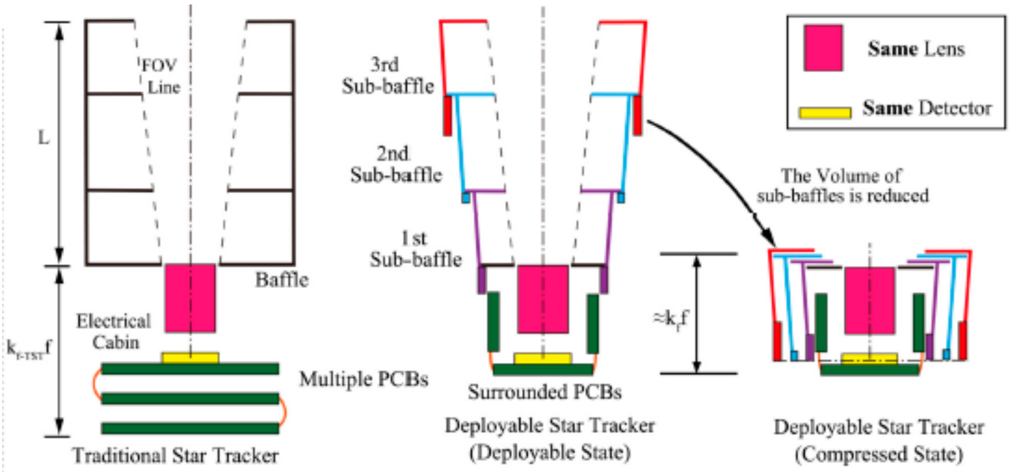

Figure 8.11: 1U telescopic segmented barrel in stowed and deployed state of Tsinghua University [14]

The pantographic baffle design of Nagy could be used as a deployment mechanism for the TIR concept [18]. The baffle for the VIS-design deploys in both the axial and radial direction. But Nagy suggested that a pantographic baffle which only deploys in the axial direction would be possible. This opens up the idea of using the pantographic baffle design for the TIR baffle [18, 31].

8.5. Baffle concept generation for TIR DST

The baffle aids in keeping the temperature stable such that the in-drift orbit budget is within the specified requirement. Furthermore, the baffle provides protection against off-axis sources reaching the detector by using stray light methodology. The TIR baffle will be designed for the 30 cm TIR design. Because the selection between the fold-mirror and straight mirror has not yet been made, both concepts have to be taken into consideration for the baffle.

The deployment of both M1 and M2 was deemed to be too complex for a demonstrator design. This ruled out the need for deployment in the axial and radial direction [31]. From the trade-off, an axially deployed baffle was the favourite which will be used to continue development with. The material and coating for the baffle is selected in Section 8.5.1. The baffle diameter and length is given in Section 8.5.2. The shape of the baffle has an effect on the mass, effective usage of volume and deployment complexity of the baffle. Two baffle shapes are selected to continue development with in Section 8.5.3.

8.5.1. Material and Coating for TIR

The baffle material remains unchanged with two layers of MLI with Magic Black coating on the interior of the baffle wall [18]. Nagy used OSR-like material on the outside of the baffle, which was used on a BepiColombo mission [59]. However, it is uncertain whether the OSR-like material applied is able to withstand being folded as it is a solid material. Therefore, no OSR-like coating is applied to the TIR baffle in this thesis. The mass of the MLI can be calculated using the processes explained by Arink [3]. The chosen MLI has a density of 146 kg/m^3. The two layers of MLI has a thickness of 0.506 mm. The Magic Black coating is available in the FRED catalogue of available coatings.

8.5.2. General size of the baffle

The baffle has to be bigger than the primary mirror in order to fit the primary mirror inside of the baffle. Furthermore, some extra room is preferred to allow for placing the secondary mirror deployment system next to the mirror. The secondary mirror deployment system is the thesis work of Hobijn [57]. According to Hobijn, a baffle spacing of 25 mm between the primary mirror and inner baffle wall allows for enough design space for a redeveloped SMSS. The baffle wall thickness with two MLI layers has a thickness of 0.506 mm. Therefore, the baffle diameter is set at 35 cm since the baffle wall has a negligible thickness. The minimal length of the baffle is then determined by looking at the length required to shade the spider from solar heat. This corresponds to a minimal baffle height extending 8 cm above the spider. When the baffle bottom corresponds to the spacecraft bus bottom for the Cassegrain straight version, the baffle length is 60 cm. For both the fold mirror and the straight version, a 60 cm long baffle will be used which extends 8 cm above the spider. This amounts to a total baffle shroud area of 1.21 m^2

8.5.3. Shape

Different baffle shapes are possible for the small scale TIR demonstrator. The deployment mechanism is dependent on the shape of the baffle. Furthermore, the shape has an influence on the supportive structure needed to obtain and maintain the shape of the baffle. Four different potential baffle shapes were considered for the small scale TIR design: cylindrical, square, octagonal and hexagonal. More complex shapes exist, but these are deemed to be unattainable for a small scale TIR demonstrator. This section is concluded by selecting two shapes which will be used to continue the development of the baffle.

TIR-Cylindrical

The feasibility of a deployable cylindrical baffle has been investigated by several students working on the DST project [3, 16, 30]. The cylindrical baffle was discarded in the baffle iteration of Arink [3]. This was primarily due to the added complexity of the deployment system to deploy a perfect cylindrical shape in both the axial and radial direction, which was also confirmed by Nagy [18]. However, the possibility of using a cylindrical shape opens up due to the lack of need to deploy the small-scale TIR baffle in radial direction. This allows the use of using a deployment mechanism which uses telescopic segments to increase the baffle length in axial direction. However, the cylindrical shape does not fully utilise the whole available area. If the available cross-sectional area is a box of unity length, the total area used by the circle would be $A_{circle} = \pi \cdot 0.5^2 = 78.5\%$.

TIR-Octagonal

The octagonal shape was selected by former DST project members working on the baffle for the 1.5m VIS DST design [3, 16]. Furthermore, the octagonal shape was selected by Nagy for a novel deployable baffle deployment concept which can be modified to any size [18]. Nagy noted that for baffles which only require deployment in the axial direction, lighter and/or simpler baffle solution exists. The octagonal shape is most suited for cases where the deployment is required in the axial and radial direction. The area of a isosceles octagon which is inscribed in a box of unit length, the octagon will cover 82.8% of the area of a square unit box [1]

TIR-Square

The square baffle represents a simplification of the cylindrical design shape. The simplification of the shape leads to less deployable arms needed to accomplish the shape [16]. The square design may use 100% of all the available area efficiently for a box-shaped CubeSat deployment fairing. Korhonen notes that the square shaped baffle needs fewer booms than the octagonal shape, which increases the reliability. The key advantage of a square shaped baffle

---

[1] Evaluated using the tool from `https://calcresource.com/geom-octagon.html` [accessed 3 January 2022]

would be the full utilisation of the available space. But a circular optic coupled with a square baffle could lead to unpredictable reflections at the corner of the baffle which could end up at the detector.

TIR-Hexagonal

An hexagonal shape was coined, as the shape has corners in which the SMSS could fit into. When modelling the hexagonal shape with a minimal outer width of 30 cm, the other dimension has to be 35 cm. The 30 by 35 cm hexagon ensures that the sides of the hexagon are all congruent. When a minimal width of the hexagon is chosen, the depth will always be larger than the width due to the hexagon sides being the same length. Resulting in a larger than necessary depth. This feature of the hexagon makes the shape less ideal for scaling the design. Thus the area of a hexagon is limited by the width of the unit box. This leads to a maximum usage of the cross-sectional area of 65% of the area of a square unit box [2]

Conclusion on Baffle Shape

An overview of the cross-sectional area of each shape can be seen in Figure 8.12. The circle fills up 78.5% of a unit square, the octagon 82.8% whereas the hexagon fills up 65 % of a unit square. In Figure 8.12 (d), the circle is overlaid on top of the octagon to distinguish the difference in cross-sectional area. When comparing the cross-sectional area, the hexagon is least effective at using the available area. Previous thesis noted that the octagon requires more structural elements to compose the octagon, resulting in a heavier baffle [3, 16, 18]. The deployment of the various structural elements decreases the deployment reliability of the octagonal shaped baffle. When axial and radial deployment is needed, the octagon shaped baffle would be more beneficial. To conclude, the hexagon shaped falls off due to its inefficient use of the available stowed volume. From the trade-off of de Vries, only axial deployment is needed for the small scale TIR model [31]. This eliminates the octagon shaped baffle because its heavier and requires a more complex deployment mechanism. Therefore, the square and cylindrical baffle were selected.

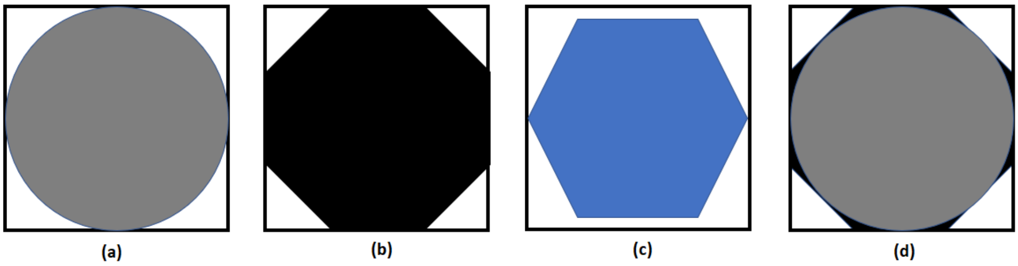

Figure 8.12: Cross-sectional area of a square of unit length filled with the cross-sectional area of a circle (a), octagon (b), hexagon (c), circle and octagon (d)

8.5.4. Baffle Concepts

The addition of baffle vanes to the TIR design serves the same purpose as for the VIS design: aid in stabilising the temperature inside of the baffle and aid in stray light mitigation. Requirement T0.2-BAF-REQ-00601 specifies that the baffle should be 25-distance away from the primary mirror. Furthermore, requirement T0.2-BAF-REQ-006-03 states that the baffle shall have a clearance of 5 mm during and after deployment between any point of the baffle and the support structure [31]. As a result, the diameter of the baffle is larger than the FOV of the optical system. By placing vanes, the entrance aperture of the baffle is reduced. The vanes are then sized to not cause vignetting. The reduction in entrance aperture diameter reduces the amount of heat that enters the baffle. The subsequent vanes are then placed at calculated positions to limit further unwanted propagation of solar heat. The vanes can be positioned at an angle to aid in reflecting incoming heat, back towards space. Therefore three different classes of baffle vane system exists: specular baffle, reflective baffle and a specular baffle with reflective vanes. The black specular baffle utilises straight vanes with a high absorption coating to absorb the incoming heat. The reflective baffle uses a combination of vanes of various geometry that have a specific orientation to reflect the incoming heat back towards space. Furthermore, the vanes need to be positioned at the correct location in order to be effective as was explained in Section 4.5.2. The reflective baffle is not possible for the deployable baffle concept, because the deployment accuracy needed is too high. The combination of a specular baffle and reflective vane might be possible. This can be achieved by placing the straight vane under an angle. Dependent on the orientation of the baffle with respect to the sun angle, the angled vane can be perpendicular with respect to the sun angle. This aids in reducing the temperature inside the baffle.

In collaboration with the DST team, the conclusion was made that a segmented baffle deployment can be achieved using a deployment method similar to those specified in Section 8.4 [31]. Depending on the top system level concept,

---

[2] Evaluated using the tool from `https://www.cuemath.com/measurement/area-of-a-hexagon/` [accessed 3 January 2022]

the baffle can be segmented into either two or three sections. When the baffle is divided into two sections, each section has a length of 30 cm. When the baffle is divided into three sections, each section has a length of 20 cm. The deployment systems featured in Section 8.4 only allow for attaching one of the segments with vanes. The detailed design of the deployment system using a segmented baffle system remains for a different thesis student to work out as given in Section 13.

In summary, the following conclusions were made:

- The baffles are made of two layers of MLI with Magic Black coating on the interior of the baffle
- The baffle has a diameter of 35 cm to account for placement of the SMSS whilst also having enough spacing between the primary mirror and the baffle
- The baffle will extend 8 cm above the spider, with a baffle total length of 60 cm
- The cylindrical and square shape are chosen as suitable geometries
- The baffle can be divided into either two or three sections
- The top section of the baffle can be used to attach vanes
- The baffle vanes can either be straight, angled or a combination of straight and angled vanes
- A fully reflective baffle is not possible because the deployment accuracy needed is too high

These conclusions resulted in two baffle shapes with varying vane configurations. These configurations and the name of the baffle concept can be found in Table 8.1.

Table 8.1: Overview of the different baffle configurations and their names

Number of vanes	Cylindrical Baffle	Square Baffle	Note
0 vanes	C-0V	SQ-0V	Possible with two and three segmented baffle
1 vane	C-1V	SQ-1V	Possible with two and three segmented baffle
7 vanes	C-7V	SQ-7V	Three segmented baffle
11 vanes	C-11V	SQ-11V	Two segmented baffle
2 vanes and 3 angular vanes	C-3AV-2V	SQ-3AV-2V	Three segmented baffle
6 vanes and 3 angular vanes	C-3AV-6V	SQ-3AV-6V	Two segmented baffle

The straight vanes consists of two layers of MLI with the Acktar Magic Black coating on the backside. The straight vanes are perpendicular to the baffle wall, thus orientated at a 90 degree angle. Further specification of the straight vanes are given in Table 8.2

Table 8.2: Straight vane distance and depth for the TIR design

Vane #	Distance from baffle entrance [mm]	Depth [mm]
Vane 1	0	19
Vane 2	27	20
Vane 3	55	20
Vane 4	82	21
Vane 5	109	21
Vane 6	137	22
Vane 7	164	22
Vane 8	191	22
Vane 9	219	23
Vane 10	246	23
Vane 11	273	24

Likewise, the angular vanes consists of two layers of MLI with the Acktar Magic Black coating on the backside. The specification of the angled vanes are given in Table 8.3.

Table 8.3: Angled vane distance and depth

Angled Vane #	Distance from baffle entrance [mm]	Depth [mm]	Angle [^{o}]
Angled Vane 1	0	40	30
Angled Vane 2	47	42	30
Angled Vane 3	98	44	30
Angled Vane 4	153	45	30

9
Thermal Analysis of the TIR Baffles

In this Section, the thermal analysis of the various TIR baffle concepts from Section 8 Table 8.1 are given. These thermal baffles should make the TIR concept comply to the thermal requirement of ensuring that the in-orbit drift budget is less than $\Delta Z \leq 20\mu m$. Due to the legacy thermal model in ESATAN, only the straight version of the DST is used to purely assess the baffle performance. Even though the fold mirror design is not used for the thermal analysis, it can still be assumed that the performance abilities of the baffle are transferable to the fold mirror design [11]. Because the design is the same for both the straight and fold-mirror design, from the primary mirror towards the entrance of the baffle. This chapter compares the cylindrical and square baffle with varying vane arrangements using straight and angular vanes. First, the thermal analysis of the cylindrical baffles are given in Section 9.1. Followed by the square baffles in Section 9.2. Finally, a conclusion to the baffle performance is given in terms of thermal performance in Section 9.3.

9.1. Thermal Analysis of Cylindrical Baffles

In this Section, the thermal analysis of the cylindrical baffles are given. First, the bare cylindrical baffle without any vanes is given in Section 9.1.1. Followed by thermal analysis of a cylindrical baffle with straight vanes: C-1V in Section 9.1.2, C-7V in Section 9.1.3 and C-11V in Section 9.1.4. Then, the thermal analysis of the baffle with angular vanes is given for baffle C-3AV-2V in Section 9.1.5 and baffle C-3AV-6V in Section 9.1.6.

9.1.1. Thermal Analysis of C-0V

In this section, the thermal analysis of baffle C-0V is given. Baffle C-0V has no vanes. The temperature of the various components contributing towards the in-drift orbit budget can be seen in Figure 9.7. The thermal range is given in Table 9.1. The various important orbital positions are given in Figure 9.2. The maximum temperature of the interior baffle wall is reached at 750 s of the orbit, at which the baffle absorbs the most solar heat. From there on, the angle of the baffle relative to the sun changes which causes the baffle temperature to decrease until 1400 s into the orbit. At 1400s, the baffle is perpendicular to the sun vector and the interior baffle wall starts to receive solar heat. The interior baffle wall receives solar heat until the DST reaches the eclipse region at 1570 s. The temperature difference of the interior baffle wall is 10 K from 1400 to 1570 seconds. During the eclipse phase of the orbit, the temperature of the DST decreases due to the absence of solar heat. The eclipse phase ends at 3750 s, at which the temperatures increase again. However, the temperature of the root CORE hinges does not increase immediately upon exiting eclipse. The root CORE hinges do not receive direct solar heat. Rather, they are warmed up by radiative heat transfer from parts around the root CORE hinge. At 3750 s, the solar heat is again absorbed by the internal baffle wall, booms, rods and top CORE hinges. This leads to a temperature increase in those components. At 3900 s, the solar radiative thermal coupling with the internal baffle wall significantly reduces. As a result, less solar heat is absorbed by the internal baffle wall. This results in a temperature drop. At 4100 s, the orientation of the baffle with respect to the solar heat vector is large enough again to increase the temperature of the internal baffle wall. The temperature of the CORE hinges follow the temperature swings as the baffle. The difference is that the top CORE hinge is more subjected to a larger temperature downward swing, because it is less surrounded by warmer components. In addition, the radiative coupling with cold space is larger for the top CORE hinge. This is visible by the temperature of the top CORE hinge, which drops to a lower temperature than the root CORE hinge when entering eclipse. The larger change in temperature of the booms and baffle can be attributed to the thin wall thickness, resulting in a low mass. The low mass leads to a quick change in temperature in response to a changing environment. Therefore, the temperature swing of the baffle and boom are larger than the swings of the heavier CORE hinges.

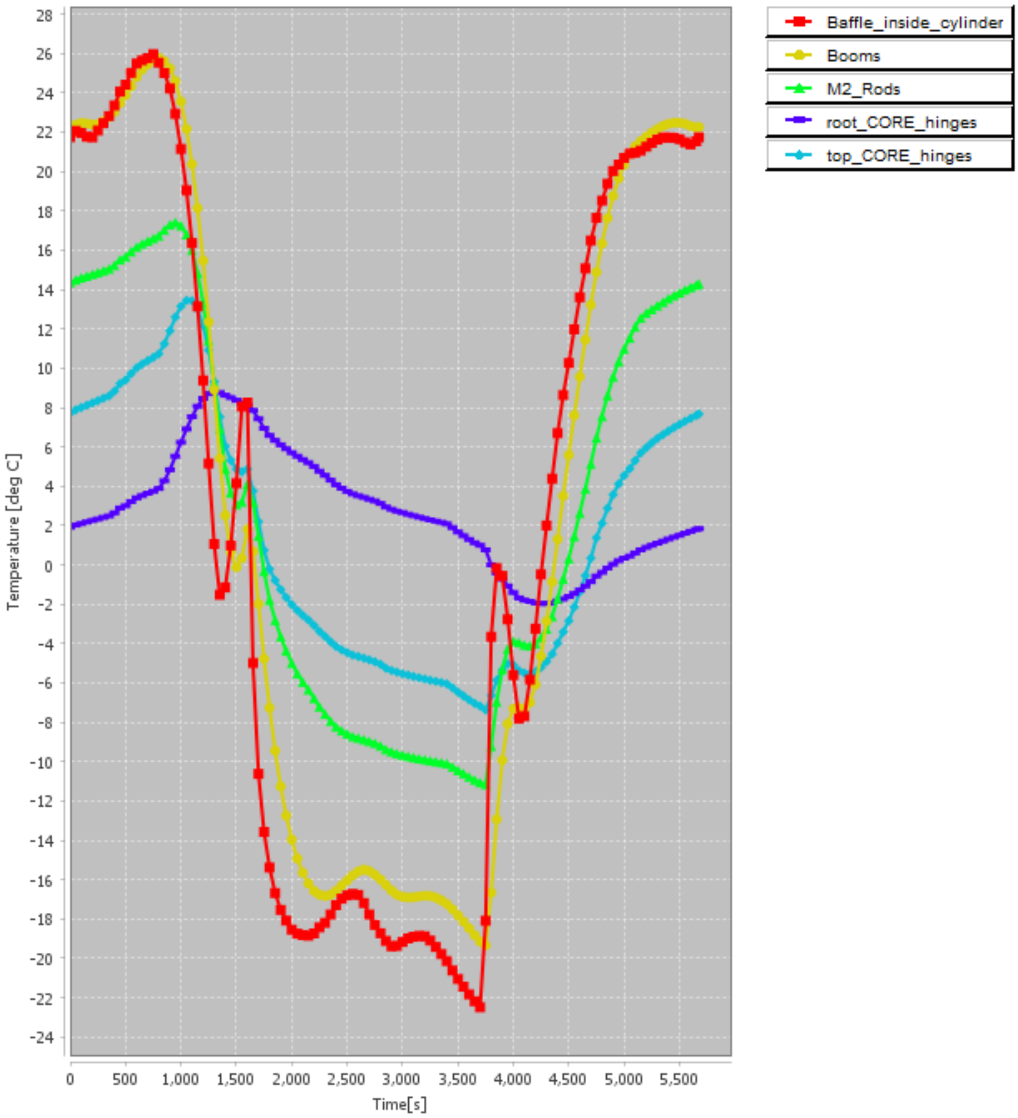

Figure 9.1: C-0V: Average temperatures of the booms, rods (denoted as M2_Support), CORE hinges (SMSS_Root_hinges and SMSS_top_hinges) and interior baffle wall

Table 9.1: Maximum and minimum temperatures of the baffle interior, booms, rods and CORE hinges of baffle model C-0V

	Baffle interior	Booms	Rods	Top CORE	Root CORE Hinges
Min T [°C]	-22.49	-19.34	-11.16	-1.96	-7.37
Max T [°C]	25.96	25.77	17.417	8.81	13.44
T Range [°C]	48.45	45.11	28.57	10.78	20.82

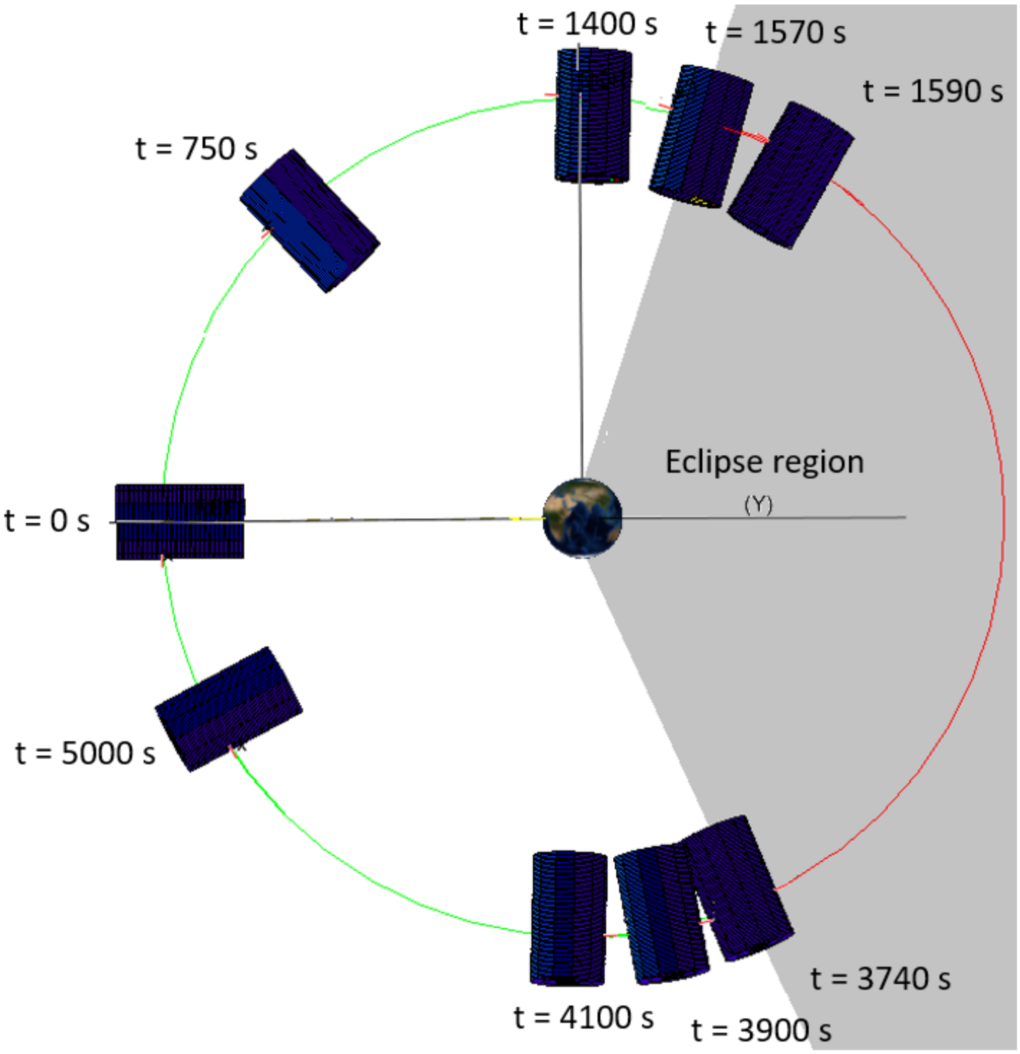

Figure 9.2: The orbital position of the DST with some key orbital position throughout the orbit

9.1.2. Thermal Analysis of C-1V

The thermal analysis of baffle C-1V, which has one vane at the entrance aperture largely resembles the temperature profile of C-0V. On a closer look, the single vane reduces the temperature ranges of the various components by 1.7 to 2.6 K. The vane at the entrance aperture puts a shadow on the baffle wall, which also causes the boom to be slightly cooled. As a result, the maximum temperature of the baffle wall is lower. This also reduces the radiative heat coupling between the wall and boom, which lowers the maximum temperature of the boom. Furthermore, the shadow caused by the vane reduces the maximum temperature of the top CORE hinge by 2.5K. As a consequence of the cooler baffle, the root CORE hinge temperatures are also reduced.

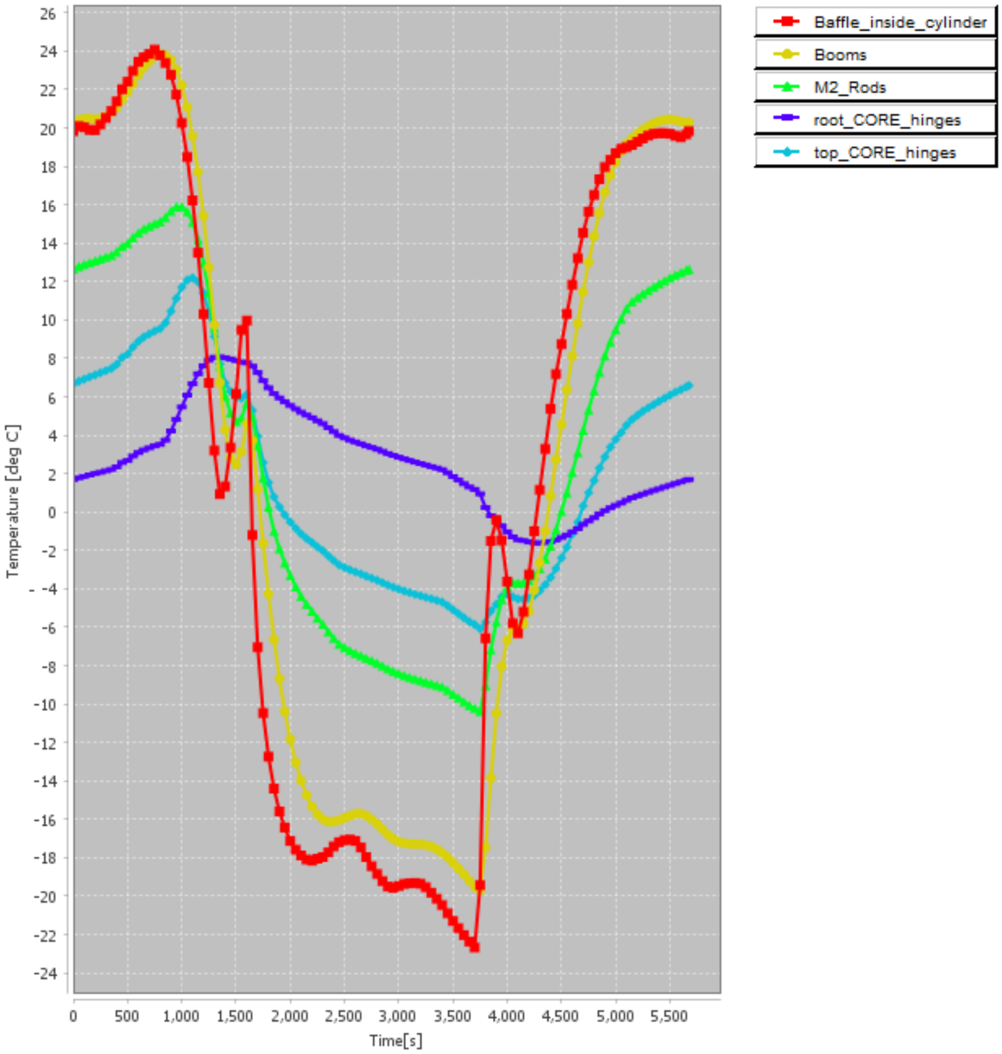

Figure 9.3: C-1V: Average temperatures of the booms, rods (denoted as M2_Support), CORE hinges (SMSS_Root_hinges and SMSS_top_hinges) and interior baffle wall

Table 9.2: Maximum and minimum temperatures of the baffle interior, booms, rods and CORE hinges of baffle model C-1

	Baffle interior	Booms	Rods	Top CORE	Root CORE Hinges
Min T [°C]	-22.67	-19.7	-10.37	-1.61	-6.08
Max T [°C]	24.07	23.87	15.91	6.57	12.20
T Range [°C]	46.74	43.57	26.28	8.19	18.28

9.1.3. Thermal Analysis of C-7V

By comparison, the added 6 more vanes compared to design C-1V does cause a reduction in temperature. The reduction in temperature ranges compared between C-1V and C-7V is less than between C-1V and C-0V. This means a diminishing return in temperature reduction by adding more vanes. It can be seen however, that the temperature increase and decrease happening between 1400 seconds to 1570 seconds has a lower amplitude of 5.5 K.

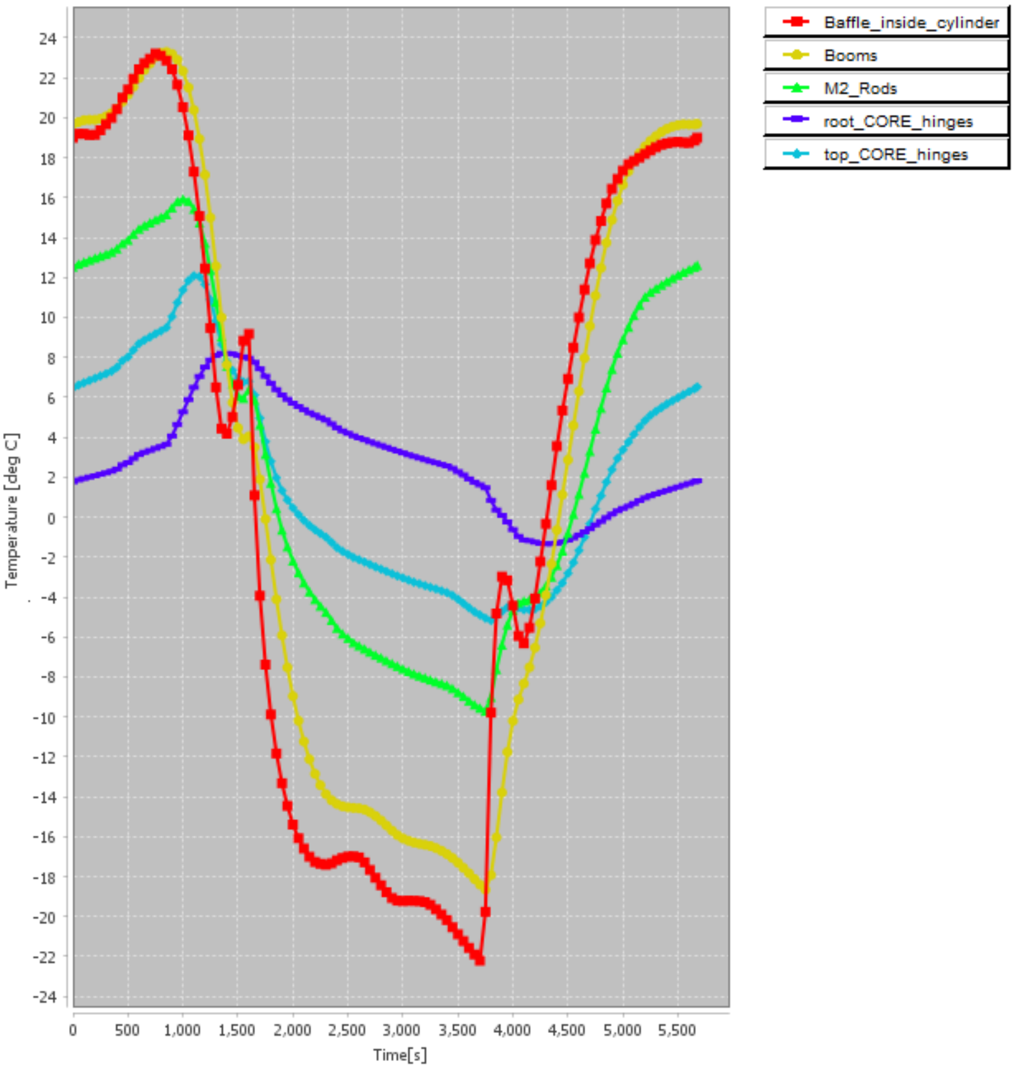

Figure 9.4: C-7V: Average temperatures of the booms, rods (denoted as M2_Support), CORE hinges (SMSS_Root_hinges and SMSS_top_hinges) and interior baffle wall

Table 9.3: Maximum and minimum temperatures of the baffle interior, booms, rods and CORE hinges of baffle model

	Baffle interior	Booms	Rods	Top CORE	Root CORE Hinges
Min T [°C]	-22.20	-18.66	-9.71	-1.34	-5.18
Max T [°C]	23.22	23.29	15.94	8.21	12.09
T Range [°C]	45.42	41.95	25.65	9.54	17.27

9.1.4. Thermal Analysis of C-11V

Design C-11V is the design for a baffle consisting of two baffle segments. By extension, the same effects of increasing the number of vanes of C-7V is seen here. The increased number of vanes lowers the amplitude between 1400 to 1570 s to 4.5 K.

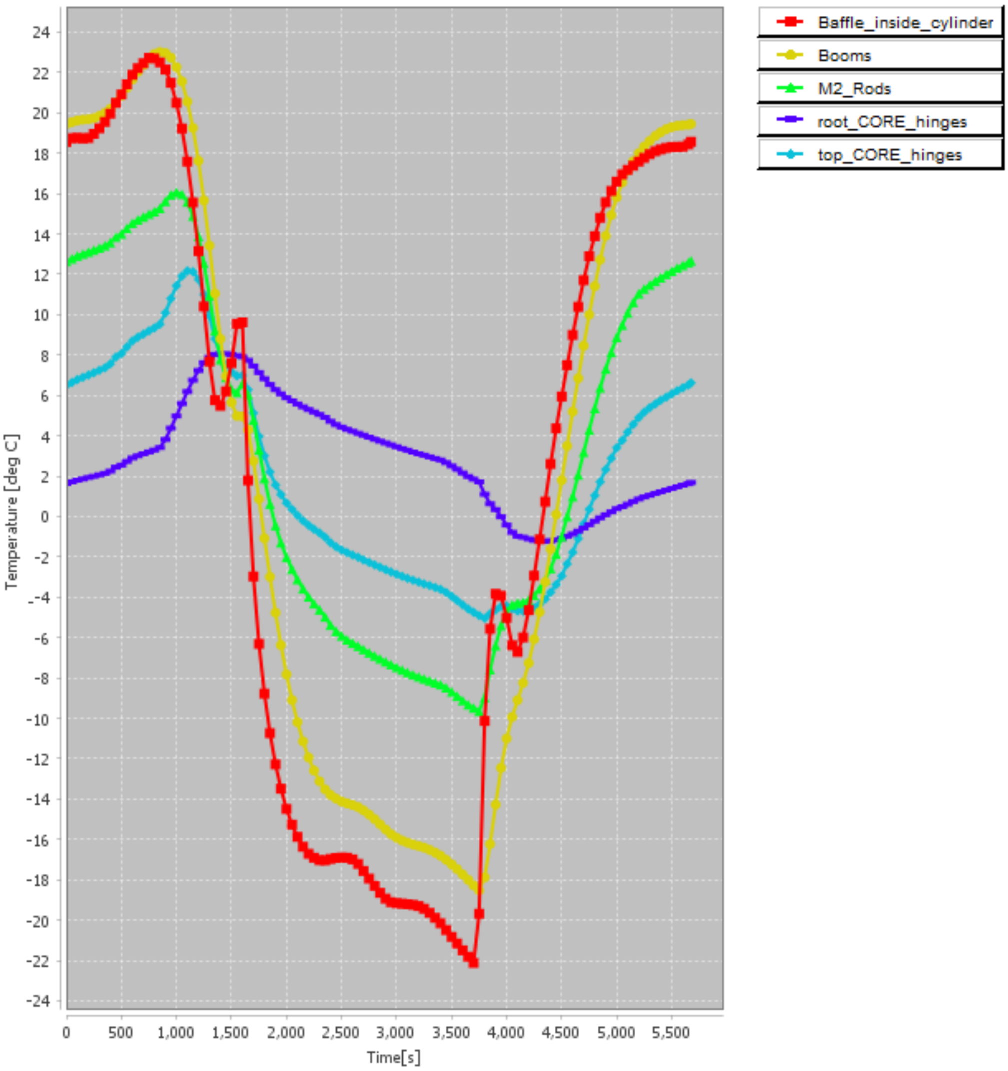

Figure 9.5: C-11V: Average temperatures of the booms, rods (denoted as M2_Support), CORE hinges (SMSS_Root_hinges and SMSS_top_hinges) and interior baffle wall

Table 9.4: Maximum and minimum temperatures of the baffle interior, booms, rods and CORE hinges of baffle model: C-11V

	Baffle interior	Booms	Rods	Top CORE	Root CORE Hinges
Min T [°C]	-22.08	-18.50	-9.64	-1.22	-5.03
Max T [°C]	22.75	23.01	16.08	8.14	12.27
T Range [°C]	44.84	41.50	25.72	9.35	17.30

9.1.5. Thermal Analysis of C-3AV-2V

Design C-3AV-2V is the baffle design for a three-segmented baffle. This means that the thermal performance of C-3AV-2V can be compared to C-7V. The difference in temperatures of the components is very similar to C-7V. The difference in temperature range is the largest for the booms. This can be attributed to the angular vanes which reflect more solar heat towards the entrance aperture than the straight vanes. The temperature difference of the interior baffle wall between 1400 to 1570 s is 2.2 K. The interior baffle wall heats up less due to the angular vanes, which causes a lower change in temperature of the interior baffle wall.

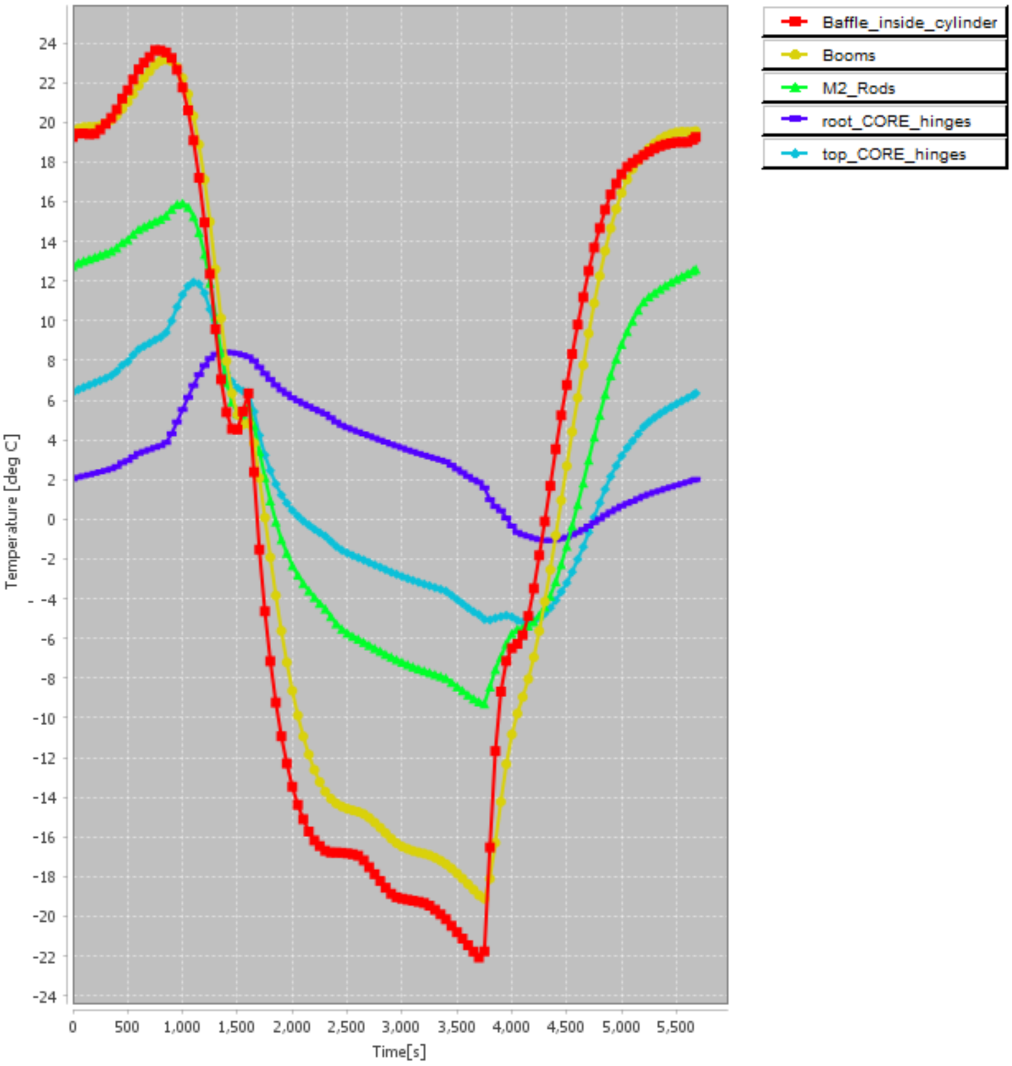

Figure 9.6: C-3AV-2V: Average temperatures of the booms, rods (denoted as M2_Support), CORE hinges (SMSS_Root_hinges and SMSS_top_hinges) and interior baffle wall

Table 9.5: Maximum and minimum temperatures of the baffle interior, booms, rods and CORE hinges of baffle model C-3AV-2V

	Baffle interior	Booms	Rods	Top CORE	Root CORE Hinges
Min T [°C]	-22.07	-19.11	-9.28	-1.06	-5.18
Max T [°C]	23.63	23.16	15.93	8.42	11.95
T Range [°C]	45.70	42.27	25.21	9.49	17.13

9.1.6. Thermal Analysis of C-3AV-6V

Design C-3AV-6V adds more straight vanes behind that of C-3AV-2V. As predicted, the temperature ranges of the component decreases due to the addition of more vanes. However, the added vanes are added in the portion of the baffle which does not receive sunlight. Therefore those vanes act like a thermal storage system, which stores some warmth due to conductive coupling.

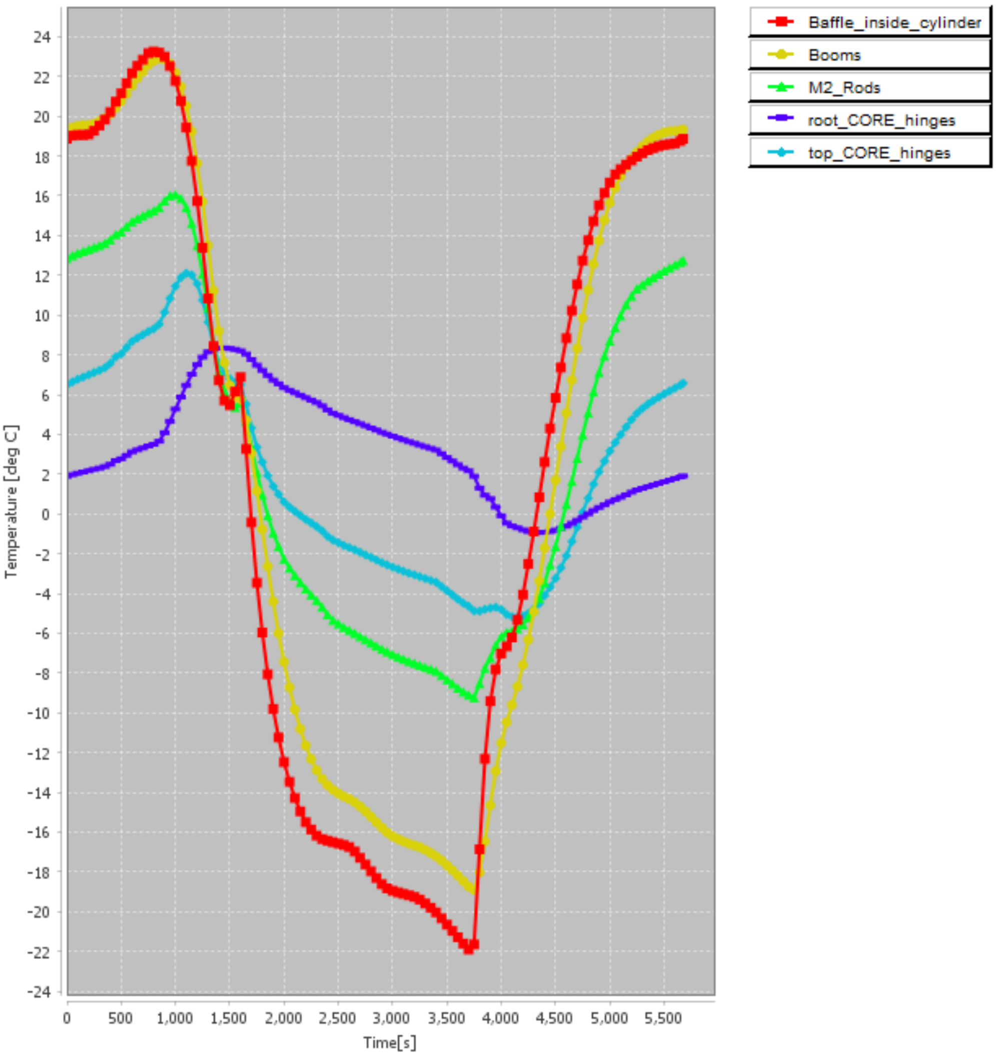

Figure 9.7: C-3AV-6V: Average temperatures of the booms, rods (denoted as M2_Support), CORE hinges (SMSS_Root_hinges and SMSS_top_hinges) and interior baffle wall

Table 9.6: Maximum and minimum temperatures of the baffle interior, booms, rods and CORE hinges of baffle model C-3AV-6V

	Baffle interior	Booms	Rods	Top CORE	Root CORE Hinges
Min T [°C]	-21.89	-18.91	-9.23	-0.94	-5.18
Max T [°C]	23.25	22.89	16.06	8.35	12.11
T Range [°C]	45.14	41.80	25.29	9.28	17.29

9.2. Thermal Analysis of Square Baffles

In this Section, the thermal analysis of the square baffles are given. First, the bare square baffle without any vanes is given in Section 9.2.1. Followed by thermal analysis of a square baffle with straight vanes: SQ-1V in Section 9.2.2, SQ-7V in Section 9.2.3 and SQ-11V in Section 9.2.4. The thermal analysis of the square baffle with angular vanes is given for baffle SQ-3AV-2V in Section 9.2.5 and baffle SQ-3AV-6V in Section 9.2.6.

9.2.1. Thermal Analysis of SQ-0V

The thermal analysis of SQ-0V is similar to that of C-0V. The difference is the higher in-orbit drift budget, which is 1.4 μm larger than that of C-0V. The maximum temperature of the components with the SQ-0V are higher. The minimum temperature of the components are also lower. Therefore the the temperature ranges of SQ-0V are larger than that of C-0V. By comparison, the temperature range of the baffle is increased by 4.1 K. The temperature range of the booms are increased by 2.8K. The temperature ranges of the CORE hinges are increased by about 1.4 K for the top and 1.8 K for the root hinges. The temperature difference between 1400 to 1570 s of the interior baffle wall is 10K.

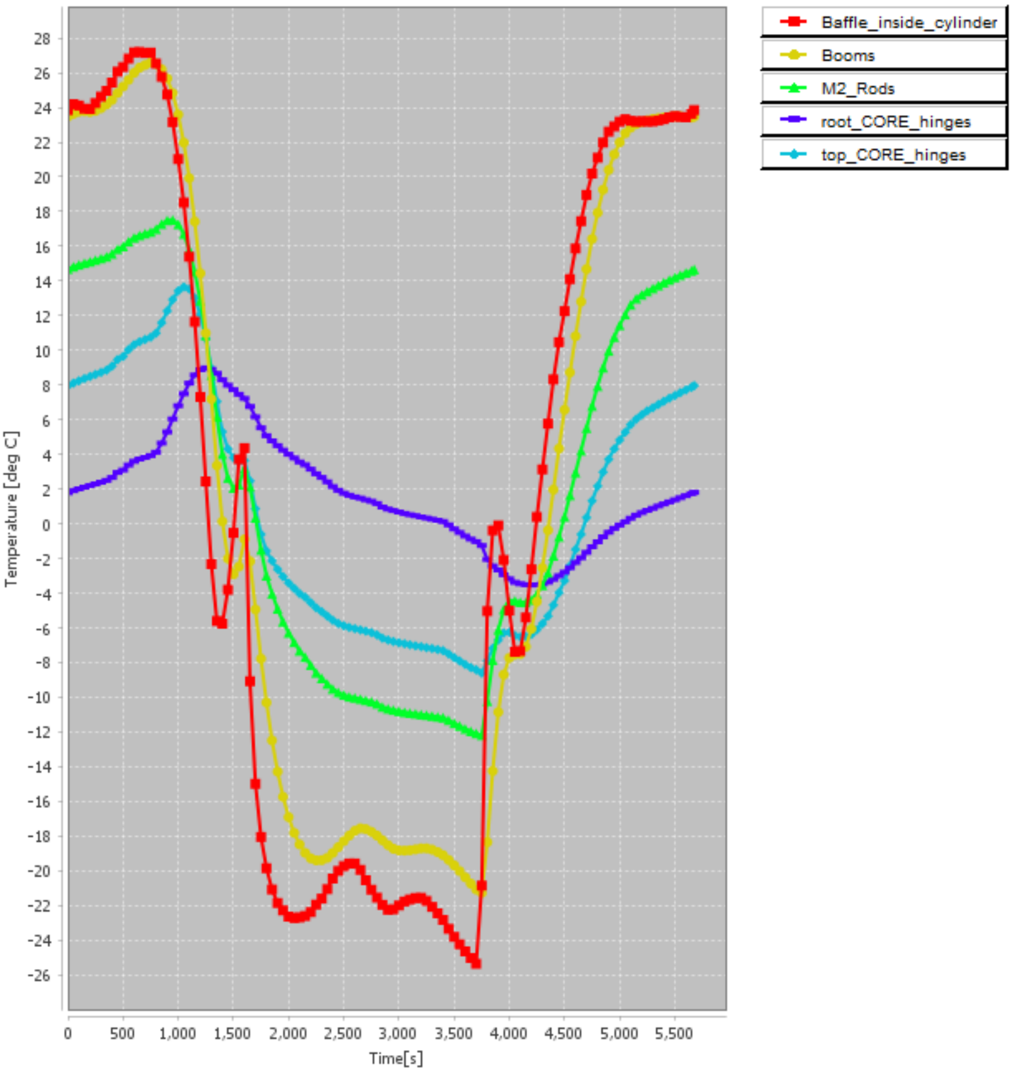

Figure 9.8: SQ-0V: Average temperatures of the booms, rods (denoted as M2_Support), CORE hinges (SMSS_Root_hinges and SMSS_top_hinges) and interior baffle wall

Table 9.7: Maximum and minimum temperatures of the baffle interior, booms, rods and CORE hinges of baffle model SQ-0V

	Baffle interior	Booms	Rods	Top CORE	Root CORE Hinges
Min T [°C]	-25.35	-21.27	-12.18	-3.53	-8.60
Max T [°C]	27.19	26.59	17.52	8.99	13.65
T Range [°C]	52.55	47.87	29.69	12.52	22.25

9.2.2. Thermal Analysis of SQ-1V

The effect of adding one vane at the entrance aperture has the same consequence for SQ-1V as it did for C-1V. Therefore, the same conclusions with C-1V can be made. Comparing SQ-1V with C-1V yet again, the temperature ranges of SQ-1V are higher. Furthermore, the in-drift orbit budget for SQ-1V is also higher than C-1V. The temperature difference of the interior baffle wall between 1400 to 1570 s is 9 K.

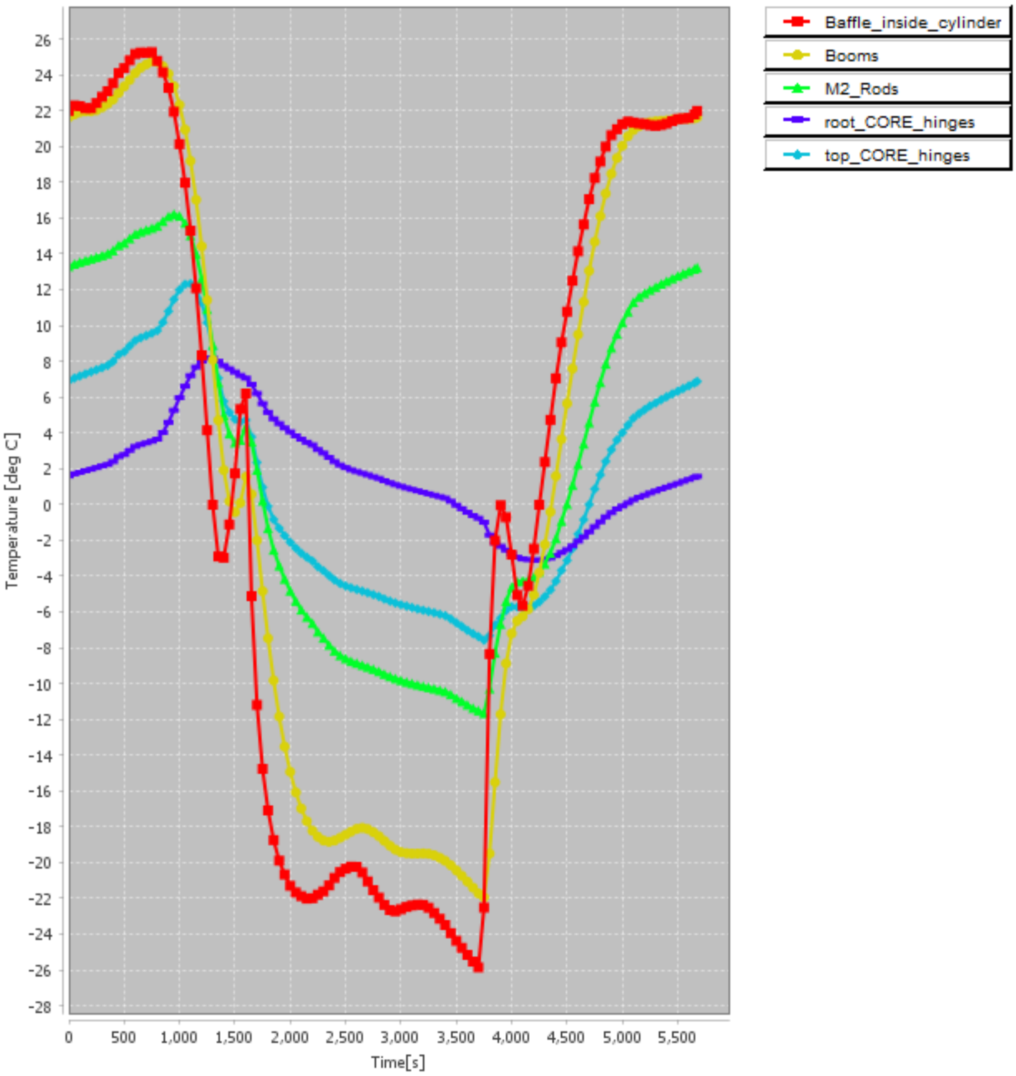

Figure 9.9: SQ-1V: Average temperatures of the booms, rods (denoted as M2_Support), CORE hinges (SMSS_Root_hinges and SMSS_top_hinges) and interior baffle wall

Table 9.8: Maximum and minimum temperatures of the baffle interior, booms, rods and CORE hinges of baffle model SQ-1V

	Baffle interior	Booms	Rods	Top CORE	Root CORE Hinges
Min T [°C]	-25.85	-21.94	-11.66	-3.10	-7.58
Max T [°C]	25.26	24.74	16.22	8.17	12.33
T Range [°C]	51.11	46.68	27.88	11.28	19.91

9.2.3. Thermal Analysis of SQ-7V

Similar to the analysis given to C-7V, the added vanes reduce the temperature experienced by the components. The temperature reduction per vane is again diminished. The temperature difference of the interior baffle wall between 1400 to 1570 s is reduced to 5.5 K. The maximum and minimum temperatures are decreased, due to the stabilising effect of the temperature of the added vanes.

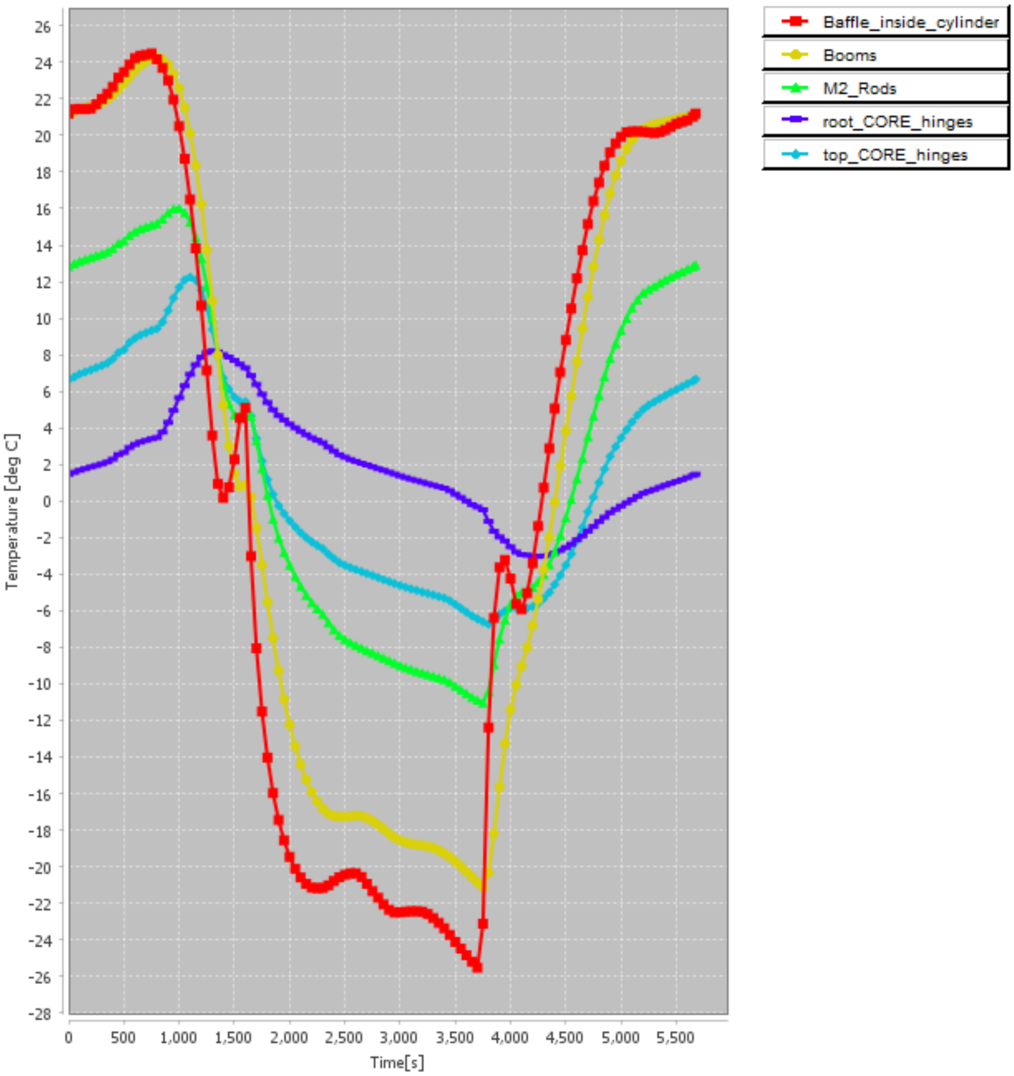

Figure 9.10: SQ-7V: Average temperatures of the booms, rods (denoted as M2_Support), CORE hinges (SMSS_Root_hinges and SMSS_top_hinges) and interior baffle wall

Table 9.9: Maximum and minimum temperatures of the baffle interior, booms, rods and CORE hinges of baffle model C-7V

	Baffle interior	Booms	Rods	Top CORE	Root CORE Hinges
Min T [°C]	-25.52	-21.13	-11.03	-3.02	-6.74
Max T [°C]	25.48	24.29	16.02	8.22	12.25
T Range [°C]	50.00	45.42	27.05	11.24	18.99

9.2.4. Thermal Analysis of SQ-11V

The addition of 4 additional vanes behind the vanes placed with SQ-7V leads to a reduction experienced by the components. Therefore, the temperature ranges are reduced in comparison to C-7V due to the added vanes. The temperature difference of the interior baffle wall between 1400 to 1570 s is reduced to 4.1 K, which is also reduced due to the addition of 4 extra vanes. The maximum and minimum temperatures are decreased, due to the stabilising effect of the temperature of the added vanes. The design of SQ-11V is suitable for a two-segmented baffle

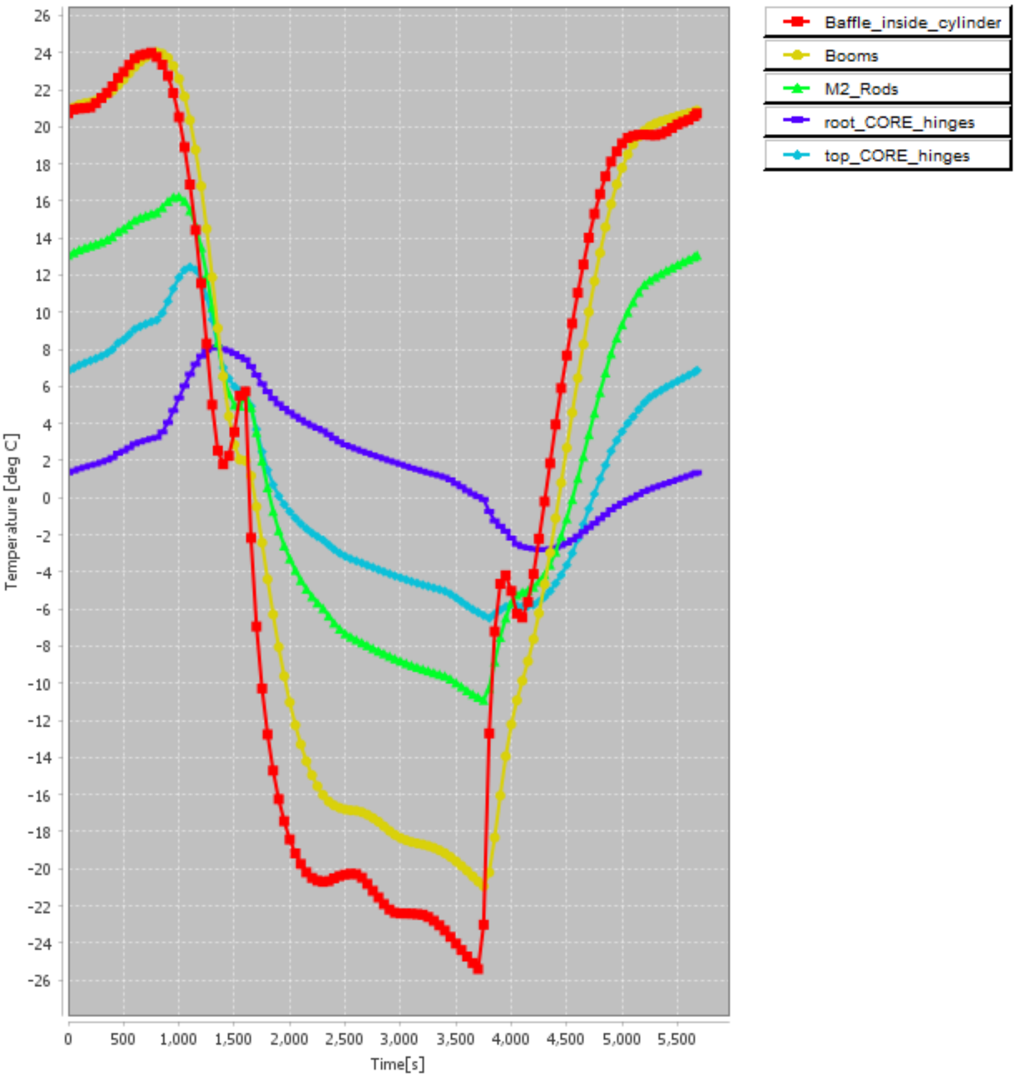

Figure 9.11: SQ-11V: Average temperatures of the booms, rods (denoted as M2_Support), CORE hinges (SMSS_Root_hinges and SMSS_top_hinges) and interior baffle wall

Table 9.10: Maximum and minimum temperatures of the baffle interior, booms, rods and CORE hinges of baffle model C-11V

	Baffle interior	Booms	Rods	Top CORE	Root CORE Hinges
Min T [°C]	-25.40	-20.94	-10.89	-2.79	-6.49
Max T [°C]	23.99	24.02	16.24	8.11	12.44
T Range [°C]	49.39	44.96	27.13	10.90	18.93

9.2.5. Thermal Analysis of SQ-3AV-2V

Similar to the design of C-3AV-2V, the design of SQ-3AV-2V is applicable to a three-segmented baffle. The thermal performance of SQ-3AV-2V can be compared to that of SQ-7V. The temperature ranges of the components are similar to those experienced by SQ-7V. The temperature difference of the interior baffle wall between 1400 to 1570 s is 2.2 K. The interior baffle wall heats up less due to the angular vanes, which causes a lower change in temperature of the interior baffle wall. The most notable difference, is the temperature difference of the interior baffle wall between 1400 to 1570 s which is 2 K. This can be attributed to the reflective function of the angled vanes.

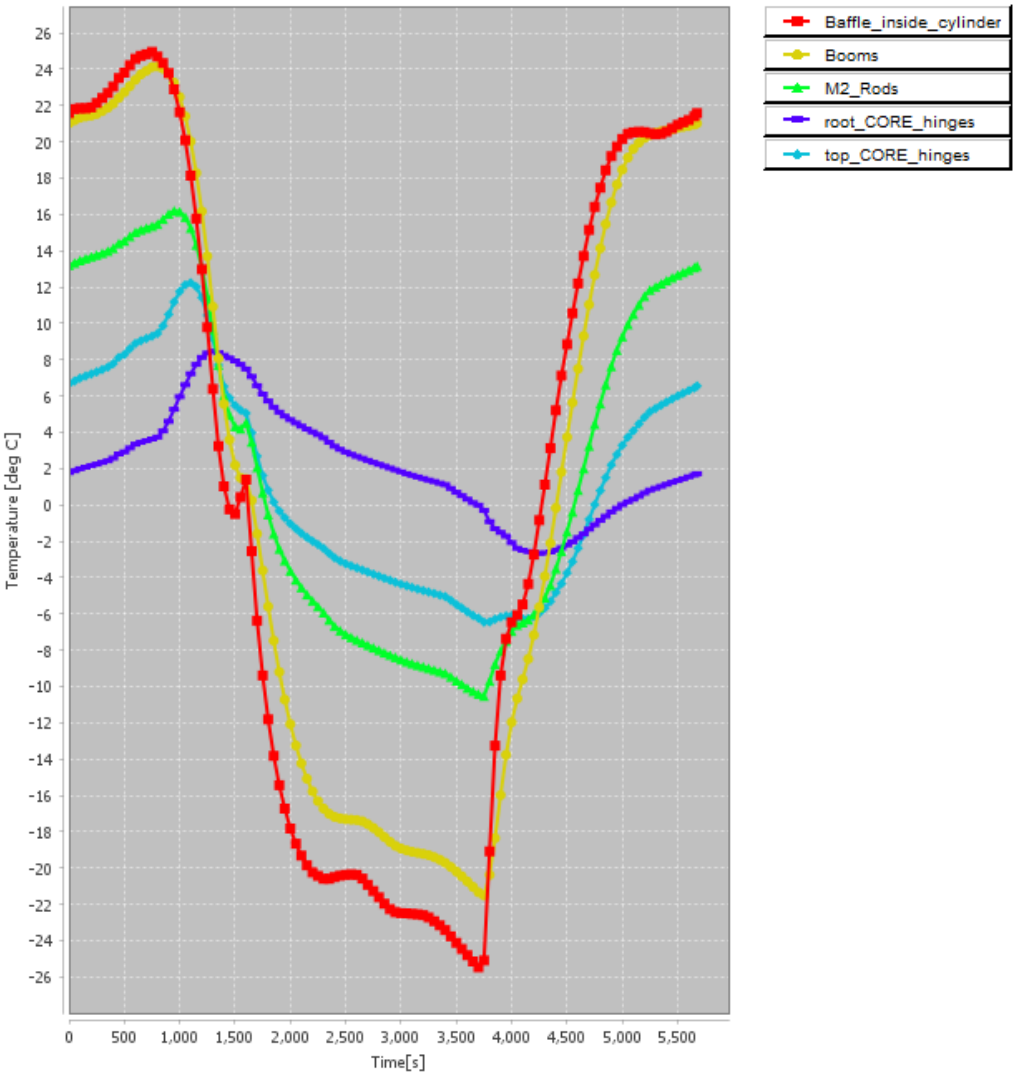

Figure 9.12: SQ-3AV-2V: Average temperatures of the booms, rods (denoted as M2_Support), CORE hinges (SMSS_Root_hinges and SMSS_top_hinges) and interior baffle wall

Table 9.11: Maximum and minimum temperatures of the baffle interior, booms, rods and CORE hinges of baffle model SQ-3AV-2V

	Baffle interior	Booms	Rods	Top CORE	Root CORE Hinges
Min T [°C]	-25.46	-21.51	-10.52	-2.65	-6.46
Max T [°C]	24.95	24.15	16.20	8.45	12.24
T Range [°C]	50.41	45.66	26.72	11.11	18.70

9.2.6. Thermal Analysis of SQ-3AV-6V

Likewise to the thermal analysis of C-3AV-6V, design SQ-3AV-6V adds 4 more straight vanes. Likewise, the temperature ranges of the components decrease with the addition of extra vanes. The temperature difference of the interior baffle wall between 1400 to 1570 s is further reduced to 1.0 K due to the addition of extra vanes.

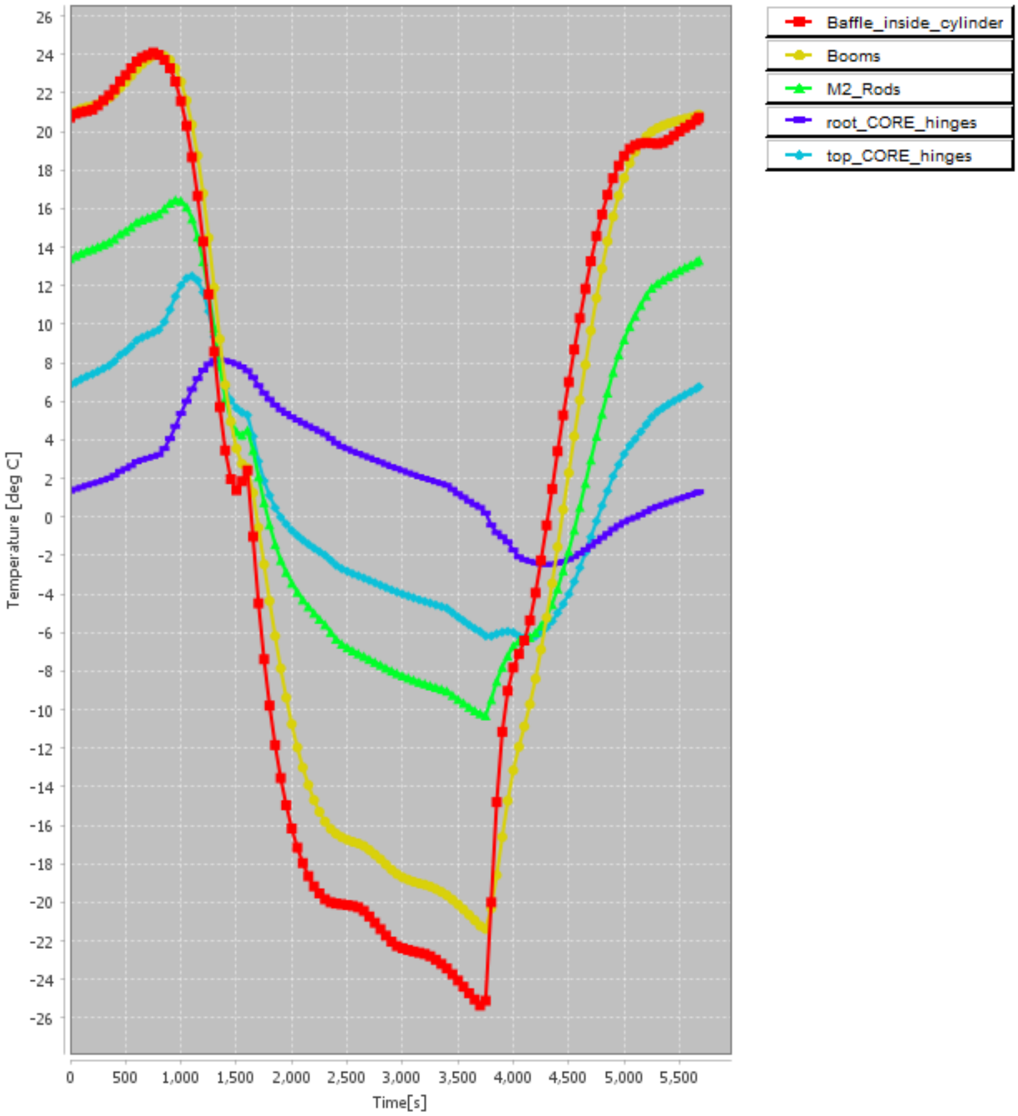

Figure 9.13: SQ-4AV-6V: Average temperatures of the booms, rods (denoted as M2_Support), CORE hinges (SMSS_Root_hinges and SMSS_top_hinges) and interior baffle wall

Table 9.12: Maximum and minimum temperatures of the baffle interior, booms, rods and CORE hinges of baffle model SQ-4AV-6V

	Baffle interior	Booms	Rods	Top CORE	Root CORE Hinges
Min T [°C]	-25.35	-21.37	-10.30	-2.46	-6.26
Max T [°C]	24.10	23.00	16.46	8.17	12.50
T Range [°C]	49.44	45.37	26.76	10.63	18.76

9.3. Comparison and Conclusion on Thermal Analysis

The in-drift orbit budget is kept within the requirements with both the cylindrical and square baffle and various vane configurations. An overview of the in-drift orbit Δz is given in Table 9.13. The largest in-drift orbit range occurs when there are no vanes placed in the system. The in-drift orbit budget is reduced by adding vanes to the baffle. The difference between no vanes and a maximum amount of vanes lead to a in-drift orbit budget decrease of a maximum $1\ \mu m$ when the highest amount of vanes are added. It can also be seen that the in-drift orbit budget for the square baffle is higher than the cylindrical baffle. This indicates that the performance of the cylindrical baffle is better than the square baffle.

Table 9.13: Overview of the in-drift orbit budget for the cylindrical and square baffle with various configurations expressed in μm

In-drift orbit	Cylindrical baffle [μm]	Square baffle [μm]
No Vanes	15.35	16.77
1 straight vane	15.23	16.65
7 straight vanes	14.45	16.15
11 straight vanes	14.13	15.78
13 straight vanes	14.27	15.77
3 angular and 2 straight vanes	14.75	16.38
3 angular and 6 straight vanes	14.4	16.06

Comparison of the temperature range of the individual components better showcase the effect of vanes. The highest decrease in temperature range occurs when one vane at the entrance aperture (design C-1V) gets added to a vaneless baffle (design C-0V). This single vane decreases the temperature range of the components by 1.5 to 2.5 K when compared to a baffle without vanes. This occurs with both the cylindrical and square baffle. The effectiveness of adding more vanes decreases. For example, the temperature range decreases between C-1V and C-11V is 0.5 to 2.2 K. The square baffles have a higher maximum temperature and lower minimum temperature than the cylindrical baffle for all baffle configurations. This leads to an increase in temperature range of the components to about 4.1 to 1.5 K higher for the square baffles. This further strengthens the conclusion that the cylindrical baffles outperform the square baffles.

The effect of adding more vanes has an effect on the rapid change in temperature prior to entering and exiting eclipse. The change in temperature goes from 10 K from a vaneless baffle to about 4.5 K for a baffle with 11 vanes. The change in distance Δz are plotted for the baffles C-0V, C-1V, C-7V and C-11V in Figure 9.14, showing that the decrease of Δz around 1500 s and increase around 4000 s becomes a more linear function when more vanes are added to the system. This linear change in distance due to thermal expansion can be better anticipated against through using an actuation system. The work of Hobijn covers the actuation system of the deployment for the secondary mirror to actively correct the in-drift orbit budget [57].

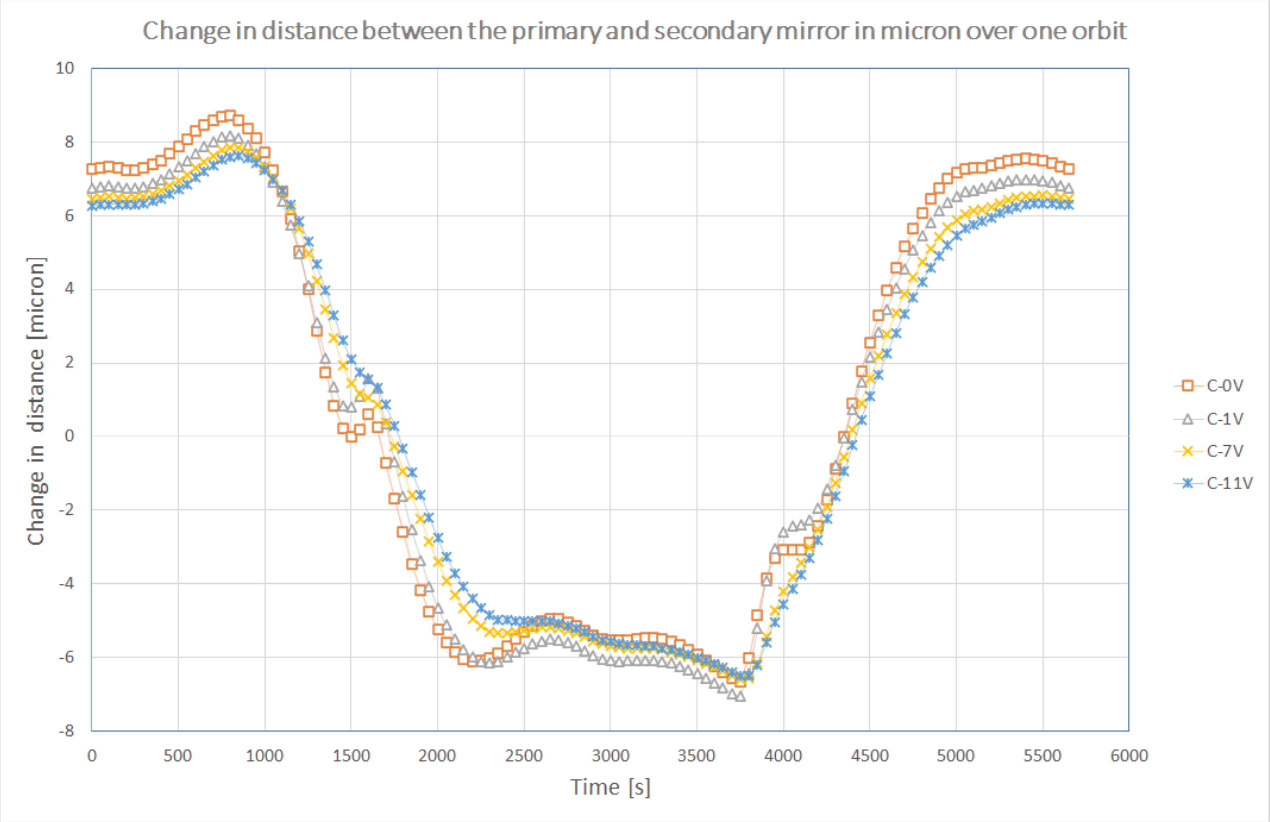

Figure 9.14: Change in distance between the primary and secondary mirror Δz over one orbit for baffles C-0V, C-1V, C-7V and C-11V

The effects of adding angular vanes can be seen in Figure 9.15. The angled vanes increase the temperature stability. The decrease and increase in distance Δz becomes a more linear function through utilisation of angled vanes. Design

C-3AV-2V and C-7V can be compared against each other because they both use a three-segmented baffle. The change in distance Δz from for example 1000 to 1500 s over the orbit, is 0.5 μm less for C-3AV-2V than for C-7V. Thus a baffle with angled vanes placed in the sunlit region of the baffle improves the temperature stability compared to a baffle with only straight vanes. Further addition of more straight vanes after the angled vanes do not have much effect as demonstrated by C-3AV-6V which has 4 more straight vanes than C-3AV-2V. From Table 9.13, the in-drift orbit budget difference is only 0.3K in favour of C-7V. The largest temperature difference is seen in the rods which hold the secondary mirror. This is due to the angular vanes reflecting more heat outwards towards the spider system. The rods are heated up to 0.4 K more with design C-3AV-2V. The effect of straight and/or circular vanes are also observed in the square baffles.

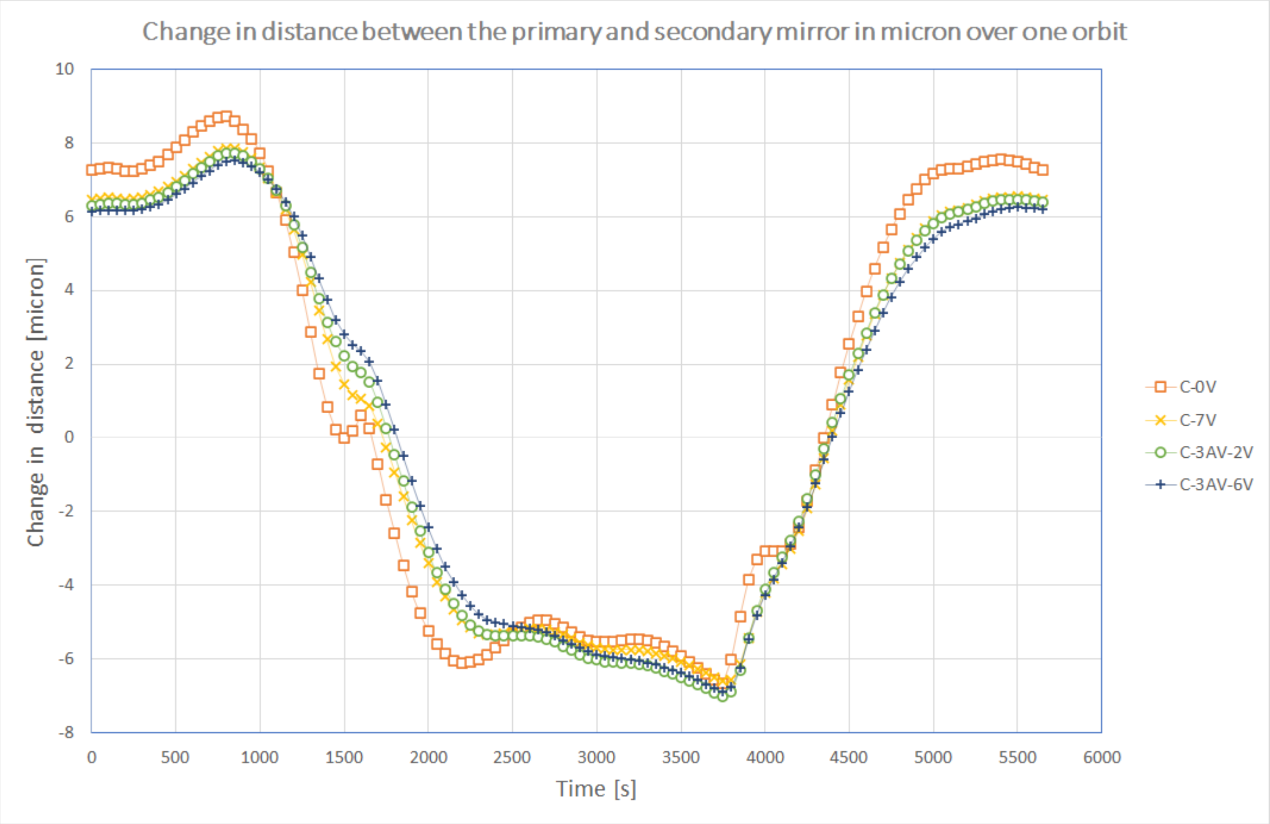

Figure 9.15: Change in distance between the primary and secondary mirror Δz over one orbit for baffles C-0V, C-7V, C-3AV-2V and C-3AV-6V

In conclusion, the cylindrical shaped baffle performs better than the square baffle. Furthermore, the temperature stability increases the most when adding one vane to a vaneless system. Adding more vanes to the baffle does result in a more temperature stable system. However, the thermal stability increase by adding more vanes quickly diminishes. The complexity of adding more vanes does not outweigh the benefit of a better temperature stability. Therefore, the cylindrical baffle with one vane i.e. design C-1V should be used.

10

Stray Light Analysis of the TIR Baffles

The stray light analysis of the TIR baffles will provide information on the ability of the baffle to minimise unwanted reflection towards the detector. Both 30 cm models as described in Section 8.2 were used to provide a stray light analysis of the baffles. First, the stray light requirement for the TIR version is given by comparison with state of the art in Section 10.1. The stray light analysis performed follow the same principles as outlined in Chapter 5. The stray light analysis for the straight and fold-mirror configuration without any baffles is given by Section 10.2. Then, the stray light performance of the cylindrical and square baffles without any baffles are given in Section 10.3. The straight vanes are then added to the baffles and their effect on the stray light performance is given in Section 10.3. The effect of replacing some of the straight vanes near the entrance aperture with angular vanes on the stray light performance is given in Section 10.5. Finally, the best performing baffles are compared to eachother and a conclusion is given in Section 10.6.

10.1. Stray Light Requirement for TIR version

This section aims to provide a stray light requirement for the DST TIR version.

The total signal from the Earth is given by the following Equation:

$$S_{earth} = F_{earth-DST} A_{FOV} \Delta\lambda B_{\lambda=10\mu m} \rho_{total} \tag{10.1}$$

First, the view factor is estimated. The observational area at a 300 km orbiting altitude and a FOV area of 7.2 by 7.2 km. This corresponds to the following view factor [60]:

$$F_{earth-DST} = \frac{A_{M1}}{A_{FOV}} \cdot \frac{4}{\pi} \left(\frac{\frac{b}{2H}}{\sqrt{1+\frac{b}{2H}^2}} arctan\left(\frac{\frac{b}{2H}}{\sqrt{1+\frac{b}{2H}^2}} \right) \right) \approx 2.5 \cdot 10^{-13} \tag{10.2}$$

The view factor F is under the assumption that the observed area is flat, b is the width of the observation area of 7.2 km and H is the orbital altitude of the DST. The DST will be observing the Earth in the 8 to 12 μm wavelength band. This corresponds to the in-band spectral radiance of [22]:

$$B(\lambda) = \frac{2hc^2}{\lambda^5} \frac{1}{e^{\frac{hc}{\lambda k_b T}} - 1} = 9.92\ W/m^2 sr \mu m = 2.38 \cdot 10^7 W/m^3 \tag{10.3}$$

Where $B(\lambda)$ is the spectral radiance of Earth at the peak wavelength λ of 10 μm, h is the Planck constant, k_b the Boltzmann constant and c the speed of light. The primary mirror has an emissivity of 0.035. The reflectivity of the primary mirror is thus $\rho = 1 - \epsilon = 1 - 0.035 = 0.965$. It is assumed that all on-axis rays will reflect from the primary mirror towards the secondary mirror, followed by transmission through the lenses to finally reaching the detector. When considering that no transmission loss occurs in the lenses, the rays are reflected twice before reaching the detector. Therefore it is assumed that the total reflectivity of the system is $\rho_{total} = 0.965^2 = 0.931225$. Then the total heat that is being reflected by the primary mirror towards the detector by observing a 7.2 by 7.2 km plane in the wavelength band of 8 to 12 μm is:

$$S_{earth} = F_{earth-DST} A_{FOV} \Delta\lambda B_{\lambda=10\mu m} \rho_{total} = 1.15 \cdot 10^{-3}\ W \tag{10.4}$$

Assuming that only 1% of that signal is acceptable as stray light, this leads to a stray light requirement of:

$$PST = S_{earth} \cdot 1\% = 1.15 \cdot 10^{-5} \tag{10.5}$$

This correlates to a log(PST) of -5 for the TIR concepts. Comparison to existing TIR systems provide some insight on the relative stray light performance of the TIR concept. Landsat 9 hosts the updated version of the Thermal Infrared Sensor 2 (TIRS-2) which aims to improve the stray light issues that were present with TIRS-1 instrument [61]. These improvements were to counter the unpredicted out-of-field scatter from a mechanical bracket. Though the TIRS-1 is plagued by this signal, a software fix was implemented to reduce the effect of stray light for the TIRS-1 instrument. The changes to TIRS-2 aims to prevent the effect of stray light through a hardware fix by applying baffle vanes. The stray light value for the TIRS-2 instrument is documented to be in the range of 1E-02 to 1E-07 from an off-axis angle between 0 to 30°. This corresponds to a log(PST) of -2 to -7 for the TIRS-2 instrument. The Antarctic Survey Telescope (AST3-3) uses a near infra-red camera to conduct the Kunlun Infrared Sky Survey in the central wavelength of 2.375 μm [62]. The AST3-3 achieves a PST of 1.0E-4 to 1.0E-6, corresponding to a log(PST) of -4 to -6. The Xi'an Insitute of Optics and Precision Mechanics calculated the stray light level achieved for a LEO space camera [63]. They calculated that for a LEO camera, the stray light illuminance should be in the order of 1E-4 i.e. log(PST) of -4. The total illuminance which should come from the Earth was calculated for their system to be 2.9E-4 W/m^2. Comparing the stray light level of the various instruments, the highest amount of acceptable stray light level was for the TIRS-2 instrument which has a PST of 1E-2. Therefore, the DST TIR version should not have a stray light performance worse than 1E-2 or log(PST) above -2. The setup of the stray light analysis is done through applying the same method as applied in Section 5.3. The validation of the correct optical model of the TIR versions were performed in Section 8.2.

10.2. Stray Light Analysis: No Baffle

In this section, the stray light analysis is given for the DST TIR straight and fold mirror version without any baffle. The straight version will be denoted by the '-s' suffix. When the fold mirror design is used, it will be denoted by the suffix '-fm'. The stray light plot for both versions can be seen in Figure 10.1. The PST is given in log scale, with base number 8. This means that when no rays are registered by the detector, the PST has the value of 0. When the log(0) of base 8 is calculated, this represents a -8 value on the log scale. Therefore the fold mirror design without a baffle does not register any rays hitting the detector at 0, 2 and 4°. There is however, a peak at 14° for the fold mirror design. This implies that there may be a straight shot or internal reflections from the source towards the detector. For the straight version, there seems to be a very slight amount of rays hitting the detector at 0°. From 4 to 13° the stray light performance worsens, indicating that there are some rays hitting the detector. The detector also receives more rays at 20 degrees for the straight version without a baffle. This indicates that the fold mirror design has a better intrinsic capability of reducing the amount of stray light reaching the detector. Note that the presented result of the stray light performance of the DST without a baffle is skewed as was explained in Section 5.4. The actual stray light performance of the TIR DST without a baffle would be way worse due to absence of protection against off-axis angles which would otherwise be blocked by a wall.

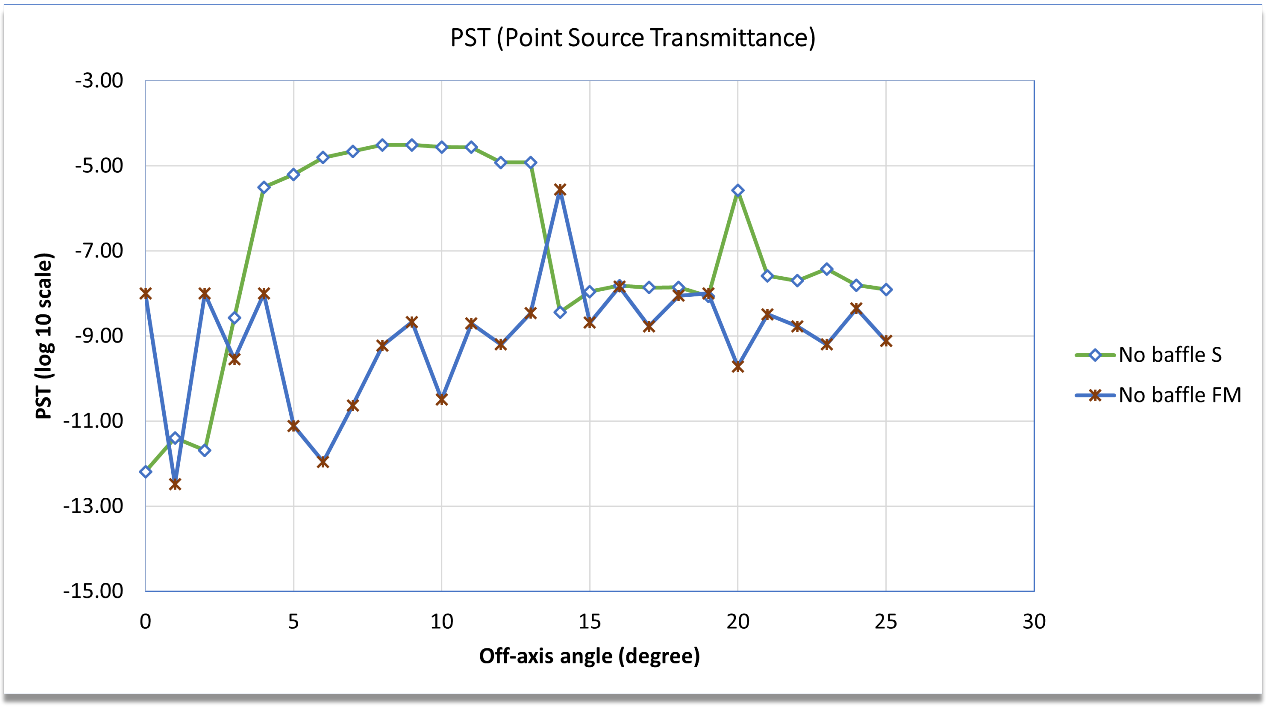

Figure 10.1: PST analysis of the TIR straight and fold mirror without any baffles

10.3. Stray Light Analysis: Vaneless Baffles

In this section, the stray light analysis is given for the cylindrical and square baffle without vanes for both the straight and fold mirror design. In Figure 10.2, it can be seen that the same peaks are present which also occurred with the baffleless analysis of Section 10.2. Due to the cylindrical baffle, there is no longer an angle at which no stray light hits the detector. This indicates that at certain angles, the baffles introduce some scatter towards the detector. This is logical, since the off-axis rays in the analysis are captured by the baffle and are redirected towards the detector. The analysis of the square baffle exhibits the same conclusion as can be seen in Figure 10.3. Combining both analyses in Figure 10.4, it can be seen that with the SQ-0V-S performs better than C-0V-S below 4°. For the fold mirror system, SQ-0V-FM trends slightly below C-0V-FM.

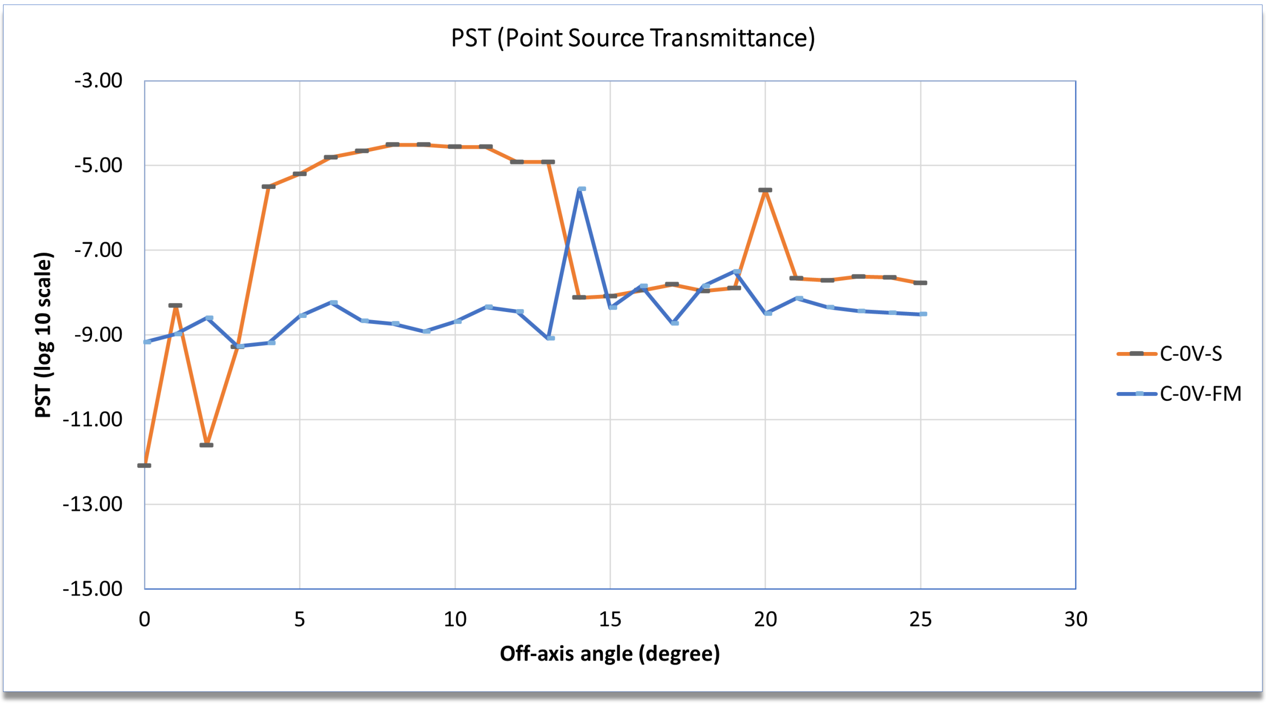

Figure 10.2: PST analysis of the TIR design with cylindrical baffle without vanes

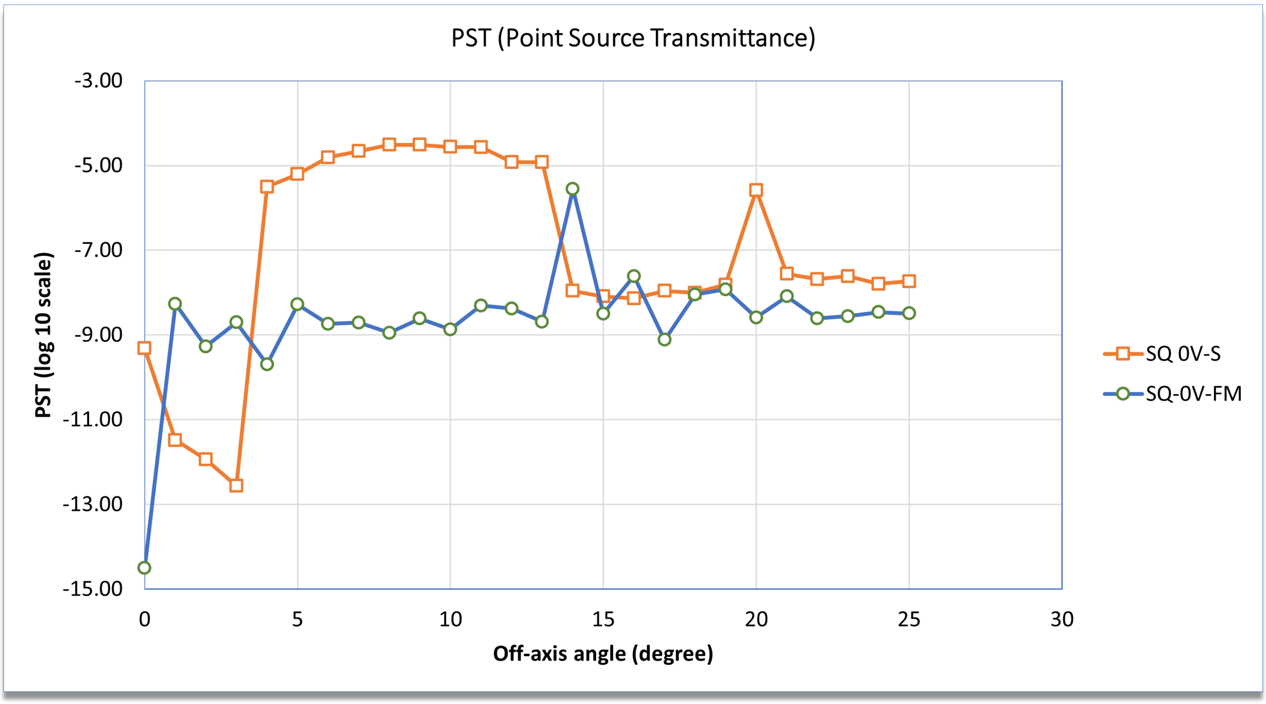

Figure 10.3: PST analysis of the TIR design with square baffle without vanes

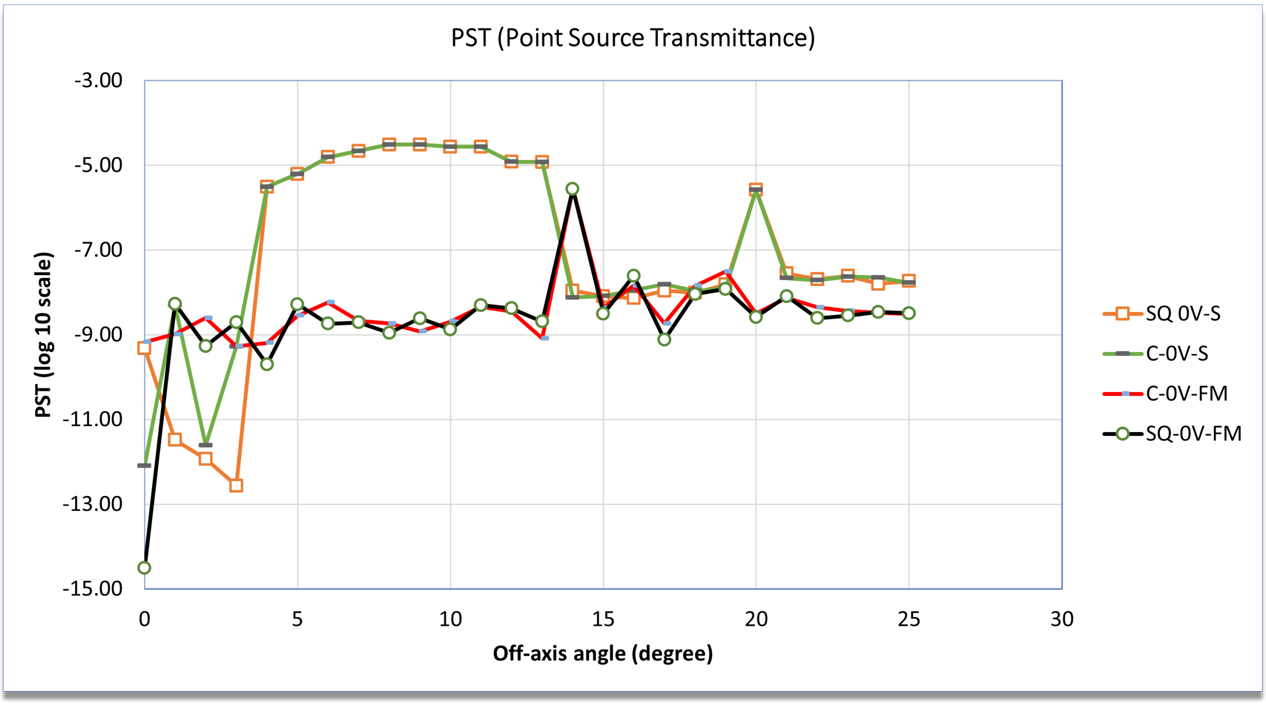

Figure 10.4: PST analysis of the cylindrical and square baffle without vanes

10.4. Stray Light Analysis: Baffles with Straight Vanes

In this section, the stray light analysis is given for the cylindrical and square baffle with straight vanes for both the straight and fold mirror design. First, the analysis of the cylindrical baffle with straight design is given in Figure 10.5. It can be seen that C-1V-S performs the best below 4°, followed by C-0V-S. There does not seem to be a distinct difference between C-7V-S and C-11V-S, as the lines closely track eachother. Furthermore, the performance of all the four baffles does not differ at off-axis angles higher than 4°. This indicates that the added effect of more straight vanes does not have a major influence on the stray light design. The exception is at 24°, where both C-7V-S and C-11V-S have an increased level of stray light. This can be caused by multiple reflections which bounce between the multiple vanes to ultimately reach the detector.

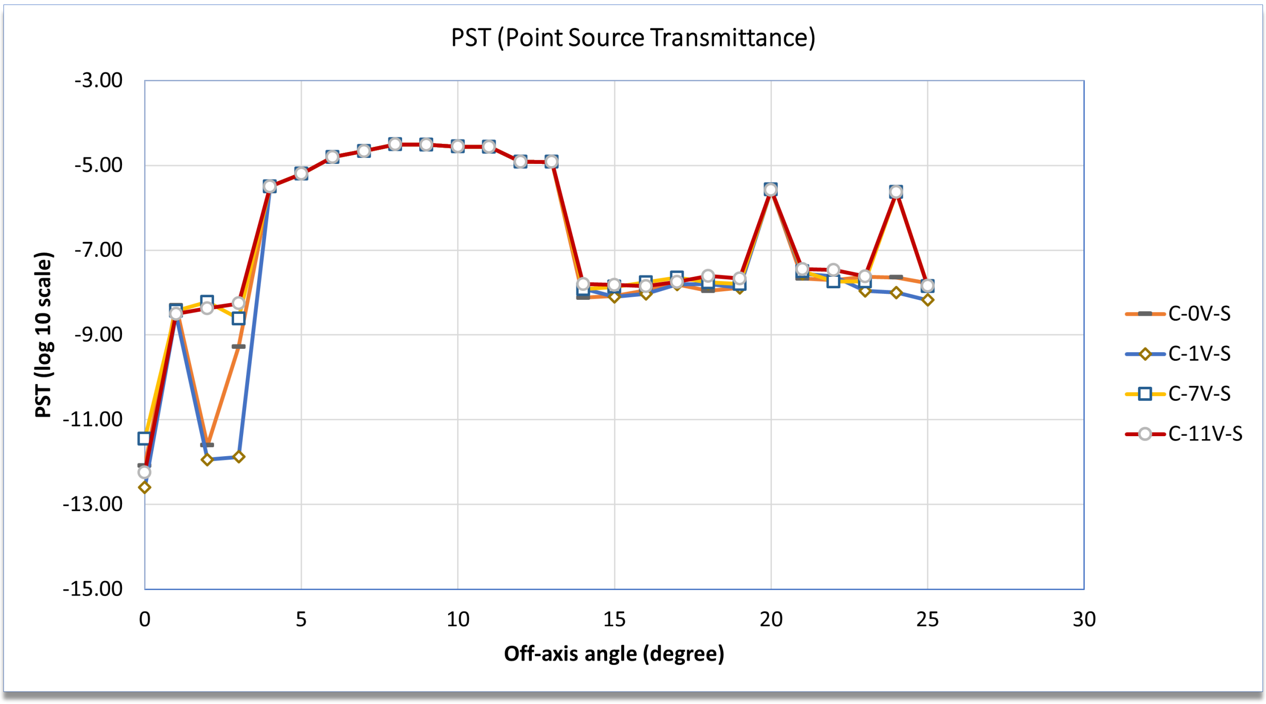

Figure 10.5: PST analysis of the straight TIR design with cylindrical baffle and straight vanes

The stray light analysis of the cylindrical baffle with the fold mirror design is given in Figure 10.6. The initial performance between 0 to 2° is best for C-1V-FM which treads below the other curves. Furthermore, C-0V-FM and C-1V-FM are continuously below the baffle with 7 and 11 vanes. This further indicates that the baffle with more vanes are slightly outperformed by the baffles C-0V-FM and C-1V-FM.

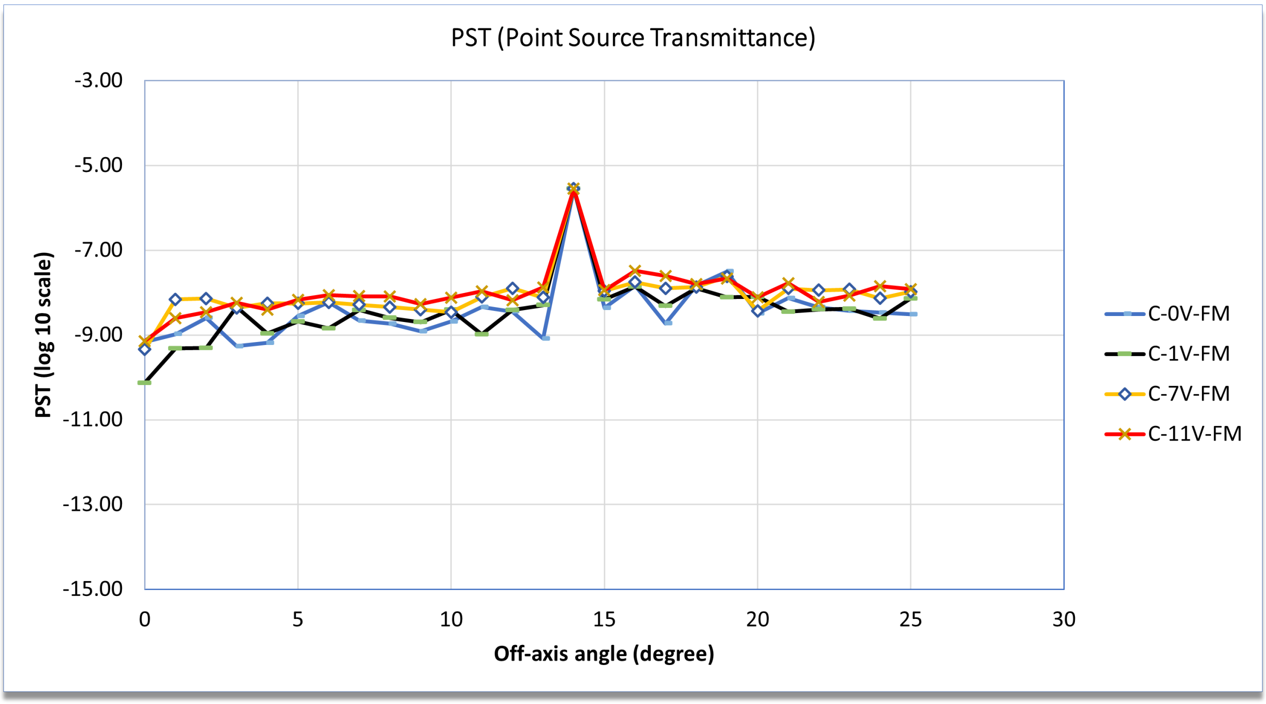

Figure 10.6: PST analysis of the fold-mirror TIR design with cylindrical baffle and straight vanes

The stray light analysis of the square baffle with the straight design is given in Figure 10.7. The performance of SQ-0V-S is slightly better than the other baffles shown in this figure for an angle up to 3°. From 4° onwards, there does not seem to be a major difference between the stray light performance. Which indicates that multiple vanes for the square design does not affect the stray light performance.

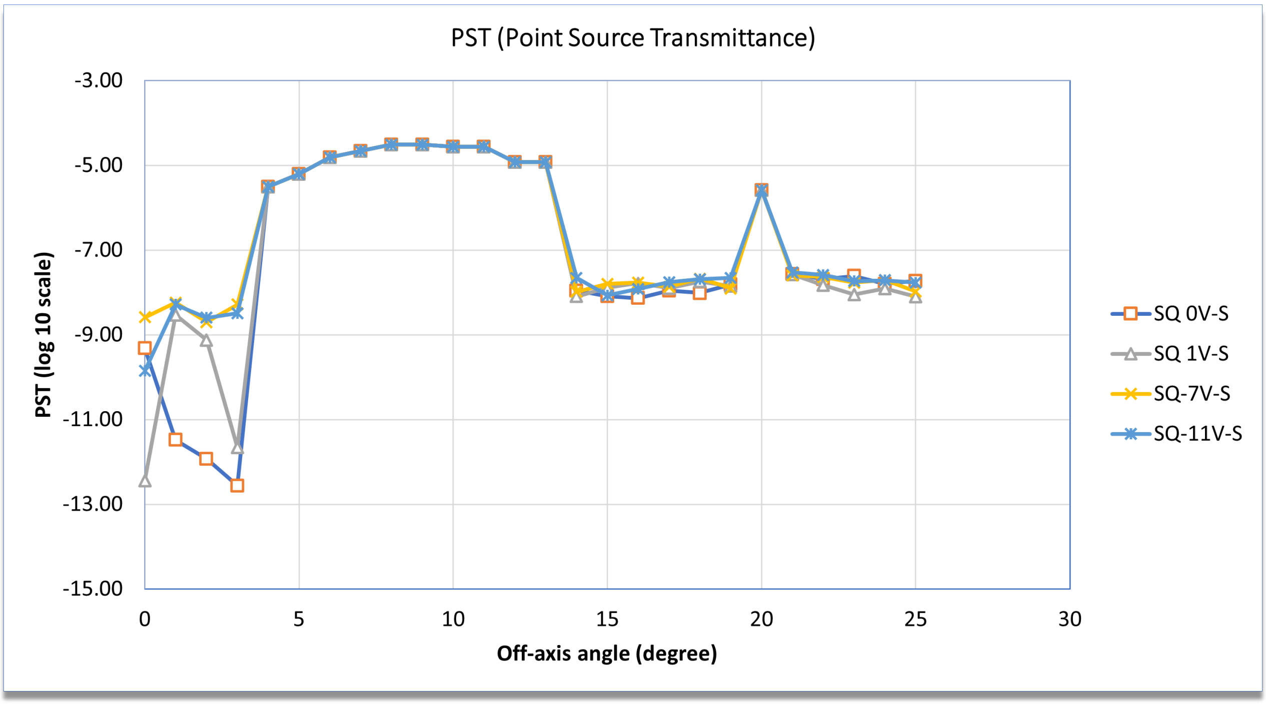

Figure 10.7: PST analysis of the straight TIR design with square baffle and straight vanes

The stray light analysis of the square baffle with the fold mirror design is given in Figure **??**. For the fold mirror design, both SQ-0V-FM and SQ-1V-FM outperform C-7V-FM and C-11V-FM. Since the lines of SQ-0V-FM and SQ-1V-FM are continuously below the lines of the other two baffles. There does seem to be peak at 3° for SQ-7V-FM which might be caused by unguided reflections off of the vanes. The reflections could be caused by the corners of the square baffle, due to the asymmetric shape of a square baffle around the radial axis. This peak does not seem to occur for SQ-11V-FM. This might be because the reflection is blocked off by one of the vanes of SQ-11V-FM which SQ-7V-FM does not have.

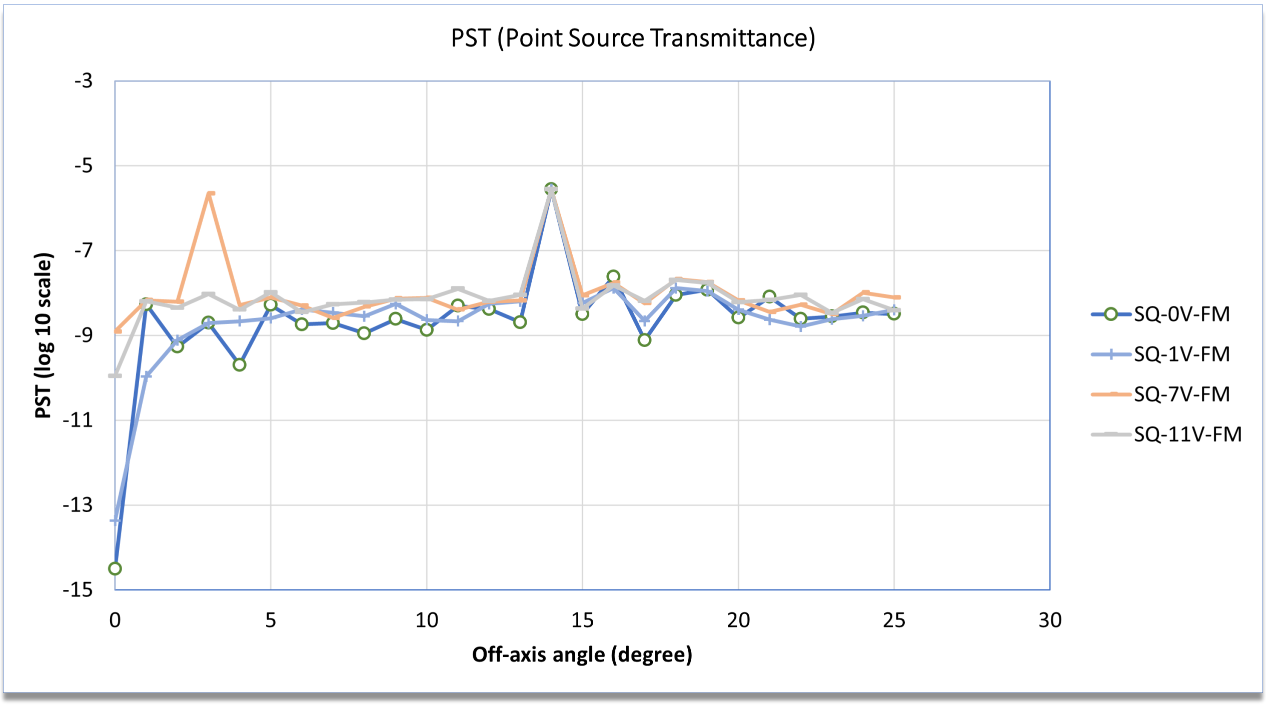

Figure 10.8: PST analysis of the fold-mirror TIR design with square baffle and straight vanes

10.5. Stray Light Analysis: Baffles with Angular and Straight Vanes

In this section, the stray light analysis is given for the cylindrical and square baffle with straight and angular vanes for both the straight and fold mirror design. First, the analysis of the cylindrical baffles with the straight version is given in Figure 10.9. It can be seen that C-0V-S is continuously below the stray light levels of C-3AV-2V-S and C-3AV-6V-S, indicating that the combination of angular vanes worsens the stray light performance. Baffle C-3AV-2V-S has peaks which the other baffles do not exhibit at 1 and 16 degree. This can indicate that the vanes after C-3AV-2V-S which are positioned in C-3AV-6V-S absorb some of the scattered stray light caused by C-3AV-2V-S.

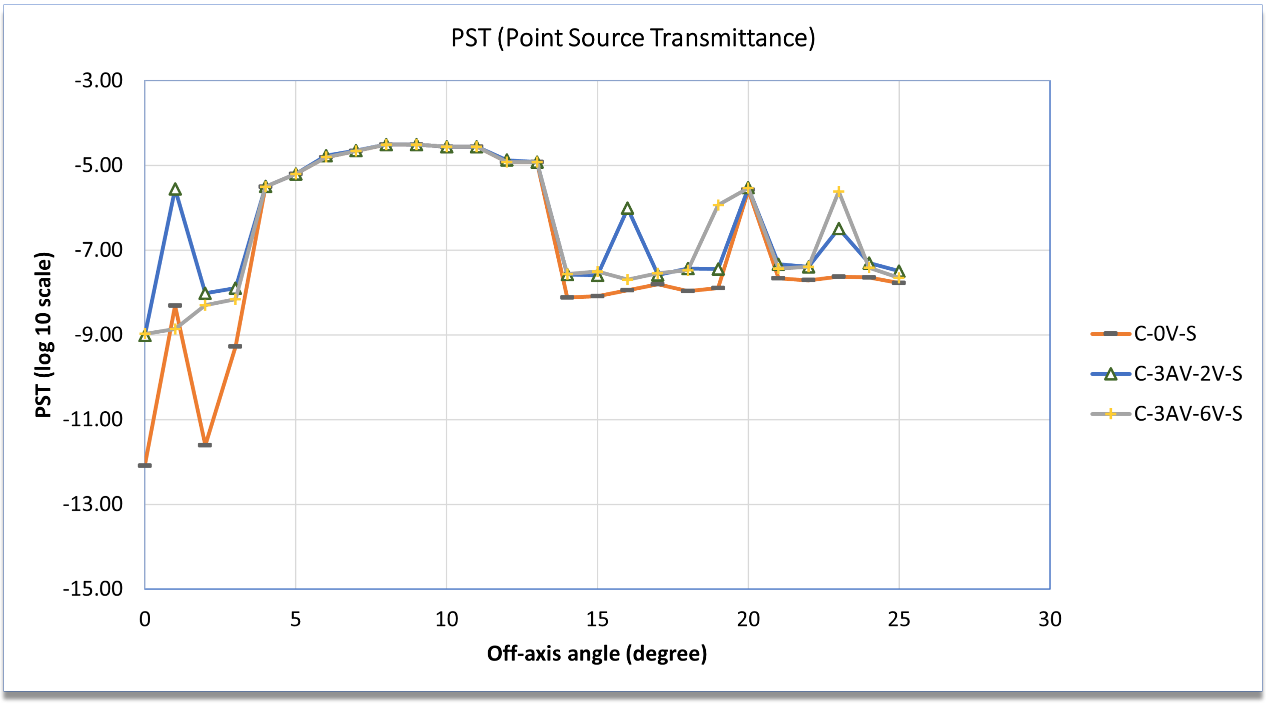

Figure 10.9: PST analysis of the straight TIR design with baffles C-0V, C-3AV-2V and C-3AV-6V

The analysis of the angular vanes with cylindrical baffle and fold mirror is given in Figure 10.10. Again, C-0V-FM perform better than the cylindrical baffles with angular vanes. Because the stray light of C-0V-FM is lower than the other two. The baffle C-3AV-2V-FM produces a peak at 16°. The stray light is again absorbed by the vanes of C-3AV-6V-FM, which therefore does not exhibit the same peak at 16°. Both C-3AV-2V-FM and C-3AV-6V-FM exhibit a peak at 23°, which the vaneless baffle does not exhibit.

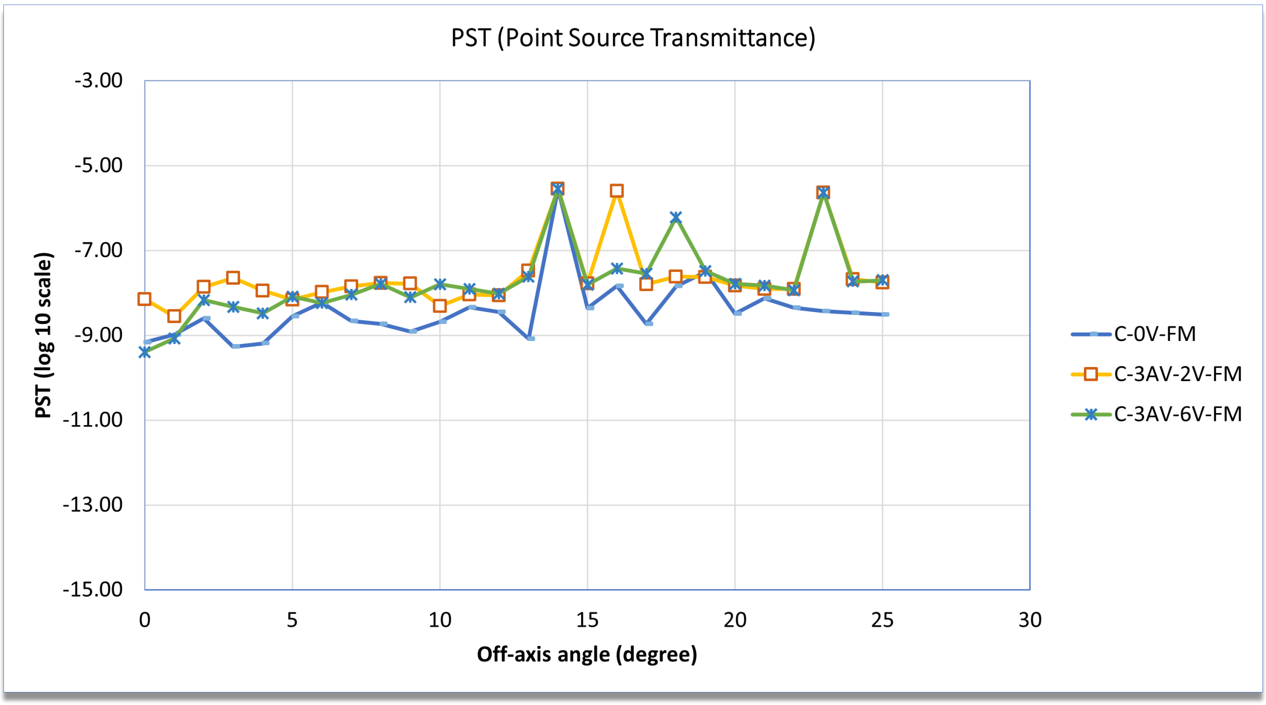

Figure 10.10: PST analysis of the fold-mirror TIR design with baffles C-0V, C-3AV-2V and C-3AV-6V

The analysis of the angular vanes with square baffle and straight design is given in Figure 10.11. It can be seen that SQ-0V-S also outperforms SQ-3AV-2V-S and SQ-3AV-6V-S below 4°. At off-axis angles higher than 4°, the performance of the baffles does not seem to alter much.

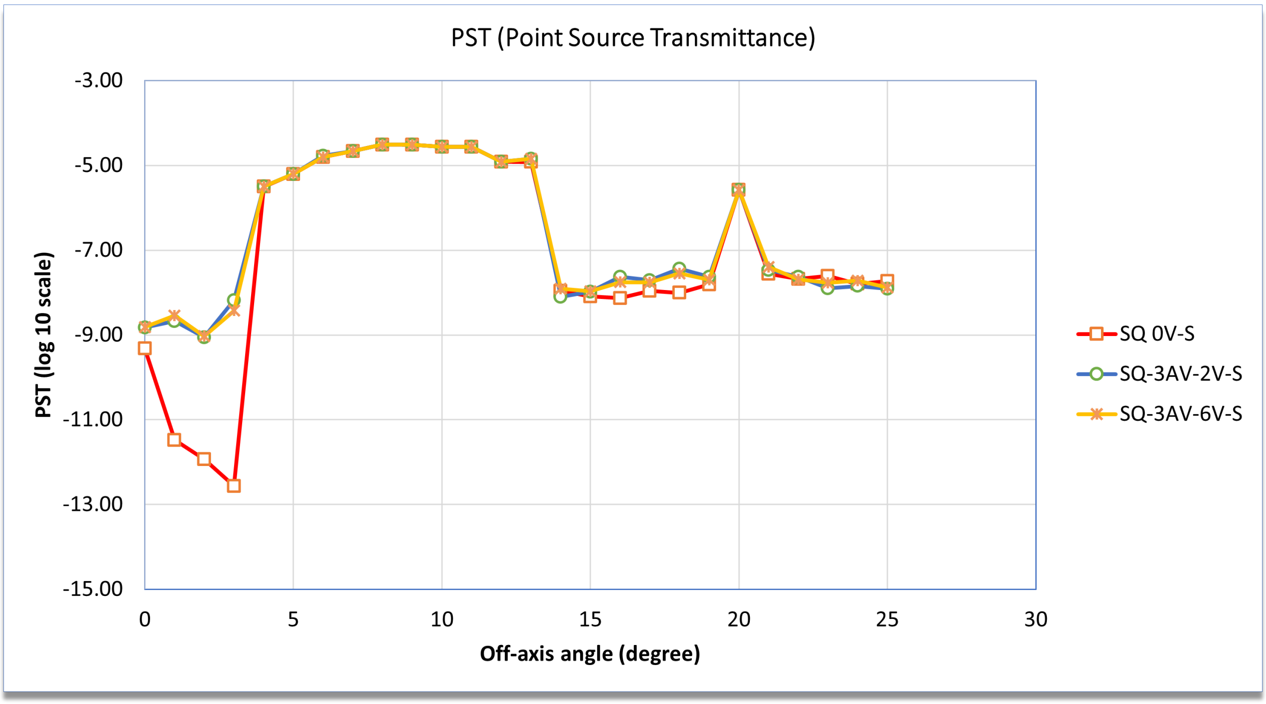

Figure 10.11: PST analysis of the straight TIR design with baffles SQ-0V, SQ-3AV-2V and SQ-3AV-6V

The analysis of the angular vanes with square baffle and fold mirror is given in Figure 10.10. Again, SQ-0V-FM performs better than SQ-3AV-2V-FM and SQ-3AV-6V-FM. The peak at 10° with SQ-3AV-2V-FM is not present with SQ-3AV-6V-FM. Most likely because the vanes of SQ-3AV-6V-FM blocks the scattered light from SQ-3AV-2V-FM from reaching the detector.

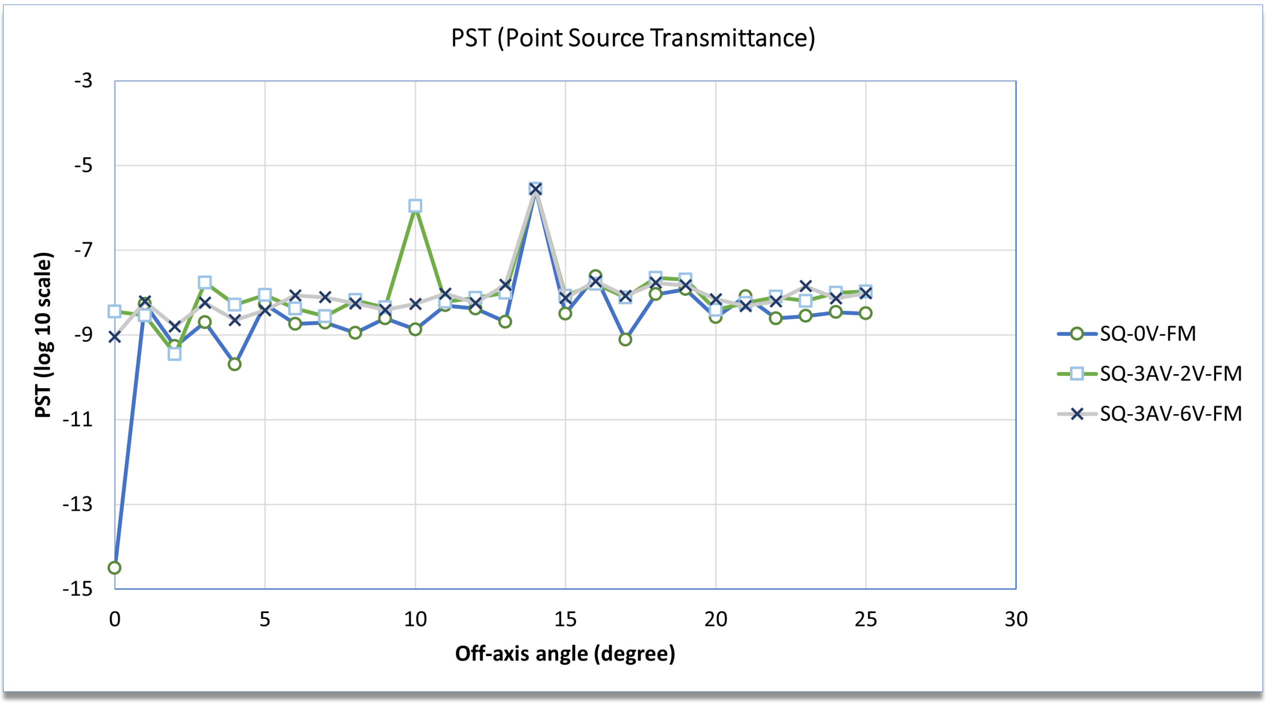

Figure 10.12: PST analysis of the fold-mirror TIR design with baffles SQ-0V, SQ-3AV-2V and SQ-3AV-6V

10.6. Stray Light Analysis: Comparison and Conclusion on TIR Baffles

In this section, the baffles are compared to eachother for a three segmented baffle. The baffles are compared to eachother for the following configurations: no vanes, single vane, seven vanes and three angular vanes with 2 straight vanes.

The stray light performance of cylindrical baffle with a straight design can be seen in Figure 10.13. The combination of C-1V-S has the least amount of stray light reaching the detector, followed by C-0V-S. The worst performer is baffle C-3AV-2V-S, which also exhibits several peaks. The baffles have the same stray light performance from 4 to 13 degrees. Comparison of C-7V-S to C-1V-S does not seem to indicate that the baffle with more vanes has a benefit in reducing the stray light performance.

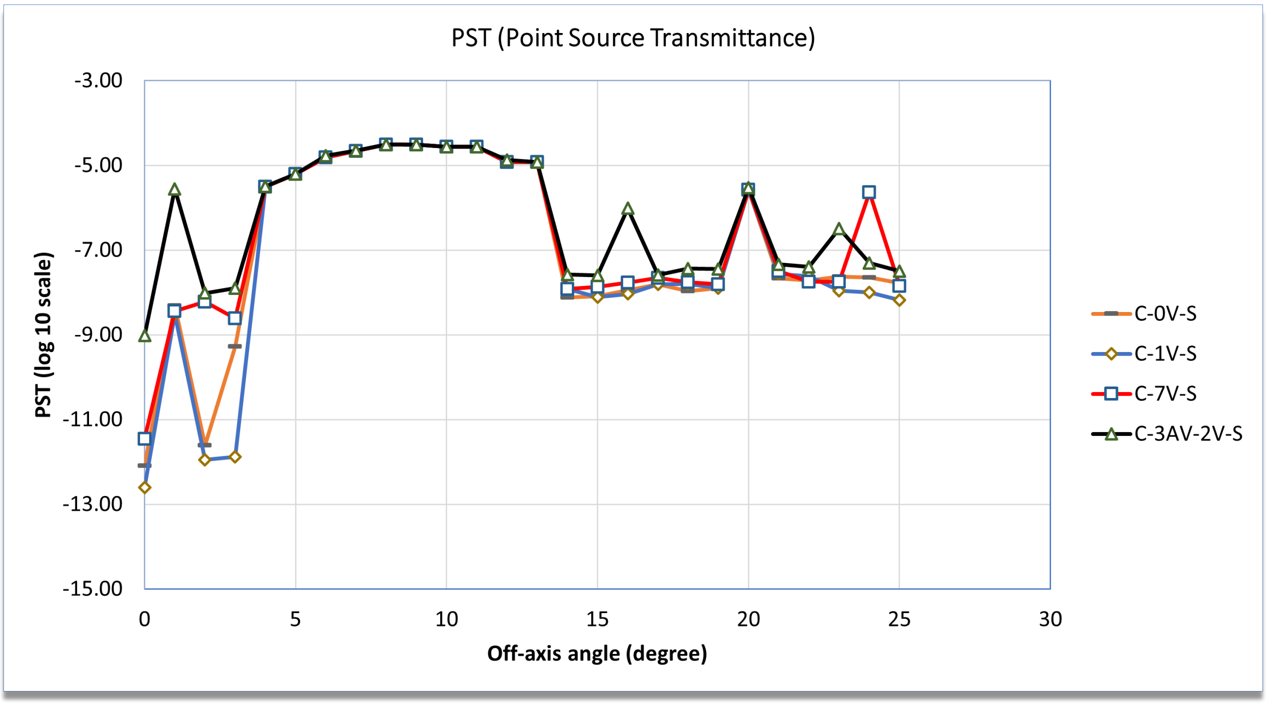

Figure 10.13: PST analysis of the straight TIR design for various cylindrical baffles

The stray light performance of the cylindrical baffles with the fold-mirror configuration is shown in Figure 10.14. Both C-0V-FM and C-1V-FM are at a lower stray light level than C-7V-FM and C-3AV-2V-FM. Baffle C-3AV-2V-FM looks to be the worst in terms of stray light performance. Furthermore, baffle C-3AV-2V-FM exhibits peaks at 16 and 23° which the other baffles do not have. These peaks can be caused by uncontrolled scatter in the baffle due to the angled orientation of the vanes near the baffle entrance. Baffle C-7V-FM also performs worse than C-0V-FM and C-1V-FM.

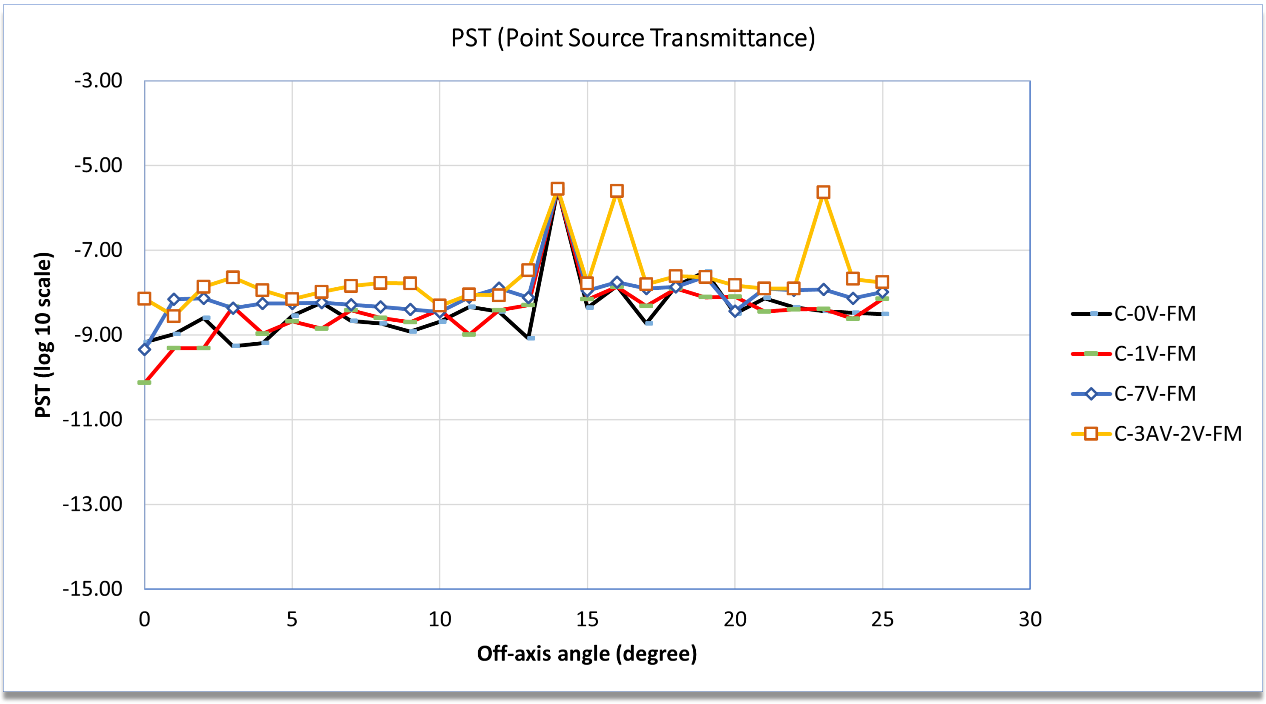

Figure 10.14: PST analysis of the fold-mirror TIR design for various cylindrical baffles

The stray light performance of the square baffles with the straight configuration is shown in Figure 10.15. At angles below 4° it is apparent that SQ-0V-S and SQ-1V-S perform better than SQ-7V-S and SQ-3AV-2V-S. As was the case with the cylindrical baffle, the square baffles have the same stray light performance from 4 to 13 degrees.

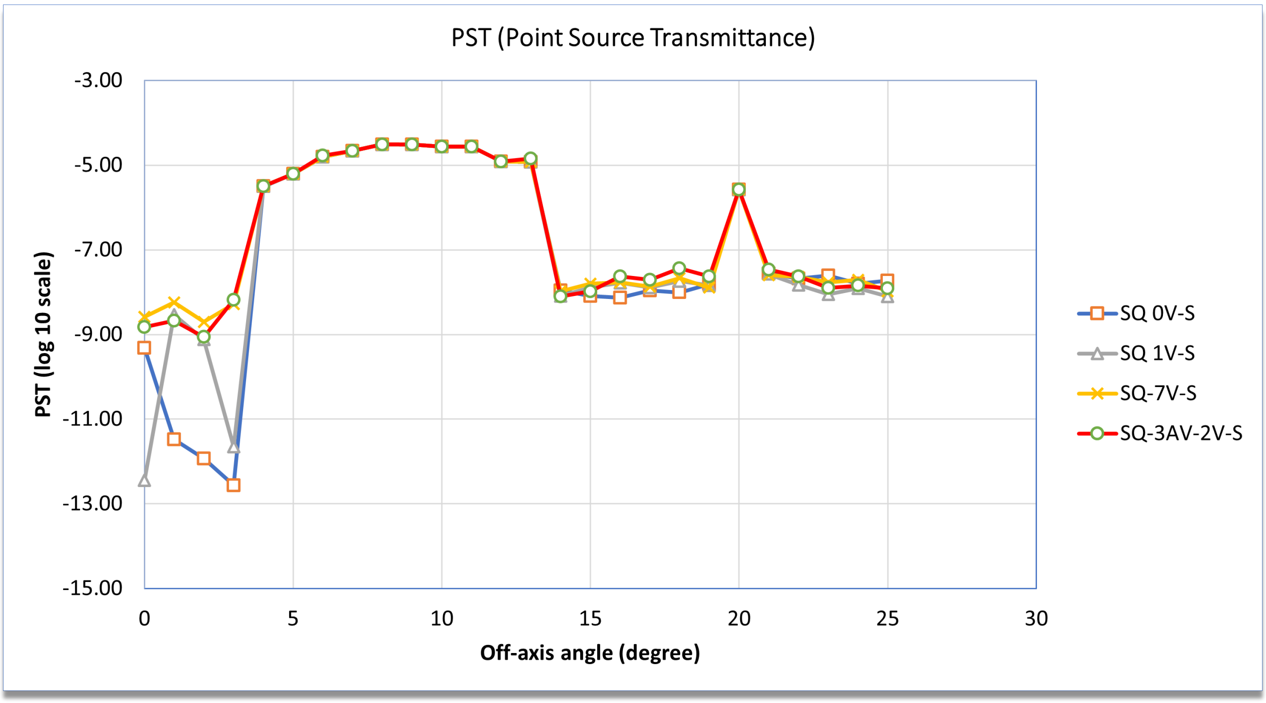

Figure 10.15: PST analysis of the straight TIR design for various square baffles

The stray light performance of the square baffles with the fold-mirror configuration is shown in Figure 10.16. Baffles SQ-0V-FM and SQ-1V-FM perform better than SQ-7V-FM and SQ-3AV-2V-FM as they have a lower amount of stray light reaching the detector. At 3°, baffle SQ-7V-FM has a peak of increased stray light reaching the detector which the other baffles do not have. Baffle SQ-3AV-2V-FM also has a peak at 10 degree which the other baffles do not have.

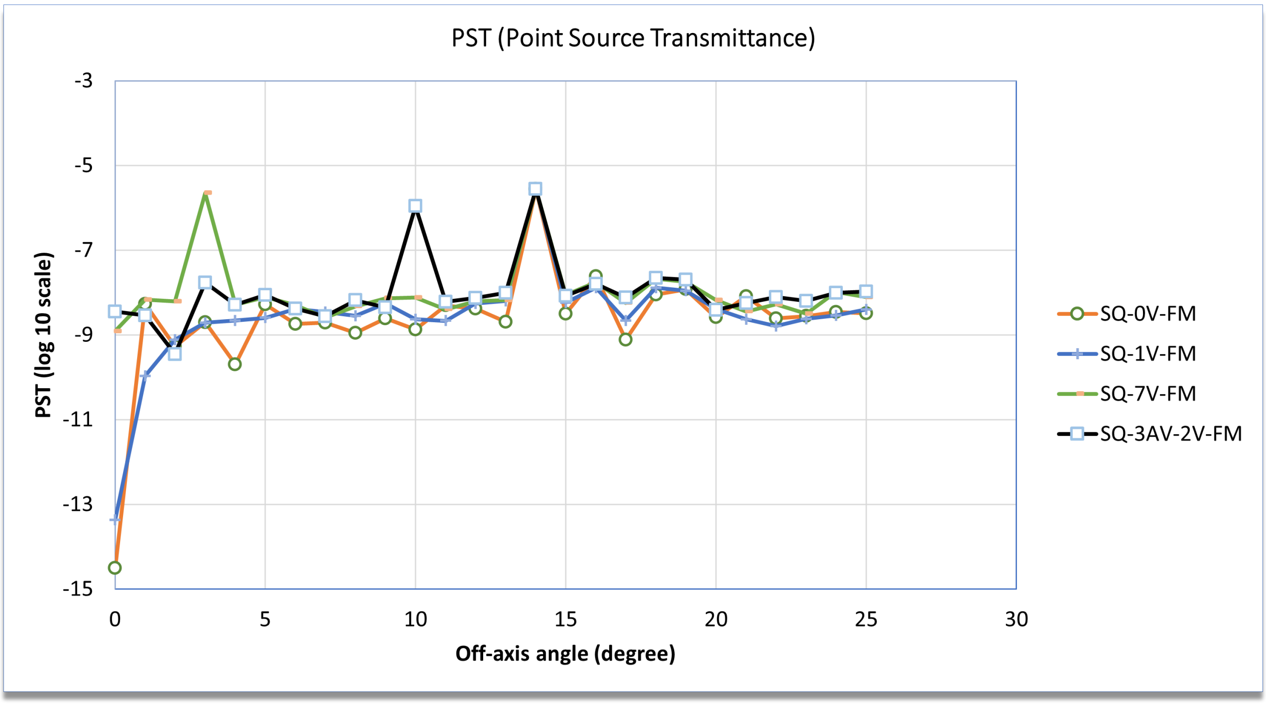

Figure 10.16: PST analysis of the fold-mirror TIR design for various square baffles

Comparison of the best performs for each of the comparisons, baffles SQ-1V-S, C-1V-S, C-1V-FM and SQ-1V-FM are taken and compared to eachother in Figure 10.17. Comparison of the straight DST configuration, there does not seem to be a large difference between the performance of SQ-1V-S and C-1V-S. The only visible difference is that C-1V-S has a lower amount of stray light reaching the detector at 2°. There is also no clear difference between C-1V-FM and SQ-1V-FM. The fold-mirror does not have a large variation in stray light performance over varying angles compared to the straight design. This is because the detector in the fold-mirror configuration is not in the same optical axis as the incoming light into the baffle. The straight version shows that from 4 to 13°, the stray light performance of the baffles are equal. This is most likely caused by optical design in combination of the size and orientation of for example stops and housing. The straight version performs worse than the fold-mirror design in terms of stray light performance.

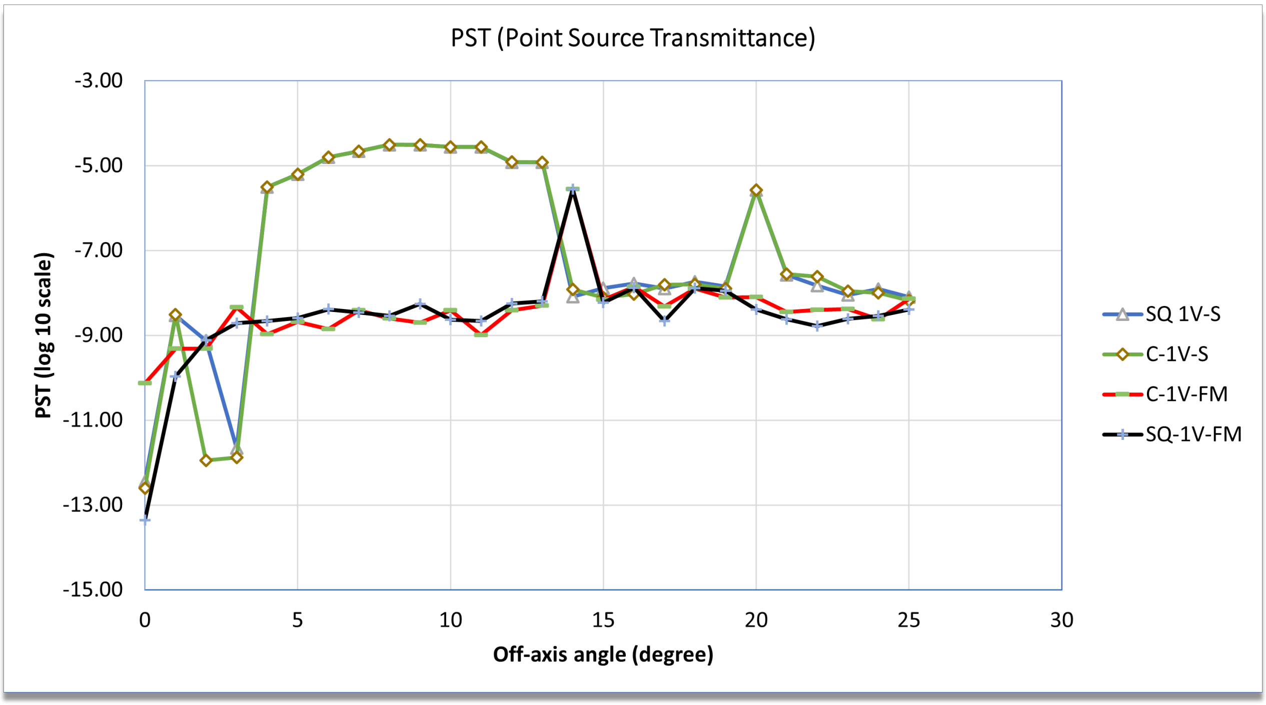

Figure 10.17: PST analysis of various baffles with 1 vane for both the straight and fold-mirror design

In conclusion, the baffle with one single vane at the entrance aperture performs the best in terms of reducing the stray light performance. The addition of multiple vanes causes more scatter within the baffle, which can lead to adverse performance in the optical system. The square version is asymmetric around the radial direction of the incoming light, which contributes to an irregular scattering of the square vanes. This leads to the square baffle being more unpredictable in terms of stray light performance. The addition of angular vanes further worsens the stray light performance. The fold-mirror performs better because the detector is not in the same axis as the incoming light. However, this is not a reason to disregard the straight version as a potential systems design due to the above mentioned factors. It should be noted that the stray light requirement is set at log(PST) = -5 according to Section 10.1. Both concepts do have some angles at which the PST is near or slightly above this set boundary. However, it can be noted that both concepts do not use the final SMSS, which is still under design [57]. In addition, the design of the internal surfaces is not finalised. Since the straight DST version barely exceed the stray light requirement, this can be deemed as a correctable deficiency. Note that the results presented of the no baffle cases do not represent the actual stray light performance. The stray light performance is far worse when no baffle is used, because protection from off-axis angles is absent. However, computing this case would take much computing time.

11

TSE Analysis of the TIR Baffles

Every structure radiates thermal energy, the amount of energy radiated is dependent on their temperature and emissivity value [28]. TSE is the radiation of thermal energy of each system component which can be picked up as noise by the detector operating in the TIR domain. If this thermal self-emission energy reaches the infrared detector, it contribute towards a stray light signal in the detectable thermal wavelength range. The DST TIR instrument operates in the 8 to 12 micron wavelength [31]. The detection of TSE is dependent on the ability of the detector to pick up the TSE signal. First, Section 11.1 describes the TSE and the formulae related to picking up the TSE. Furthermore, Section 11.1 describes the process on how the TSE is calculated through a reverse ray trace. Then, the of thermal and ray-trace models have to be combined. From the thermal model, the temperature data is acquired which is to be used for the ray-trace model. The ray-trace model further needs some modification in order to correctly assign the temperature nodes to the ray-trace model. These steps are explained in Section 11.2. The ray-trace analysis is a time exhaustive process, therefore a sensitivity analysis was performed in Section 11.3. The sensitivity analysis provides the accuracy needed to obtain suitable results. The 2D image of the TSE signal which reaches the detector can be made and is given in Section 11.4, this can provide input for software to smoothen out the TSE signal. The major contributors to the total TSE provides insight in which components form the major constituents to the TSE signal in Section 11.5. This information can help in the quest of reducing the TSE influence. The thermal resolution due to the TSE is given in Section **??**. Finally, the conclusion on TSE is given in Section 11.6.

11.1. Thermal Self Emission: Theory

The TSE in power with units W can be analysed using the following Equation [62, 64]:

$$TSE = \sum_{all\ objects} L_{object} A_{detector} (\frac{\Omega_{object}}{\pi}) = \sum_{all\ objects} \epsilon f \sigma T^4 A_{detector} (\frac{\Omega_{object}}{\pi}) \tag{11.1}$$

The TSE evaluated in irradiance with the unit $\frac{W}{m^2}$ can be analysed using the following Equation:

$$TSE = \sum_{all\ objects} L_{object} \frac{\Omega_{object}}{\pi} = \sum_{all\ objects} \epsilon f \sigma T^4 (\frac{\Omega_{object}}{\pi}) \tag{11.2}$$

In which ϵ is the emissivity coefficient of the object, σ the Stefan-Boltzmann constant, T the temperature of the object in K. The blackbody fractional power f can be computed with Equation 11.3, which FRED does with the scriptFing command *BlackBodyFractionalEnergy* [17].

$$f = \frac{\int_{\lambda_1}^{\lambda_2} L_{BB}(T_0, \lambda) d\lambda}{\int_{\lambda=0}^{\lambda_\infty} L_{BB}(T_0, \lambda) d\lambda} \tag{11.3}$$

The remaining unitless term Ω_{object}/π is then called the projected solid angle or Geometrical Configuration Factor (GCF). The power received by each object is numerically equal to its projected solid angle when the rays from the detector has a radiance equal to L = 1/ $(\pi \cdot A_{detector})$ [65]. The TSE according to Equation 11.1 is given in W. By omitting the multiplication by the detector area $A_{detector}$, the TSE will be given in irradiance with the unit $\frac{W}{m^2}$. The TSE in irradiance allows for creating a 2D image of the TSE at the detector. This will be performed in Section 11.4. The power received by each object can be retrieved through using a Graphical User Interface (GUI) function within FRED. Another method of obtaining the incident surface power is through calling the scripting command *GetSurfIncidentPower(node)* in which the node is the specified element radiating TSE. Both methods require the set-up of a reverse ray-trace. The process of setting up a reverse ray-trace can be accomplished through the following steps [64]:

1. Place a Lambertian source at the location of the detector
2. Make the reverse ray-trace source equal in size of the detector
3. Specify the emitted detector power Φ

4. Specify the ray direction

Placement of the source for the reverse ray-trace ensures that surfaces seen by the detector i.e. critical surfaces are appropriately modelled. The size of the reverse ray-trace source is specified in FRED by inputting the correct the X and Y semi-aperture values. The source of the reverse ray-trace has to be equal in size of the detector when analysing the total TSE, therefore the same X and Y semi-aperture values of the detector should be used for the source. This ensures that the source radiance is equal to L = $1/\ (\pi \cdot A_{detector})$.

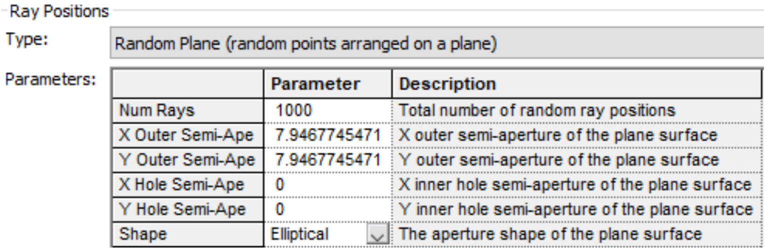

Ray Positions

Type: Random Plane (random points arranged on a plane)

Parameters:

	Parameter	Description
Num Rays	1000	Total number of random ray positions
X Outer Semi-Ape	7.9467745471	X outer semi-aperture of the plane surface
Y Outer Semi-Ape	7.9467745471	Y outer semi-aperture of the plane surface
X Hole Semi-Ape	0	X inner hole semi-aperture of the plane surface
Y Hole Semi-Ape	0	Y inner hole semi-aperture of the plane surface
Shape	Elliptical	The aperture shape of the plane surface

Figure 11.1: The X and Y semi-aperture of the source is set equal to the size of the detector which ensures that the source radiance is equal to L=$1/(\pi \cdot A_{detector})$ necessary to obtain the total thermal self emission through a reverse ray trace

The emitted detector power Φ in W was proven to be equal to [65]:

$$\Phi = sin^2\theta \tag{11.4}$$

In which θ corresponds to the half angle of the angular emission of the source. If the source emits into a hemisphere i.e. $\theta = 90°$, then the power is logically equal to 1 W. This follows from the radiative transfer of a right circular cone with a radiance of L = $1/\ (\pi \cdot A_{detector})$:

$$\Phi = L \cdot A_{det} \cdot \Omega = L \cdot A_{det} \cdot (\pi \cdot sin(\theta)^2) \tag{11.5}$$

The source can be specified in FRED to propagate into a random direction into a certain angular angle. The ray direction of the reverse ray-trace has to be pointed towards the entrance aperture. In a forward ray-trace, the source propagates towards the $(0, 0, 1)$ X, Y, Z-location. Therefore, in a reverse ray-trace the source has the forward direction in the opposite direction, thus towards $(0, 0, -1)$. The source can radiate into a cone smaller than 90 degrees. For example, it becomes less critical to let the source emit into a hemisphere when there is no relevant hardware at wide angles. In order to increase the efficiency of an analysis, the source can be specified to emit into a cone with $\theta \leq 90°$. This can be done in FRED by specifying the X and Y-angle semi-aperture degree [64]. The combination of the appropriate direction, location, size and power of the reverse ray-trace source is needed to accurately obtain the GCF through calling the GUI function "Surface Incident/Absorbed Power". An example of a source emitting into a random direction into a 15 degree cone i.e. hemisphere, can be seen in Figure 11.2.

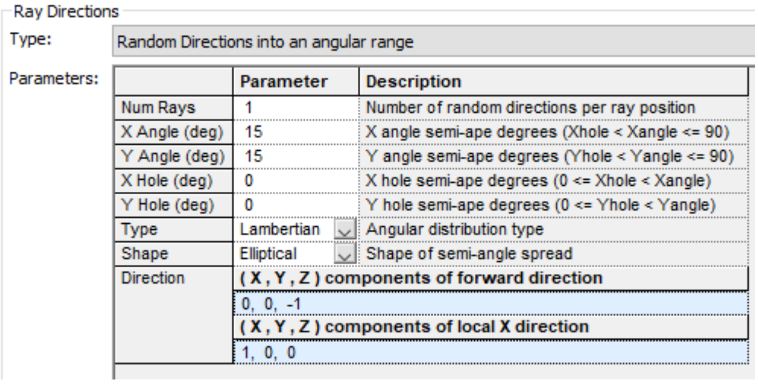

Ray Directions

Type: Random Directions into an angular range

Parameters:

	Parameter	Description
Num Rays	1	Number of random directions per ray position
X Angle (deg)	15	X angle semi-ape degrees (Xhole < Xangle <= 90)
Y Angle (deg)	15	Y angle semi-ape degrees (Yhole < Yangle <= 90)
X Hole (deg)	0	X hole semi-ape degrees (0 <= Xhole < Xangle)
Y Hole (deg)	0	Y hole semi-ape degrees (0 <= Yhole < Yangle)
Type	Lambertian	Angular distribution type
Shape	Elliptical	Shape of semi-angle spread
Direction	**(X , Y , Z) components of forward direction** 0, 0, -1 **(X , Y , Z) components of local X direction** 1, 0, 0	

Figure 11.2: Ray direction settings in FRED for a backward ray trace emitting into a cone with $\theta = 15$ °

The accuracy of the TSE 2D image is dependent on the number of rays traced and the number of pixels being evaluated. Both factors greatly influence the computation time. An increase in the number of rays leads to every pixel having to be evaluated by more rays. Increases in the amount of pixels leads to a quadratic increase in computational time. Performing the TSE in a backwards ray-trace ultimately needs far fewer rays than a forward ray-trace. This was proven by Pfisterer, who accomplished a more accurate result using a backward ray-trace which needed 50x fewer rays [65]. The sensitivity of the TSE to the number of rays traced can be found in Section 11.3

11.2. TSE Nodes

The remaining terms in assessing TSE in Equation 11.1 are the temperature T and emissivity ϵ of the object. The emissivity can be obtained through specification of the applied material on the object. The temperature of the object can be obtained through a thermal analysis programme such as ESATAN. In FRED, a CAD-file can be imported to make the mechanical object. This mechanical object is divided into structural element, each defined by a structural node. Auxiliary data such as the temperature and emissivity can be assigned to each node through manual input or using a script. In order to shorten the process of assigning auxiliary data, a script is used which sets the temperature of items in batch. The items in batch can be grouped together as there is no variation in material property and minimal variation of less than 0.1 K in temperature. The nodes are grouped into the following groups:

- Primary mirror
- Secondary mirror
- Spider
- Internal optics
- Optical house and stops
- Top CORE hinge 1
- Top CORE hinge 2
- Top CORE hinge 3
- Top CORE hinge 4
- Boom 1
- Boom 2
- Boom 3
- Boom 4

Note that the bottom CORE hinge is not taken into consideration. The current optical design of the primary mirror utilises a full circular optic. The primary mirror thus blocks the light from reaching the bottom CORE hinge. The mechanical design uses an old SMSS design. The new SMSS design improvement is under investigation by Hobijn [57]. The position of the SMSS does not have a major influence on the TSE analysis because it partially blocks light and creates a shadow. The booms would have also created a shadow if the booms were placed on the outside of the primary mirror. Since any boom would create a shadow, the preliminary analysis of the TSE using the old position and size of the boom suffices. Because the influence of the booms on the TSE will most likely not cause an order of magnitude in noise contribution [11]. The top CORE hinges and booms are grouped separately due to the uneven thermal load input from the sun. Depending on the angle of incidence of the sun, the baffle will partially reflect heat to the nearest components. The number system of the CORE hinge and booms stems from the definition of quadrants, as illustrated in Figure 11.3.

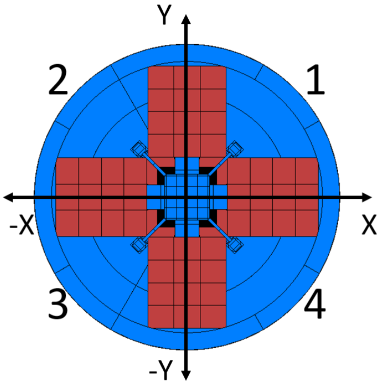

Figure 11.3: Number system used for the CORE hinge and booms according to quadrant number system

The internal baffle wall and internal side of the vane are subject to large temperature swings. This is due to the shape of the baffle, which shades some local region but not every region of the internal baffle wall. As a result, some local region of the internal baffle wall receives more thermal radiation than other regions. These local areas are the internal baffle wall near the entrance aperture and the internal wall of the baffle vane as can be seen in Figure 11.4. These heated up regions have a higher local temperature and thus require these temperatures to be accurately assigned to the nodes in the FRED model.

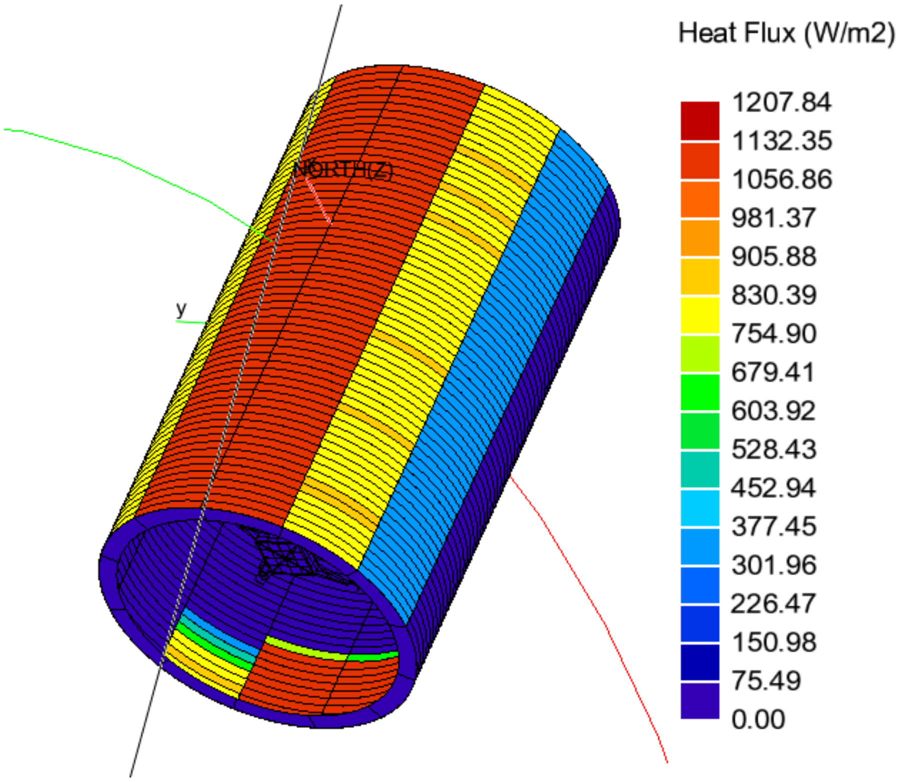

Figure 11.4: Heat flux on a cylindrical baffle in $[\frac{W}{m^2}]$ without taking into account individual material thermal optical properties

The original CAD model of the baffle used for stray light modelling has a low number of structural nodes. For example, the top half of the cylinder is represented in only two nodes: the internal wall and external wall of the top half. This can be seen in Figure 11.5. Discretisation of the CATIA model into several nodes is needed in order to match the discretisation used in ESATAN. This can be achieved by applying a mesh to the model, which allows for splitting the surface into multiple surfaces. The result can be seen in Figure 11.6. The cylindrical baffle wall in CATIA is divided into 12 segments of 30 degrees along the circumference and 14 faces of 1 cm along the height of the baffle. This discretisation corresponds to the same discretisation of the baffle used in ESATAN, with the exception of the bottom half of the baffle. As can be seen in Figure 11.4, direct radiation of the internal baffle wall due to the Sun is up to a maximum of 10 cm from the entrance. This maximum irradiance occurs prior to entering eclipse and shortly after exiting eclipse as depicted in Figure 11.4. Note that the baffle vane obscures the view of the first vane. Additional 4 cm of the internal baffle wall is taken due to the local radiative and conductive heating, followed by a single node of 46 cm which represents the remainder of the internal baffle wall.

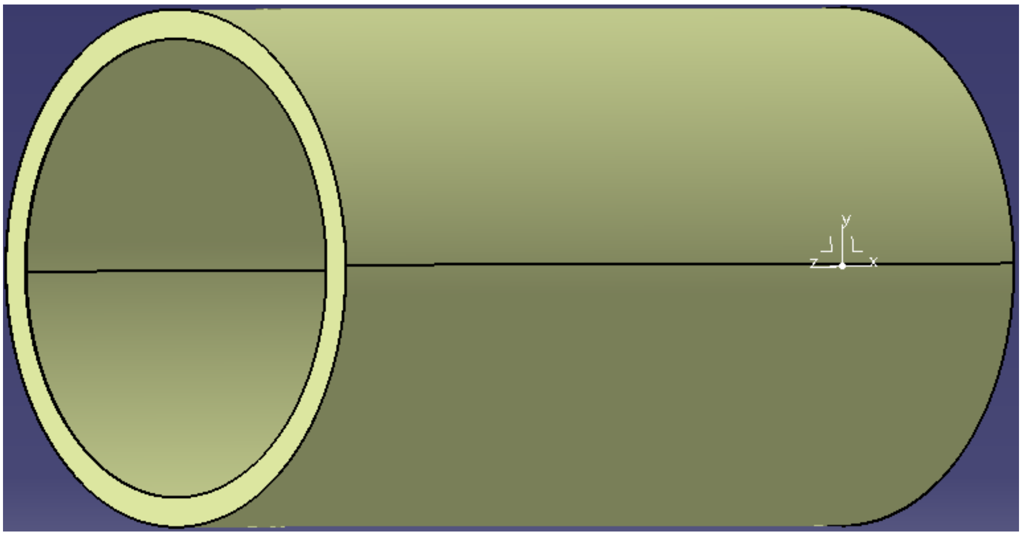

Figure 11.5: The cylindrical baffle wall without extra discretisation

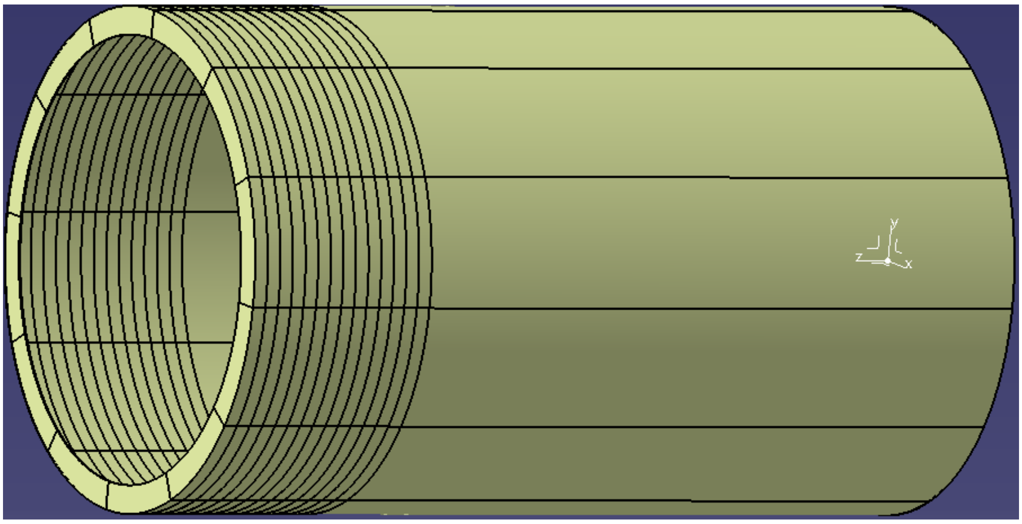

Figure 11.6: The cylindrical baffle wall from Figure 11.5 is discretised into multiple nodes at the areas of interest

Following the discretisation of nodes, the temperature of the nodes are taken at the following orbital positions according to the radiative case set in ESATAN:

1. At t = 0 s, when the bottom of the spacecraft is parallel to the line of sight of the sun with Earth at 90 degrees
2. At t = 1580 s, the moment before entering eclipse,
3. At t = 1600 s, the moment after entering eclipse,
4. At t = 3740 s, the moment before exiting eclipse,
5. At t = 3760 s, the moment after exiting eclipse,

At the orbital time of t = 0 s, the Sun vector and the z-axis of the spacecraft are parallel to eachother. The Sun directly illuminates the outside wall of the bottom of the baffle. The orbital angle according to ESATAN convention is 0 ^{o}. At t = 1580s, the spacecraft is at an orbital angle of 105 ^{o} and is right before entering eclipse. The spacecraft has been receiving sun light since exiting eclipse from the prior orbit. The components are at its maximum temperature at this moment. When the eclipse is entered, the baffle wall starts cooling down due to the absence of solar radiative heating. The moment before exiting eclipse, the temperature of the spacecraft should be at its lowest. This is due to the spacecraft not receiving solar heat for the longest duration of time. After exiting eclipse at t = 3740 s, the spacecraft will start heating up due to the added solar heat component. The orbital angle at t = 3740 s is 249 ^{o}. The solar heat component will also heat up the internal baffle wall. When the orbital angle is at 270 ^{o} the sun no longer heats up the internal baffle wall. The sun will heat up the spacecraft up to t = 1580 s. The orbit is visualised in Figure 11.7 which represents the eclipse and sunlit period.

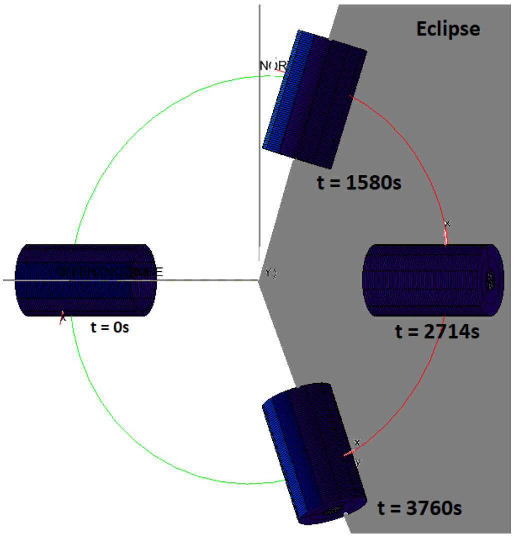

Figure 11.7: Visualisation of the eclipse and sunlit region of the orbit

11.3. TSE sensitivity analysis

The accuracy of the TSE image is dependent on the number of rays traced and the pixel sampling size used. In order to determine the amount of rays needed to provide an accurate enough data, the average irradiance is plotted against the total amount of rays traced. When a large amount of rays is traced, the signal from each ray is smoothed out over the detector. The irradiance of pixels near the edge of the detector is of several magnitudes smaller than the irradiance from pixels near the center. As can be seen in Figure 11.8, the edge of the detector is of two orders of magnitudes smaller than the rest. This is due to the positioning of the field stops which block off off-axis rays, limiting the self view of the spacecraft.

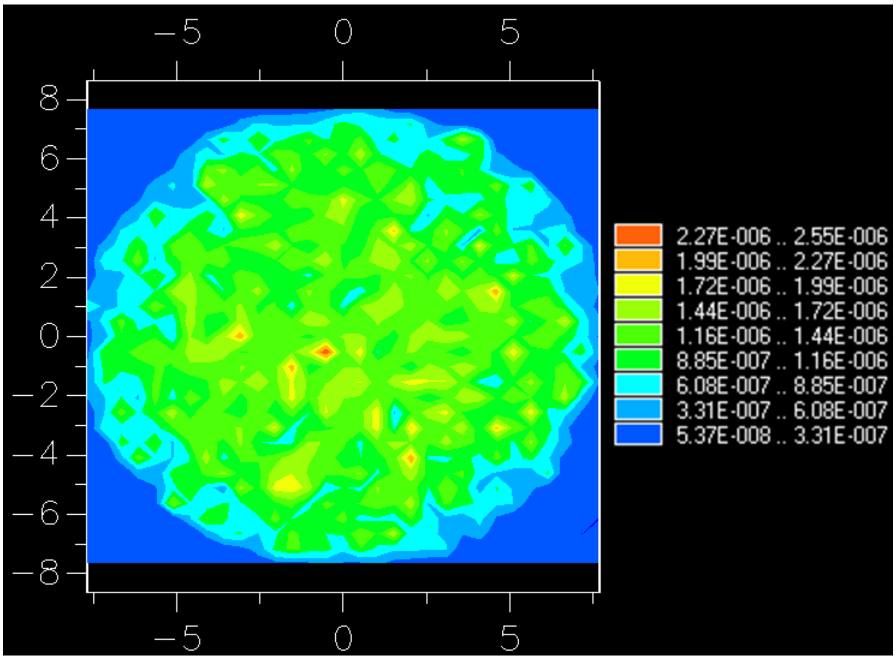

Figure 11.8: TSE irradiance distribution over the detector of a source tracing 2E5 rays at t = 3760 s

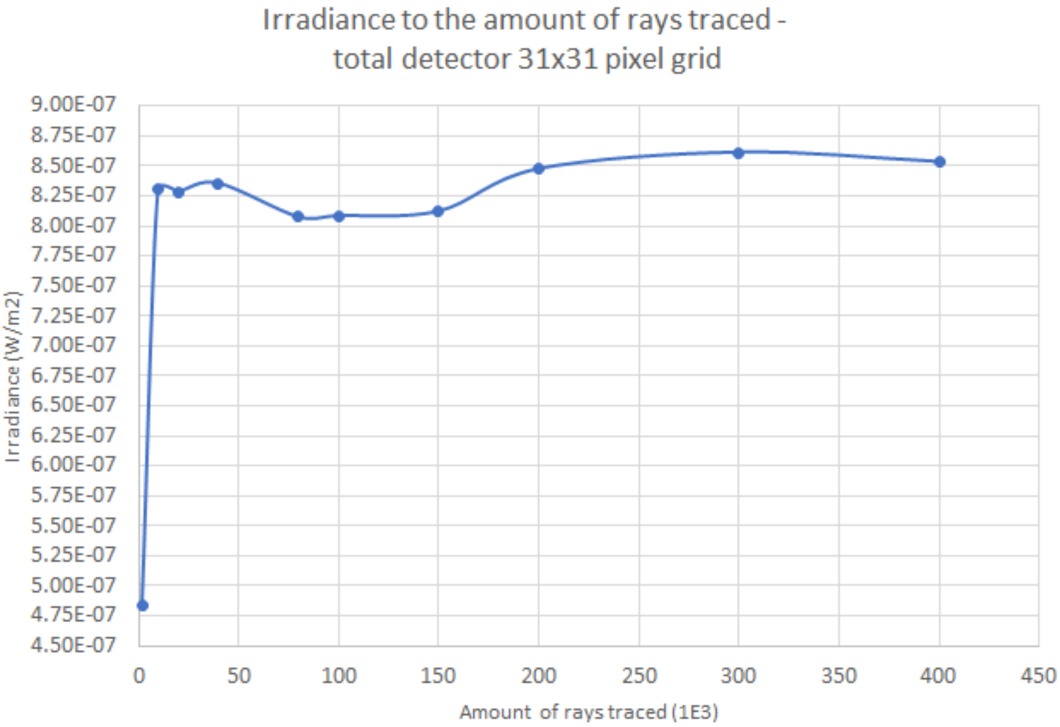

Figure 11.9: Average irradiance due to TSE in relation to the amount of rays traced from $2E3$ to $4E5$

Figure 11.9 represents the average irradiance over the entire detector. The average irradiance is taken from a source of $2E3$ to $4E5$ rays for the orbital case of t = 3740 s. At a low amount of rays traced of between $2E3$ to $8E4$ rays, the irradiance to amount of rays fluctuates. With the reverse ray-trace, only a small portion of all rays traced end up on a surface outside of the spacecraft bus due to the applied stops and internal house. When a low amount of rays is traced, the irradiance contribution of a single ray hitting a warmer element has more impact on the irradiance distribution as visualised in Figure 11.10.

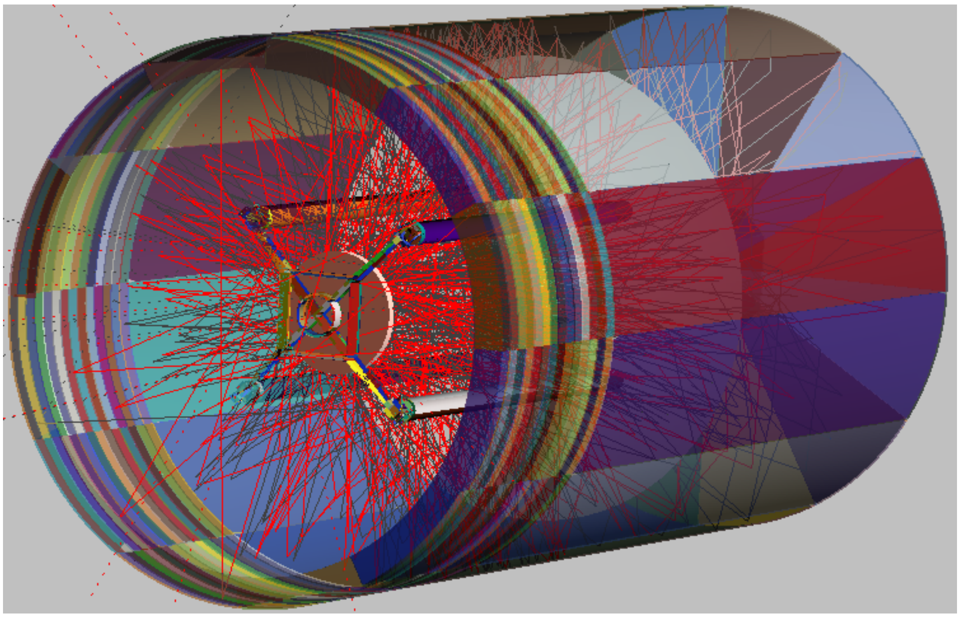

Figure 11.10: 2E2 rays are backward traced from the detector, showing that only a few rays end up near the front of the baffle

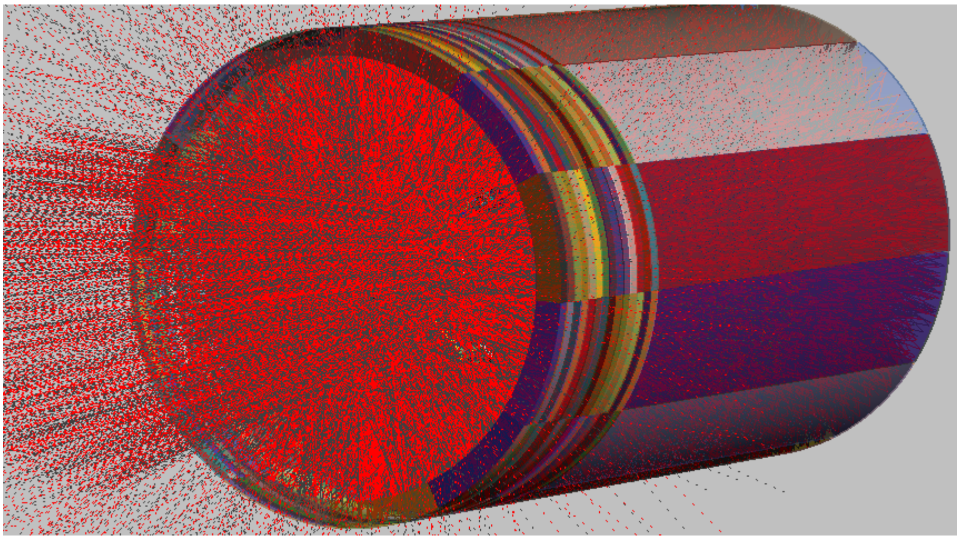

Figure 11.11: 2E4 rays are backward traced from the detector, a lot more rays end up near the front of the baffle

With a sufficient amount of rays traced, the irradiance contribution of a single ray hitting a warm element is smoothed out. By comparison, Figure 11.11 shows the same ray trace as Figure 11.10 but with two orders of magnitude more rays. It can be clearly seen that a lot more rays from the detector end up hitting the front of the baffle. As a consequence, the impact of a single ray is dampened when using a significant amount of rays, leading to a more accurate situation. As a result, the trend line of the irradiance to total amount of rays traced shows an asymptotic regression line. It can be seen from Figure that the amount of rays traced might reach an asymptote value of approximately $8.75E-7\ W/m^2$ of average irradiance over the detector. In order to reach an accuracy within 2.5% of the asymptote, a ray trace of using 2E5 rays should be used. This is the number of rays which will be used to develop the 2D image. As a reference, the original FRED TSE script selected a 250 ray source and a pixel sampling size of 31x31 [17].

11.4. TSE: 2D image

The irradiance due to TSE can be visualised by generating a 2D image of the TSE effect. In order to generate a 2D image of the TSE, raster-scanning of the source from pixel to pixel and calculation of the TSE at each pixel is needed. The FRED script which generates the thermal 2D image will raster-scan the source from pixel to pixel and calculate the TSE at each pixel [17]. This will be accomplished by analysing the irradiance of each pixel, which allows for the generation of a 2D image. The script will thus perform the following operations:

1. Reset the dimension of the source according to the pixel sampling size
2. Reset the source power according to the specified source direction
3. Loop through the position of each pixel
4. Perform a ray trace at each pixel location
5. Calculate the irradiance of each pixel through utilisation of Equation 11.2
6. Write the irradiance to a readable text-file to generate the desired 2D image

The result of the irradiance due to TSE are plotted at different locations in the orbit with a ray trace using 2E5 rays. The 2D images due to TSE at t = 75 s can be seen in Figure 11.12, at which the image is most affected by TSE. These 2D images can be used to determine the software fix needed to reduce the image artifacts due to TSE[66].

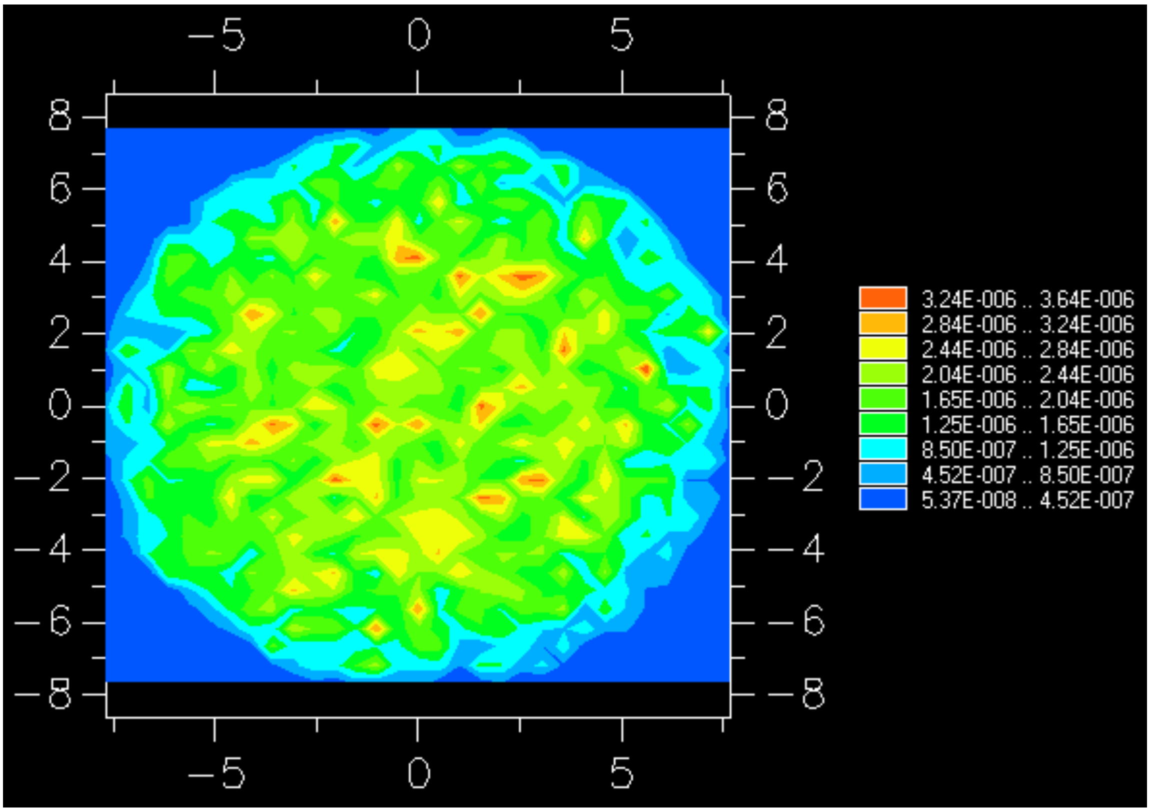

Figure 11.12: TSE irradiance distribution over the detector of a source tracing 2E5 rays at t = 750 s

At t = 1580 s, the 2D image due to TSE can be found in Figure 11.13. Because the elements inside of the baffle are less hot, the hotspots presented at a lower intensity. This is logical because the temperature of a component greatly influences the TSE.

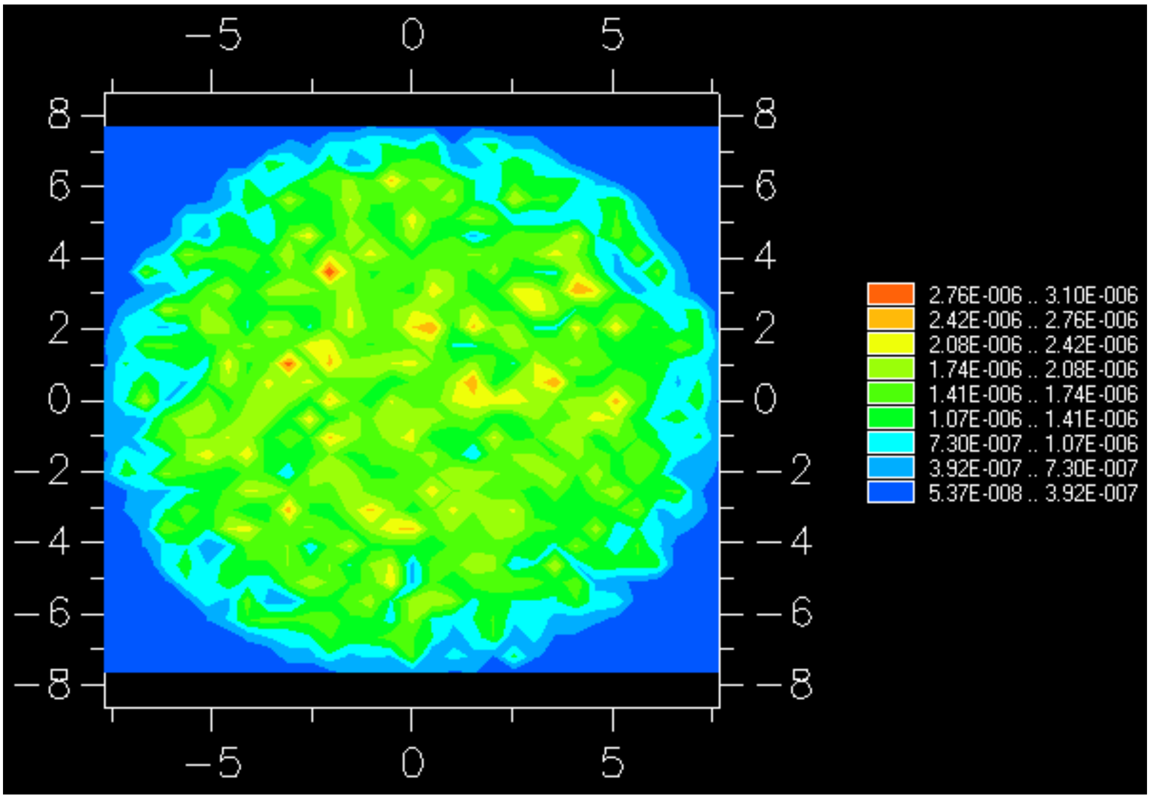

Figure 11.13: TSE irradiance distribution over the detector of a source tracing 2E5 rays at t = 1580 s

At t = 3740 s, the elements inside of the baffle are at the coolest point. The largest peak has decreased from 3.64E-6 W/m^2 at t = 750 s, to 2.36E-6 W/m^2 at t = 3740 s.

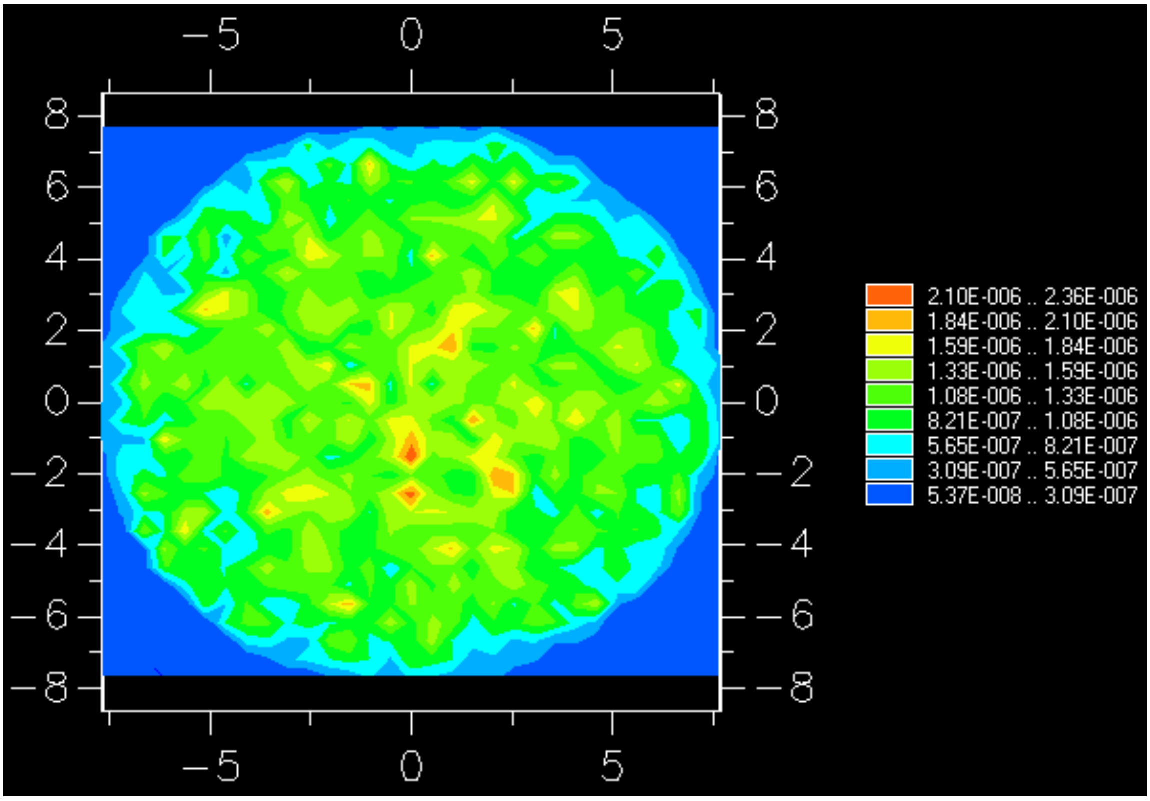

Figure 11.14: TSE irradiance distribution over the detector of a source tracing 2E5 rays at t = 3740 s

11.5. Total TSE Contribution

In this section, the contribution of the TSE of the components is discussed. In order to obtain the total TSE, the backward ray trace source is made equally large to the detector surface. This is in contrast to obtaining the 2D image as was explained in Section 11.4. Because the source is made larger than with the 2D image analysis, the average amount of rays per source size decreases. Therefore, more rays are needed to evaluate the total TSE contribution due to the increase in source area. The total TSE is evaluated for four different amount of rays from 2E5 to 2E6 rays. The orbital timestamp chosen to evaluate the TSE is at t = 3740 s. The total TSE contribution of the entire spacecraft according to the amount of rays traced is given in Table 11.1. It can be seen that the total TSE converges towards a value of approximately 2.8E-4 W/m^2. Using 1E6 rays for evaluating the total TSE leads to a TSE of 2.74E-4 W/m^2. This is within 2.5% of the analysis using 2E6 rays. Therefore, the total TSE evaluated with 1E6 rays should provide a good representation of the total TSE. The TSE signals enters the internal optical house. As a result, the optics will raise in temperature and will pass on the TSE signal towards the next optics mainly through radiative heat transfer. With each subsequent passing, a part of the heat will be dissipated and weakened in signal due to radiative and conductive loss to the surrounding elements. This will continue until the TSE signal reaches the detector. The detector will thus only experience the TSE signal from the last optical element[58].

Table 11.1: Total TSE and the amount of rays traced at orbital timestamp of t = 3740s

Total amount of rays [-]	Total TSE [W/m^2]
2E5	3.4E-4
3E5	2.93E-4
1E6	2.74E-4
2E6	2.75E-4

The contribution per component is grouped according to Section 11.2, along with the contribution of the baffle in Table 11.2 at t = 3740s. From this table, the contribution of the spider is clearly the largest at 62.05%. In addition, the secondary mirror has self-view from the detector, which is logical since it has a direct path from the detector to the secondary mirror. Whereas there is no direct path from the primary mirror to the detector. Therefore the TSE contribution of the primary mirror is smaller than the secondary mirror. The internal optics except for their edges are set at full transmission, leading to a small percentage in contribution. The tabulated approach allows for changing the temperature or emissivity value of the component, without having to perform the ray trace again. Note that the temperature in the overall TSE tables are rounded off. However, these numbers are not rounded off in the analysis.

Table 11.2: Overall TSE contribution per group along with the grouped contribution, temperature and emissivity of each group at the orbital timestamp of t = 3740s

	T_{avg} [K]	Emissivity [-]	GCF [-]	TSE [W]	Contribution
Primary mirror	273	0.035	1.76E-3	1.18E-6	0.44%
Secondary mirror	278	0.035	8.71E-2	6.47E-5	23.86%
Internal optics	200	0.035	2.33	4.01E-6	1.48%
Optical house and stops	200	0.01	3.38E-1	1.92E-5	7.09%
Spider	262	0.99	1.13E-2	1.68E-4	62.05%
Top CORE hinge 1	267	0.99	4.00E-6	6.7E-8	0.03%
Top CORE hinge 2	267	0.99	2.03E-6	3.43E-8	0.01%
Top CORE hinge 3	267	0.99	1.7E-5	2.87E-7	0.11%
Top CORE hinge 4	268	0.99	2.72E-7	4.55E-9	0.002%
Boom 1	253	0.99	2.24E-4	2.82E-6	1.04%
Boom 2	253	0.99	2.39E-4	3.01E-6	1.11%
Boom 3	253	0.99	2.3E-4	2.90E-6	1.07%
Boom 4	253	0.99	2.25E-5	2.84E-6	1.05%
Baffle	251	0.84	1.9E-4	1.79E-6	0.66%
Total	-	-	2.77	2.75E-4	100%

Evaluating the total TSE at the warmest point of the orbit at t = 1580s, the total TSE and contribution can be found in Table 11.3. Due to the Sun radiating the internal baffle wall, the components near the baffle entrance warm up as expected. Even though some regions of the internal baffle wall reaches a temperature of 415K, the TSE contribution of the baffle is still small. It can be concluded from these two total TSE analyses, that the largest contributing factor to the TSE is the spider. In order to reduce the contribution of the spider if needed, the spider can either be made smaller, reduce the temperature of the spider or have a lower emissivity value. Because the self-view of the baffle is very small, the contribution of the baffle to the TSE is only 1%. But due to radiative coupling of the baffle to the other components, the other components such as the booms and CORE hinge and spider heat up as well.

Table 11.3: Overall TSE contribution per group along with the grouped contribution, temperature and emissivity of each group at the orbital timestamp of t = 1580s

	T_{avg} $[K]$	Emissivity $[-]$	GCF $[-]$	TSE $[W]$	Contribution
Primary mirror	280	0.035	1.76E-3	1.40E-6	0.39%
Secondary mirror	280	0.035	8.71E-2	6.92E-5	19.26%
Internal optics	200	0.035	2.33	4.01E-6	1.12%
Optical house and stops	200	0.01	3.38E-1	1.92E-5	5.36%
Spider	276	0.99	1.13E-2	2.41E-4	67.02%
Top CORE hinge 1	278	0.99	4.00E-6	8.82E-8	0.02%
Top CORE hinge 2	280	0.99	2.03E-6	4.55E-8	0.01%
Top CORE hinge 3	280	0.99	1.7E-5	3.81E-7	0.11%
Top CORE hinge 4	278	0.99	2.72E-7	5.98E-9	0.002%
Boom 1	277	0.99	2.24E-4	4.83E-6	1.35%
Boom 2	276	0.99	2.39E-4	5.10E-6	1.42%
Boom 3	276	0.99	2.3E-4	4.91E-6	1.37%
Boom 4	277	0.99	2.25E-5	4.94E-6	1.35%
Baffle	285	0.84	1.9E-4	4.37E-6	1.22%
Total	-	-	2.77	3.59E-4	100%

Shortly after entering eclipse, the temperature drops. This is visible in the temperature of the baffle and components near the baffle entrance. The effect on the thermal self emission of the component is given in Table 11.4.

Table 11.4: Overall TSE contribution per group along with the grouped contribution, temperature and emissivity of each group at the orbital timestamp of t = 1600s

	T_{avg} [K]	Emissivity [-]	GCF [-]	TSE [W]	Contribution
Primary mirror	280	0.035	1.76E-3	1.34E-6	0.39%
Secondary mirror	280	0.035	8.71E-2	6.64E-5	19.35%
Internal optics	200	0.035	2.33	4.01E-6	1.17%
Optical house and stops	200	0.01	3.38E-1	1.92E-5	5.60%
Spider	276	0.99	1.13E-2	2.29E-4	66.74%
Top CORE hinge 1	267	0.99	4.00E-6	8.46E-8	0.02%
Top CORE hinge 2	279	0.99	2.03E-6	4.38E-8	0.01%
Top CORE hinge 3	279	0.99	1.7E-5	3.67E-7	0.11%
Top CORE hinge 4	279	0.99	2.72E-7	5.74E-9	0.002%
Boom 1	277	0.99	2.24E-4	4.61E-6	1.34%
Boom 2	277	0.99	2.39E-4	4.87E-6	1.42%
Boom 3	277	0.99	2.3E-4	4.69E-6	1.37%
Boom 4	277	0.99	2.25E-5	4.64E-6	1.35%
Baffle	282	0.84	1.9E-4	3.81E-6	1.11%
Total	-	-	2.77	3.43E-4	100%

When exiting the eclipse, the contribution of the TSE per component was already given by Table 11.2. The baffle continuous to rotate towards the sun and at t = 0 s, the bottom of the baffle wall is pointed towards the sun. The contribution of the TSE per component at t = 0 s is given by Table 11.5.

Table 11.5: Overall TSE contribution per group along with the grouped contribution, temperature and emissivity of each group at the orbital timestamp of t = 0s

	T_{avg} [K]	Emissivity [-]	GCF [-]	TSE [W]	Contribution
Primary mirror	276	0.035	1.76E-3	1.27E-6	0.31%
Secondary mirror	279	0.035	8.71E-2	6.59E-5	16.32%
Internal optics	200	0.035	2.33	4.01E-6	1.00%
Optical house and stops	200	0.01	3.38E-1	1.92E-5	4.76%
Spider	288	0.99	1.13E-2	2.83E-4	70.05%
Top CORE hinge 1	280	0.99	4.00E-6	8.76E-8	0.02%
Top CORE hinge 2	280	0.99	2.03E-6	4.41E-8	0.01%
Top CORE hinge 3	280	0.99	1.7E-5	3.69E-7	0.09%
Top CORE hinge 4	280	0.99	2.72E-7	5.91E-9	0.002%
Boom 1	294	0.99	2.24E-4	6.25E-6	1.55%
Boom 2	294	0.99	2.39E-4	6.66E-6	1.65%
Boom 3	294	0.99	2.3E-4	6.44E-6	1.59%
Boom 4	294	0.99	2.25E-5	6.33E-6	1.57%
Baffle	293	0.84	1.9E-4	4.28E-6	1.06%
Total	-	-	2.77	4.04E-4	100%

The maximum temperature of the baffle internal wall is reached at approximately 750 s into the orbit. The temperatures of the components are increased. This in turn leads to the highest TSE values for the DST during the whole orbit as can be seen in Table 11.6.

Table 11.6: Overall TSE contribution per group along with the grouped contribution, temperature and emissivity of each group at the orbital timestamp of t = 750s

	T_{avg} [K]	Emissivity [-]	GCF [-]	TSE [W]	Contribution
Primary mirror	279	0.035	1.76E-3	1.32E-6	0.32%
Secondary mirror	280	0.035	8.71E-2	6.64E-5	16.07%
Internal optics	200	0.035	2.33	4.01E-6	0.97%
Optical house and stops	200	0.01	3.38E-1	1.92E-5	4.66%
Spider	290	0.99	1.13E-2	2.90E-4	70.23%
Top CORE hinge 1	283	0.99	4.00E-6	9.11E-8	0.02%
Top CORE hinge 2	283	0.99	2.03E-6	4.59E-8	0.01%
Top CORE hinge 3	283	0.99	1.7E-5	3.84E-7	0.09%
Top CORE hinge 4	283	0.99	2.72E-7	6.16E-9	0.002%
Boom 1	298	0.99	2.24E-4	6.59E-6	1.60%
Boom 2	297	0.99	2.39E-4	6.98E-6	1.69%
Boom 3	297	0.99	2.3E-4	6.72E-6	1.63%
Boom 4	298	0.99	2.25E-5	6.65E-6	1.61%
Baffle	298	0.84	1.9E-4	4.52E-6	1.09%
Total	-	-	2.77	4.13E-4	100%

11.6. Conclusion on TSE

Each structural element within a system emits thermal noise. Because the detector for the TIR DST operates in the thermal infrared domain, it is capable of picking up the thermal radiation from its own structure. This TSE signal will contribute as stray light. Generation of a 2D image of the TSE provides information on the influence of TSE as stray light. If the TSE signal is high enough, image artifacts could be present on the taken thermal image. These image artifacts can be minimised through for example applying a software fix [66]. The software fix reduces the artifacts which are determined through comparison with a baseline thermal image. The baseline thermal image is an image pointed at for example cold space [11]. The image artifacts that show up on the baseline thermal image are then only from TSE. Throughout the orbit, the influence due to TSE changes due to the changing thermal environment. This is due to the rotation of the spacecraft relative to the sun or the spacecraft moving in or out of eclipse. The TSE is most severe at t = 800 s, which produces a TSE peak of 3.64 W/m^2 on the detector. Therefore, multiple baseline thermal images need to be taken at several instances in the orbit to establish the baseline reading of only the TSE of the spacecraft itself. When looking at the primary contributor to the TSE noise, the spider mechanism stands out with a 70% contribution. The second largest contributor to TSE is the secondary mirror at 16 %. The design of the baffle effectively minimises the TSE signal from the baffle to 1% of the total TSE.

Several strategies were identified in reducing the TSE. As the detector pixel will only see the last optical element, cooling the temperature of the last optical element is highly efficient at reducing the TSE that will be observed by the detector. Furthermore, the detector should be thermally insulated from the rest of the spacecraft. This is achieved through a cooled detector module which surrounds the detector. Reduction of the TSE signal entering the internal optical house can be achieved by reducing the GCF, the temperature or applying a low emissivity coating.

12

Trade-off and Baffle Selection: DST TIR

The results of the various analysis can be combined to form a graphical trade-off. The criteria used to determine the graphical trade-off are the stray light performance, thermal performance and the deployment complexity of each baffle. The shape of the baffle was determined through thermal analysis in Section 9.3 to be in favour of the cylindrical baffle class. The cylindrical baffle provided a consistent decrease in in-orbit drift of 1 μm less than the square baffle variations across the various different baffle vane arrangements. Thus the options for the graphical trade-off used, are only the cylindrical baffles. The main objective of the baffle is to decrease the in-orbit drift and provide a suitable temperature range for the components whilst being feasible. The secondary objective is to comply to the stray light requirements. Therefore, the weight criteria of the stray light is less than the criteria for the thermal performance and deployment complexity. The baffles comply to the stray light requirements. The side note is that a new stray light analysis should be performed after including the updated SMSS and internal optical house. Because the current stray light analysis of the baffles is performed with old SMSS design. This can be the cause of the cylindrical baffles with the straight optical design, to be on or right over the edge of compliance with the stray light requirements. The thermal performance of the baffles was formed from the thermal analysis on the baffles, in which baffle C-0V had the highest range in temperature of the components. The other baffles had a more favourable decrease in temperature ranges. The deployment complexity was filled in based upon the team discussion regarding the deployment feasibility of the concepts. The baffle with no vane and one vane were deemed to have the highest chance of probability of having a successful deployment. This is because the C-0V and C-1V vane do not inhibit the deployment of the other subsystems. Baffle concept with multiple straight vanes i.e. C-7V, C-11V, C-3AV-2V, C-3AV-6V have multiple vanes at which multiple points of failures can occur. The deployment of the angular vanes were deemed to be significantly more complex due to the cone shape. The scores of the graphical trade-off for the cylindrical baffle concepts is summarised in Table 12.1.

Table 12.1: Graphical trade-off for the TIR baffle selection

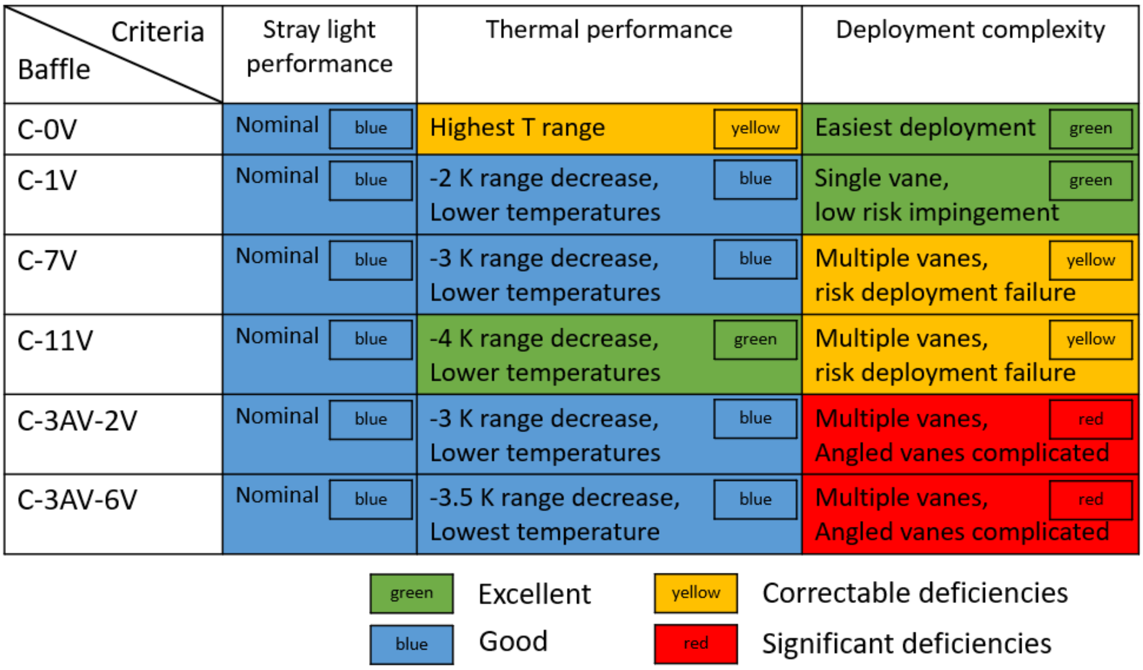

Criteria / Baffle	Stray light performance	Thermal performance	Deployment complexity
C-0V	Nominal blue	Highest T range yellow	Easiest deployment green
C-1V	Nominal blue	-2 K range decrease, Lower temperatures blue	Single vane, low risk impingement green
C-7V	Nominal blue	-3 K range decrease, Lower temperatures blue	Multiple vanes, risk deployment failure yellow
C-11V	Nominal blue	-4 K range decrease, Lower temperatures green	Multiple vanes, risk deployment failure yellow
C-3AV-2V	Nominal blue	-3 K range decrease, Lower temperatures blue	Multiple vanes, Angled vanes complicated red
C-3AV-6V	Nominal blue	-3.5 K range decrease, Lowest temperature blue	Multiple vanes, Angled vanes complicated red

green	Excellent	yellow	Correctable deficiencies
blue	Good	red	Significant deficiencies

From this graphical trade-off, the best performing baffle is C-1V. The selected baffle for the TIR concept is therefore C-1V i.e. the cylindrical baffle with one vane at the entrance of the baffle. Baffle C-1V can be seen in Figure 12.1 with the straight DST version. The baffle is suited for use of both the fold-mirror and the straight DST version according to top-level systems considerations. The baffle has a length of 60 cm, because this length of the baffle would still be suitable for use with the longer straight version. The baffle extends 8 cm above the spider, such that baffle shades the spider. This prevents rapid warm-up and cooling down of the spider through preventing radiative heat transfer from the sun to the spider. The baffle has a diameter of 35 cm. This leads to a total, MLI area of 1.21 m^2. The extra space between the primary mirror and the baffle wall ensures enough room for the secondary mirror support structures to be deployed. The vane has a depth of 19 mm to prevent vignetting. The baffle can be divided into either two segments of 30 cm or three segments of 20 cm. The baffle and vane consists of two layers of MLI with a Magic Black coating on the internal baffle wall for a total wall thickness of 0.506 mm [18]. The bulk density of MLI is 146 kg/m^3 which gives a total baffle wall mass of 0.09 kg without the deployment system.

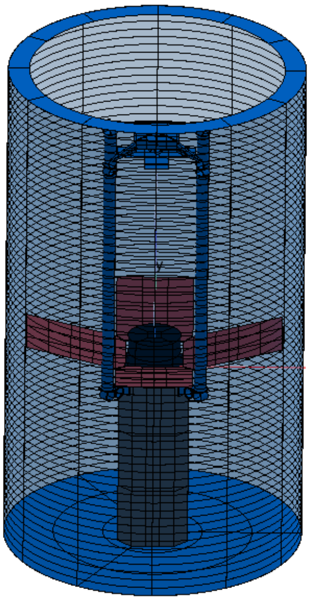

Figure 12.1: The final baffle design for the TIR version: baffle C-1V

The stray light performance of C-1V is comfortably within the requirements when comparing to the state-of-art of TIR Earth-Observation satellites. Due to the single vane, there are less surfaces to cause random scatter within the baffle. The design of the optical system for stray light protection was already good due to the usage multiple stop surfaces. The fold-mirror presented a better stray light performance than the straight version. This is because after the rays hit the fold-mirror, the ray direction is changed. The off-axis rays miss the fold-mirror. While the accepted rays propagate further towards the detector.

13

Conclusion and Future Work

13.1. Conclusion

The thesis goal was reached by providing a design for the deployable baffle for the VIS and TIR DST which improves the stability of the temperature and keep the stray light level low. The stray light from TSE of the TIR DST baffle only contributes to 1% of the total TSE entering the system. The improvements made with the baffle contribute to better observational data by minimising noise.

Obtaining this goal was reached through answer the research questions. The main research question was:
"Can the drift between the primary and secondary mirror of the DST be reduced by applying stray light design methodology?"
Improvement of the baffle through application of stray light reducing geometries i.e. vanes, lead to a more stable temperature environment. This decreases the effect of thermal expansion i.e. drift on the distance between the primary and secondary mirror. The compliance to the in-orbit drift for the VIS-DST baffle from Arink was at 13% [3]. Through applying more vanes and changing the orientation of the baffle, the compliance increased to 40% for the VIS design during the observation phase of the orbit. The baffle for the TIR design has a compliance of 100% to the in-orbit drift budget. This can be attributed to the relaxed budget. Because the operating wavelength was increased for the TIR to 8 micron.

This was accomplished through answering the research questions:
Which factors influence the drift between the primary and secondary mirror?"
Temperature changes leads to thermal expansion and compression of the components, which changes the position i.e. drift or defocus between components. The temperature change is related to a change in environment. The largest difference in drift is caused by the spacecraft moving in and out of eclipse. Decreasing the temperature range through which the components are exposed to, decreases the amount of drift. The components which largely influence the drift are the hinges, booms and rods which hold the secondary mirror. Minimising the temperature change of these components minimises the drift.

"Which changes to the baffle can be made by applying stray light methodology?"
From literature study, multiple methods for stray light design appeared. There are two baffle concepts: an absorbing baffle and a reflective baffle design. The more commonly used absorbing baffle, uses high absorptive coatings to absorb as much incoming light as possible. The other type is the reflective baffle. The reflective baffle uses reflective coatings or materials and are often enhanced with reflective vane designs. The reflective vanes are placed under a very specific angle or have a unique curvature. This is done such that the focus point of each vane works together as a reflective system. These reflective vanes are highly sensitive to change in orientation. The wrong orientation of a reflective vane greatly diminish their performance. The deployment accuracy needed for reflective vanes is deemed to be too difficult for reflective baffle systems with the current technology. The geometry of the baffle was also investigated. The cylindrical baffle is the most common baffle, because of the symmetry along the radial direction. This symmetry eliminates the occurrence of surfaces joining together into a corner, which can induce more scatter. Approximation of the cylindrical baffles are for example the square, hexagon and octagonal shaped baffle which has one symmetrical plane along the radial direction. However, these shapes lead to joining of corners which is less than ideal. Another change to the baffle which can be made is the implementation of a sugar scoop. The sugar scoop takes away some of the baffle wall area. This can result in removal of walls which would otherwise reflect light back into the baffle. The removal of baffle wall area furthermore leads to weight savings.

"How do these changes influence the thermal stability within the baffle?"
Application of vanes act as a barrier to block the further propagation of light entering the baffle. Logically, larger vanes block off more light from entering the baffle. Utilisation of low absorbing coatings reduce the thermal energy that is absorbed. Furthermore, the energy that the rays carries on each subsequent bounce become less. Multiple

vanes lead to a decrease in temperature of the components. The addition of one vane to a vaneless baffle gave the largest decrease in temperature. Adding more vanes results in a decrease in temperature of the components. However, the decrease in temperature for the components became less effective with each addition of a subsequent vane. Angled vanes could reflect part of the energy outwards towards space. The baffles using angled vanes had less of a temperature change due to either entering or exiting eclipse. Utilisation of angled vanes lead to a reduction in temperature range of up to 3 K. Therefore having a more stable temperature environment. The sugar-scoop baffle has a more open design, which does not maintain the heat well within the spacecraft. This leads to a rapid decrease in temperature and leads to large temperature swings, which increases the in-orbit drift a lot. Furthermore, it needs to be paired with a system to rotate the baffle (or spacecraft) with the orientation of the sun. Such that the long face of the baffle is continuously facing the sun. The selected shape of the baffle which can most closely wrap around the shape of the primary mirror is the most effective at minimising temperatures. This is because the cross-sectional area determines how much thermal energy is received by the baffle. The smallest cross-sectional area is the cylindrical shape, in case a circular primary mirror is used. The cylindrical baffle had the lower temperature range compared to a square shaped baffle. The orientation of the baffle can influences the allowed vane depth. For example, the rotation of the baffle for the VIS design allowed for the vanes to have a larger depth according to the imposed requirement. Due to the larger depth, the vanes were larger and hence block off more light from reaching the detector.

"How do these changes influence the stray light performance of the system?"
Reduction in total amount of light entering the baffle improves the stray light performance of a system. This can be achieved by the application of vanes. Logically, larger vanes block off more light, therefore increasing the stray light performance. Multiple vanes block off and reduce the energy of light on each subsequent bounce. However, the addition of more vanes, does increase the amount of surfaces on which light can scatter. As a result, the stray light performance was diminished on some off-axis angle due to the induced scatter. The usage of more angled vanes lead to more unpredicted scatter directions, leading to a worsening stray light performance. In the analysis of the stray light performance, it became apparent that the VIS DST already had an inherent good protection against stray light. Rays from off-axis sources that are reflected from M1 to M2 are largely rejected and do not pass through the field stop. This already blocks off a lot of stray light. Furthermore, placement of additional stop surfaces limit further propagation of off-axis rays. For the TIR version, the stray light performance was close to or slightly exceeded the stray light requirement for the TIR straight version. Since there are still inefficiencies in the system left, the slight under performance of the straight version is deemed to be a correctable deficiency. Improvements to the stray light performance can be obtained through further optimisation of the internal optical house. The fold-mirror TIR design had a full compliance to the stray light requirement for every baffle. The influence of TSE was also analysed for the TIR DST. The largest contributor to the TSE signal was by far the contribution of the spider at 70%. Even though temperatures of the baffle interior wall were high, the view the detector made with the baffle was very small. As a result, the baffle contribution to TSE was only 1%.

13.2. Recommendations and Future Work

In this section, the recommendation and future work that have appeared from the work on the thesis is given. Some items may be future work or remain open for the next generation of DST members to work out. Due to the various type of analyses and designs, not everything could be sufficiently explored or worked out in detail. The recommendation and future work is split up into two segments: top-level and design refinements.

13.2.1. Top-Level

The recommendations on top-level decisions is given in this Section. These are decisions that the team should make, along with their stakeholders. The compliance to the in-orbit drift budget for the VIS baffle falls short at 40%. The passively cooled baffle does not suffice in bringing down the defocus between M1 and M2 such that it falls within the in-orbit drift budget. Some possible top-level decisions which could aid the VIS DST are given in this section. The combination of improvements hopefully leads to a full compliance to the in-orbit drift budget. The analysis on the TIR DST baffle shows that the feasibility is high. However, some top-level decisions still need to be taken or investigated to converge towards one TIR design.

Change in Orbital Parameters: VIS DST

Both the VIS DST and TIR DST are currently designed to operate in a sun-synchronous orbit around the Earth. As a result, the spacecraft moves in and out of the eclipse of the Earth. This causes a large swing in temperature, which causes thermal expansion. One possibility could be to change the orbit towards a dawn-dusk orbit. The dawn-dusk orbit puts a shadow on some components but illuminates the opposite part with sunlight. The implementation of a dawn-dusk orbit could decrease the temperature swings, which minimise the in-orbit drift. The more stable dawn-dusk orbit paired with a sugar-scoop baffle could further increase the compliance to the in-orbit drift budget for the VIS DST design.

Actively Cooled Baffle: VIS DST

An actively cooled baffle for the VIS DST could bring down the experienced temperature fluctuations. In the sunlit period of the orbit, active cooling can bring down the temperature. Whereas heaters during the eclipse period could bring the temperature up. This decreases the temperature range of the components. However, an actively cooled baffle puts a large demand on the power budget for the DST. This could require additional solar panels will lead to an increase in weight and cost of the VIS DST.

Sunshield: VIS DST

The usage of a sunshield could be implemented. If the sunshield is able to provide a (near) constant shadow of the DST, it can create a stable operating temperature environment. This decreases the variation in thermal expansion, which is favorable for the in-orbit drift budget. However, the implementation of a sunshield requires it to be deployable and controllable.

Optical Model: TIR DST

It remains unclear whether the fold-mirror design should be used over the straight design. The top-level design on which optical model should be selected for the TIR DST is still dependent on the performance of the cooling requirements for the detector. The fold-mirror design reduces the cooling needs for the detector. The cooling of the detector might require the usage of additional appendages such as a radiator surface. The placement for the radiator panel is made easier with the fold-mirror design. This is because it will be easier to place the radiator in the shade of the spacecraft. The choice for optical system also depends on the need for carrying-over lessons learned from the small-scale to the large-scale TIR DST. One of the downsides of using the fold-mirror design is the difficulty to scale up to a much larger system. The fold-mirror increases with the size of M1. This could lead to a large spacecraft bus which dimensions is paired to the size of the fold-mirror, making it unattractive to use for a large scale design.

13.2.2. Design Refinements

This section discusses further refinements for both the VIS and TIR DST. The refinements presented in this section are non exhaustive to the DST, rather they came up during this thesis work.

Internal Optical House Design & SNR Ratio: TIR DST

Currently, the internal optical house has not been optimised or fully developed yet for the TIR DST. Some stops are present in the optical design, along with a rough cylinder placed around the internal optics. Internal baffling or vanes can improve the blockage or even decouple the detector from thermal noise. Furthermore, it remains a question whether the internal optical house needs to be cooled and to what temperature. Therefore, development of the internal optical house will provide more information on detector cooling needs and the overall thermal design. The designed baffle suppresses the noise signals from thermal, stray light and TSE sources. After selecting the detector, the signal to noise ratio can be calculated for the DST. From this analysis, the required temperature of the detector module and detector can be calculated. This will provide design requirements for the thermal cooling and design of the detector and detector module.

Spider Redesign

In the TSE analysis, it became apparent that the largest contributor to TSE was the spider structure. The spider structure should be redesigned to make it smaller. Reducing the influence of the spider on the TSE could be achieved by reducing the GCF, temperature or apply a different coating. The spider design used for the TIR DST was a simply scaled down version of the spider. Redesign of the spider, by making it smaller or less in the FOV of the detector can reduce the GCF. If the spider is made smaller, there is less area which can absorb thermal energy. The application of a different coating with lower emissivity can furthermore decrease TSE from the spider.

Baffle Deployment System TIR DST

The baffle deployment system for the TIR DST has not been detailed yet. Similar thesis work to Nagy his deployment system for the VIS DST, could be done for the TIR DST [18]. In which a thesis is dedicated to designing a deployment system for the TIR DST.

Bibliography

[1] D. Dolkens, *A Deployable Telescope for Sub-Meter Resolutions from MicroSatellite Platforms.* Master Thesis, Delft University of Technology, 2015.

[2] S. Pepper, *Design of a primary mirror fine positioning mechanism for a deployable space telescope.* Master Thesis, Delft University of Technology, 2018.

[3] J. W. Arink, *Thermal-Mechanical Design of a Baffle for the Deployable Space Telescope.* Master Thesis, Delft University of Technology, 2019.

[4] E. Fest, *Stray Light Analysis and Control.* SPIE: Society of Photo-Optical Instrumentation Engineers, 2013. ISBN: 9780819493255.

[5] D. F. Rock, A. D. Warren, and A. J. Lewanski, "Use Of Reflective Baffles For Control Of Aperture Heat Loads And Stray Radiation," in *Optical Systems Engineering II*, vol. 0330, pp. 60 – 67, International Society for Optics and Photonics, SPIE, 1982.

[6] G. Peterson, S. Johnston, and J. Thomas, *Specular Baffles.* SPIE: Society of Photo-Optical Instrumentation Engineers, 1993.

[7] J. Haring and N. Pastuszka, "Design considerations for compound parabolic concentrators," 2018. URL: `https://www.optiforms.com/download/cpc-essentials/` [Retrieved: 2 Februari 2020].

[8] P. A. Warren, M. J. Silver, B. J. Dobson, and H. A. MacEwen, "Experimental characterization of deployable outer barrel assemblies for large space telescopes," in *UV/Optical/IR Space Telescopes and Instruments: Innovative Technologies and Concepts VI*, vol. 8860, pp. 49 – 61, International Society for Optics and Photonics, SPIE, 2013.

[9] K. Seiferlin, S. Chakraborty, K. Gunderson, J. Fischer, B. Lyuthi, D. Pizza, M. Rieder, M. Sigrist, N. Thomas, and T. Weigel, "Design and manufacture of a lightweight reflective baffle for the bepicolombo laser altimeter," *Optical Engineering*, vol. 46, no. 4, April 2007.

[10] K. S. et al, "Exo-c stdt final report," *NASA*, March 2015.

[11] D. Dolkens. Personal communication.

[12] I. Akkerhuis, *Deployable Space Telescope, redesign of the Secondary Mirror Support Structure.* Delft University of Technology, 2020.

[13] J. Shore, R. Blows, A. Viquerat, G. S. Aglietti, D. Gooding, and G. Richardson, "a New Generation of Deployable Optics for Earth Observation Using Small Satellites," no. September, 2019.

[14] X. Liu, F. Xing, S. Fan, and Z. You, "A compressed and high-accuracy star tracker with on-orbit deployable baffle for remote sensing cubesats," *Remote Sensing*, vol. 13, no. 13, 2021.

[15] DigitalGlobe, "Satellite information." `https://www.digitalglobe.com/resources#resource-table` [Retrieved: 17 December 2019].

[16] E. Korhonen, *Design of a Deployable Baffle for the Deployable Space Telescope.* Master Thesis, Delft University of Technology, 2019.

[17] P. Engineering, "Photon engineering optical software and services." `https://photonengr.com/` [Retrieved: 17 July 2020].

[18] V. Nagy, *Design of a Novel Deployable Baffle for a Deployable Space Telescope.* Master Thesis, Delft University of Technology, 2021.

[19] L. Wood, "Euroconsult report on satellite-based earth observation: Market prospects to 2026." `https://www.businesswire.com/news/home/20171219006127/en/` [Retrieved: 17 December 2019].

[20] G. Denis, A. Claverie, X. Pasco, J.-P. Darnis, B. de Maupeou, M. Lafaye, and E. Morel", “"towards disruptions in earth observation? new earth observation systems and markets evolution: Possible scenarios and impacts",” *"Acta Astronautica"*, vol. "137", pp. "415 – 433", "2017".

[21] M. Smith, “Enhancedview news not so rosy for geoeye.” `https://spacepolicyonline.com/news/enhancedview-news-not-so-rosy-for-geoeye/` [Retrieved: 17 December 2019].

[22] A. Kamp, *Space Instrumentation Engineering lecture notes AE4880*. Delft University of Technology, 2007.

[23] B. V. Putten, *Design of the Deployment Mechanism for the Primary Mirror Elements of a Deployable Space Telescope*. Master Thesis, Delft University of Technology, 2017.

[24] M. Corvers, *Design of a Primary Mirror Deployment Mechanism for a Deployable Space Telescope*. Master Thesis, Delft University of Technology, 2018.

[25] M. Bass, V. N. Mahajan, and E. V. Stryland, *Handbook of Optics Volume II*. McGraw-Hill, 2010. ISBN: 978-0-07-163314-7.

[26] A. Krikken, *Design of the Secondary Mirror Support System for the Deployable Space Telescope*. Master Thesis, Delft University of Technology, 2018.

[27] M. Voorn, *Initiating the Testing Phase of a Deployable Space Telescope: An Experimental Characterisation of Hysteresis in CORE Hinges*. Master Thesis, Delft University of Technology, 2019.

[28] P. Bely, *The Design and Construction of Large Optical Telescopes*. Springer, New York, 2003. ISBN: 0-387-95512-7.

[29] P. Yoder, *Mounting Optics in Optical Instruments*. SPIE Press, second edition, 2008. ISBN: 978-0-8194-7129-1.

[30] T. van Wees, *Thermal Modelling and Analysis of the Deployable Space Telescope*. Master Thesis, Delft University of Technology, 2019.

[31] R.-J. de Vries, *Implementation of an automated Systems Engineering Toolset in the DST project*. Delft University of Technology, 2021.

[32] P. Giesen and E. Folgering, *Design guidelines for thermal stability in opto-mechanical instruments*, vol. 5176, pages 126-135. Optomechanics 2003, 2003.

[33] J. Doenecke, “Survey and evaluation of multilayer insulation heat transfer measurements,” in *International Conference On Environmental Systems*, SAE International, jul 1993.

[34] D. G. Gilmore, *Spacecraft Thermal Control Handbook*. The Aerospace Press, 2002. EAN: 9781884989117.

[35] T. Megson, *Aircraft Structures for Engineering Students*. Elsevier Science, 2012. ISBN: 9780080969060.

[36] NASA, “The sunshield webb.” `https://jwst.nasa.gov/content/observatory/sunshield.html` [Retrieved: 17 December 2019].

[37] L. Kauder, *Spacecraft Thermal Control Coatings References*. NASA Center for Aerospace Information, 2005.

[38] V. Y. Terebizh, “Optimal baffle design in a cassegrain telescope,” *Experimental Astronomy*, vol. 11 (3):, pp. 171 – 191, 2017.

[39] P. S. R.A. Rondeau, D.R. Askins, *Composite Materials Handbook*, vol. 2. SAE International, 2005. ISBN: 978-0-7680-8450-4.

[40] L. Boer. Personal communication.

[41] J. Viertl, R. Greger, M. D. Domenico, L. Francou, M. Ellouzi, S. Blum, K. Kudielka, T. Weigel, E. R. Grond, and D. Piazza, “Development of a light-weight beryllium Cassegrain telescope: from the optical design to the performance measurement,” in *Optical Systems Design 2012* (L. Mazuray, R. Wartmann, A. P. Wood, M. C. de la Fuente, J.-L. M. Tissot, J. M. Raynor, D. G. Smith, F. Wyrowski, A. Erdmann, T. E. Kidger, S. David, and P. Benítez, eds.), vol. 8550, pp. 355 – 362, International Society for Optics and Photonics, SPIE, 2012.

[42] D. Boyd and H. Kuiper, “The Compound Parabolic/Elliiptic Lightshades: Near-Optimal Shading for Cold Radiators,” vol. 2000-01-2278, SAE Technical Paper, 2000.

[43] C. Smits, “Strooilichtanalyse aan passive koelers,” Master’s thesis, Technische Universiteit Eindhoven, 1997.

[44] K. Du, K. Yin, H. Li, S. Liao, and F. Long, "Design and analysis of a novel self-deployable baffle," in *International Symposium on Photoelectronic Detection and Imaging 2013: Infrared Imaging and Applications* (H. Gong, Z. Shi, Q. Chen, and J. Lu, eds.), vol. 8907, pp. 1316 – 1324, International Society for Optics and Photonics, SPIE, 2013.

[45] T. Weigel, E. Rugi-Grond, and K. Kudielka, "Straylight analysis of the bepicolombo laser altimeter," *Proc. SPIE, Optical Design and Engineering III*, vol. 7100, 2008.

[46] E. Rugi-Grond, T. Weigel, A. Herren, and M. D. Calvo, "Reflective baffle for Bepicolombo mission," in *International Conference on Space Optics — ICSO 2006*, vol. 10567, pp. 990 – 998, International Society for Optics and Photonics, SPIE, 2019.

[47] R. Li and S. Wang, "Thermal analysis of the baffle structure of the solar space telescope," *Science China Physics, Mechanics and Astronomy*, vol. 53, no. 9, 2010.

[48] R. P. Breault, "Problems And Techniques In Stray Radiation Suppression," pp. 2–23, sep 1977.

[49] X. Zhong, Z. Su, G. Zhang, Z. Chen, Y. Meng, D. Li, and Y. Liu, "Analysis and reduction of solar stray light in the nighttime imaging camera of luojia-1 satellite," *Sensors*, vol. 19, no. 1130, 2019.

[50] M. Patel, *Spacecraft Power Systems.* CRC Press, 2005. ISBN: 0-8493-2786-5.

[51] K. Wakker, *Fundamentals of Astrodynamics.* Delft University of Technology, 2015.

[52] B. Research, "Asap - breault research." `https://www.breault.com/software/asap-nextgen` [Retrieved: 17 July 2020].

[53] L. R. Corporation, "Tracepro." `https://lambdares.com/` [Retrieved: 17 July 2020].

[54] D. Dolkens and H. Kuiper, "Design and end-to-end modelling of a deployable telescope," in *International Conference on Space Optics — ICSO 2016* (B. Cugny, N. Karafolas, and Z. Sodnik, eds.), vol. 10562, pp. 630 – 638, International Society for Optics and Photonics, SPIE, 2017.

[55] Acktar, "Vacuum Black." `https://www.acktar.com/product/vacuum-black/` [Retrieved: 23 Februari 2021].

[56] V. Parma, "Cryostat design," *CAS-CERN Accelerator School: Superconductivity for Accelerators - Proceedings*, pp. 353–399, 2014.

[57] C. Hobijn. Personal communication.

[58] H. Kuiper. Personal communication.

[59] J. Antonenko, "Bepicolombo technology status review. eads-st," 2005.

[60] A. Smith, "Ecss-e-hb-31-01-part1a-2011," in *ECSS-E-HB-31-01-Part1A-2011*, no. December, pp. 443–458, Imperial College Press, feb 2004.

[61] M. Montanaro, J. McCorkel, J. Tveekrem, J. Stauder, A. Lunsford, E. Mentzell, J. Hair, and D. Reuter, "Landsat 9 Thermal Infrared Sensor 2 preliminary stray light assessment," *International Geoscience and Remote Sensing Symposium (IGARSS)*, vol. 2018-July, pp. 8853–8856, 2018.

[62] J. R. Zheng, J. Lawrence, R. Content, V. Churilov, K. Zhang, X. Yuan, and H. Lu, "Antarctic Surveying Telescope (AST3-3) NIR camera for the Kunlun Infrared Sky Survey (KISS): thermal optimization and system performance," *Modeling, Systems Engineering, and Project Management for Astronomy VI*, vol. 9911, no. June, p. 99111H, 2016.

[63] Y. Du, Y. He, H. Chen, W. Xin, and B. Xue, "Calculation method of earth-atmosphere stray light illuminance on low-orbit space cameras," *Journal of Multimedia*, vol. 8, no. 6, pp. 699–704, 2013.

[64] R. Irvin. FRED - Photon Engineering, Personal communication.

[65] R. N. Pfisterer, *Clever tricks in optical engineering*, vol. 5524. oct 2004.

[66] A. Gerace and M. Montanaro, "Derivation and validation of the stray light correction algorithm for the thermal infrared sensor onboard landsat 8," *Remote Sensing of Environment*, vol. 191, pp. 246–257, 2017.

A

Scripts

A.1. Updated Solution Control (ESATAN)

```
C
      NLOOP=100
      RELXCA=0.01
      CALL SOLVFM
C
C
      TIMEND=5674.57667425507
      OUTINT=50
      NLOOP=100
      RELXCA=0.01
      DTIMEI=20.0
      CALL SOLCYC('SLCRNC',0.01D0,0.01D0,5674.57667425507D0,30,' ','NONE')
C
      CALL SLCRNC
C
```